

AN ABSTRACT OF THE THESIS OF

David B. Haley for the degree of Master of Science in Mechanical Engineering presented on June 3, 2011.

Title: Performance Characterization of an Integrated Microscale Hydrogen Combustor Recuperator and Oil Heat Exchanger

Abstract approved:

Vinod Narayanan

Experiments on a novel, microscale hydrogen combustor heat exchanger (μ CHX) are presented in this thesis. The μ CHX has been designed to efficiently transfer thermal energy to a heat transfer fluid for use in desorption of hydrogen from a metal hydride storage system of a hydrogen-powered fuel cell vehicle. The experimental study demonstrates proof of concept for the design and examines the effect of varying selected fluidic and geometric conditions on the overall efficiency of the μ CHX.

The small-scale device characterized in this thesis is a unit cell consisting of a combustion channel, a recuperator channel and an oil heat exchange channel. This unit cell device has the potential to be scaled up to a reactor in the tens of kilowatts range required for a vehicle scale system. Combusted gases flow back through the device in a counter-flow configuration between the combustion channel and the oil channel, preheating the inlet gas stream and transferring heat to the oil. Platinum has been selectively deposited on the stainless steel inner wall of the combustion channel to facilitate heterogeneous combustion of hydrogen and air. The performance of the μ CHX is characterized based on a global efficiency, defined as the ratio of the energy transferred to the oil stream compared to the energy content of the supplied hydrogen gas.

The effects of residence time, equivalence ratio and average oil temperature have been investigated. Repeated testing of the catalyst over 80 hours indicated stable and repeatable results. Maximum hydrogen conversion in excess of 92 % was achieved for residence times

greater than 20 ms at a stoichiometric equivalence ratio. Efficiencies above 90 % were obtained for equivalence ratios greater than 0.5 and for average oil temperatures between 63 °C and 105 °C. Experiments were conducted with catalyst deposited over 87 % and 20 % of the channel length. The longer catalyst demonstrated the highest efficiency and hydrogen conversion.

This work was performed concurrently with the development of a CFD model by Ghazvini and Narayanan [1] with preliminary comparisons showed qualitatively good agreement. A preliminary design and financial analysis of a full size combustor was developed based on the demonstrated performance of the μ CHX.

©Copyright by David B. Haley
June 3, 2011
All Rights Reserved

Performance Characterization of an Integrated Microscale Hydrogen Combustor Recuperator
and Oil Heat Exchanger

by
David B. Haley

A THESIS

submitted to

Oregon State University

in partial fulfillment of
the requirements for the
degree of

Master of Science

Presented June 3, 2011
Commencement June 2012

Master of Science thesis of David B. Haley presented on June 3, 2011

APPROVED:

Major Professor, representing Mechanical Engineering

Head of the School of Mechanical, Industrial, and Manufacturing Engineering

Dean of the Graduate School

I understand that my thesis will become part of the permanent collection of Oregon State University libraries. My signature below authorizes release of my thesis to any reader upon request.

David B. Haley, Author

ACKNOWLEDGEMENTS

I'm very grateful for the many people who have directly or indirectly supported me with this research. To my wife Sarah: for being a constant source of support, especially during the late nights and weekends spent in the lab. To my parents: for instilling in me the desire to learn and perform my best. To Dr. Vinod Narayanan: for his advice, patience and support. To Dr. Raymond Brooks: for his guidance and support with the financial analysis. To Jack Rundel: for his much-needed assistance with all the MBI facilities, most notably the laser tool, atomic layer deposition tool and the sputter tool. To Teresa Sawyer: for her assistance with SEM imaging. To Florian Kapsenberg and Ruander Cardenas: for their ideas and engineering experience. To Nick Auyeung: for his assistance with the gas chromatograph. To Dr. Brian Paul and Leif Steigleder: for providing the cost model of combustor that was necessary for the financial analysis. To the United States Department of Energy: for the financial support under grant DE-FC36-09G019005.

TABLE OF CONTENTS

	<u>Page</u>
1. INTRODUCTION	2
2. LITERATURE REVIEW	6
2.1. Hydrogen Combustion	6
2.1.1. Reactions for Heterogeneous Hydrogen Combustion	6
2.1.2. Catalysts for Heterogeneous Hydrogen Combustion.....	7
2.2. Micro-Scale Combustors.....	9
2.2.1. Combustors with Heat Recuperators	12
2.2.2. Microscale Integrated Combustor Heat Exchangers.....	15
2.3. Integrated Combustor Oil Heat Exchangers.....	18
2.4. Summary	19
3. SCOPE AND OBJECTIVES	21
4. EXPERIMENTAL FACILITY	23
4.1. Design Requirements	23
4.2. Design Considerations for Test Section	24
4.2.1. Design Simplification	24
4.2.2. High Temperature Gas Sealing.....	25
4.2.3. Oil Channel Sealing.....	26
4.3. Final μ CHX Assembly	27
4.3.1. Measurement of Internal Dimensions.....	32
4.4. Operational Parameters of μ CHX.....	34
4.4.1. Variation of Channel Height	35
4.4.2. Variation of Equivalence Ratio.....	35
4.5. Test Facility.....	37

TABLE OF CONTENTS (Continued)

	<u>Page</u>
4.5.1. Data Acquisition	42
4.5.2. Instrumentation and Equipment.....	43
4.6. Safety Considerations.....	45
4.7. Failure Modes	46
4.7.1. Flashback.....	49
4.7.2. Sustained Homogeneous Combustion in Test Section	49
4.7.3. Hydrogen Leak in Test Section.....	50
4.7.4. Sustained Oil Pump Failure	50
4.7.5. Heat Exchanger Failure	50
4.7.6. Hydrogen Leak in Flow Loop	51
4.7.7. Power Failure	51
4.7.8. Uncombusted Hydrogen in Exhaust	51
4.7.9. Leak in Oil Loop.....	51
5. CATALYST DEVELOPMENT.....	53
5.1. Catalyst Deposition Techniques.....	53
5.1.1. Sputtered Pd onto Stainless Steel	53
5.1.2. Wet-Deposited Pt onto Etched Stainless Steel.....	55
5.2. Catalyst Configurations Used in Experiments	59
6. EXPERIMENTAL PROCEDURE.....	61
6.1. Startup Procedure.....	61
6.2. Operational Procedure.....	66
6.3. Shutdown Procedure	68
6.4. Emergency Shutdown Procedure	70

TABLE OF CONTENTS (Continued)

	<u>Page</u>
6.5. Hydrogen Cabinet Operation.....	71
7. DATA ANALYSIS	73
7.1. Calibration.....	73
7.1.1. Thermocouple Calibration.....	73
7.1.2. Absolute Pressure Transducer Calibration.....	74
7.1.3. Differential Pressure Transducer Calibration.....	76
7.1.4. Gas Chromatograph Calibration	77
7.2. Stability.....	79
7.2.1. Steady State Determination.....	79
7.2.2. Temperature Stability.....	80
7.2.3. Oil Flow Rate Stability.....	81
7.2.4. Gas Flow Rate Stability.....	82
7.2.5. Gas Chromatograph Repeatability.....	83
7.3. Heat Loss Estimation	84
7.4. Equations Used in Analysis	86
7.4.1. Operating Parameters.....	86
7.4.2. Efficiency Parameter	87
7.4.3. Heat Loss Calculations	88
7.5. Uncertainties	89
8. RESULTS AND DISCUSSION.....	93
8.1. Experimental Matrix.....	93
8.2. Heat Loss Estimation	95
8.3. Repeatability Experiments.....	99

TABLE OF CONTENTS (Continued)

	<u>Page</u>
8.3.1. Stability of Catalyst Shim B.....	99
8.3.2. Stability of Catalyst Shim C.....	103
8.4. Variation of Residence Time.....	105
8.4.1. Catalyst Shim B Residence Time Experiments	105
8.4.2. Catalyst Shim C Residence Time Experiments	113
8.5. Variation of Equivalence Ratio	119
8.6. Variation of Average Oil Temperature	125
8.7. Variation of Catalyst Length	128
8.8. Variation of Catalyst Position.....	131
9. PRELIMINARY DESIGN OF A LARGE ARRAY COMBUSTOR HEAT EXCHANGER.....	139
9.1. Design Considerations.....	139
9.2. Channel Arrangement	140
9.3. Internal Fluid Distribution and Optimization	142
9.4. Design Results and Discussion	146
10. FINANCIAL ANALYSIS.....	150
10.1. Introduction	150
10.2. Methodology	150
10.2.1. 12 kW CHX Cost Model	150
10.2.1. Cash Flow Analysis.....	152
10.2.2. Sales Estimate.....	153
10.3. Results and Discussion	154
10.4. Conclusions	157
11. CONCLUSIONS AND RECOMMENDATIONS	158

TABLE OF CONTENTS (Continued)

	<u>Page</u>
11.1. Conclusions	158
11.2. Recommendations for Future Investigation.....	160

LIST OF FIGURES

<u>Figure</u>	<u>Page</u>
Fig. 1.1: Specific energy of energy storage materials (Adapted from [1]).....	2
Fig. 1.2: Current status of hydrogen system technologies [5].....	3
Fig. 2.1: Hydrogen ignition on platinum and palladium foils (Adapted from [24])	9
Fig. 2.2: Temperature profiles with varying thermal conductivity walls (Adapted from [12])	12
Fig. 2.3: Schematics of heat recuperating combustors (Adapted from [36]): (a) linear counterflow (CF), (b) 2 turn Swiss roll (SR), (c) toroidal Swiss roll	13
Fig. 2.4: Temperature response of cross-flow combustor/heat exchanger (Adapted from [13])	17
Fig. 3.1: μ CHX unit cell design concept.....	21
Fig. 4.1: Schematic of design simplification.....	25
Fig. 4.2: Oil channel sealing schematic	26
Fig. 4.3: Cross sectional schematic of μ CHX	27
Fig. 4.4: Exploded μ CHX.....	29
Fig. 4.5: Partially exploded μ CHX.....	30
Fig. 4.6: Assembled μ CHX, topside	30
Fig. 4.7: Assembled μ CHX, underside	31
Fig. 4.8: Image of actual μ CHX assembly	32
Fig. 4.9: Channel height measurement schematic (Flow into page)	33
Fig. 4.10: Residence time effects of channel height variation.....	35
Fig. 4.11: Residence time effects of equivalence ratio variation.....	36
Fig. 4.12: Test facility schematic.....	38
Fig. 4.13: Instrumentation schematic	42

LIST OF FIGURES (Continued)

<u>Figure</u>	<u>Page</u>
Fig. 5.1: Stainless steel before and after etching.....	56
Fig. 5.2: Evaporated platinum precursor on stainless steel shim	57
Fig. 5.3: Reduced platinum catalyst on stainless steel shim.....	58
Fig. 5.4: SEM image of wet deposited Pt on catalyst shim B.....	58
Fig. 6.1: System check procedure	63
Fig. 6.2: Startup procedure	65
Fig. 6.3: Continuous operation procedure.....	67
Fig. 6.4: Shutdown procedure	69
Fig. 6.5: Emergency shutdown procedure	71
Fig. 7.1: Temperature calibration for thermocouple #1.....	74
Fig. 7.2: Absolute pressure calibration for PX32 pressure transducer #1	75
Fig. 7.3: Differential pressure calibration for DP15-24 pressure transducer.....	77
Fig. 7.4: Differential pressure calibration for DP15-36 pressure transducer.....	77
Fig. 7.5: Gas chromatograph return for calibration gas	78
Fig. 7.6: Typical time series temperature data (Exp. 10)	80
Fig. 7.7: Stability of outlet temperatures at steady state operation (Exp. 10)	81
Fig. 7.8: Stability of oil flow rate at steady state operation (Exp. 10)	82
Fig. 7.9: Stability of gas flow rates at steady state operation (Exp. 10)	83
Fig. 7.10: Black box heat flow schematic of μ CHX.....	85
Fig. 8.1: Schematic of CFD model geometry [1]	95
Fig. 8.2: Resistance model of conduction heat losses	96
Fig. 8.3: Heat flow ratios for various internal surface temperatures	98

LIST OF FIGURES (Continued)

<u>Figure</u>	<u>Page</u>
Fig. 8.4: Catalyst shim B combustion repeatability test temperature profiles.....	100
Fig. 8.5: Schematic of μ CHX with catalyst shim B.....	101
Fig. 8.6: Lateral temperatures of exp. 23 with catalyst shim B	102
Fig. 8.7: Catalyst shim C combustion temperature repeatability.....	104
Fig. 8.8: Schematic of μ CHX with catalyst shim C.....	104
Fig. 8.9: μ CHX performance for residence time variation experiments with catalyst shim B	106
Fig. 8.10: Centerline temperature profiles of residence time variation experiments with catalyst shim B.....	107
Fig. 8.11: Schematic of μ CHX with catalyst shim B	107
Fig. 8.12: Normalized heat losses for variation of residence time experiments with shim B	109
Fig. 8.13: Sensitivity analysis of oil density and specific heat (Data from 21 ms exp. 10).....	110
Fig. 8.14: Pressure drop for residence time experiments with catalyst shim B	112
Fig. 8.15: μ CHX performance for residence time variation experiments with catalyst shim C	113
Fig. 8.16: Centerline temperature profiles for residence time variation experiments with catalyst shim C.....	114
Fig. 8.17: Schematic of μ CHX with catalyst shim C.....	115
Fig. 8.18: Temperature variation along combustion channel at varying residence times with catalyst shim C.....	116
Fig. 8.19: Normalized heat loss for variation of residence time experiments with shim C.....	117
Fig. 8.20: Efficiency and pressure drop with catalyst shim C	119

LIST OF FIGURES (Continued)

<u>Figure</u>	<u>Page</u>
Fig. 8.21: μ CHX performance for equivalence ratio variation experiments with catalyst shim B.....	120
Fig. 8.22: Centerline temperature profiles for equivalence ratio variation experiments	121
Fig. 8.23: Schematic of μ CHX with catalyst shim B.....	122
Fig. 8.24: Heat losses for variation of equivalence ratio experiments with shim B	123
Fig. 8.25: Pressure drop for equivalence ratio tests with catalyst shim B.....	124
Fig. 8.26: Comparison of experimental equivalence ratio variation results with CFD simulation	125
Fig. 8.27: Effects of average oil temperature variation with catalyst shim B.....	126
Fig. 8.28: Centerline temperature profiles of average oil temperature variation experiments.....	127
Fig. 8.29: Schematic of μ CHX with catalyst shim B.....	127
Fig. 8.30: Centerline temperature profile comparison between catalyst shim B and C	129
Fig. 8.31: Schematics of μ CHX's with catalyst shims B and C	129
Fig. 8.32: Schematics of μ CHX's with catalyst shims C and C-rev.....	131
Fig. 8.33: Effect of catalyst position variation	133
Fig. 8.34: Heat loss for variation catalyst position experiments	134
Fig. 8.35: Temperature profiles for residence time variation experiments with shim C-rev	135
Fig. 8.36: Temperature variation along combustion channel at varying residence times with catalyst shim C-rev	136
Fig. 8.37: Centerline temperature profiles of variation of catalyst position experiments.....	137
Fig. 8.38: Inlet pressure for variation of catalyst position experiments.....	138
Fig. 9.1: Schematics of (a) supported spans and (b) unsupported spans.....	140

LIST OF FIGURES (Continued)

<u>Figure</u>	<u>Page</u>
Fig. 9.2: Full size CHX channel arrangement (Cross-section).....	141
Fig. 9.3: Side profile of shim stackup	142
Fig. 9.4: Lateral header schematic (Side view, header flows into page)	144
Fig. 9.5: Triangular header schematic (Top view, header flows into page).....	145
Fig. 9.6: Hexagonal and pentagonal header schematic (Top view, header flows into page).....	145
Fig. 9.7: Preliminary 12 kW combustor design	147
Fig. 9.8: Exploded view of a single stack of shims	148
Fig. 10.1: Manufacturing costs at varying production levels (Data from Steigleder et al.)	151
Fig. 10.2: Estimated annual H ₂ fuel cell vehicle sales (Adapted from [51]).....	154
Fig. 10.3: Projected annual and cumulative net revenue.....	155

LIST OF TABLES

<u>Table</u>	<u>Page</u>
Table 2.1: Heterogeneous hydrogen combustion reactions on platinum [8,15,16]	7
Table 2.2: Micro-scale combustion experiments	10
Table 2.3: Micro-scale combustor experiments with heat recuperators.....	14
Table 2.4: Micro-scale combustor heat exchanger experiments	16
Table 4.1: PEEK oil channel insert fit at different operating temperatures	27
Table 4.2: ESI 5330 settings for shim fabrication	28
Table 4.3: Measurements μ CHX channel heights.....	34
Table 4.4: Experimental Equivalence Ratio Limits.....	37
Table 4.5: Heat transfer fluid properties (Adapted from [43]).....	41
Table 4.6: Data acquisition system	43
Table 4.7: Facility instrumentation	44
Table 4.8: Facility equipment	45
Table 4.9: Failure modes and effects analysis legend	47
Table 4.10: Failure Modes and Effects Analysis	48
Table 5.1: Catalyst deposition techniques.....	53
Table 5.2: Sputtered palladium shear test	55
Table 5.3: Catalyst configuration details	59
Table 6.1: Notes to standard operating procedures	61
Table 7.1: Gas chromatograph calibration sensitivity and uncertainty.....	79
Table 7.2: Repeatability of gas chromatograph analysis	84
Table 7.3: Uncertainties of measured parameters (Exp. 10).....	90
Table 7.4: Estimation of unknown uncertainties.....	91

LIST OF TABLES (Continued)

<u>Table</u>	<u>Page</u>
Table 7.5: Uncertainty of calculated parameters (Exp. 10)	91
Table 7.6: Uncertainty of H ₂ content due to leakage	92
Table 8.1: Testing matrix of μ CHX experiments	94
Table 8.2: Resistance model parameters	97
Table 8.3: Repeatability tests using shim B	99
Table 8.4: Operating conditions for repeatability test of shim C	103
Table 8.5: Variation of catalyst length experiments.....	128
Table 8.6: Heat losses and inlet pressures for variation of catalyst length experiments.....	131
Table 8.7: Catalyst positions for variation of catalyst location experiments	132
Table 9.1: Header design comparison for a 30 kW CHX.....	146
Table 9.2: Full size combustor comparison	149
Table 10.1: Cost categories and classification	152
Table 10.2: Sensitivity analysis on breakeven point.....	156

LIST OF APPENDICES

<u>Appendix</u>	<u>Page</u>
APPENDIX A. PART DRAWINGS OF COMBUSTOR COMPONENTS.....	167
APPENDIX B. LABVIEW VI.....	173
APPENDIX C. FACILITY CHANGES FOR FULL SIZE CHX EXPERIMENTS.....	175
APPENDIX D. ALTERNATIVE CATALYST DEPOSITION METHODS	176
D.1. Anodized Aluminum.....	176
D.2. Palladium/Carbon Paint	176
APPENDIX E. INITIAL TESTING WITH CATALYST SHIM A.....	178
APPENDIX F. CALIBRATION PARAMETERS.....	180
APPENDIX G. EXPERIMENTAL DATA.....	181
APPENDIX H. THERMAL NON-UNIFORMITIES IN μ CHX	188
APPENDIX I. FULL SIZE CHX CALCULATOR.....	190
APPENDIX J. CALCULATIONS FOR FINANCIAL ANALYSIS.....	192

LIST OF APPENDIX FIGURES

<u>Figure</u>	<u>Page</u>
Fig. A.1: CAD drawing of bottom plate	167
Fig. A.2: CAD drawing of catalyst plate	168
Fig. A.3: CAD drawing of combustor/recuperator shim	169
Fig. A.4: CAD drawing of oil part	170
Fig. A.5: CAD drawing of oil plate	171
Fig. A.6: CAD drawing of oil plate	172
Fig. D.1: Anodized aluminum prior to catalyst deposition	176
Fig. E.1: Time series temperature profile of catalyst shim A	178
Fig. H.1: Image of back side of catalyst shim B after ~80 hours of combustion	188
Fig. H.2: Damaged PEEK insert	189
Fig. H.3: Repaired PEEK insert	189
Fig. I.1: Excel® calculator for determining full size CHX dimensions.....	190
Fig. I.2: Excel® calculator for determining full size CHX dimensions	191
Fig. J.1: Calculations for financial analysis, years 0 – 5	192
Fig. J.2: Calculations for financial analysis, years 6 – 10	192
Fig. J.3: Calculations for financial analysis, years 11 – 15	193

LIST OF APPENDIX TABLES

<u>Table</u>	<u>Page</u>
Table F.1: Thermocouple Calibration Parameters	180
Table F.2: Thermocouple Offset Parameters	180
Table F.3: Absolute Pressure Transducer Calibration Parameters	180
Table G.1: Data from stability experiments with shims B and C	181
Table G.2: Data from variation of residence time experiments with shim B	182
Table G.3: Data from variation of residence time experiments with shim C	183
Table G.4: Data from variation of equivalence ratio experiments with shim B	184
Table G.5: Data from variation of average oil temperature experiments with shim B	185
Table G.6: Data from variation of average oil temperature experiments with shim B	186
Table G.7: Data from variation of residence time experiments with shim C-rev	187

NOMENCLATURE

l	Catalyst Length (mm)
A_c	Channel Cross Section Area (mm ²)
H	Channel Height (mm)
L	Channel Length (mm)
W	Channel Width (mm)
ρ	Density (g/cm ³)
D	Diameter (mm)
ε	Efficiency
ΔH_{298}°	Enthalpy Change of Reaction at 25 °C and 101.3 kPa (kJ/mol)
Φ	Equivalence Ratio
\dot{Q}	Heat Transfer Rate (W)
C_{H_2}	H ₂ Concentration (%)
η_c	H ₂ Conversion
$q_{H_2,LHV}$	Lower Heating Value for H ₂ (J/g)
\dot{m}_i	Mass Flow Rate of Component i (g/s)
\dot{n}_i	Molar Flow Rate of Component i (mol/s)
\mathcal{M}_i	Molar Mass of Component i (g/mol)
n_i	Moles of Deposited Catalyst (mol)
P	Pressure (kPa)

t_{res}	Residence Time (ms)
Re	Reynolds Number
c_p	Specific Heat (J/g-K)
Γ	Surface Site Density (mol/cm ²)
T	Temperature (°C)
U_i	Uncertainty of Component i
V	Velocity (m/s)
μ	Viscosity (kg/s-m)
\dot{V}	Volumetric Flow Rate (ml/min)

PERFORMANCE CHARACTERIZATION OF AN INTEGRATED
MICROSCALE HYDROGEN COMBUSTOR RECUPERATOR AND OIL
HEAT EXCHANGER

1. INTRODUCTION

Concern about pollution and the future availability of fossil fuels has spurred interest and research into alternative fuels and fuel carriers. Hydrogen has received a lot of interest as an alternative energy carrier because of its clean burning characteristics: the combustion reaction of hydrogen and oxygen produces only water vapor and releases a significant amount of heat, shown in Eq. (1.1). The reverse reaction is also possible via electrolysis, and is one of multiple methods for producing hydrogen gas. Other production methods include steam methane reforming, partial oxidation, coal gasification and thermal cracking [2]. As an energy carrier, hydrogen has a much higher energy density, on a mass basis, than other common materials, as shown in Fig. 1.1.

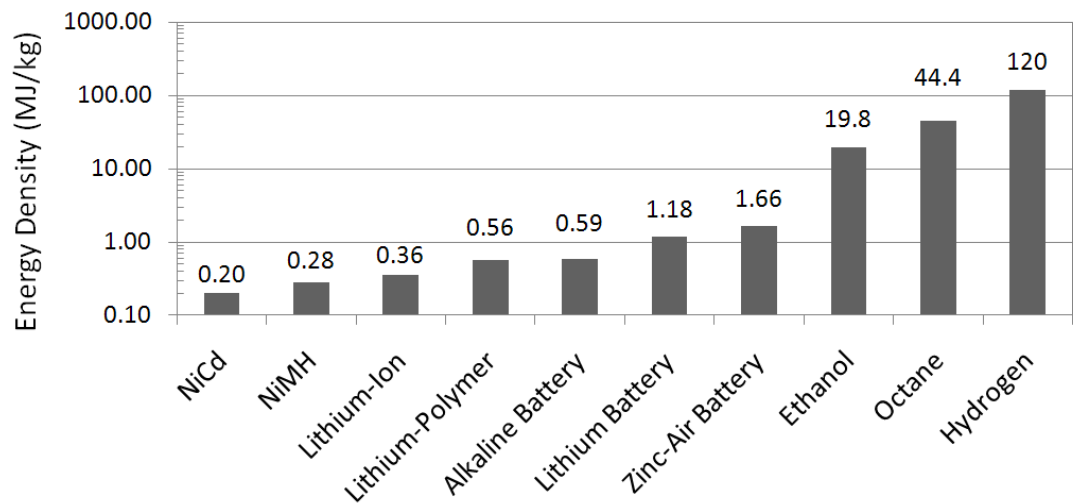
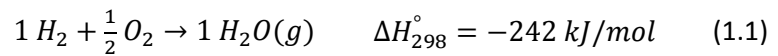


Fig. 1.1: Specific energy of energy storage materials (Adapted from [1])

Hydrogen powered vehicles are a very appealing concept due to their carbon-neutral operation. However, there are many technical challenges that need to be overcome in order for these vehicles to become a commercial reality. This is especially true in regards to storage systems for hydrogen powered vehicles. Volumetrically efficient storage is difficult because hydrogen gas is much less dense than diesel and gasoline. For example, a liter of octane contains almost as much energy as four liters of liquid hydrogen at 20 K or three thousand

liters of hydrogen gas at standard temperature and pressure. The primary hydrogen storage systems currently available are cryogenic liquid and compressed gas. However, cost and safety concerns remain for these storage systems for automotive applications [4].

Additionally, the U.S. Department of Energy (DOE) has specified performance targets for hydrogen storage systems for gravimetric and volumetric capacity. The current status of hydrogen storage technologies compared to the DOE performance targets is shown in Fig. 1.2. The 2015 targets are 5.5 % H₂ by weight and 40 g of H₂ per liter with ultimate targets of 7.5 % H₂ by weight and 70 g H₂ per liter. Additional performance targets have been set regarding system cost, delivery temperature and pressure, operating temperature range, transient response, cycle life and more [5]. These targets are for the complete storage system, not just the material.

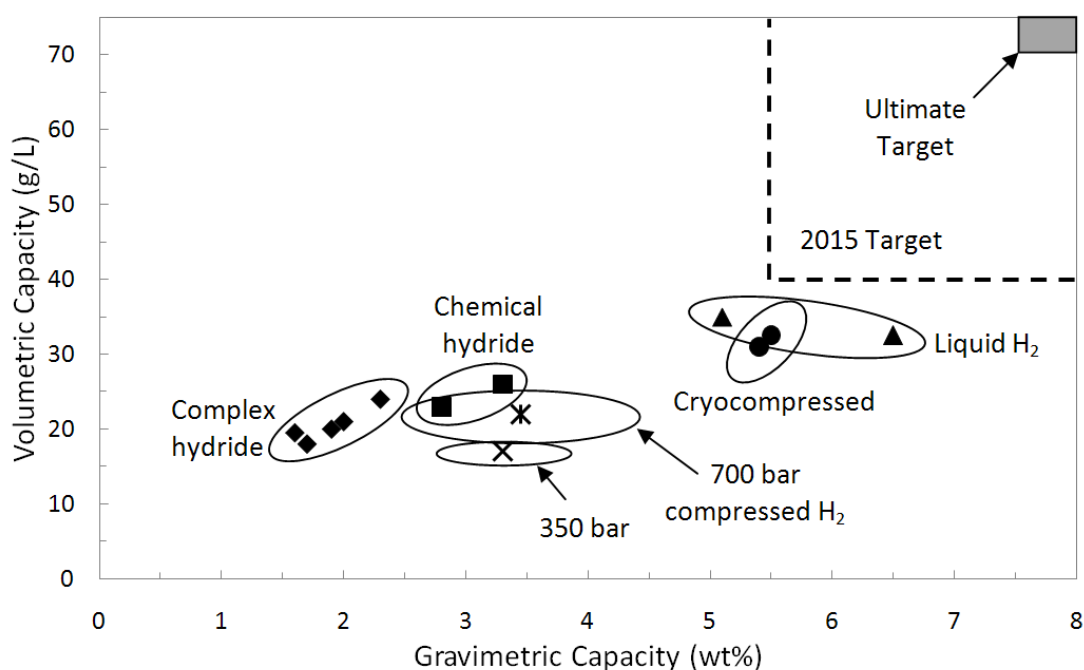


Fig. 1.2: Current status of hydrogen system technologies [5]

Complex metal and chemical hydrides require more development in order to meet the DOE performance targets. An additional challenge faces these hydride storage systems that isn't present in the compressed or liquid H₂ storage systems: the process of adsorbing hydrogen

for hydrides is an exothermic chemical reaction while the discharge process is endothermic. The desorption temperature varies between 70 °C and 400 °C, with the highest performing materials typically requiring the highest desorption temperatures [6]. These high temperatures cannot be supplied by the waste heat from the fuel cell in a hydrogen powered vehicle.

Hydrogen combustors are therefore being investigated as potential methods to supply the heat needed to sustain the discharge cycle [7]. Burning a portion of the stored hydrogen onboard the vehicle to produce heat is a practical solution. This can be implemented by burning a small portion of hydrogen and transferring the resulting heat to a fluid for circulation through the tank. In order for a hydrogen combustor to satisfy the requirements of a hydride storage system, it must be able to heat a heat transfer fluid to the temperature required by the hydride while consuming as little hydrogen as possible. The ideal combustor would have low mass, low volume and generate heat from combustion at high efficiencies. These characteristics would allow the use of higher performing chemical or metal hydrides while minimizing the impact on the total storage system mass and volume in order to meet the DOE's gravimetric and volumetric targets.

Given that any hydrogen used to generate heat for desorption cannot be used to propel the vehicle, maximizing the efficiency of the heater is critical. It is also important for the combustor to start up rapidly and have a fast response to flow rate changes. These are important to fulfill the demands of varying driving conditions while maximizing fuel efficiency. Also, different vehicles will have different requirements for hydrogen storage systems. A hydrogen powered bus will certainly have very different storage requirements than a hydrogen powered sports car. This illustrates the importance for these systems to be scalable. The scalability and efficiency of microchannel devices have the potential to meet the both these requirements of the heater.

The research presented in this thesis is an initial step in the development of a novel, compact and efficient microscale hydrogen combustor heat exchanger (μ CHX) that transfers heat to a heat transfer fluid that is used as a heat source to desorb hydrogen from a hydride based storage system of a hydrogen powered vehicle. This experimental study examines the effect

of channel height, flow rate, equivalence ratio and catalyst deposition on the overall efficiency of the μ CHX.

2. LITERATURE REVIEW

The research presented in this thesis is a novel design of a micro-scale combustion reactor, utilizing hydrogen gas as the fuel source with the purpose of transferring the generated heat to a circulating oil loop. The related research areas can be divided into three sections: hydrogen combustion, micro-scale combustors and integrated combustor oil heat exchangers. The salient details of these research areas are presented in this chapter in order to provide context for the research of this thesis.

2.1. Hydrogen Combustion

Hydrogen gas has a wide range of combustion, from 4 to 75 percent by volume in air. The combustion reaction can occur as a homogeneous or heterogeneous reaction. The homogeneous reaction is a gas-phase reaction while the heterogeneous reaction is a surface reaction. Combined homogeneous and heterogeneous reactions are possible and have been demonstrated, both purposefully and accidentally, by multiple investigators [8,9]. Heterogeneous hydrogen combustion has been demonstrated to occur in the presence of platinum catalyst at ambient conditions without requiring an ignition source [9-14].

2.1.1. Reactions for Heterogeneous Hydrogen Combustion

Heterogeneous hydrogen combustion is a set of chemical reactions that take place simultaneously on the surface of a catalyst. The generally accepted chemical reactions for heterogeneous hydrogen combustion on platinum are listed in Table 2.1. These reactions can be divided into three categories: adsorption reactions, surface reactions and desorption reactions. Reaction rate coefficients are available from various studies [8,15,16]. The primary limitation of these reactions has been shown to be diffusion of the gas species to the catalyst [15], with a secondary limitation being the adsorption and desorption reactions [8]. A concurrent numerical investigation is being performed by Ghazvini et al. [1], so more details on the reaction equations are not provided here. Also, the reactions pertaining to homogeneous combustion are not listed due to their suppression at the small characteristic length scales being considered.

Table 2.1: Heterogeneous hydrogen combustion reactions on platinum [8,15,16]

Adsorption Reactions	Surface Reactions	Desorption Reactions
$\text{H}_2 + 2\text{Pt(s)} \rightarrow 2\text{H(s)}$	$\text{H(s)} + \text{O(s)} \leftrightarrow \text{OH(s)} + \text{Pt(s)}$	$2\text{H(s)} \rightarrow \text{H}_2 + 2\text{Pt(s)}$
$\text{H} + \text{Pt(s)} \rightarrow \text{H(s)}$	$\text{H(s)} + \text{OH(s)} \leftrightarrow \text{H}_2\text{O(s)} + \text{Pt(s)}$	$2\text{O(s)} \rightarrow \text{O}_2 + 2\text{Pt(s)}$
$\text{O}_2 + 2\text{Pt(s)} \rightarrow 2\text{O(s)}$	$\text{OH(s)} + \text{OH(s)} \leftrightarrow \text{H}_2\text{O(s)} + \text{O(s)}$	$\text{H}_2\text{O(s)} \rightarrow \text{H}_2\text{O} + 2\text{Pt(s)}$
$\text{O} + \text{Pt(s)} \rightarrow \text{O(s)}$		$\text{OH(s)} \rightarrow \text{OH} + \text{Pt(s)}$
$\text{H}_2\text{O} + 2\text{Pt(s)} \rightarrow \text{H}_2\text{O(s)}$		
$\text{OH} + \text{Pt(s)} \rightarrow \text{OH(s)}$		

Note: Surface species are denoted by (s) and Pt(s) denotes a bare platinum surface site

When the reaction equations in Table 2.1 are incorporated into a numerical model, the surface site density (Γ) is a parameter that must be specified. Fundamentally, greater numbers of catalytic sites results in more rapid combustion. This parameter is highly dependent on the surface area of the support and the catalyst deposition method. While this parameter can be determined using methods available in literature, such as BET measurements [17], some researchers instead select the number of surface sites that best fit their experimental data [12]. This parameter can range from $2.72 \times 10^{-9} \text{ mol/cm}^2$ for polycrystalline Pt [8,16] to $4.98 \times 10^{-7} \text{ mol/cm}^2$ for wet deposited Pt on a porous Al_2O_3 support [12]. Many researchers use porous supports to increase the effective surface area of catalyst, thereby increasing the catalyst surface site density and the rate of combustion.

The reaction equations for palladium are identical to those for platinum with Pd(s) replacing Pt(s). The differences between the reactions of these two catalytic materials are the reaction rates. Heterogeneous reaction rates of H_2 / O_2 mixtures on platinum and palladium surfaces were determined by matching experimental data to a numerical model by Deutschmann et al. [15].

2.1.2. Catalysts for Heterogeneous Hydrogen Combustion

Catalytic combustion of hydrogen typically utilizes noble metals in order to facilitate the heterogeneous oxidation reaction of hydrogen and oxygen. Most researchers use platinum

(Pt) as the catalyst for this reaction because the reaction pathways are better understood and characterized [9-14,18,19]. The quenching distance for homogenous combustion of hydrogen is about 0.65mm for a stoichiometric mixture [20], but can vary depending on equivalence ratio, wall temperature and wall material [21]. However, there is interest in using palladium (Pd) as the catalyst due to the higher cost of platinum. Both platinum and palladium have been investigated in the research presented here.

There are a wide variety of methods for depositing a noble metal catalyst onto the walls of a combustor [22]. Typically the catalyst is deposited onto a support material in order to enhance the surface area available for the reaction. A common method is wet-deposition, often called a wash coating. While the exact composition can vary widely between researchers, the majority of the studies in micro-scale combustion have utilized an aqueous solution of dissolved H_2PtCl_6 . Alternative deposition methods include plasma vapor deposition [8], chemical vapor deposition and electroplating, among others. Some researchers instead use noble metal foils [18] or wires [23] in their experiments.

Experimental and numerical ignition studies of hydrogen on noble metal foils were conducted by Deutschmann et al. [15] and Behrendt et al. [24], respectively. Both platinum and palladium foils were investigated for H_2/O_2 mixtures, diluted in N_2 to 6 % by volume. The ignition temperature as a function of equivalence ratio trend from their experimental and numerical study is shown in Fig. 2.1. Both noble metals demonstrated lower ignition temperatures for lower equivalence ratios. Palladium was found to have lower ignition temperatures than platinum, particularly at low equivalence ratios. However, different researchers report differing ignition temperatures. Some investigators have observed ignition at room temperature with wet deposited Pt catalysts [9-13,25] while others required preheating to a certain level with Pt wire [23,26]. It appears that wet deposited Pt catalysts tend to have lower ignition temperatures than Pt wire or foil.

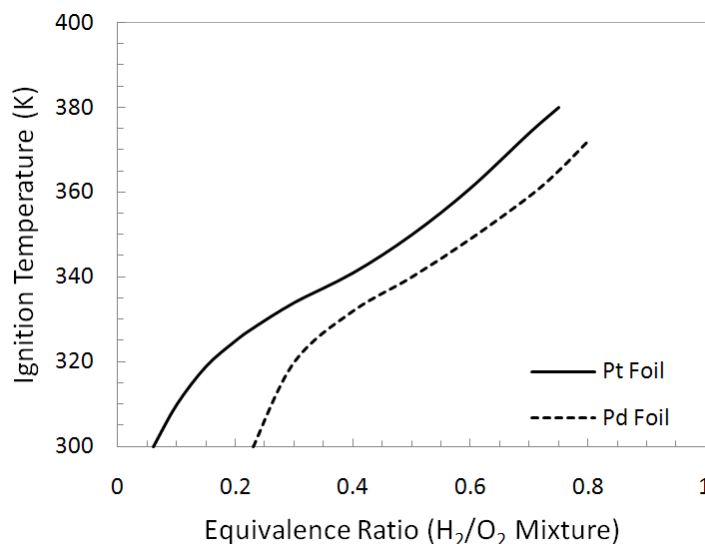


Fig. 2.1: Hydrogen ignition on platinum and palladium foils (Adapted from [24])

2.2. Micro-Scale Combustors

A micro-scale combustor is a reactor that has channels with characteristic length scales on the order of tens to hundreds of micrometers. These devices are often comprised of an array of parallel channels with a high surface area to volume ratio. The high surface area to volume ratio is advantageous for both heat transfer and for heterogeneous chemical reactions. Under laminar flow conditions, the convective heat transfer coefficient is inversely proportional to the channel hydraulic diameter, allowing micro-channel devices to operate with higher heat transfer coefficients than traditional devices. Additionally, the micro-channel dimensions result in short diffusion times, causing narrower residence time distributions. These factors can allow micro-channel devices to avoid heat and mass transfer limitations faced by traditional devices [27]. Furthermore, micro-channel based combustors have been shown to be intrinsically safe for gas compositions that are within the explosive regime due to flame suppression at sub-millimeter dimensions [26].

There are also disadvantages associated with the use of micro-channel devices. First, the pressure drop is often much greater across a micro-channel device due to small channel sizes. Often the challenge in designing a micro-channel device is balancing the gains in heat

and mass transfer with the increased pressure drop of smaller channels [28]. Micro-reactors are often constructed by bonding a series of etched plates and it can be difficult to completely seal these joints. Also, obtaining uniform flow distribution to all channels can be difficult, particularly when increasing the number of channels in a micro-channel device.

A summary of the literature available for micro-scale combustion experiments is presented in Table 2.2. The experiments presented in this table are specifically focused on catalytically sustained hydrogen combustion in micro-channels. Other investigators use similar combustor designs and catalysts, but burn propane (C_3H_8) [12,29] or methane (CH_4) [16,30] instead.

Table 2.2: Micro-scale combustion experiments

Exp.	Reactor	Catalyst	Test Conditions	Details/Findings
Veser (2001) [26]	Quartz $L = 20$ mm $D_i = 0.6$ mm	0.15 mm Pt wire	H_2 / O_2 (N_2 dilution) $\Phi = 0 - 1.6$ $\dot{Q}_{H_2} = 0 - 50$ W $t_{res} = 0.25 - 0.6$ ms	No homogeneous reaction \uparrow temp. with $\uparrow \varphi$ Max. temp near $\varphi = 1$
Norton et al. (2004) [9]	Alumina $L = 40$ mm $W = 10$ mm $H = 0.25, 1$ mm	Pt on alumina	H_2 / Air $\Phi = 0 - 1.3$ $\dot{Q}_{H_2} = 0 - 100$ W $t_{res} = 3, 12$ ms	Auto-ignition 99% conv. for $H = 0.25$ mm HH reaction for $H = 1$ mm
Norton et al. (2006) [12]	Stainless Steel $L = 50$ mm $W = 10$ mm $H = 0.3$ mm	Pt on anodized aluminum	H_2 / Air & C_3H_8 / Air Air, SS, Cu spreaders $\Phi = 0 - 1$ $\dot{Q}_{H_2} = 0 - 100$ W $t_{res} = 4.5$ ms	H_2 / Air : auto-ignition C_3H_8 / Air : no auto-ignition \uparrow thermal conductivity reduces “hot spots”
Choi et al. (2008) [10]	Ceramic $L = 10$ mm $W = 10$ mm $H = 1.5$ mm	Pt on porous ceramic	H_2 / Air Varied Pt loading $\Phi = 0.2, 1$ $\dot{Q}_{H_2} = 1 - 50$ W $t_{res} = 9 - 90$ ms	Auto-ignition 97-98% fuel conversion Negligible impact on conv. for \uparrow Pt loading

\uparrow : Increase, \downarrow : Decrease, sccm: standard cubic centimeters per minute, t_{res} : residence time, conv: Fuel Conversion, HH: Homogeneous/Heterogeneous

Veser [26] investigated the heterogeneous combustion of hydrogen over a platinum wire catalyst in a 0.6 mm quartz tube. No flames or explosions were observed in the quartz tube, instead, the platinum wire glowed white hot as a result of the combustion reaction. This

indicated intrinsically safe combustion operation. Exhaust temperatures were found to increase with increasing equivalence ratio with the maximum typically occurring near unity. Veser also conducted a theoretical investigation of H_2 / O_2 explosion limits and concluded that micro-combustors are intrinsically safe with characteristic dimensions smaller than 1 mm.

Ceramic hydrogen micro-combustors were developed Norton et al. [9] with 250 μm and 1000 μm channel heights. The channel dimensions were 1 cm wide by 5 cm long and a flow rate of 2000 sccm was maintained for all tests. Platinum catalyst was deposited with a wet-impregnation method along the last 4 cm of each combustor. The authors found that both lean and rich mixtures would self-ignite without requiring preheating. For the 250 μm channel, the maximum combustor wall temperature increased with greater equivalence ratios with the maximum occurring at an equivalence ratio of 0.8. A wall temperature of about 900 $^{\circ}C$ was observed for the 250 μm channel combustor while the peak wall temperature for the 1000 μm channel was about 1100 $^{\circ}C$ at the same equivalence ratio. For the 1000 μm channel, combined homogenous/heterogeneous combustion caused temperature hysteresis for $\sim 0.32 \leq \Phi \leq \sim 0.55$. Complete conversion of hydrogen was achieved for all equivalence ratios for the 250 μm channel while $\Phi > 0.3$ was required for the 1000 μm channel.

A “tunable” hydrogen combustor was fabricated by Norton et al. [12] that allowed the thermal properties of the wall to be adjusted. This was accomplished by mounting 3.2 mm metal slabs of differing thermal conductivities to the 0.79 mm thick wall of the reactor. The entire assembly was then wrapped in high temperature insulation. These metal slabs acted as thermal spreaders to reduce thermal gradients. Silver paste was used between the wall and the heat spreader to minimize thermal contact resistance. Higher thermal conductivity materials were found to reduce localized hot spots and improve temperature uniformity along the reaction chamber as shown in Fig. 2.2. These experiments were conducted at $\Phi = 0.6$ and a heat input of 72 W. Temperature profiles similar to those shown for stainless steel and copper in Fig. 2.2 were expected for the present research due to the similar catalysts and wall materials. The platinum catalyst was wet deposited as 0.007 M H_2PtCl_6 acid onto

anodized alumina supports inside the reactor. Both hydrogen/air mixtures and propane/air mixtures were tested. While hydrogen was found to be self-igniting, propane required heat input to initiate combustion.

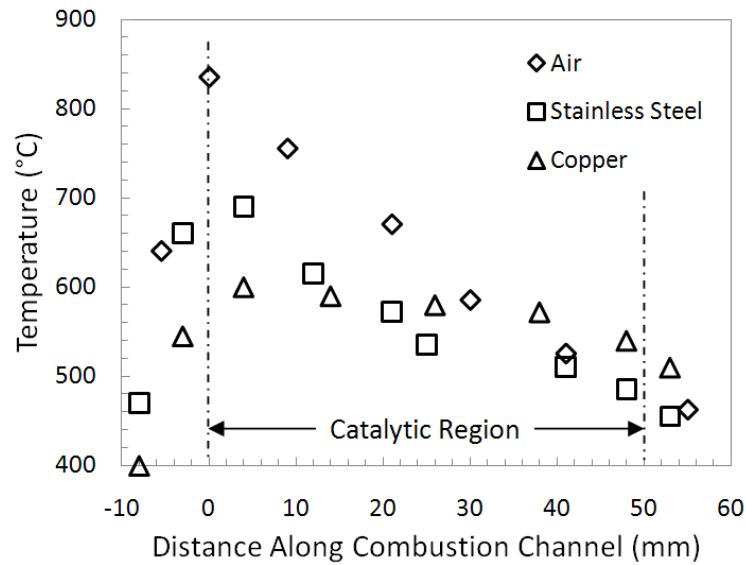


Fig. 2.2: Temperature profiles with varying thermal conductivity walls (Adapted from [12])

Choi et al. [10] demonstrated that heterogeneous catalytic combustion of hydrogen occurs in the sub-millimeter scale without requiring ignition or preheating. While combustion occurred immediately, the reactor required ten to thirty minutes to reach steady state operation because of the thermal mass of the reactor. Steady state operation was achieved more rapidly with greater flow rates of hydrogen due to the increase in heat generation. Increasing the concentration of platinum catalyst on the porous support was found to have no impact for the Pt loadings tested between 0.4 – 3.7 weight percent of the support. This indicated that residence time was not the limiting parameter in the performance of this combustor.

2.2.1. Combustors with Heat Recuperators

Combustors with integrated heat recuperators in various forms have been studied since the 1970's. In 1971, Weinberg [31] proposed "recirculating heat" to improve the efficiency of combustion processes. Then in 1975, Lloyd and Weinberg [32] fabricated a spiral counterflow

combustor, now often referred to as a “Swiss roll” type combustor. In 1978, Jones et al. [33] described various combustor designs that incorporated heat recuperation characteristics through various combinations of conduction, convection, radiation, and mass transfer. Schematics of the different heat recuperating combustors are shown in Fig. 2.3. The following heat recuperating combustors have recently been developed: counterflow combustors [23,34]; Swiss roll combustors [14,18,19,35-38]; and toroidal Swiss roll combustors [36]. A summary of the most applicable experimental investigations available for combustors with heat recuperators is presented in Table 2.3.

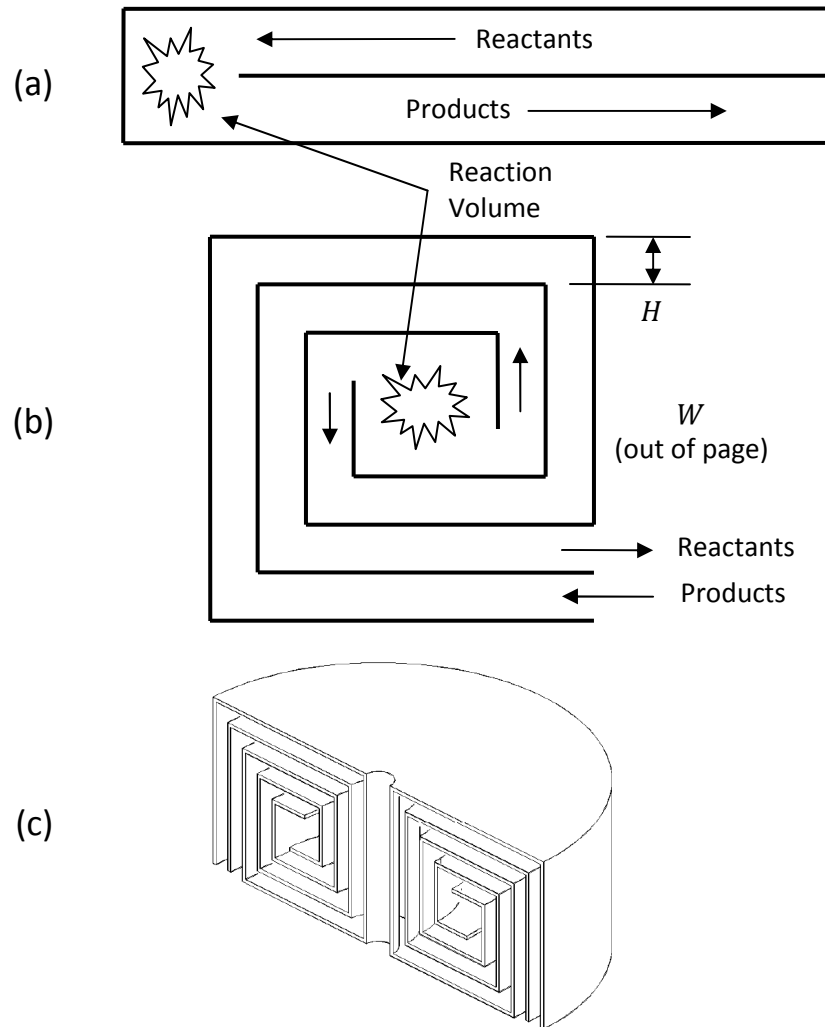


Fig. 2.3: Schematics of heat recuperating combustors (Adapted from [36]): (a) linear counterflow (CF), (b) 2 turn Swiss roll (SR), (c) toroidal Swiss roll

Table 2.3: Micro-scale combustor experiments with heat recuperators

Exp.	Reactor	Ignition	Test Conditions	Details/Findings
Peterson et al. (2000) [23]	SS & quartz CF $D_{i,SS} = 0.17$ mm $D_{o,SS} = 0.30$ mm $D_{i,qz} = 0.52$ mm	Heated Pt wire	H_2 / Air $\Phi = 0.83$ $\dot{Q}_{H_2} = 0 - 0.74$ W	Ignition occurred around 390 – 490 K Large radiation heat losses Stable down to 200 mW
Vican et al. (2002) [14]	Alumina $A_c = 800$ μm^2 $L = 100$ mm 2 Turn SR	Pt on alumina & igniter	H_2 / Air $\Phi = 0.2 - 1$ $\dot{Q}_{H_2} = 2 - 15$ W	Auto-ignition Pt degraded above 300 °C HH at higher heat inputs
Ahn et al. (2005) [18]	Inconel $W = 50$ mm $H = 1.5$ mm 3.5 Turn SR	Pt foil & igniter	C_3H_8 / Air $Re = 1 - 2000$ $\Phi = 0 - 60$ Catalytic vs. gas phase ignition	Catalytic reactions stable at lower temperatures and lower Re
Kim et al. (2005) [35]	Stainless Steel $W = 50$ mm $H = 16, 27$ mm 3, 4 Turn SR	Igniter	C_3H_8 / Air $V = 0 - 6$ m/s $\Phi = 0.4 - 2$ Varied Geometries	Lowest V stable at $\phi \approx 1$ $\eta \uparrow$ with $V \downarrow$ Max NO_x at $\phi \approx 1$

↑: Increase, ↓: Decrease, CF: Counter Flow, SR: Swiss Roll, η : thermal efficiency, NO_x : Nitrous Oxides

Peterson et al. [23] developed a hydrogen combustor with counterflow heat recuperator. A Pt wire coil was located at the end of stainless steel tube containing the flowing reactants. A larger quartz tube was then placed around the Pt wire catalyst and stainless steel tube, forming an annulus for the products to flow through and preheat the incoming reactants. The Pt wire had to be preheated to around 390 – 490 K in order to initiate combustion. After that, the reaction was self-sustaining. However, an estimated 80 percent of the heat generated was lost, primarily due to radiation from the quartz tube. This research was continued by Hatfield et al. [34] burning propane in a similar combustor/recuperator.

Vican et al. [14] developed a Swiss roll type hydrogen combustor as a heat source for a thermoelectric device. The reactor was 12.5 x 12.5 x 5 mm in size, formed out of an alumina ceramic using a stereolithographic technique before wet-depositing a Pt catalyst. As expected, surface temperature increased with hydrogen energy input. Lower hydrogen flow rates were sustained with catalytic combustion while the higher hydrogen flow rates resulted

in combined homogeneous/heterogeneous combustion. Operating temperatures above 300 °C caused the platinum catalyst to degrade and no longer auto-ignite at room temperature. While the authors claimed that this degradation was consistent with available literature, the surveyed literature here suggests otherwise [9-13,16,39].

A typical Swiss roll type burner was developed by Ahn et al. [18] for the purpose of investigating the extinction limits of propane-air mixtures. Platinum foil catalysts or a resistance wire was used to initiate the reaction, depending on the test condition. The gas phase reactions required higher Reynolds number flows in order to stabilize, while catalytic combustion was stable at low Reynolds numbers. Also, the catalytically sustained reactions were stable at lower temperatures than the gas-phase reactions.

Kim et al. [35] tested Swiss roll combustors of various sizes using propane as the fuel. Homogeneous flames were ignited using an electric spark at the center of the combustor. In general, equivalence ratios near unity could be stabilized at the lowest flow velocities while lean and rich mixtures required higher velocities for stable flames. They also found that the efficiency increased for combustors with larger surface area to volume ratios for a given flow velocity. However, these smaller combustors could not maintain combustion at lower velocities and lower temperatures. Operation of the combustor produced nitrous oxides (NO_x), with the smaller combustor producing more NO_x than the larger combustor. Stoichiometric equivalence ratios were found to produce the most NO_x .

2.2.2. Microscale Integrated Combustor Heat Exchangers

There are a wide variety of motivations for developing combustors as heat sources, including transferring heat to a flowing gas stream [13], to a flowing liquid stream [7], to a thermoelectric device [25,39] to support an endothermic chemical reaction [11,40] and even as a heat source for cold-water scuba divers [41]. These types of combustors can all be considered as integrated combustor heat exchangers. Experiments on micro-scale hydrogen combustors with integrated heat exchangers are detailed in this section and are summarized in Table 2.4.

Table 2.4: Micro-scale combustor heat exchanger experiments

Exp.	Reactor	Catalyst	Combustion Conditions	Details/Findings
Janicke et al. (2000) [13]	Stainless Steel X-Flow $L = 10$ mm (est.) $W = 0.2$ mm $H = 0.14$ mm 1500 Channels (est.)	Pt on alumina	H_2 / O_2 (N_2 Dilution) Varied Pt Loading $\Phi = 1$ $\dot{Q}_{H_2} = 72$ W $t_{res} = 20$ ms (est.)	Low Pt required preheating High Pt auto-ignited ↓ induction time for ↑ runs ~35% efficiency
Ryi et al. (2005) [11]	Inconel - SMR $L = 17$ mm $W = 0.5$ mm $H = 0.25$ mm 550 Channels	Pt-Sn on alumina	H_2 / Air $\Phi = 0.95$ $\dot{Q}_{H_2} = 170$ W $t_{res} = 21$ ms	Auto-ignition 700 – 800 °C Operation < 40% system efficiency 100% fuel conversion
Federici et al. (2006) [25]	Stainless Steel - TE $L = 60$ mm $W = 8$ mm $H = 0.3$ mm	Pt on anodized alumina	H_2 / Air $\Phi = 1$ $\dot{Q}_{H_2} = 88$ W $t_{res} = 6$ ms	~0.8% system efficiency ~3% TE efficiency > 99.9% fuel conversion

↑: Increase, ↓: Decrease, t_{res} : residence time, SMR: Steam Methane Reforming, X-Flow: Cross-Flow Heat Exchanger, TE: Thermo-Electric

Janicke et al. [13] fabricated an integrated hydrogen combustor cross-flow type heat exchanger. A platinum catalyst was deposited on an aluminum oxide support. The combustion channel dimensions were 140 x 200 μ m and the heat exchanger channels were 70 x 100 μ m with an approximate reactor volume of 1 ml. This reactor required preheating to about 80 °C in order to initiate combustion at low catalyst loadings. The higher Pt loading did not require preheating and ignited after an induction period of approximately 20 minutes. The temperature response of the higher Pt reactor with a reactant flow rate of 600 ml/min stoichiometric flow of O_2 and H_2 diluted in 1000 ml N_2 /min is shown in Fig. 2.4. Successive experimental trials reduced the induction period of the reactor. They also found that the hydrogen was completely combusted. The overall efficiency of the system was around 35 percent, with 25 W of heat being transferred to the N_2 cooling gas from the 72 W of heat generated from H_2 combustion and the rest being lost. The authors noted that better insulation would likely reduce heat losses; however, they did not differentiate between the

unrecoverable heat losses to the products and the potentially recoverable heat losses due to insufficient insulation.

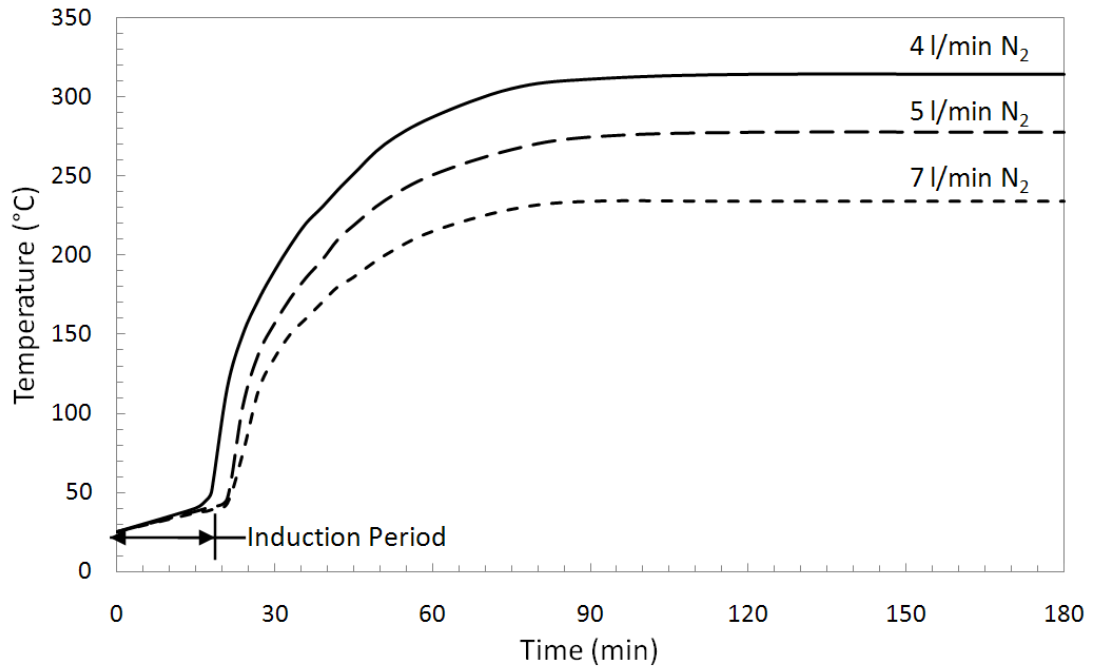


Fig. 2.4: Temperature response of cross-flow combustor/heat exchanger (Adapted from [13])

A micro-reactor utilizing hydrogen combustion was developed as a heat source for steam methane reforming (SMR) by Ryi et al. [11]. The channels were chemically etched in Inconel (250 μm by 500 μm) and diffusion bonded between stainless steel plates. The Pt-Sn catalyst was deposited via a wet-impregnation method following an alumina wash-coat. This reactor initiated combustion at room temperature and required 2.5 hours to reach an operating temperature between 700 and 800 $^{\circ}\text{C}$ with a stoichiometric mixture of hydrogen and air. The reformer was operated with typical residence times around 21 ms. Including the SMR reaction, 25 – 37 % of the input H_2 energy was regenerated as H_2 from the SMR reaction. The authors suggested incorporating a heat recovery system to improve the efficiency by recovering heat from the ~ 800 $^{\circ}\text{C}$ exhaust gas. While this is a novel combustor/heat exchanger concept, the rationale of burning H_2 to generate H_2 remains unclear.

Federici et al. [25] developed a combustor with an integrated thermoelectric device to generate electricity from hydrogen combustion. The same combustor design developed by Norton et al. [12] was integrated with a thermoelectric device. Thermal uniformity across the thermoelectric device is important for maximizing the efficiency of the thermoelectric, necessitating the use of an additional thermal spreader on the combustor. Roughly 22 percent of heat generated from combustion was lost in the exhaust, indicating the potential of heat recuperation for increasing the performance of the device. This thermoelectric combustor was able to generate around 1 W of gross electrical power at roughly 0.8 percent system efficiency.

2.3. Integrated Combustor Oil Heat Exchangers

To the author's knowledge, only one integrated hydrogen combustor oil heat exchanger has been developed. Sandia National Labs [7] developed hydrogen combustor to transfer 30 kW of heat to a circulating oil flow. The purpose of Sandia's design was to transfer thermal energy from combustion to a heat transfer fluid (oil), which was circulated through a metal hydride hydrogen storage system to cause desorption of hydrogen. The combustion channels were designed to transfer heat to the adjacent oil channels in a co-flow configuration. The combustion channel height and oil channel height were 3.4 mm and 0.76 mm, respectively. The combustion channels were coated with a high temperature furnace paint mixed with a palladium carbon powder. While the authors stated that the purpose of the catalyst was to avoid the high temperatures of homogenous combustion, the channel size is large enough that homogeneous reactions are not necessarily suppressed. As previously discussed, combined homogeneous/heterogeneous combustion can occur in channels as small as 1 mm [9]. This combustor operated at a fixed equivalence ratio of $\Phi = 0.26$. A cross-flow thermal recuperator was used to preheat the incoming gases with the excess heat in the exhaust gas with channel heights of 0.76 mm.

This combustor transferred 30 kW of heat to the oil with 90 percent efficiency at the maximum power level. The greatest efficiencies of 90 – 95 percent were achieved at an outlet oil temperature of 100 °C, with efficiencies of 80 – 85 percent for oil temperatures of

150 °C. Oil temperatures of 165 °C resulted in efficiencies of less than 80 percent. The oil was preheated before entering the combustor and the flow rate was relatively high, resulting in small oil temperature rise across the combustor. Therefore, the reported oil temperature is approximately equal to the average oil temperature in the combustor. Increased hydrogen conversion was achieved at higher operating temperatures; however, this also caused greater thermal losses to the exhaust gas and to the environment. Between 2 – 8 percent of the heat was lost to the exhaust gas, depending on the operating temperature. The heater's size envelope was 32 x 38 x 30 cm, not considering the insulation.

2.4. Summary

The findings of the literature discussed here were used to direct the development of the combustor heat exchanger for this research. The most useful findings are as follows:

- The complete combustion of H_2 at residence times between 4 and 40 ms reported by multiple investigators [9,11-13] was useful as a target range of residence times in the design of the experimental facility.
- The trend of increased ignition temperatures for increased equivalent ratios reported by Deutschmann et al. [15] was useful for estimating the required preheat temperature to initiate combustion. While some investigators reported room-temperature ignition [11,12], others devices required preheating [13,23]. These reports helped guide the decision to incorporate a preheating mechanism into the design of the test article.
- The catalyst deposition method utilized by Norton et al. [12] was adapted for use in this research. Also, the temperature profile to that obtained with the stainless steel heat spreader from this paper was used for comparison to the experiments conducted as part of this thesis due to the similar wall material.
- A counter-flow recuperator, similar to that used by Peterson et al. [23], was utilized in the design concept used for this thesis.

- The performance of the combustor/heat exchanger developed by Sandia was used as a comparison because of the similar design goals. In particular, it was desired to develop a device of equivalent or improved efficiency with a smaller size envelope.

The current status of research in micro scale combustors has demonstrated that catalytic hydrogen combustion can be utilized to generate high temperatures in small packages. However, only a few investigators [11,13,25] have developed potential applications for this technology. The research presented in this thesis builds upon the aforementioned investigations to present an additional application for micro scale hydrogen combustion.

3. SCOPE AND OBJECTIVES

There is a need for a compact combustor that transfers heat to oil at high efficiencies. While the combustor developed by Sandia [7] represents an important first step in developing this technology, additional improvements are needed in order to obtain a compact design suitable as a component in the hydrogen storage system of a hydrogen powered vehicle. As an additional step toward the development of full size (12 – 30 kW) combustor heat exchanger (CHX), this research presents the experimental performance characterization of a single unit cell of a microscale hydrogen combustor heat exchanger (μ CHX).

The design concept for a unit cell of a microscale hydrogen combustor heat exchanger is shown in Fig. 3.1. Air and H_2 flow through the center channel where the combustion reaction will be facilitated by a noble metal catalyst. The hot gases will then flow back between the combustion channel and the oil channels. This design was selected in order to recapture excess heat in the exhaust and protect the oil from the high temperatures of combustion. This was both to improve the efficiency of the system and reduce the potential of exceeding the temperature limit of the oil. All adjacent fluid streams are in a counterflow arrangement in order to maximize the outlet oil temperature and minimize the exhaust gas temperature for maximum efficiency. A full size device would be composed by scaling up the design with hundreds of these unit cells in a single device.

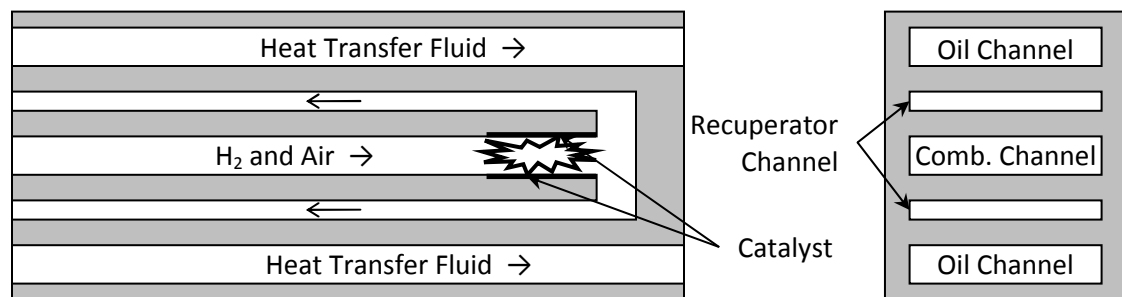


Fig. 3.1: μ CHX unit cell design concept

The first objective of this research was to demonstrate proof of concept of the unit cell design. The second objective was to characterize the efficiency of the device, defined as the ratio of heat gained by the oil, normalized by the available energy input from H_2 . This was to

be performed by obtaining global measurements of the fluid temperatures, pressures and flow rates. A major task involved the setup of an elaborate experimental facility to enable such experiments to be performed. The facility was built in order to provide experimental validation of a computational fluid dynamics (CFD) numerical simulation of a similar geometry. The CFD investigation was conducted concurrently by Ghazvini et al. [1] and is an ongoing investigation. The validation is to be accomplished by matching the experimentally obtained system efficiencies and H₂ conversion efficiencies to the CFD model for a variety of residence times, equivalence ratios and average oil temperatures. This will provide the information needed in order to optimize the unit cell design using the CFD model before fabricating and testing a full size CHX.

4. EXPERIMENTAL FACILITY

An experimental facility was developed in order to conduct the proof-of-concept experiments for the μ CHX unit cell concept and is described in this chapter. This included designing and fabricating a test article, along with procuring the instrumentation and equipment necessary to obtain the desired global measurements. Additionally, a safety analysis was conducted in order to determine the risks associated with potential failure modes.

4.1. Design Requirements

The designs of the test section and test facility were developed in consideration of many factors. As this is a proof of concept experiment, a significant amount of design development was involved in realizing the initial concept into an experimental prototype. The designs of the test section and test facility were conducted concurrently in order to minimize the projected experimental uncertainty. In order to meet the objectives listed in the previous chapter, the test section needed to have the following design requirements:

- Adjustable combustion channel and recuperator channel height
- Easy disassembly of the device to replace the catalyst or channel shims
- Uniform flow distribution
- No condensation of water within the recuperator channel
- Stringent safety standards
- Reactor must be able to be preheated
- Minimized heat losses and measurement uncertainties

The above pertain to the design of the reactor. The facility was designed and built around the reactor in order to provide it with the required inlet and exit conditions. The experimental facility, which includes the test section and the flow loop, was designed according to these requirements. It was important to be able to disassemble the device to be able to modify the internal characteristics of the device, such as the channel heights and catalyst bed. Changing the catalyst shim was particularly important because it would allow for different catalyst

types, locations and lengths to be tested. Uniform flow was necessary in order to validate the 2D CFD model being concurrently developed by Ghazvini et al. [1]. Condensation of water within the recuperator channel was undesirable because it could block the channel, causing non-uniform flow and increased pressure drop. Stringent safety standards were necessary for the experimental facility due to the extreme flammability of hydrogen gas. It was critical to minimize any potential H_2 release and dilute any H_2 discharge to below the 4 percent lower explosive limit (LEL, by volume). Some investigators [13,23] reported that preheating was required to initiate combustion, so a preheating mechanism was determined to be necessary for the μ CHX. In order to accurately determine the performance of the μ CHX, it was necessary to minimize heat losses and measurement uncertainties.

4.2. Design Considerations for Test Section

The design of the test section was developed such that the μ CHX could be reconfigured to investigate the effect of changing the geometric parameters. This complicated the design substantially because of the three types of fluid streams that needed to be sealed. With one combustion channel, two exhaust channels and two oil channels, even a single unit cell would have five separate channels to seal. Permanent sealing techniques could have been employed to seal the test section, but this would not have allowed for the μ CHX to be reconfigured for different experiments. Also, an internal flow distribution system was required that would provide uniform flow in each channel. Many design iterations were considered before a practical design was developed. The more significant design considerations are discussed below.

4.2.1. Design Simplification

Initially, the μ CHX was designed to test the performance of a complete unit cell. However, the five fluid streams caused significant difficulties in designing the device both to seal and be reconfigured. The internal flow distribution system also posed a challenge because the large aspect ratio channels needed to converge into a more manageable plenum for attaching fittings. By designing the μ CHX based on half of the previously described unit cell,

shown in Fig. 4.1, several advantages were obtained. The second recuperator channel and the second oil channel were eliminated, significantly simplifying the seal design. Also, the simplification allowed the combustion channel to be accessed for spatial temperature measurements. However, removing these channels from the design increased the potential for heat losses. Insulation was placed around the entire μ CHX to minimize the impact of these heat losses.

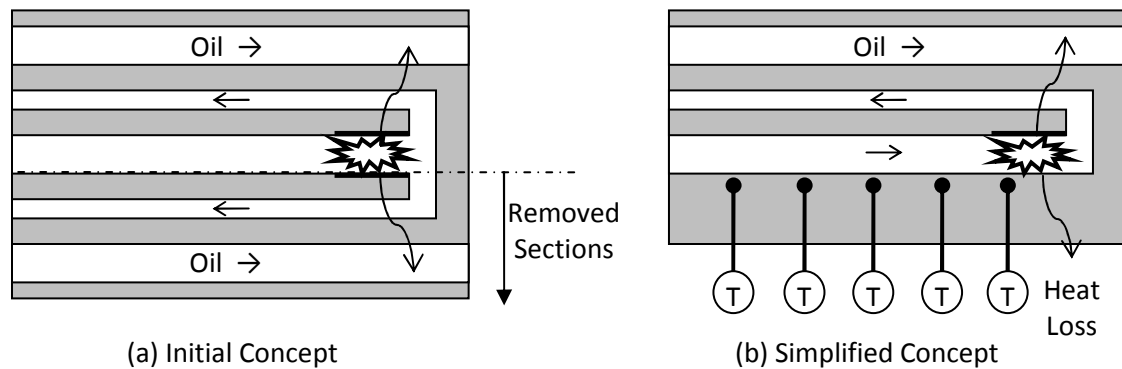


Fig. 4.1: Schematic of design simplification

4.2.2. High Temperature Gas Sealing

Based on the previous studies of microscale hydrogen combustion, gas temperatures up to 800 °C in the combustion channel were anticipated. This meant that o-rings could not be used to seal the gas channels. It was decided that shims of varying thickness would be used both to form and seal the gas channels. Copper is a relatively soft metal when compared to stainless steel and was initially selected as the shim material for the gas channels. The change in channel height due to compression of the shims was neglected because it was calculated to be more than an order of magnitude below the uncertainty of the shim thickness.

With a melting temperature around 1100 °C, it was anticipated that copper would be able to handle the anticipated high temperatures of combustion. Compressing alternating layers of copper and stainless steel shims was initially implemented in order to seal the gases at high temperatures. However, the copper shims partially fused to the stainless steel during

preliminary testing, making the μ CHX very difficult to disassemble. Stainless steel shims were then utilized to avoid this problem.

There was some initial difficulty in obtaining a good seal with the compressed shims. Several design iterations were performed, increasing the bolt size and reducing the bolt spacing in order to increase and more uniformly distribute the compressive force on the shims. Leakage was never entirely eliminated, but was reduced to less than 0.1 % of the minimum gas flow rate tested.

4.2.3. Oil Channel Sealing

The oil was not expected to reach temperatures in excess of 200 °C. This allowed for o-rings to be used in order to seal the oil channel. The design developed based on the copper shims for sealing the gases required a relatively large, machined slot for the oil channel. In order to form a microchannel for the oil, a high temperature plastic insert, PEEK, was designed to fit into the slot. PEEK has a higher coefficient of thermal expansion than stainless steel, so the PEEK insert was manufactured slightly narrower than the width of the oil channel cavity. At room temperature, this allowed for easy insertion of the PEEK into the oil channel slot, as shown in Fig. 4.2. At operating temperatures above 170 °C, the PEEK insert expanded to fill the width of the slot, as shown in Table 4.1.

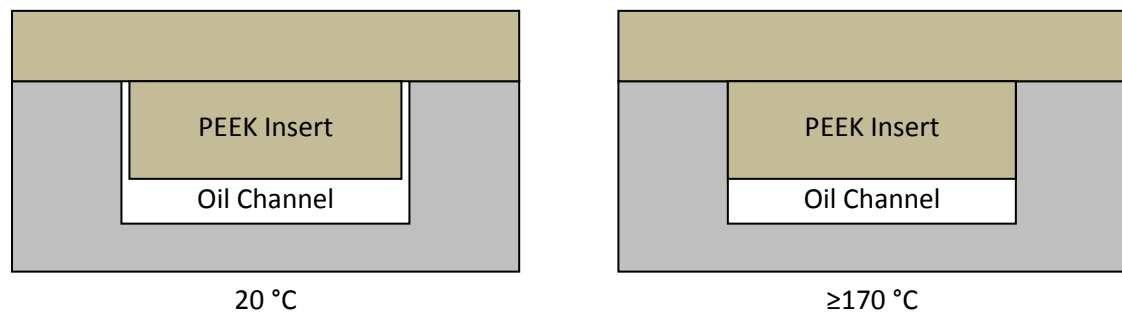


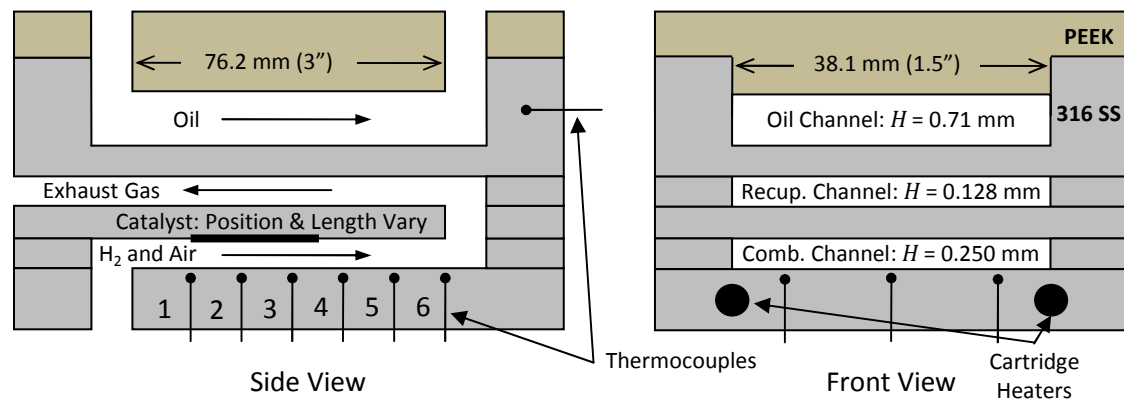
Fig. 4.2: Oil channel sealing schematic

Table 4.1: PEEK oil channel insert fit at different operating temperatures

	Stainless Steel	PEEK	Difference
Thermal Expansion ($^{\circ}\text{C}^{-1}$)	1.73E-05	4.70E-05	N/A
Width at 20 $^{\circ}\text{C}$ (mm)	38.097	37.929	-0.168
Width at 100 $^{\circ}\text{C}$ (mm)	38.150	38.072	-0.078
Width at 150 $^{\circ}\text{C}$ (mm)	38.183	38.161	-0.022
Width at 170 $^{\circ}\text{C}$ (mm)	38.196	38.196	0.000
Width at 200 $^{\circ}\text{C}$ (mm)	38.216	38.250	0.034

4.3. Final μCHX Assembly

The cross-sectional view of the μCHX design based on the above design consideration is shown in Fig. 4.3. Compressed air and hydrogen flow into the combustor plane where they react in the presence of a noble metal catalyst. After combusting, the resulting gases flow into the upper recuperator plane. These hot exhaust gases flow between the incoming combustion gases and the heat transfer fluid. The exhaust gases heat the combustion gases up to the temperature required for combustion while simultaneously heating the heat transfer fluid.

Fig. 4.3: Cross sectional schematic of μCHX

This μCHX consists of a single set of channels, 38.1 mm (1.5 in) wide and 76.2 mm (3 in) long. Plenums were used to distribute and collect each fluid stream. The combustion channel,

recuperator channel and catalyst plate were cut from shim stock material of various thicknesses. The copper and stainless steel shims were fabricated using an ESI 5330 UV Laser μ Via Drill that is located in the MBI facilities. The laser settings used for fabricating the shims are listed in Table 4.2. The large stainless steel components and PEEK parts were machined by an external vendor. Detailed part drawings are located in Appendix A.

Table 4.2: ESI 5330 settings for shim fabrication

Part Name	Material	Shim Thickness	Power	Cutting Speed	Repetitions	Depth Increment
Cu Channel Shims	Copper	0.100 mm 0.150 mm 0.250 mm	5 W	60 mm/s	45	0.050 mm
SS Channel Shims	316 SS	0.125 mm 0.250 mm	5 W	100 mm/s	30	0.050 mm
Catalyst Shim	316 SS	0.250 mm	5 W	100 mm/s	30	0.050 mm
Mask	304 SS	0.050 mm	1.75 W	160 mm/s	55	0.050 mm
Mask Support	304 SS	0.300 mm	5 W	100 mm/s	30	0.050 mm

The shims forming the gas channels were sandwiched between two thicker, stainless steel plates, shown in Fig. 4.4. This assembly is bolted together with 3/8" – 24 socket head cap screws, spaced 1" on center. These bolts are tightened with a torque wrench to apply even pressure on the shims. The high pressure on the shims causes them to act as a gasket, sealing the channels in the μ CHX.

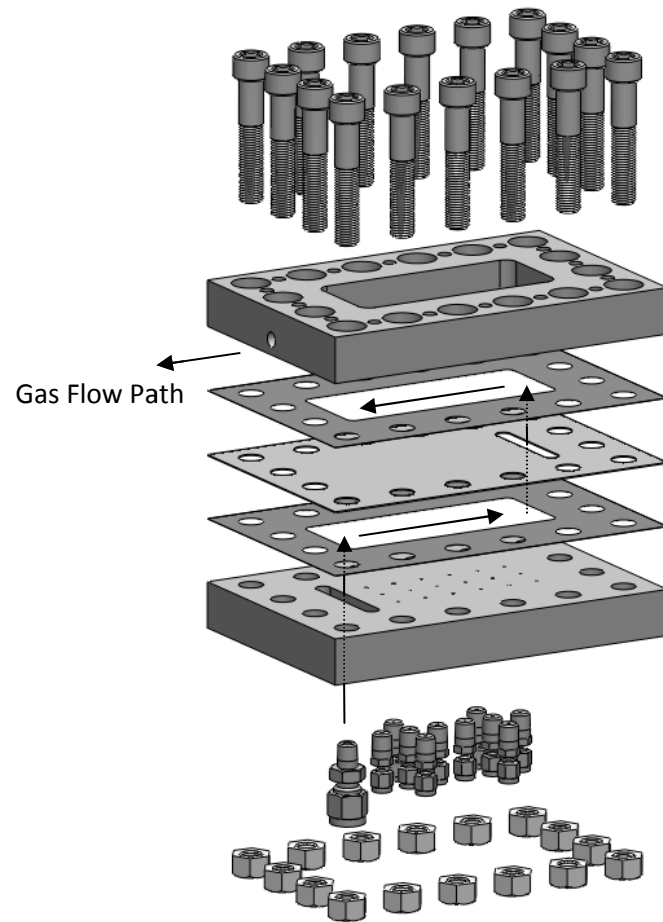


Fig. 4.4: Exploded μ CHX

A separate set of bolts was used to compress the o-rings sealing the oil channel, shown in Fig. 4.5.

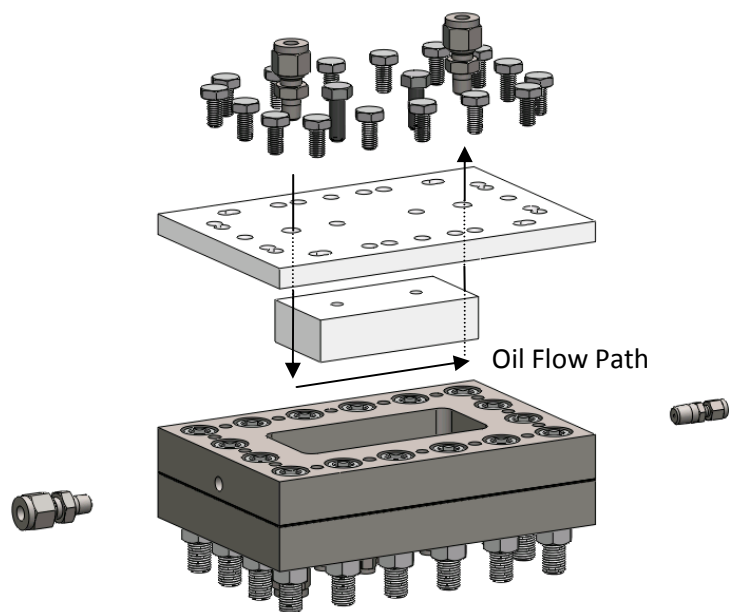


Fig. 4.5: Partially exploded μ CHX

Tube fittings were attached to the top, bottom and side of the assembly as headers, shown in Fig. 4.6.

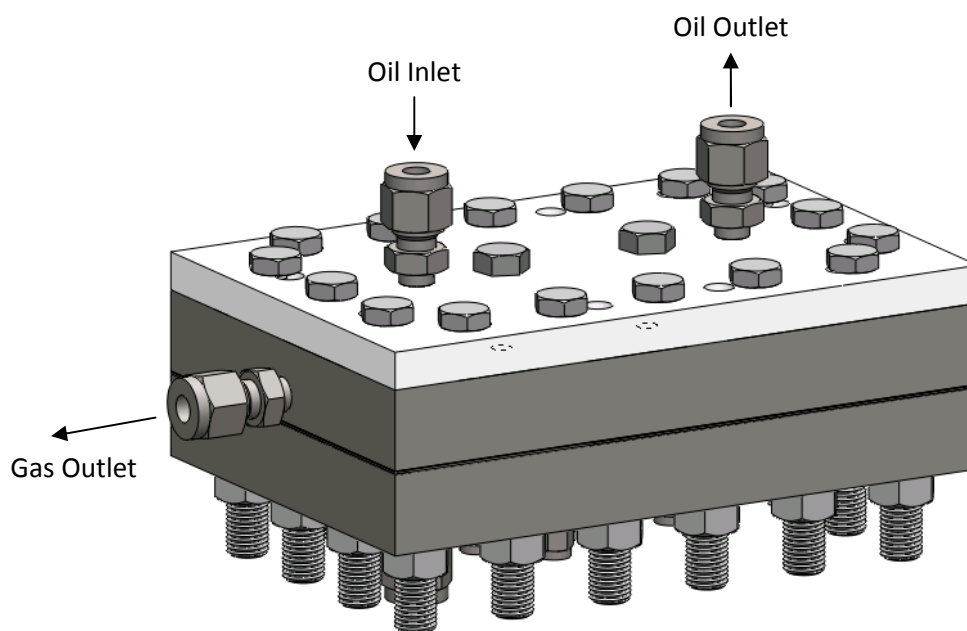


Fig. 4.6: Assembled μ CHX, topline

There was a 3x6 array of thermocouple ports with 12.7 mm (0.5 in) spacing, located 0.5 mm (0.020 in) below the combustion channel, shown in Fig. 4.7. Up to 10 K-type thermocouples may be used in these ports at a time due to a limited number of data acquisition channels. These ports allow for temperature profile measurements along the length and the width of the combustion channel to allow observation of the temperature variations caused by catalytic combustion. There is also a thermocouple port on the side of the μ CHX to obtain temperature measurements of the μ CHX body. Cartridge heaters were inserted into holes in the stainless steel base to help bring the μ CHX up to the temperature required to initiate combustion.

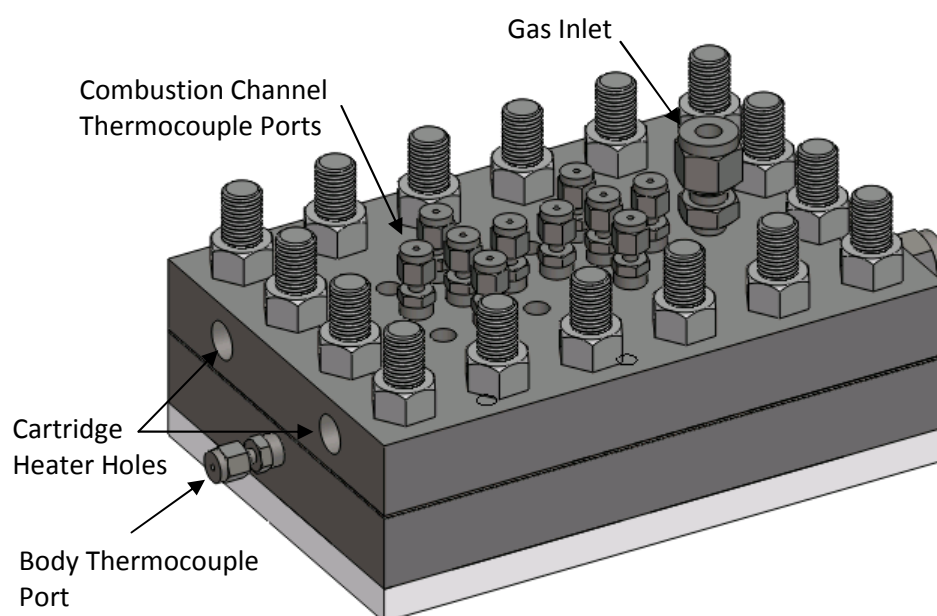


Fig. 4.7: Assembled μ CHX, underside

An image of the final μ CHX assembly is shown in Fig. 4.8. Finally, the entire μ CHX assembly was wrapped with four layers (4 cm total) of high temperature insulation blanket (Pyrogel® XT) to minimize thermal losses.

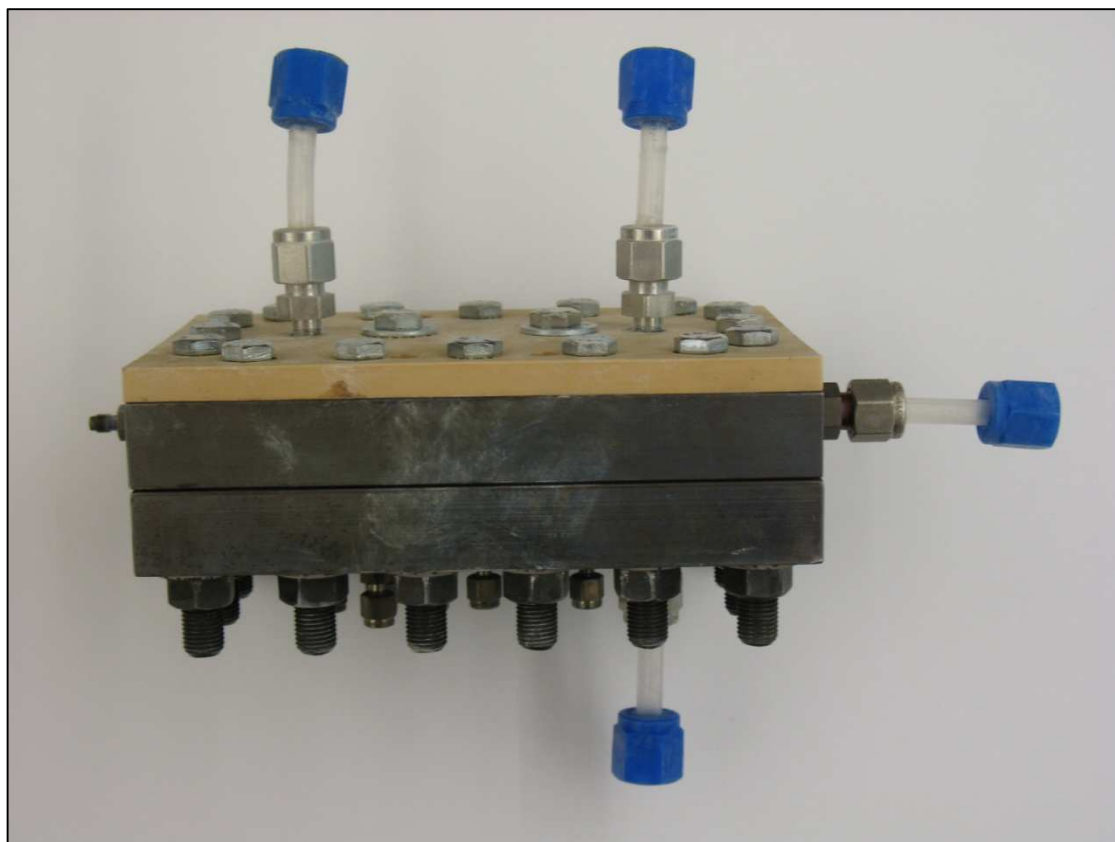


Fig. 4.8: Image of actual μ CHX assembly

4.3.1. Measurement of Internal Dimensions

The internal dimensions of the μ CHX were determined by measuring the heights of all components before, during and after assembly. The height of the combustion channel, recuperator channel and the catalyst shim were determined by measuring the shim thickness prior to assembly. The schematic shown in Fig. 4.9 indicates the measurements required in order to calculate the heights of the internal features. The oil channel height was designed to be 700 microns (0.028 in). A smaller oil channel was initially desired; however, it proved too difficult to obtain a smaller height with reasonable uncertainty. The length of the combustion channel was determined such that the diffusion time scale was significantly smaller than the residence time through the channel. Details regarding the operating conditions of the μ CHX are described in Section 4.3.1.

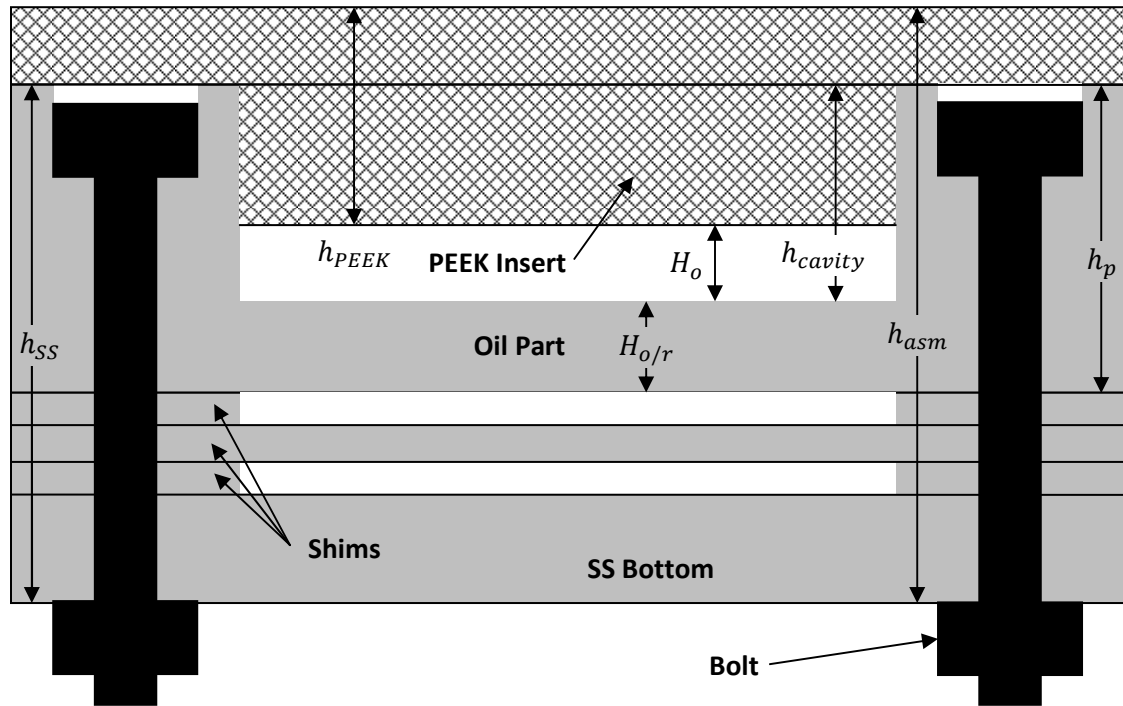


Fig. 4.9: Channel height measurement schematic (Flow into page)

The height of the oil channel was calculated as:

$$H_o = h_{asm} - h_{SS} + h_{cavity} - h_{PEEK} \quad (4.1)$$

where h_{PEEK} and h_{cavity} had to be measured prior to assembly. Measurement of h_{SS} had to be performed after the stainless steel parts had all been bolted together, but before the PEEK parts were inserted. Once the PEEK parts were inserted, h_{asm} could be obtained and H_o could be calculated. The height of the stainless steel between the oil channel and the recuperator channel was calculated as:

$$H_{o/r} = h_p - h_{cavity} \quad (4.2)$$

where both h_p and h_{cavity} were measured prior to any components being assembled.

Table 4.3: Measurements μ CHX channel heights

	Value (mm)	Uncertainty (mm)
Oil Part Thickness	19.194	0.018
Oil Part Depth	17.336	0.034
Oil Recup thickness	1.859	0.039
Assembled PEEK Parts	24.387	0.076
Assembled Combustor, wo/PEEK	38.871	0.056
Assembled Combustor, w/PEEK	46.629	0.121
Oil Channel Height	0.707	0.157
Comb. Shim Thickness	0.250	0.005
Recup. Shim Thickness	0.128	0.004

4.4. Operational Parameters of μ CHX

The μ CHX was designed to be operated over a wide range of experimental conditions while being able to accurately quantify the performance characteristics. The operating conditions dictated the test section and the test facility design. The effects of varying channel height, equivalence ratio and flow rate were considered. All the calculations were performed for a non-combusting flow based on the inlet conditions. It was assumed that the μ CHX was discharging to ambient pressure, so the inlet pressure was no greater than required to drive flow through the system. The residence time is a critical parameter for combusting flows, with shorter residence times potentially causing incomplete hydrogen conversion. Short residence times result from increased flow rates, smaller channel heights and shorter catalyst lengths. It was desired to be able to test residence times between 5 – 50 ms. Different full scale flow ranges were considered for the air and H_2 mass flow controllers in order to obtain the desired residence time range for the μ CHX geometry. The impact of the mass flow controller flow ranges on residence time for variation of channel height and equivalence ratio are presented in sections 4.4.1 and 4.4.2, respectively.

4.4.1. Variation of Channel Height

One of the distinct advantages of the modular design of the μ CHX was that different combustion channel heights could be investigated. The impact on residence time by changing the channel height is shown in Fig. 4.10. This chart was determined assuming that the full length of the combustion channel was coated with catalyst. Decreasing the length of catalyst coating would result in a proportional decrease in residence time. Residence time is presented as a function of total gas flow rate, which is held constant during a given experimental run.

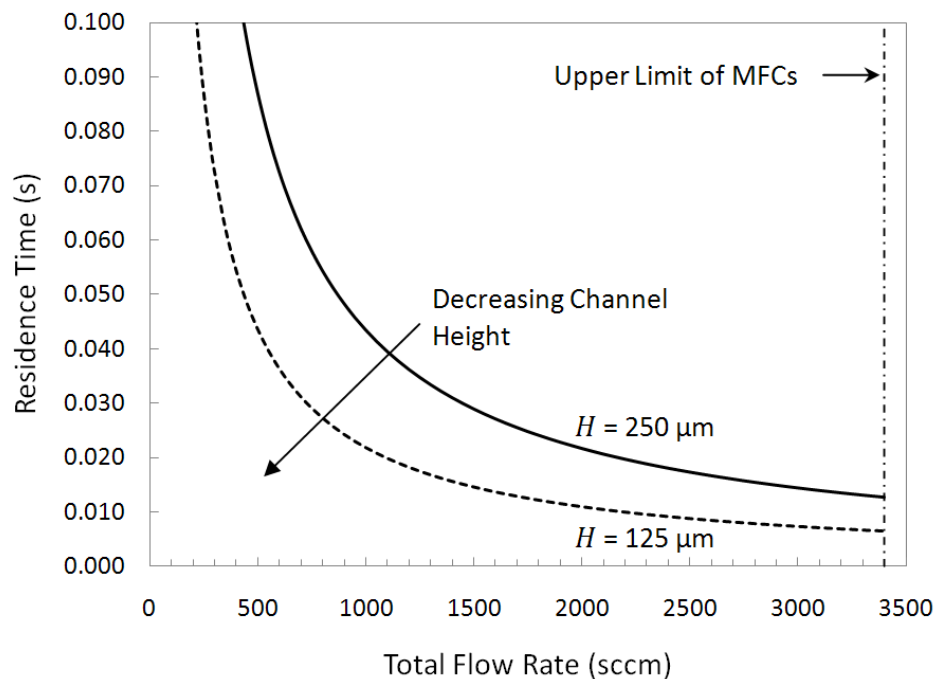


Fig. 4.10: Residence time effects of channel height variation

4.4.2. Variation of Equivalence Ratio

The effects on residence time for variations in equivalence ratio were also considered. This is presented as a function of hydrogen flow rate in Fig. 4.11, for a channel height fixed at $250 \mu\text{m}$ and for 100 % of the channel covered with catalyst. Also shown on the secondary axis is

the heat input rate corresponding to the hydrogen flow rate. The heat input rate was calculated as:

$$\dot{Q}_{H_2} = \dot{m}_{H_2} q_{H_2,LHV} \quad (4.3)$$

where $q_{H_2,LHV}$ is the lower heating value for H_2 . The hydrogen flow rate is an important basis of comparison because it is directly related to the amount of energy available from the combustion reaction. Higher heat generation rates were desired in order to minimize the ratio of heat losses.

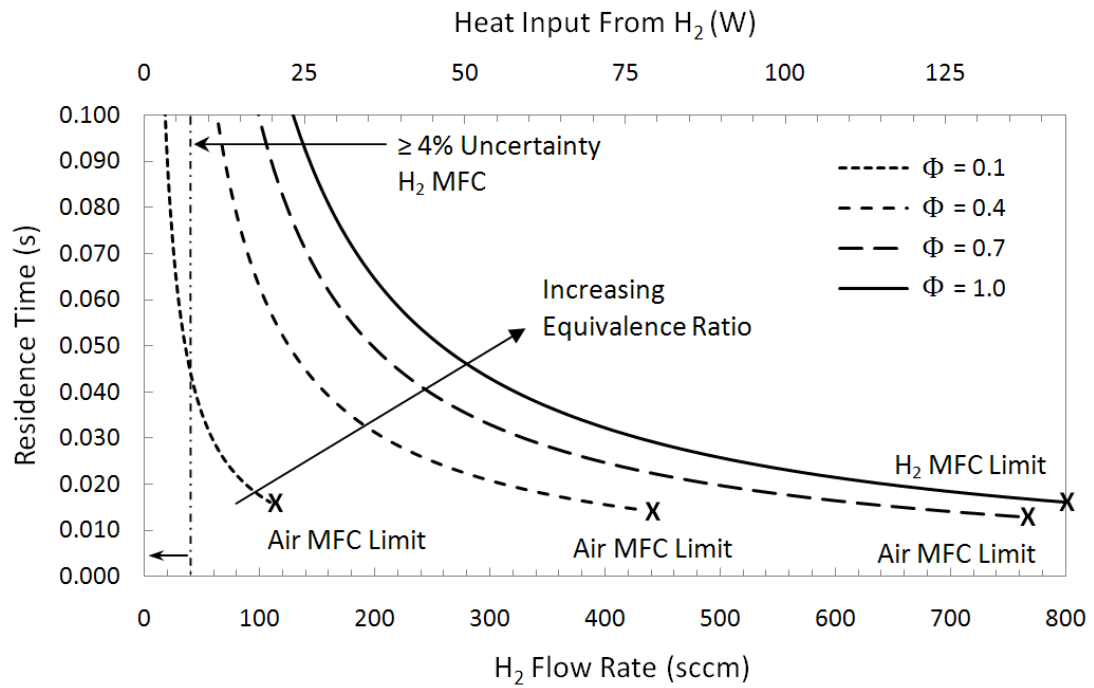


Fig. 4.11: Residence time effects of equivalence ratio variation

For a set hydrogen flow rate, lower equivalence ratios result in higher air flow rates. As a result, not all equivalence ratios can be conducted for the full range of flow rates shown in Fig. 4.10. All equivalence ratios could be tested at total flow rates ≤ 2600 sccm and the higher flow rates limit the equivalence ratio range, as shown in Table 4.4.

Table 4.4: Experimental Equivalence Ratio Limits

Total Flow Rate (sccm)	Minimum Φ	Maximum Φ
≤ 2600	0	$1 <$
2700	0.09	1
2800	0.18	0.95
2900	0.27	0.91
3000	0.37	0.87
3100	0.46	0.83
3200	0.55	0.79
3300	0.64	0.76
3400	0.73	0.73

4.5. Test Facility

A schematic of the test facility is shown in Fig. 4.12. The facility was located in the Hydrogen Lab at the Microproducts Breakthrough Institute (MBI). MBI is located in Building 11 on the Hewlett Packard campus in Corvallis. The entire test facility was located within a vent hood for safety. The instrumentation installed in the experimental facility is listed in Table 4.7 and include the manufacturer, model number, range, and manufacturer-specified uncertainties for each instrument. The equipment in the facility is listed in Table 4.8. Compressed hydrogen, nitrogen, dry air and process cooling water were available inside the vent hood. The pressure of each gas was regulated down from the line pressure to around 200 kPa (30 psi) for the experiments. A check valve with a 70 kPa (10 psi) crack pressure was attached to each line in order to prevent H₂ backflow into the other lines. Nitrogen was not used for combustion experiments, but was used to purge the H₂ lines as part of the shutdown procedure. A normally closed solenoid valve was installed on the H₂ line as a safety feature. Mass flow controllers (MFCs) for H₂ and air were used to regulate the flow rates of each gas to control the residence time and equivalence ratio. Flashback arrestors with an internal check valve were installed downstream of the MFCs to prevent potential explosions from propagating upstream.

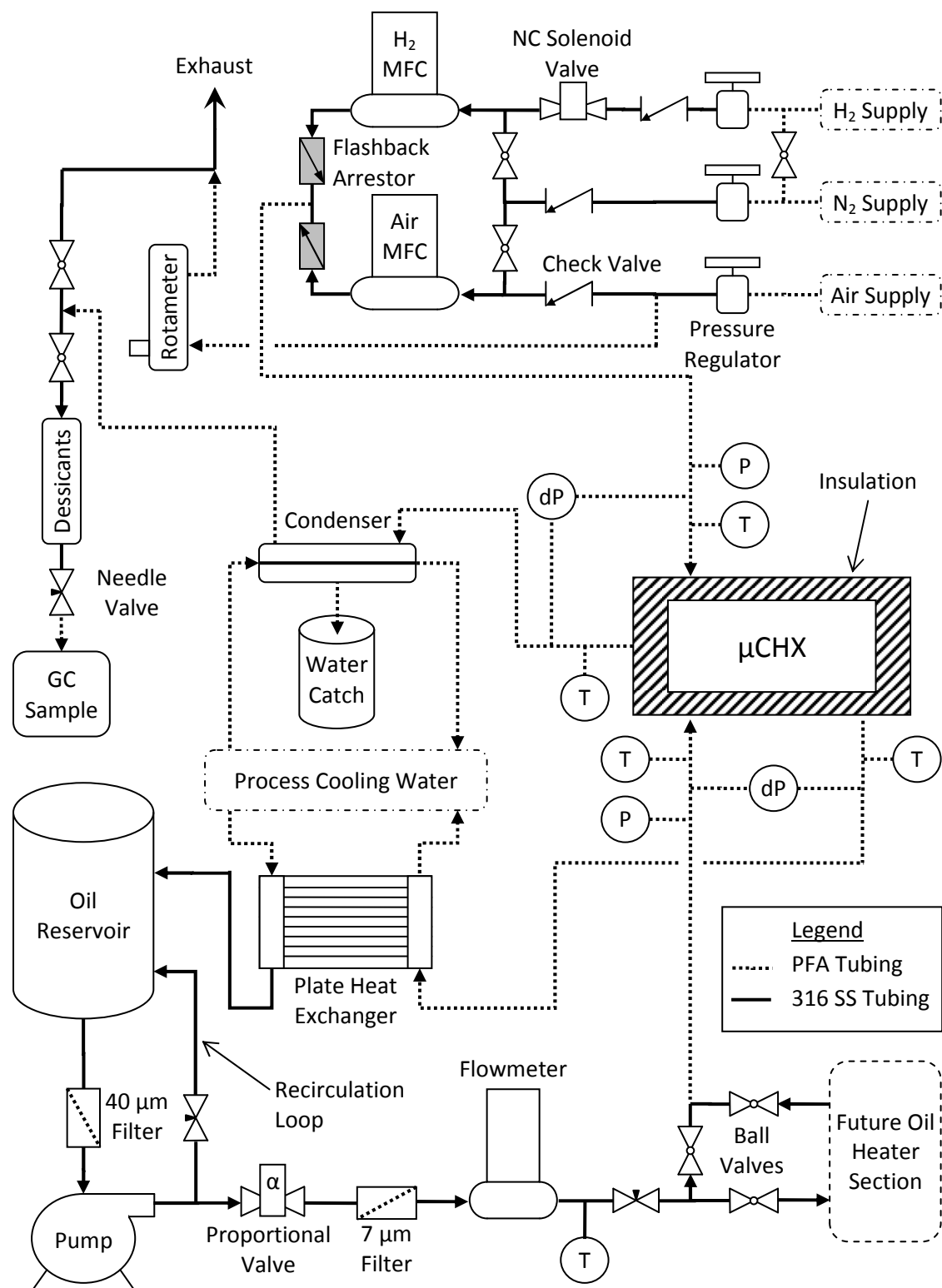


Fig. 4.12: Test facility schematic

High temperature PFA tubing was used to deliver the gas mixture and oil to the μ CHX. This tubing was used extensively due to its flexibility and low thermal conductivity. The gas and oil temperatures and absolute pressures were measured at the inlets. Differential pressures between the inlet and outlet of both the gas and oil channels were also measured. Also, the outlet temperatures were measured with thermocouples. All connections to the μ CHX were made with PFA tubing. The μ CHX was wrapped in four layers of high temperature, Pyrogel XT insulation. Both of these considerations were implemented to minimize conduction heat losses.

Paratherm MG oil was used as the heat transfer fluid and was stored in a plastic reservoir before being pumped through the flow loop. The oil flow rate was primarily adjusted by varying the pump speed. Further refinement of the flow rate was made by adjusting the proportional valve and needle valve on the recirculation loop. The flow rate of oil to the μ CHX was measured with a positive displacement flow meter. The oil temperature was measured immediately following the flow meter in order to determine the mass flow rate of the oil. It was initially desired to have the ability to preheat the oil prior to it entering the μ CHX. This heater section was not incorporated into the flow loop; however, a set of bypass valves allow for this to be used in future investigations. The hot oil exiting the μ CHX was cooled with water in a plate-type heat exchanger before being discharged to the reservoir. Thermocouples and pressure sensors were attached to the oil and gas inlets and exits in order to measure the temperature rises and pressure drops across the μ CHX.

In order to measure the exhaust gas composition with a gas chromatograph (GC), the water vapor formed from combustion first had to be removed from the exhaust; this was done in a two step process. First, the exhaust gas flowed through a condenser cooled with water where the water vapor condensed and was collected. The condenser was a custom built, counter-flow shell and tube heat exchanger approximately 25 cm long. If a GC sample was to be collected, the gas was passed through two desiccant filters to further dry the air before being collected in a sample bag. During standard operation, the exhaust was diluted before being released into the vent hood. This was done because if combustion was not occurring in the μ CHX, then the exhaust gas would be in the flammable range (4-75% by volume) and was

therefore diluted with air at approximately 80,000 ml/min. The maximum flow setting for the H₂ MFC was 800 ml/min, so an air flow rate of 80,000 ml/min would bring the H₂ concentration below 1 % for any operating condition. Dilution flow rate was manually adjusted and measured with a rotameter.

The heat transfer fluid used in this flow loop was Paratherm MG. It is stable and has a slight flammability risk according to the National Fire Protection Association (NFPA). A secondary heat transfer fluid, Paratherm LR, has a moderate flammability risk and was considered for tests at low operating temperatures. The outlet oil temperature was anticipated to be above the flashpoint of both fluids for the majority of operating conditions. This fire risk was mitigated by designing the oil flow loop such that all sections containing oil above the flashpoint were located within the vent hood. The details of both fluids are listed in Table 4.5. It was determined that the lower operating temperature of the Paratherm LR was not required for this phase of research; consequently, all experiments were conducted using Paratherm MG as the heat transfer fluid.

Table 4.5: Heat transfer fluid properties (Adapted from [43])

	Primary Heat Transfer Fluid	Secondary Heat Transfer Fluid
Name	Paratherm MG	Paratherm LR
Max Operating Temperature	304 °C (580 °F)	249 °C (480 °F)
Min Operating Temperature	2 °C (36 °F)	-49 °C (-57 °F)
Max Film Temperature	316 °C (600 °F)	288 °C (550 °F)
Max Vapor Pressure	22.8 kPa @ 304 °C	145 kPa @ 232 °C
Vapor Pressure @ 21 °C	< 0.1 mm Hg	< 0.1 mm Hg
Health Hazard Rating	0 (Least)	1 (Slight)
Fire Hazard Rating	1 (Slight)	2 (Moderate)
Reactivity Hazard Rating	0 (Least)	0 (Least)
Environmental Requirements	None listed	Use only in a well-ventilated area
Flashpoint	149°C (300°F)	> 60°C (140°F)
Flammable Limits by Volume in air @ 25 °C	No Data	0.7 % – 5.4 %
Effect of Skin Contact	No irritation expected for direct, repeated or prolonged contact	<ul style="list-style-type: none"> • May be irritating on direct single contact • Repeated or prolonged contact of used product may cause minor skin irritation
Personal Health Protection Required	<ul style="list-style-type: none"> • Insulated clothing for hot fluids • Ventilation needed if vapor is generated during heating 	<ul style="list-style-type: none"> • No protection required for short duration exposure • For prolonged or repeated exposure, synthetic rubber (nitrile) protective covers should be worn • If material will be handled while hot, wear insulated clothing along with synthetic rubber covers • Ventilation needed if vapor is generated during heating
Handling and Storage	Store in closed containers away from heat, sparks, open flame, or oxidizing materials	<ul style="list-style-type: none"> • This material is a static accumulator • Drums must be grounded while handling • Avoid generating mist • Store in closed containers away from heat, sparks, open flame, or oxidizing materials • Protect metal drums from direct sunlight and water

4.5.1. Data Acquisition

The data acquisition system used in these experiments is shown schematically in Fig. 4.13. Data was collected through a LabVIEW virtual instrument (VI) during the experiments at a rate of approximately 0.3 Hz. This VI was also used to control the experiment and display the results in real-time. Pseudo code representations of the sections of the LabVIEW VI are provided in Appendix B.

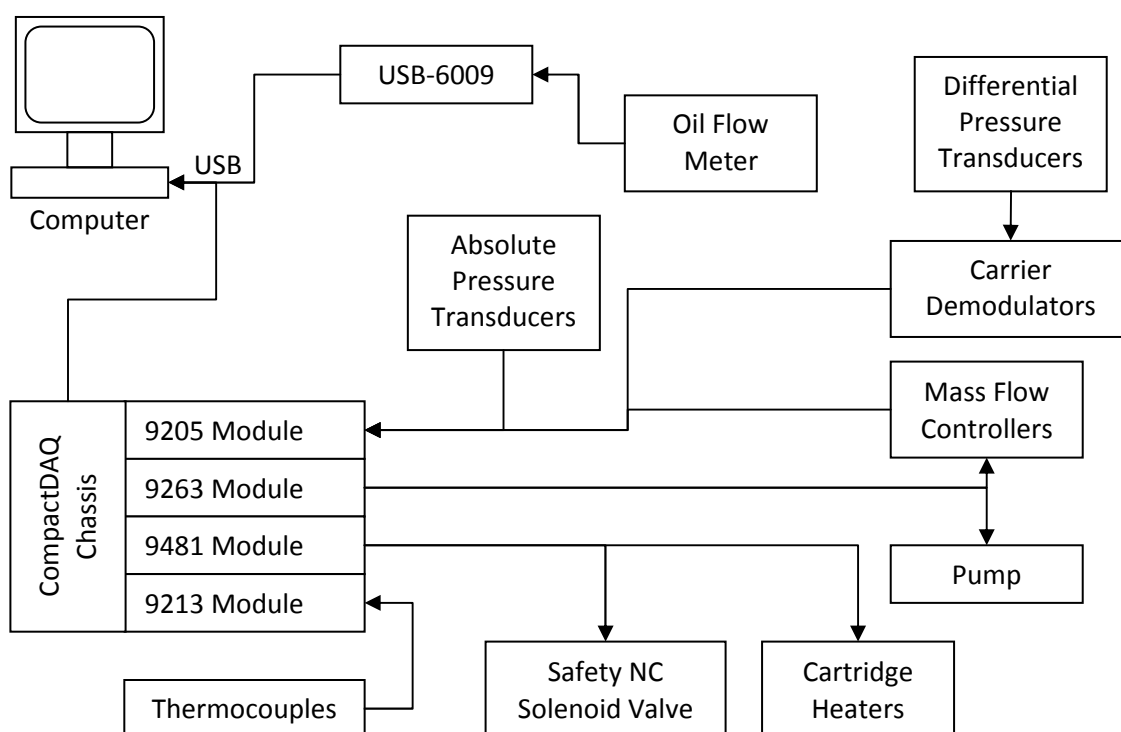


Fig. 4.13: Instrumentation schematic

The data acquisition equipment used is listed in Table 4.6. Temperatures from calibrated thermocouples were read using a National Instruments NI-9213 thermocouple module with a 24-bit, built-in cold-junction compensator. A National Instruments USB-6009 data acquisition board was used to acquire signals from the oil flow meter. A National Instruments NI-9263 analog voltage output module was used to send signals to the mass flow controllers and oil pump. A National Instruments NI-9205 analog voltage input module was used to acquire signals from the pressure transducers and mass flow controllers. A National Instruments NI-

9481 relay module was used to switch the H₂ solenoid valve and the cartridge heaters on and off.

Table 4.6: Data acquisition system

DAQ Components	Manufacturer	Model	Quantity	Range
USB Data Acquisition Board	National Instruments	USB-6009	1	8 AI, 2 AO, 12-bit DIO, 1 Counter
CompactDAQ Thermocouple Module w/Cold Junction	National Instruments	USB-9213	1	16 Channel, 24-bit
CompactDAQ Voltage Output Module	National Instruments	USB-9263	1	4 Channel, 16-bit
CompactDAQ Voltage Input Module	National Instruments	USB-9205	1	32 Channel, 16-bit
CompactDAQ Relay Module	National Instruments	USB-9481	1	4 Channel, SPST

4.5.2. Instrumentation and Equipment

The instrumentation installed in the experimental facility is listed in Table 4.7 and include the manufacturer, model number, range, and manufacturer-specified uncertainties for each instrument. The equipment in the facility is listed in Table 4.8. The equipment and instrumentation were selected in order to minimize the uncertainty in estimating the heat transfer rate.

The anticipated continuation of the research presented here would require experimental testing of a large array combustor that would generate 12 kW of heat. For this large array CHX experiment, the instruments and equipment marked by an asterisk in Table 4.7 and Table 4.8 will need to be either modified or replaced. This is because the instrumentation and equipment was specifically chosen such that the uncertainties would be within reasonably acceptable limits for the validation and performance characterization purposes of this present research. The equipment and instruments were chosen keeping the large array

experiments in mind such that minimal changes would be needed in the future. These changes are described in Appendix C.

Table 4.7: Facility instrumentation

Instrumentation	Manufacturer	Model	Quantity	Range	Manufacturer Uncertainty
H ₂ Mass Flow Controller *	Advanced Energy	AERA Transformer	1	16 - 800 sccm	±1% of setpoint (25 – 100% FS) ±0.25% of FS (2 – 25% FS)
Air Mass Flow Controller *	Advanced Energy	AERA Transformer	1	52 - 2600 sccm	±1% of setpoint (25 – 100% FS) ±0.25% of FS (2 – 25% FS)
Oil Flowmeter *	Max Machinery	213	1	1 - 1800 ml/min	±0.2% reading
Absolute Pressure Gauge	Omega	PX32B1	3	0 - 690 kPa [0-100 psia]	±0.25% of FS
K-type Thermocouples	Omega	K-type (SLE)	12	0 - 1100 °C	Greater of ±1.1 °C or ±0.4%
T-type Thermocouples	Omega	T-type (SLE)	4	-200 to 350 °C	Greater of ±0.5 °C or ±0.4%
Gas Differential Pressure Gauge *	Validyne	DP15 – 32	1	0 - 14 kPa [2.0 psi]	±0.25% of FS
Oil Differential Pressure Gauge *	Validyne	DP15 - 24	1	0 – 2.2 kPa [0.32 psi]	±0.25% of FS

Table 4.8: Facility equipment

Equipment	Supplier	Model	Quantity	Range
H ₂ NC Solenoid Valve *	ASCO	8262G2	1	N/A
H ₂ Flame Arrestor *	Concoa	532	1	345 kPa (50 psig)
Air Flame Arrestor *	Concoa	532	1	986 kPa (143 psig)
Oil Proportional Valve *	IQ Valves	930112 w/10-500 Amplifier	1	N/A
Oil Plate Heat Exchanger	McMaster Carr	8546T11	1	87 lpm, 230 °C max
Desiccant Air Dryer	McMaster Carr	7793T1	4	54 °C max
Cartridge Heaters	McMaster Carr	3618K438	2	500 W, 120 VAC, 870 °C max
Oil Pump Drive *	MicroPump	6008.340	1	N/A
Oil Pump Head *	MicroPump	6056.000	1	3.06 - 61.2 ml/min
Rotameter	Omega	FL-2044	1	10 - 100 lpm
Absolute Pressure Gauge	Omega	PX32B1	3	0 - 690 kPa (100 psia)
Pressure Regulator	Omega	PRG200-120	2	0 - 830 kPa (120 psig)
Oil	Paratherm	MG	1	2 - 304 °C
H ₂ Pressure Regulator	Swagelok	PGI-63S-PG100-LAOX	1	0 - 690 kPa (100 psig)

4.6. Safety Considerations

Safety was a primary concern during the design and operation of this research due to the usage of pressurized hydrogen. There were two major safety considerations: (1) prevention of a flame from propagating upstream, and (2) stoppage of the flow of hydrogen in the event of a leak or upstream flame propagation.

To address the first safety concern, flame arrestors were placed downstream of the mass flow controllers in the hydrogen and air lines. These are devices that prevent a flame or

explosion from propagating upstream to the air or hydrogen sources. There is a sintered material in the arrestor that passively absorbs heat, stopping a flame from moving upstream. Also, there is an internal check valve that closes in the event of a flame or explosion, preventing the gas from flow back to the MFC. The valve is automatically reset by supplying flow in the correct direction. Additional check valves are located on the H₂ line, N₂ line and air line to prevent back flow of any gases to the gas supply lines or dilution system, as shown in Fig. 4.12. These check valves provided an additional level of safety redundancy.

To address the second safety concern, the H₂ MFC contained a normally-closed solenoid valve and a secondary normally-closed solenoid valve was located on the hydrogen line between the MFC and the pressure regulator. The air MFC contained a normally-open solenoid valve. The solenoid valve on the H₂ line could be activated by one of four means: (1) an emergency button within the LabVIEW program, or (2) a LabVIEW trigger set by the μ CHX body temperature sensor, or (3) a manual switch located near the vent hood, or (4) a loss of power. These safety features were put in place through a consideration of the failure scenarios described in the next section. Also, an emergency shutdown button was located near both doors in the lab that would terminate the H₂ connection at the supply.

An emergency shutdown button was located in the LabVIEW program to stop combustion by closing the H₂ solenoid valve, setting the H₂ MFC to no flow, setting the air MFC to max flow and setting the oil to max flow. Closing the solenoid valve cuts off the flow of H₂, stopping combustion. Increasing the oil and air flow rates would begin cooling down the combustor. In the event of the LabVIEW program failure, there is a hard switch attached to the exterior of the vent hood that cuts power to the normally closed H₂ solenoid valve and turns off the cartridge heaters.

4.7. Failure Modes

Failure modes were considered using Failure Modes and Effects Analysis (FMEA) [44]. This process is a quantitative method to address failure risk for a product, system or process as shown in Table 4.9. The failure modes are ranked based on their risk priority number. This value is the product of the severity, occurrence and detection ratings. The risk priority

number indicates the relative riskiness/importance of each failure mode. The results of this analysis are tabulated in Table 4.10. The failure modes are described in further detail following the FMEA analysis. There are limitations of the FMEA, one of which being that there is no absolute threshold for acceptable and unacceptable RPN's [44]. As a result, each failure mode was subjectively evaluated based on the calculated RPN, along with their individual severity, occurrence and detection ratings.

Table 4.9: Failure modes and effects analysis legend

Severity Rating (S)	Meaning
1	Negligible Effect
2 to 3	Minor
4 to 6	Moderate
7 to 8	High
9 to 10	Very High (Results in unsafe operation)
Occurrence Rating (O)	Meaning
1	Negligible
2 to 3	Low (few failures)
4 to 6	Moderate (occasional failures)
7 to 8	High (repeated failures)
9 to 10	Very High (inevitable failure)
Advance Detection Rating (D)	Meaning
1	Negligible (certain detection)
2 to 3	Low risk (easily detected)
4 to 6	Moderate risk
7 to 8	High risk (unlikely detection)
9 to 10	Very high risk (almost undetectable)

Table 4.10: Failure Modes and Effects Analysis

Failure Mode	Effects	Severity Rating (S)	Cause(s)	Occurrence Rating (O)	Current Controls	Advance Detection Rating (D)	Risk Priority Number (RPN)
Flashback	Very high temperatures and fast upstream flame propagation.	3	Larger channel heights. Other causes unknown.	4	Flashback arrestors are located before the MFCs. Extreme temperatures will trigger program to extinguish combustion.	10	120
Sustained Homogeneous Combustion in test section	Very high temperatures. May melt test section if sustained.	9	Larger channel heights. Other causes unknown.	4	Extreme temperatures will trigger program to extinguish combustion.	2	72
Hydrogen Leak in Test Section	Fire risk	2	Improperly tightened test section. Improperly tightened fittings.	3	Entire flow loop is located within a vent hood. Test section tightened with torque wrench. CHX is pressure tested after every reassembly.	5	30
Sustained Oil Pump Failure	No oil flow, oil gets burned and CHX gets too hot	7	Equipment failure, closed valve	2	Automatic shutoff of H2 flow if a high CHX body temperature is detected.	2	28
Heat Exchanger Failure	Potential oil reservoir meltdown, pump damage, oil flow meter damage	9	inadequate cooling water flow, blocked channels	1	Oil inlet temperature to CHX. Temperature sensing label to tubing on outlet of heat exchanger for temperature observation	3	27
Hydrogen Leak in Flow Loop	Fire risk	2	Improperly tightened fittings.	2	Entire flow loop is located within a vent hood. An audible alarm goes off if vent hood fails. The H2 lines have been pressure tested to 50psi with no leakage. Pressure test flow loop after any fitting adjustment.	5	20
Power Failure	Venthood, pump, computer and flow controllers turn off.	2	City power outage	1	H2 flow is stopped by NC solenoid and NC MFC. Air continues to flow through NO MFC.	10	20
Uncombusted Hydrogen in Exhaust	Fire risk	1	Combustion not occurring	10	Entire flow loop is located within a vent hood. The exhaust gas is diluted below flammable levels if combustion were to stop.	2	20
Leak in Oil Loop	Hot oil spill	4	Leaks in oil loop	2	Personal protection equipment and proper leak testing of flow loop	2	16

4.7.1. Flashback

A flashback in the μ CHX or lines would result in very high temperatures and fast upstream flame propagation. It is likely that a flashback would melt the PFA tubing upstream of the μ CHX. Flashback arrestors were installed downstream of the MFCs to prevent flashbacks from damaging equipment if the PFA tubing did not melt. Flashback arrestors are standard components for welding systems; they have a sintered element that prevents upstream flame propagation and a check valve to prevent backflow. If a flashback is determined to have occurred, based on a high μ CHX body temperature, the LabVIEW program will automatically shut off the H_2 flow. The severity of this failure is expected to be low ($S=3$) due to the flashback arrestors. The occurrence of this failure is expected to be moderately low ($O=4$) because the μ CHX has been designed to be intrinsically safe with channel sizes that should be too small for homogeneous combustion. However, the limits of homogeneous combustion in micro-channels are not entirely understood, so there is still a chance that flashback will occur. Flashbacks cannot be detected in advance ($D=10$). This results in a cumulative RPN of 120. While this is higher than preferred, it is acceptable because the severity of the failure is considered to be low.

4.7.2. Sustained Homogeneous Combustion in Test Section

Sustained homogeneous combustion (without flashback) in the test section would result in very high temperatures and may melt the test section. To prevent sustained homogeneous combustion, the LabVIEW program will automatically shut off the H_2 flow once a high μ CHX body temperature is exceeded. This limit was set to 250 °C, which was about 90 °C below the melting point of the PEEK insert for the oil channel. The severity of this failure is high ($S=9$) because meltdown of the test section would be dangerous and damaging. The occurrence of this failure is expected to be moderately low ($O=4$) because the μ CHX has been designed to be intrinsically safe, as previously discussed in Section 4.1. This failure will occur only if sustained and it will be easily detectable with the 11 thermocouples in the μ CHX ($D=2$). This results in a cumulative RPN of 72. While this is higher than preferred, it is acceptable because it should be easily detected and stopped before it can cause damage.

4.7.3. Hydrogen Leak in Test Section

The entire flow loop is located within a vent hood. Any leaks would rise, rapidly be diluted in the air and be ventilated through the hood ($S=2$). An audible alarm goes off if vent hood fails, alerting the operator to extinguish combustion. The risk of a leak is low ($O=3$) because the test section will be tightened with torque wrench and will be pressure tested after every reassembly ($D=5$). The total RPN for this failure mode is 30, which is acceptable.

4.7.4. Sustained Oil Pump Failure

In the case of sustained oil pump failure, there will be ineffective heat exchange between the recuperator gases and oil, potentially leading to thermal runaway. If the flow of hydrogen is not stopped, there is a chance that the higher temperatures in the test section would trigger homogeneous combustion ($S=7$). This is expected to be unlikely ($O=2$). This would be easily detectable based on increasing temperatures and no oil flow. The mitigation scheme is already noted above, triggering of solenoid valves based on the μ -CHX body temperature ($D=2$). The total RPN for this failure mode is 28, which is acceptable.

4.7.5. Heat Exchanger Failure

A failure of the heat exchanger will result in hot oil entering the reservoir. This is acceptable for short periods of time as the oil reservoir is large compared to the oil flow rates and will dissipate the hot oil. If this occurs over long periods of time, then a number of potential problems would occur. First, the oil reservoir may melt, spilling hot oil in the vent hood. Second, the hot oil may damage the pump. Third, the hot oil may damage the oil flow meter. This would be dangerous and could damage expensive instruments ($S=9$). The likelihood of this failure occurring is expected to be negligible ($O=1$). In order to monitor this temperature, a temperature indicating label with a range of 0°C to 30°C (32°F to 86°F) will be applied to the tubing on the oil outlet of the heat exchanger. This label has temperature windows that change color from black to green, indicating the approximate temperature of the surface. The color then returns to black when the surface cools. The oil temperature exiting the heat exchanger should be less than 20°C . If the operator observes that the surface temperature

exceeds the range of the label, then shutting off the flow of hydrogen will stop combustion, effectively removing the heat source and preventing damage to the flow loop (D=3). This results in an RPN of 27, which is acceptable.

4.7.6. Hydrogen Leak in Flow Loop

The entire flow loop is located within a vent hood. Any leaked H₂ would rise, rapidly be diluted in the air and be ventilated through the hood (S=2). An audible alarm goes off if vent hood fails, alerting the operator to extinguish combustion. The risk of a leak is low (O=3) because the flow loop has been pressure tested to 345 kPa (50 psi) and will be retested after fitting adjustments (D=5). The total RPN for this failure mode is 20, which is acceptable.

4.7.7. Power Failure

If electrical power were to fail in the facility, the venthood would shut off and so would the data acquisition programs, active sensors, oil pump, and flow controllers. Under such a situation, the flow of hydrogen would automatically be turned off by the normally-closed solenoid valve while the air line would be kept open in order to cool the apparatus (S=2). This is expected to be of very low occurrence (O=1) and it is impossible to detect in advance (D=10). The total RPN for this failure mode is 20, which is acceptable.

4.7.8. Uncombusted Hydrogen in Exhaust

The entire flow loop is located within a vent hood. Any uncombusted hydrogen will be diluted to less than 1 percent by volume in air (S=1). This is expected to happen regularly (O=10) as this will occur during start up and if combustion goes out during an experiment. It will also be readily detectable if combustion is not occurring (D=5). The total RPN for this scenario is 20, which is acceptable.

4.7.9. Leak in Oil Loop

The oil loop is considered safe for the most part. The oil, Paratherm MG, is harmless (see Table 4.5 for details) and the only safety concern relates to its potential high temperature at

the exit of the test section. In the event of a leak during the set up or continuous operation of the system, it is possible for hot oil to spill onto the operator ($S=4$). This risk is mitigated by use of proper safety gear (gloves, eyewear) by the operator. This is unlikely to occur because the oil loop has been leak tested and the whole loop is within the vent hood ($O=2$). It will also be retested after fitting adjustments and any leaks will be clearly visible ($D=2$). The total RPN for this failure mode is 16, which is acceptable.

5. CATALYST DEVELOPMENT

Platinum and palladium catalysts were prepared on stainless steel shims for use in the μ CHX. The catalyst deposition techniques and the corresponding shims that were prepared for the experiments are described in this section. Sputtered and wet deposition methods were investigated and are described in this section. The deposition methods investigated are listed in Table 5.1 and are detailed in the sections below. Alternative methods that were considered but not fully investigated are discussed in Appendix D.

Table 5.1: Catalyst deposition techniques

Section	Technique	Catalyst	Support
5.1.1	Sputtering	Palladium	316 SS
5.1.2	Wet Deposition	Platinum	Etched 316 SS

5.1. Catalyst Deposition Techniques

Sputtered palladium on stainless steel was the initial catalyst deposition method considered. However, the catalyst shim prepared by sputter deposition was not sufficiently reactive for experimentation, as discussed in Appendix E. Other catalyst deposition techniques were also considered, but not fully implemented. Anodized aluminum is known to act as a highly porous support for wet deposited catalysts [12], but could not be adapted for use in the μ CHX. Also, the palladium/carbon paint method used by Sandia National Labs [7] was considered, but was not tested in the μ CHX. Further details on the alternative catalyst deposition methods are provided in Appendix D.

5.1.1. Sputtered Pd onto Stainless Steel

The palladium (Pd) catalyst was deposited with the AJA Orion sputter tool located at MBI. A 3.2 mm (0.125 in) thick, 51 mm (2 in) diameter palladium target was acquired for use in this tool. This was expected to provide a three-fold advantage over the wet deposition method. First, the deposition thickness could be precisely controlled because the deposition thickness

is a linear function of deposition time. Second, the manufacturer specification of spatial uniformity of sputter deposition thickness with this tool is ± 2 percent. This is much better than what was anticipated with the wet deposition technique. Third, the part was masked with laser cut shims, allowing for precise control of the catalyst location.

Thin layers of sputtered Pd were deposited onto type 316 stainless steel substrates. As previously discussed, the activity of a catalyst is directly related to the number of active sites available for catalytic reactions. Therefore, the activity of a catalyst can be improved by increasing the surface area of Pd available for reactions. The numerical model being concurrently developed assumes a uniform surface layer of Pt as the catalyst. In order to best match this model, a sputter process was desired that produced a film of Pd resembling a polycrystalline Pd sheet, similar to the plasma vapor deposited Pt film fabricated by Appel et al. [8].

A ZeScope optical profiler was used to measure the thickness of the Pd film. A silicon wafer with a 90 nm film of Al_2O_3 was used as the substrate for this test. A piece of Kapton tape was placed on the silicon wafer prior to Pd deposition at 200 °C for 3 minutes at 250 W, and left a clean edge when removed. The sputtered Pd film thickness measured at this location was 280 nm. This thickness indicates that deposition rate for Pd at this power level was approximately 1.56 nm/s.

Initially, a relatively thick layer (940 nm) was deposited onto a piece of stainless steel. However, shear testing with scotch tape completely removed the Pd from the surface. This indicated that the cohesive force between the Pd molecules was greater than the adhesive force between the Pd and stainless steel. In order to get the Pd to adhere to the surface, thinner depositions or surface preparation were required. Jayaraman et al. [45] demonstrated that sputter deposited films have better adhesion at elevated temperatures with an optimum around 400 °C. The sputter tool at MBI was limited to a maximum temperature of 200 °C, so this temperature was used instead. Palladium was sputtered on 316 SS test coupons in increments of 30 seconds at 200 °C at a DC power input level of 250 W. The results of the shear testing are listed in Table 5.2. Based on these results, a sputtering time of 60 seconds was used for shim A.

Table 5.2: Sputtered palladium shear test

Test Coupon	Deposition Time	Thickness (nm)	Shear Test Result
A	30 seconds	47	No Flaking
B	60 seconds	94	No Flaking
C	90 seconds	140	Slight Flaking

5.1.2. Wet-Deposited Pt onto Etched Stainless Steel

The 316 stainless steel shims were electrochemically etched to increase the surface roughness prior to the catalyst deposition using the process followed by Stefanov et al. [46]. An SEM image of the electrochemically etched stainless steel is shown in Fig. 5.1. The shim was masked with polyester tape (McMaster-Carr part number 7630A23) prior to etching for 60 minutes in a 5 % aqueous solution of oxalic acid at room temperature. The masking tape was necessary to confine the etching to the deposition region. The shim was etched at a potential of 15 V and drew about 7 A, resulting in a current density of approximately 0.28 A/cm². The higher current density used by Stefanov et al. of 1 A/cm² could not be obtained with the available power supply. The surface averaged roughness (S_a) of the etched surface was measured with the ZeScope profilometer at MBI and compared to the S_a of an unetched stainless steel shim. The surface roughness of the etched shim was found to have been increased by a factor of 3, from 0.123 μm to 0.383 μm .

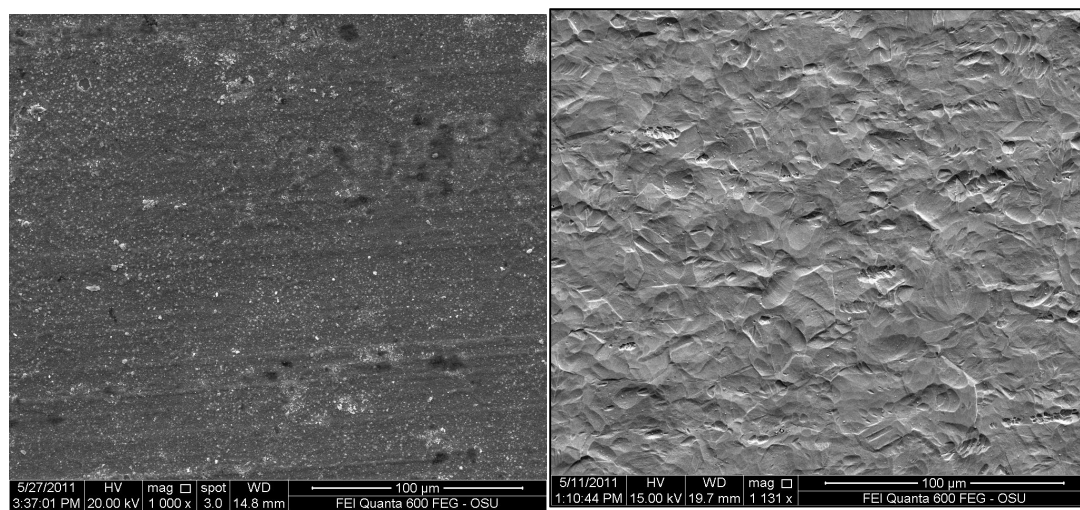


Fig. 5.1: Stainless steel before and after etching

Hydrogen hexachloroplatinate(IV) hexahydrate ($\text{H}_2\text{PtCl}_6 \cdot 6\text{H}_2\text{O}$), obtained from Sigma Aldrich, was dissolved in deionized water to prepare a 0.007 M solution for deposition on the etched substrate. A pipette was used to slowly drip this solution onto the etched portion of the steel shim. The masking tape from the etching process was left on the shim in order to contain the solution within the etched region. Once the etched region was fully covered with a liquid film of the solution, it was placed in an oven at 80 °C until the water evaporated and no liquid was visible on the surface. This process was repeated three times to completely cover the surface with the catalyst. At this point, the deposition region was black from the platinum acid. An image of the deposition on a stainless steel shim is shown in Fig. 5.2. The surface was fully covered, but not entirely uniform due to the tendency of the liquid to form into drops as the liquid evaporated.



Fig. 5.2: Evaporated platinum precursor on stainless steel shim

In order to reduce this precursor to the active platinum metal, heat treatment above 510 °C was required [47]. Common heat treatments for calcining (air atmosphere) and reducing (hydrogen/inert atmosphere) this precursor range from 500 °C to 600 °C [10,12,13,39]. The catalyst shim was assembled into the μ CHX for heat treatment. The PEEK parts of the μ CHX were not assembled (shown in Fig. 4.5), because they would melt at temperatures above 340 °C. The μ CHX was maintained at 570 – 600 °C with air flowing through for 3 hours. A 10:1 mixture of N_2 and H_2 was then flowed through the μ CHX for 4 hours during reduction. Following reduction, the upstream valves were closed to retain the hydrogen/inert atmosphere while the μ CHX was allowed to cool to room temperature. A picture of the catalyst is shown in Fig. 5.3, and the corresponding SEM image of the catalyst is shown in Fig. 5.4. Both images were acquired after the catalyst had been used for the experimental runs.



Fig. 5.3: Reduced platinum catalyst on stainless steel shim

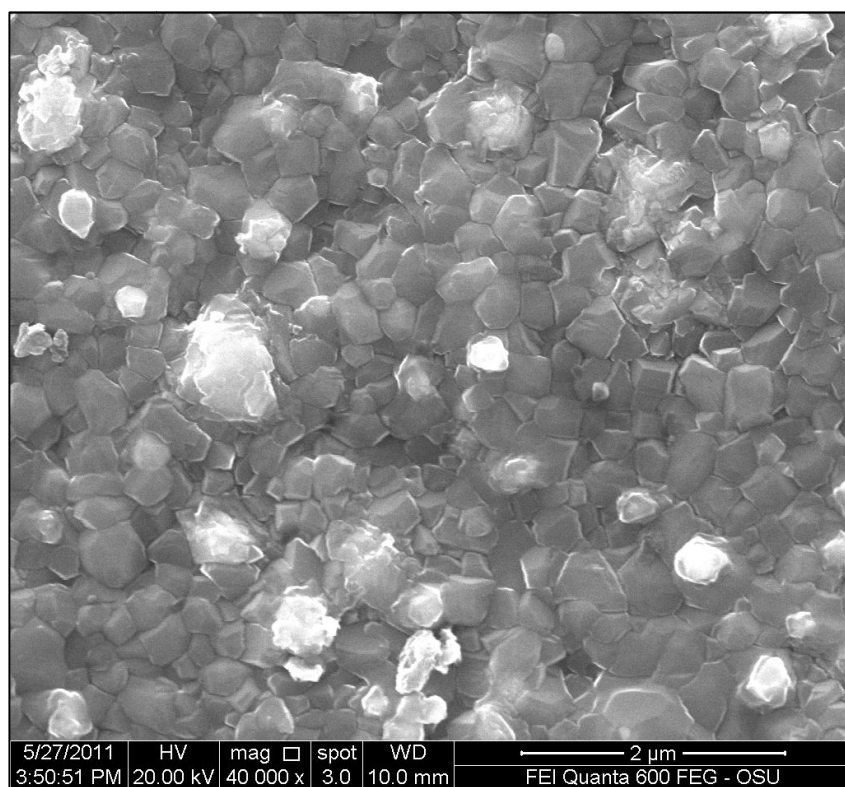


Fig. 5.4: SEM image of wet deposited Pt on catalyst shim B

5.2. Catalyst Configurations Used in Experiments

A total of three catalyst shims were used for the experiments. The details of each catalyst shim and deposition method are listed in Table 5.3.

Table 5.3: Catalyst configuration details

Catalyst Shim	Catalyst	Support	Deposition Method	Uncoated Entry Length (mm)	Catalyst Length (mm)	Initial Mass Loading (mg/cm ²)	Initial Molar Loading (mol/cm ²)
A	Pd	316 SS	Sputter	10.2	66.0	0.11	1.1×10^{-6}
B	Pt	Etched 316 SS	Wet	10.2	66.0	0.72	3.7×10^{-6}
C	Pt	Etched 316 SS	Wet	10.2	15.2	0.73	3.7×10^{-6}

A constant entry length for preheating was incorporated into each catalyst shim tested. The catalyst began immediately after the entry length. The longer catalyst lengths were tested first because they would allow for longer residence times to be obtained. Shim C was fabricated with a shorter catalyst length in order to investigate the efficiency at shorter residence times than could be achieved with shim B. The catalyst length reduction of this shim caused a decrease in residence time by a factor of 4.

The initial mass loading of catalyst was estimated for each shim based on the deposition technique used to prepare each catalyst. The initial mass loading of the sputter deposited Pd shims was calculated as:

$$\frac{m_{Pd}}{A_{cat}} = \rho_{Pd} r t_{dep} \quad (5.1)$$

where ρ_{Pd} is the density of palladium, r is the deposition rate of the palladium film and t_{dep} is the deposition time. The deposition rate was previously determined to be 1.56 nm/s. The initial mass loading of the wet deposited Pt shims was calculated as:

$$\frac{m_{Pt}}{A_{cat}} = \frac{\mathcal{M}_{Pt} M_{sol} V_{sol}}{A_{cat}} \quad (5.2)$$

where \mathcal{M}_{Pt} is the molar mass of the platinum, M_{sol} is the molar concentration of the prepared solution, V_{sol} is the volume of solution deposited onto the shim and is normalized by the planar surface area of the catalyst deposition, A_{cat} . The initial molar loading was calculated as:

$$\frac{n_i}{A_{cat}} = \frac{m_i}{\mathcal{M}_i A_{cat}} \quad (5.3)$$

where n_i is the number of moles of deposited catalyst and \mathcal{M}_i is the molar mass of the catalyst.

6. EXPERIMENTAL PROCEDURE

The experimental procedure used for the experiments is presented in this section. The procedure is broken down into four parts: (6.1) start up, (6.2) continuous operation, (6.3) shutdown and (6.4) emergency shutdown. The procedures also include safety checks that are to be performed during an experimental run. General notes referenced by these operating procedures are listed in Table 6.1. Also, the procedures for operating the hydrogen cabinet are provided in Section 6.5.

Table 6.1: Notes to standard operating procedures

Note 1	Flipping manual emergency switch to off does the following: <ul style="list-style-type: none"> • Closes H₂ solenoid • Turns off heaters
Note 2	STOP PROGRAM button in LabVIEW does the following: <ul style="list-style-type: none"> • Closes H₂ solenoid • Sets H₂ MFC to 0% • Sets air MFC to 100% • Sets oil flow to 0% • Turns off heaters
Note 3	STOP COMBUSTION button in LabVIEW does the following: <ul style="list-style-type: none"> • Closes H₂ solenoid • Sets H₂ MFC to 0% • Sets air MFC to 100% • Sets oil flow to 100% • Turns off heaters

6.1. Startup Procedure

Prior to the start of each experiment, the experimental facility was checked to ensure that it was ready for experiments to be conducted according to the flowchart shown in Fig. 6.1. Due to the use of compressed gases safety glasses were worn while working inside the vent hood. Any connections that had been modified since the last experiment were checked with a pressure decay test to ensure that the system was leak tight. The power supplies were then turned on. The MFCs required a 30 minute warm-up period before being operated. During this warm-up process, the flow loop was inspected to ensure that all the valves were open or closed appropriately. The oil lines were checked to ensure flow to the μ CHX. The water lines

were checked to ensure flow to the heat exchanger and condenser. The gas lines were checked to ensure that the dessicants were outside the flow loop. The dessicants used to dry the air prior to collection for the gas chromatograph (GC) had colored beads that changed from yellow to blue when they could no longer absorb moisture. Once a dessicant was fully blue, it was replaced with a new dessicant. Two dessicants were installed at all times to minimize the risk of moisture being introduced to the GC. The MFCs were also checked that the flow switch was set to "Normal", not "Purge". Enabling the purge function fully opened the internal solenoid valve in the MFC to allow flows greater than the specified full scale flow for purging both the MFC and lines. The entire experimental facility was contained within a vent hood so the face velocity of the vent hood was checked prior to operation. The H₂ cabinet was also checked to ensure that H₂ was being delivered to the vent hood. The instructions for operating the vent hood are described in Section 6.5.

Once the flow loop was inspected, the LabVIEW program developed for controlling the flow loop was started. Occasionally, a glitch would occur in the program and some of the instruments would not be read properly. This could typically be resolved by restarting the LabVIEW program. Data collection was initialized before the start of the experiment. The data from steady state operation was extracted at a later time. Once all this was complete, the heaters and pump were plugged in and the manual switch was flipped to the on position. This switch provided a hard disconnect to close the H₂ solenoid and turn off the cartridge heaters.

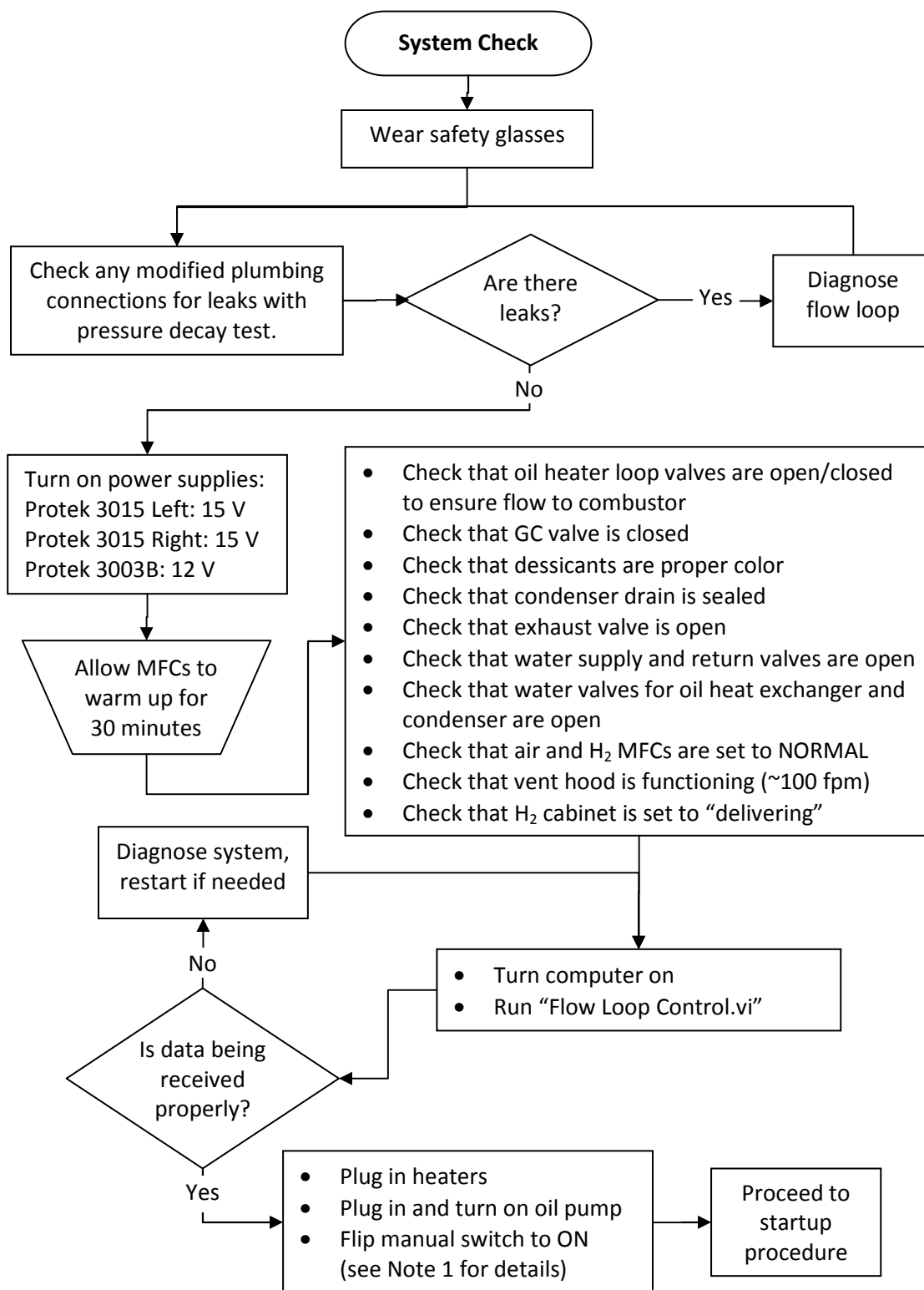


Fig. 6.1: System check procedure

With the system check completed, the experiment was started up according to the flowchart shown in Fig. 6.2. The experiments were conducted only at the pressures necessary to force the fluids through the μ CHX, so pressures no greater than 50 psig were required. Also, the H_2 flashback arrestor was limited to pressures less than 50 psig, so all pressure regulators were set below this threshold. With the air valve opened, the rotameter was adjusted in order to dilute the exhaust gas below the flammable limit in the event that combustion did not occur and H_2 was present in the exhaust. The experiments typically required preheating in order to initiate combustion. A preheat temperature, typically around 100 °C, was specified in the LabVIEW program. While combustion was occasionally initiated at lower temperatures, the μ CHX had to be operated above 100 °C in order to prevent water from condensing inside. Using cartridge heaters to reach this temperature was much faster than relying on combustion alone.

Once the desired temperature was reached with the cartridge heaters, they were turned off and unplugged. Hydrogen was then introduced to the flow loop by opening the hydrogen valve inside the vent hood and adjusting the pressure regulator as needed. Using the LabVIEW user interface, the gas flow rate, equivalence ratio and oil flow rate were set. A lean mixture was typically supplied; however, a stoichiometric mixture was used on occasion. Combustion was often observed after a lag of about a minute due to the N_2 purge gas initially in the H_2 lines. The thermocouples located along the combustion channel provided initial indication of combustion. The oil and exhaust temperatures would eventually rise, but they had a much slower response. If combustion was not observed, a higher preheat temperature would typically help. If this did not work, sometimes a richer gas mixture was required in order to observe combustion occurring. If changes to either of these parameters did not initiate combustion, then the catalyst was determined to be unreactive. Once combustion was achieved, the experiment proceeded to the continuous operation procedure.

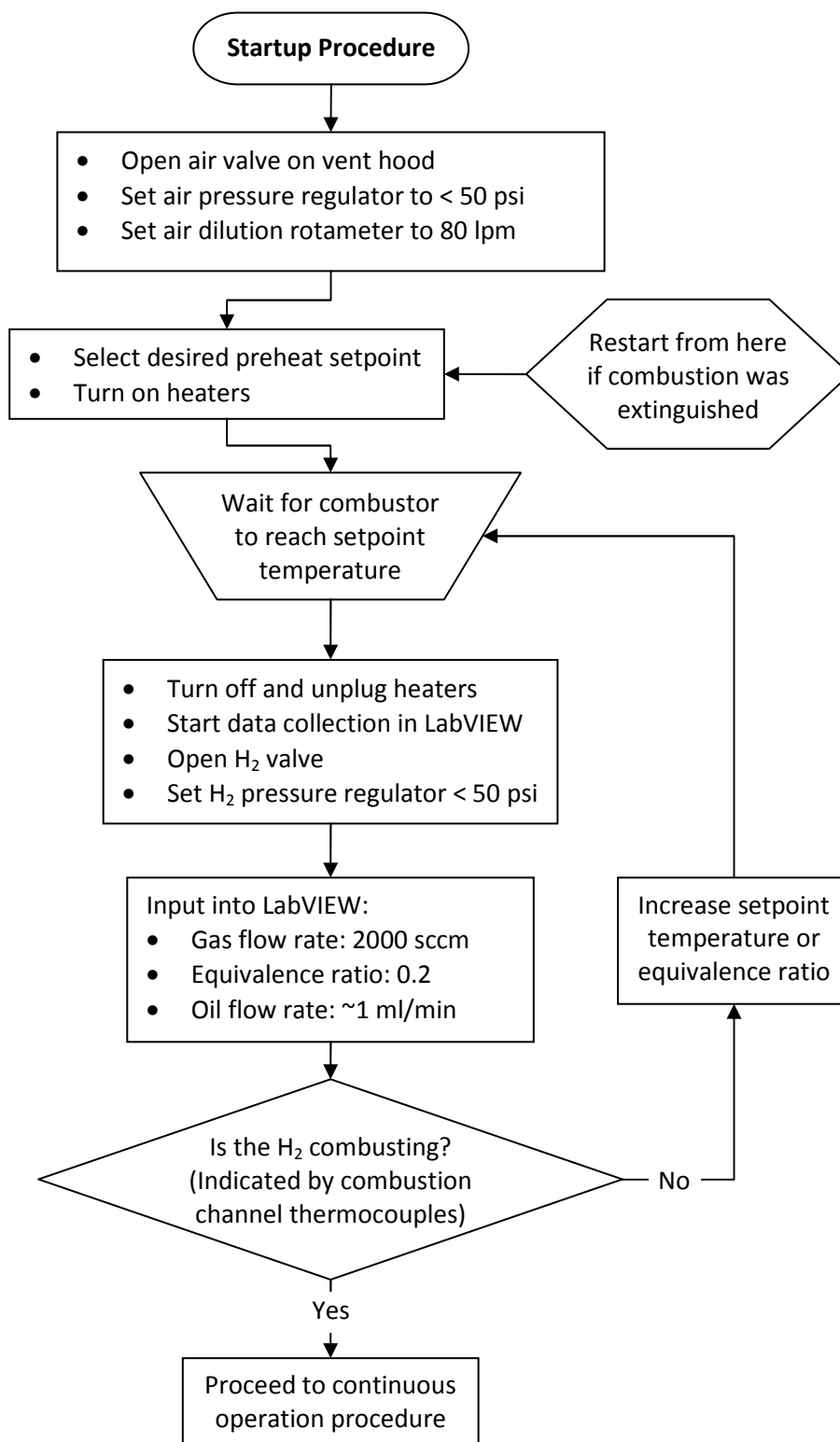


Fig. 6.2: Startup procedure

6.2. Operational Procedure

The flowchart of the operating procedure is shown in Fig. 6.3. With combustion occurring in the μ CHX, the desired gas flow rate and equivalence ratio was input into LabVIEW. Due to the large thermal mass of the μ CHX, it took multiple hours to reach steady state operation. To accelerate this process, increasing the oil flow rate was often set after waiting until temperatures were near the anticipated operating temperatures. With the oil flow rate set at the desired level, the exhaust temperature was monitored in order to make sure that it did not drop below 100 °C. Below this point, water would condense inside the μ CHX. Combinations of lean equivalence ratios, low gas flow rates or high oil flow rates sometimes caused the temperatures to drop below this threshold. If this occurred, a different combination of set points was selected in order to achieve higher operating temperatures.

Once the temperatures stabilized, a gas sample was collected for analysis in a gas chromatograph. An Agilent 490 GC was used to analyze the gas samples. This GC was not initially integrated into the flow loop, so samples for these experiments were collected in sample bags for analysis at a later time. Once the gas sample was collected, a different combination of flow conditions were selected for another experiment or the shutdown procedure was initiated.

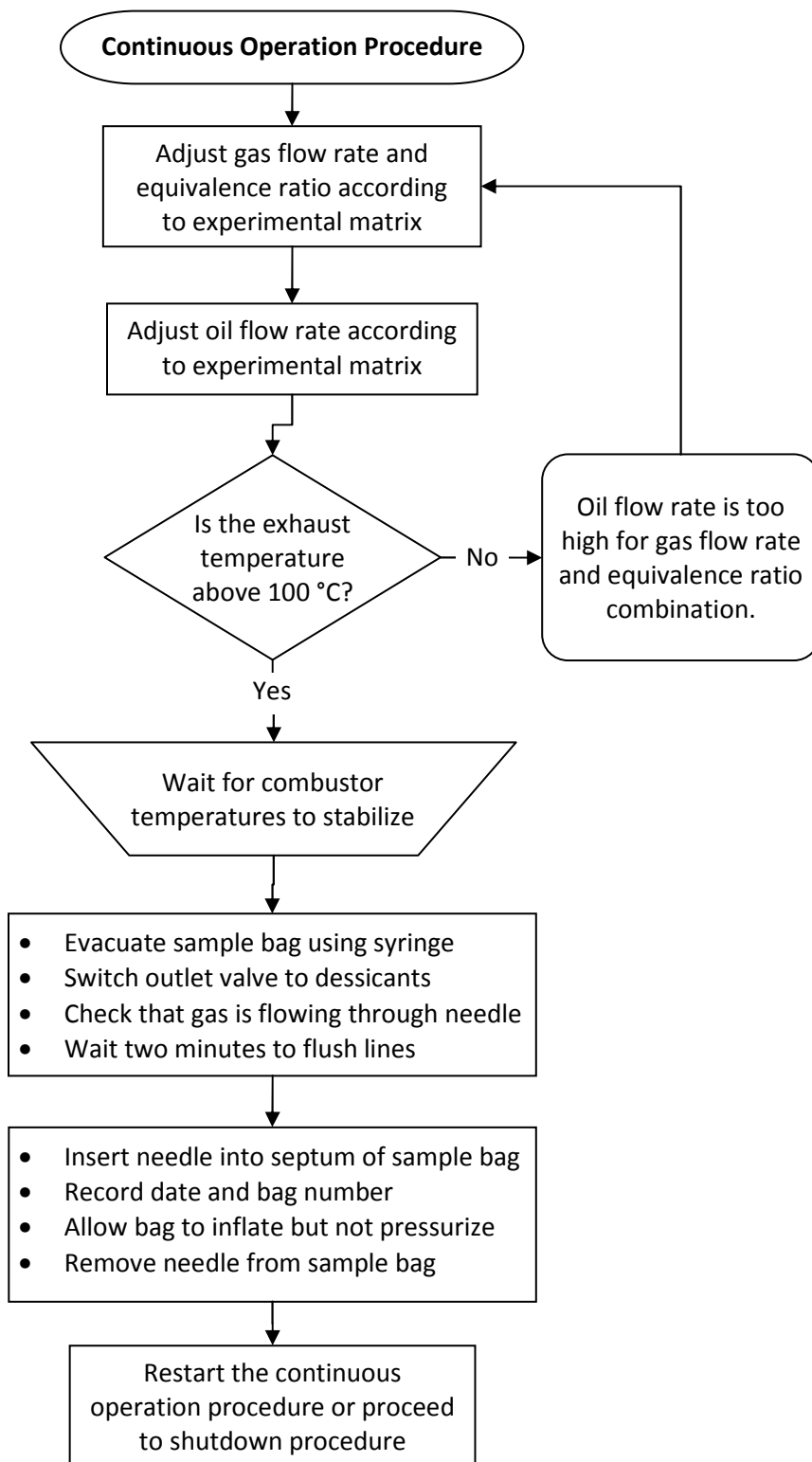


Fig. 6.3: Continuous operation procedure

6.3. Shutdown Procedure

After all the data and samples from the experiment had been collected, the series of steps were performed in order to safely shutdown the system. A flow chart of this procedure is shown in Fig. 6.4. The oil pump was adjusted to its maximum value in order to begin cooling down the μ CHX and the H_2 supply valve inside the vent hood was closed. At this point, the MFC was still supplying H_2 , safely depressurizing the line. Once the pressure on the H_2 pressure regulator dropped to around 10 psig, the N_2 valve on the vent hood was opened. Once this was done, the plug valve connecting the N_2 and H_2 lines was opened and the H_2 MFC was set to "Purge". This sequence was followed in order to completely purge any remaining H_2 from the line. Once the purge was completed, the valves were closed, the LabVIEW program was stopped and the equipment was turned off.

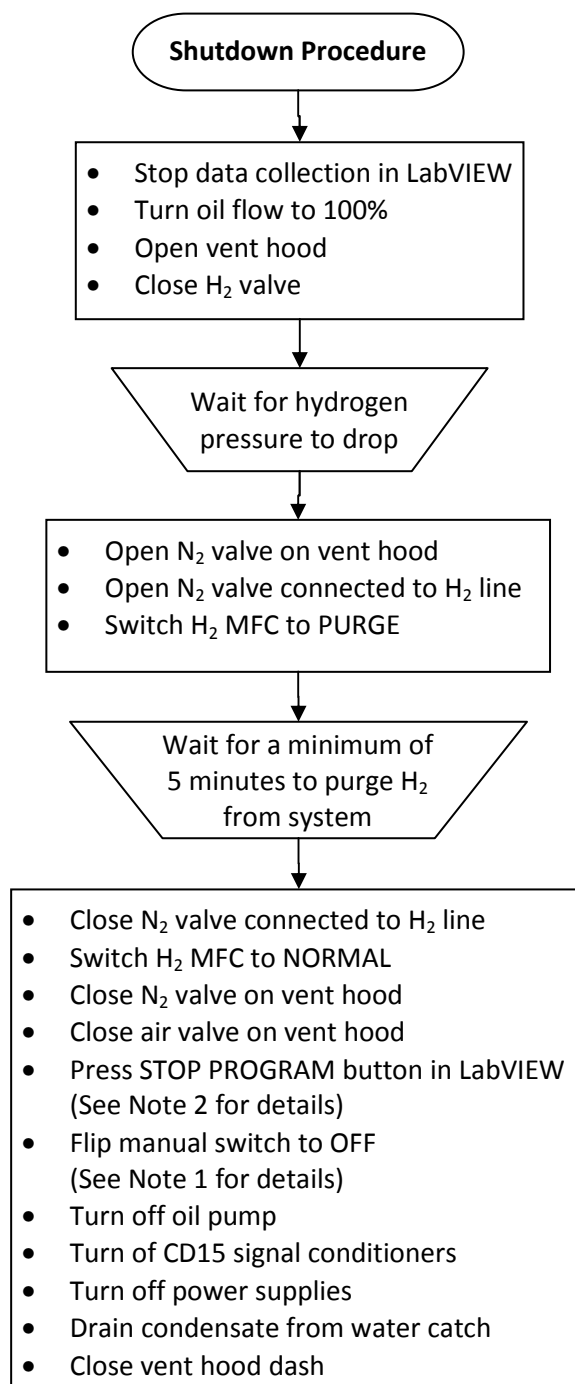


Fig. 6.4: Shutdown procedure

6.4. Emergency Shutdown Procedure

In the event of an emergency situation, a flowchart describing the emergency shutdown procedure was prepared and is shown in Fig. 6.5. During the course of the experiments, it was never necessary to follow this procedure. However, it was posted on the vent hood with the rest of the operating procedures as a general safety precaution. Intrinsic safety procedures were coded into the LabVIEW program in order to limit the extent of thermal runaway. The general purpose of this procedure was to cut the H_2 flow to extinguish combustion and maximize the flow rates of air and oil through the device. While the oil flow rate could not be adjusted if the LabVIEW program was inoperable, the H_2 flow could be stopped by turning off the manual switch located on the vent hood. Setting the air MFC to purge would allow more air to flow through the system than could be set via the LabVIEW interface. If these steps did not resolve the situation, then it would probably be necessary to press the emergency button located near either exit and obtain help to bring the system under control. This button would sound an alarm and cut the flow of hydrogen at the cabinet.

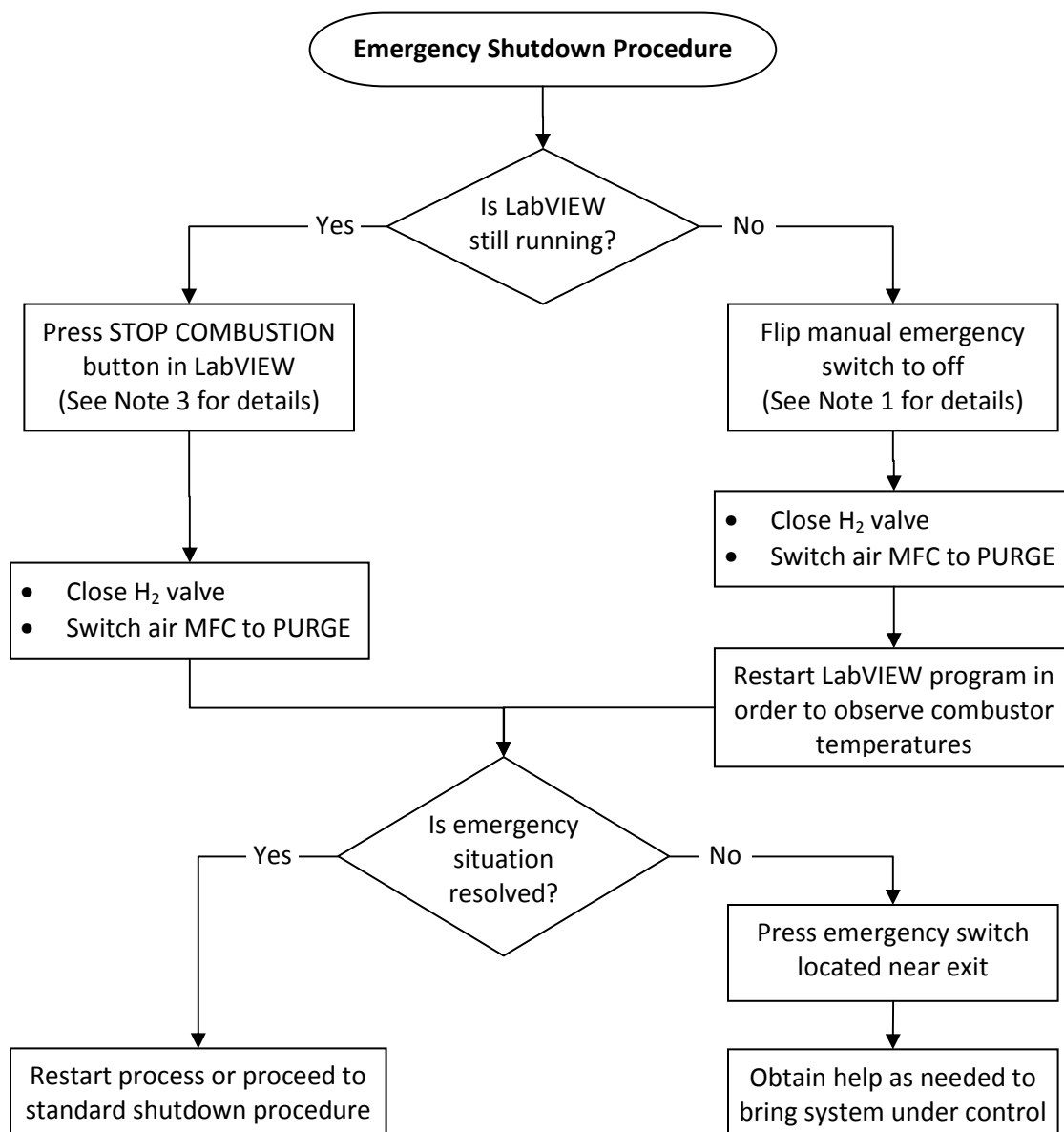


Fig. 6.5: Emergency shutdown procedure

6.5. Hydrogen Cabinet Operation

The H₂ cylinders were contained within a cabinet outside the lab where experiments were performed. Hydrogen was supplied to the vent hood from this cabinet. The cabinet contained two isolated compartments, each of which could hold two cylinders of H₂ in parallel. In the event that the cylinders in one compartment were depleted, the cabinet

would automatically switch to the cylinders in the other compartment. The cabinet was a complex system that will not be described in complete detail here; instead, the basic principles of operation for conducting the experiments are described. The cabinet had a touch screen interface for controlling the cabinet. Each compartment had three modes of operation: offline, standby and delivering. With both compartments offline, activating one of the compartments would set it to the delivering mode. If one compartment was delivering, activating the other compartment would set it to standby mode. If the cylinder pressure in the delivering compartment fell below a user specified level, the cabinet would automatically take that compartment offline and set the other compartment to delivering. This allowed for uninterrupted H₂ flow. A compartment could be activated or deactivated by pressing the appropriate button on the touch screen interface. This would bring up a dialog box requesting a password. Pressing the box marked '***', then pressing 'ok' would activate or deactivate the compartment. On occasion, the H₂ distribution manifold located next to the H₂ cabinet needed to be activated. This was performed with the following sequence: selecting 'Ops', selecting 'Activate' for side A, then entering '1' as the password.

7. DATA ANALYSIS

This chapter discusses the calibration methodology and stability characteristics of important measured parameters. The equations used in the data analysis are identified, followed by a discussion of the uncertainty analysis.

7.1. Calibration

Calibration was performed for the thermocouples, absolute pressure transducers and differential pressure transducers. The details of these calibrations are described in sections 7.1.1 through 7.1.3.

The factory calibrations were used for the mass flow controllers and the oil flow meter. The mass flow controllers were calibrated by the manufacturer for full scale flow rates of 2600 sccm and 800 sccm for air and hydrogen, respectively. The calibration uncertainty of the mass flow controllers was 1 % of the setpoint for flow rates greater than 25 % of the full scale flow rate. For flow rates between 2 – 25 % of full scale, the uncertainty of the mass flow controllers was 0.25 % of full scale. The oil flow meter was calibrated by the manufacturer to within 0.2 % of the measured flow rate for flow rates between 1 – 1800 ml/min.

7.1.1. Thermocouple Calibration

The thermocouples were calibrated using an Omega handheld calibrator PCL-1B with an attached NIST-traceable RTD standard (± 0.30 °C). A temperature-controlled chiller with Paratherm MG oil was used to perform a calibration of the T-type thermocouples to within 0.36°C over the range 15°C to 185°C. The K-type thermocouples that measured the exhaust temperature of the gas and body temperature of the μ CHX were calibrated to within 0.55°C over the same range. The complete thermocouple calibration results are listed in Appendix F. A sample calibration curve for T-type thermocouple #1 is shown in Fig. 7.1.

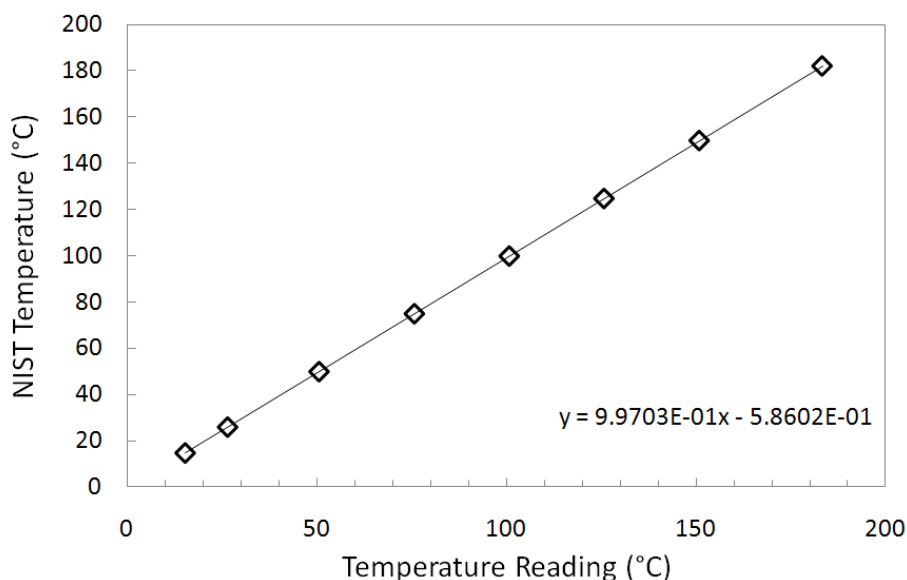


Fig. 7.1: Temperature calibration for thermocouple #1

A zero-point calibration has been performed on the other K-type thermocouples. The thermocouples and NIST-traceable RTD standard were inserted into a mixture of crushed ice and water. The zero point obtained in this manner was used to offset the raw thermocouple readings to a known point. The complete offset parameters from the zero point calibration are listed in Appendix F. These thermocouples were specified by the manufacturer to conform to the Special Limits of Error (SLE) with an uncertainty of 1.1°C or 0.4 % of the measured temperature, whichever is greater. These specified uncertainties were used for the uncertainty calculations. The temperature readings of these thermocouples are only for monitoring the temperature of the μ CHX and do not require the additional accuracy provided by a complete calibration. Also, a high temperature calibration with greater accuracy would have been difficult to obtain due to the high temperature range that was expected for these thermocouples.

7.1.2. Absolute Pressure Transducer Calibration

The Omega PX32 absolute pressure transducers were calibrated against an Omega handheld calibrator PCL-1B with a NIST-traceable absolute pressure module rated from 0 – 689.5 kPa (± 0.345 kPa). The PX32's require an excitation voltage between 10 – 15 volts and provide a

voltage output of 3 millivolts per excitation volt. The power supply was set to 12.0 volts for this calibration, resulting in a maximum output of 36 mV at 689.5 kPa. All experiments were conducted with the power supply set at 12.0 V to ensure that the calibration could correctly be applied. During the initial setup of the calibration experiment, it was observed that there was so much noise that the signal was completely obscured. The noise was eliminated by grounding the shielded wire. The low output voltages were very sensitive to electrical interference, making grounding a necessity. The calibration was performed using compressed air with the calibrator and pressure transducers located in parallel. The pressure was controlled via an upstream pressure regulator. The calibration was performed by ramping the pressure up from atmospheric pressure, to the maximum pressure, then back down to atmospheric pressure. This procedure was performed in order to include any effects of hysteresis in the calibration. The calibration curve for the PX32 #1 is shown in Fig. 7.2. There are two indistinguishable data points at every location, except the maximum pressure, indicating that the effects of hysteresis are negligible. The maximum calibration uncertainty was for PX32 #1 with an uncertainty of 1.74 kPa. The complete calibration parameters for the PX32 pressure transducers are listed in Appendix F.

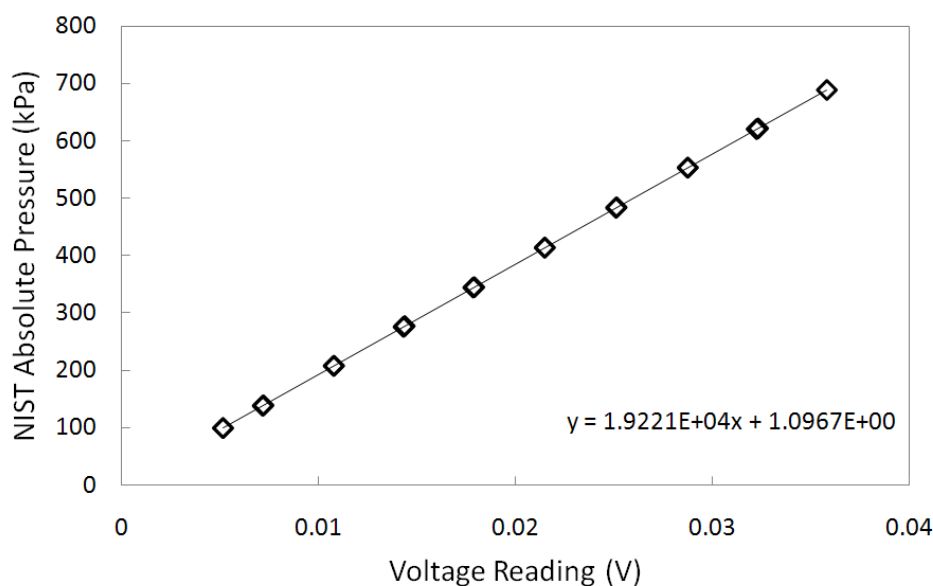


Fig. 7.2: Absolute pressure calibration for PX32 pressure transducer #1

7.1.3. Differential Pressure Transducer Calibration

The DP15-24 and DP15-36 differential pressure modules were calibrated using the same Omega handheld calibrator with a differential modules that rated from 0 – 2491 Pa (± 1.49 Pa) and 0 – 49.8 kPa (± 29.9 Pa), respectively. A custom-built differential pressure calibration facility was used for these calibrations. Each calibration was performed using the same facility and the same procedure. The high pressure side of the pressure gauge and the high pressure side of the calibrator were connected to opposing ends of a $\frac{1}{4}$ " tee fitting. This assembly was connected with another tee fitting on a compressed air line discharging to atmospheric pressure. An adjustable valve on the exit of this pipe was used to control the back pressure. The low pressure sides of the pressure gauge and calibrator were also connected to opposing ends of a $\frac{1}{4}$ " tee fitting. The remaining side was left open to atmosphere. This use of tee fittings ensured that the pressure gauge and calibrator were responding to pressure variations at the same location. Using a pressure regulator to control the upstream pressure resulted in more unstable pressures than using adjustable valves. As a result, the upstream valve on the compressed air line and the adjustable valve at the pipe exit and were used in combination to achieve steady pressures. The DP15-24 pressure transducer was calibrated over the range of 0 – 2200 Pa with an uncertainty of 20.2 Pa. The corresponding calibration curve is shown in Fig. 7.3. The DP15-36 pressure transducer was calibrated over the range of 0 – 34.7 kPa with an uncertainty of 0.152 kPa. The corresponding calibration curve is shown in Fig. 7.4.

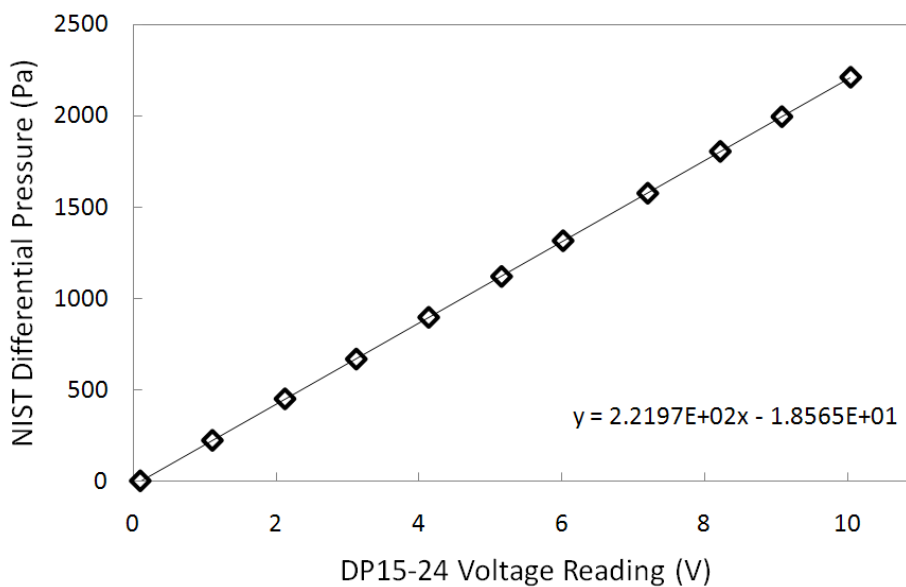


Fig. 7.3: Differential pressure calibration for DP15-24 pressure transducer

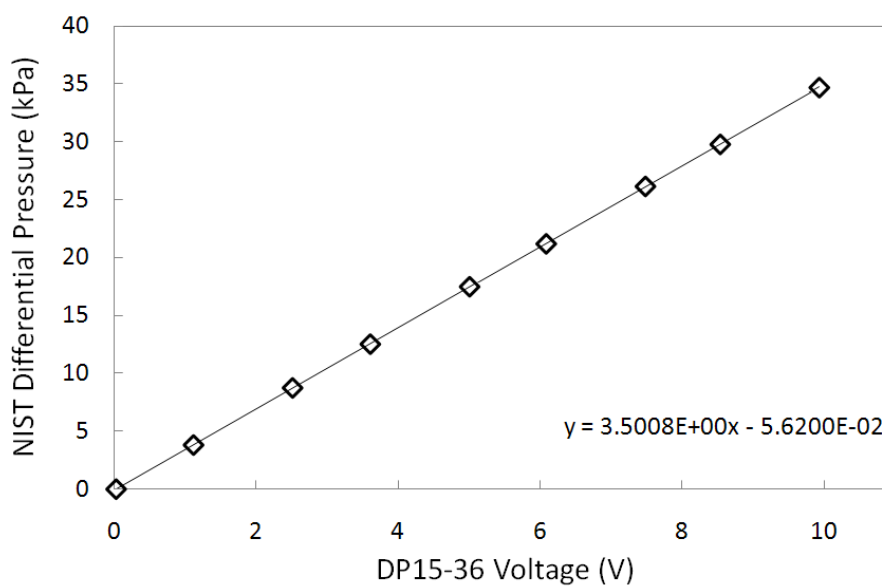


Fig. 7.4: Differential pressure calibration for DP15-36 pressure transducer

7.1.4. Gas Chromatograph Calibration

An SRI 8610C gas chromatograph (GC) with a thermal conductivity detector (TCD) and helium ionization detector (HID) was used for analyzing the hydrogen concentration in the exhaust

gas. Helium at 5 psi was used as the carrier gas and the GC was operated under isothermal conditions of 41 °C. The GC was calibrated using a gas mixture of 0.8 % H_2 (± 0.016 %, balance air) from MESA Specialty Gases. An SKC 0.5 L sample bag was filled with the calibration gas and a 1 ml syringe was subsequently used to inject the gas into the GC. The capillary column in the GC causes each gas to flow through at different rates, resulting in different elution times. The return strength of each gas was then obtained as a function of elution time, shown in Fig. 7.5.

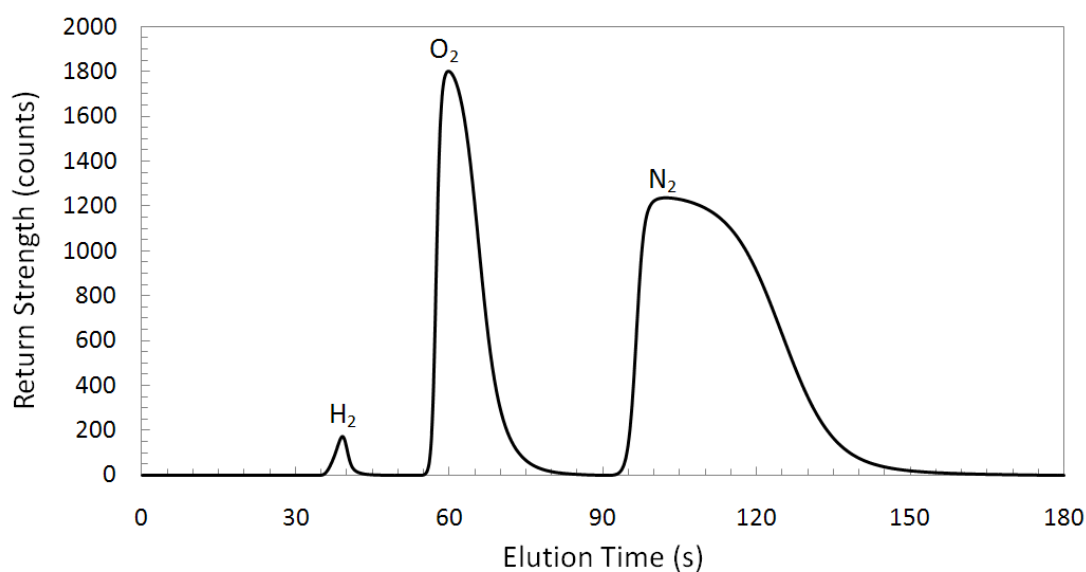


Fig. 7.5: Gas chromatograph return for calibration gas

PeakSimple software was used to identify the peaks and integrate the signal return. Distinct peaks for H_2 and O_2 were observed, but only the H_2 data was necessary for the analysis. For consistency, an injection volume of 0.9 ml was used for the calibration gas and for all samples. Three samples of the calibration gas were analyzed in succession to determine the total uncertainty of the calibration. The calibration data for H_2 is listed in Table 7.1.

Table 7.1: Gas chromatograph calibration sensitivity and uncertainty

Gas	Elution Time	Sensitivity	Uncertainty
H ₂	39.2 (s)	694.75 (counts/%H ₂)	0.034 %

Higher concentrations H₂ calibration gases were not available in the timeframe available for using the GC. The systematic error associated with a potentially inaccurate calibration may have introduced an unaccounted error into the conversion calculations. Future investigations should obtain the calibration gases required to calibrate the GC over a much larger range of H₂ concentrations.

7.2. Stability

The experiments all targeted steady state operation. For each experiment, data was collected for the duration of the experiment, including the transient and steady state regions. The steady state region was then extracted and analyzed. This section discusses how steady state operation was determined and how stable the important measured parameters were during steady state.

7.2.1. Steady State Determination

In order to extract the steady state data, it was important to determine when steady state operation had been achieved. A sample time series of important temperatures is shown in Fig. 7.6. This data is from the base case experiment (Exp. 10) and is representative of the data collected in each experiment. The oil and gas outlet temperatures were critical for calculating the energy balance, so these temperatures were carefully monitored. The body temperature responded the most slowly to the operating conditions of the μ CHX; therefore, it was also monitored to determine when steady state operation had been achieved. The temperature measured by the thermocouple nearest the inlet to the combustion channel (Comb. TC1) is also shown because it responded the most rapidly to the combustion reaction. For this particular experiment, an outlet oil temperature around 150 °C was desired in order to obtain an average oil channel temperature around 85 °C. The oil flow rate was

adjusted occasionally in order to obtain the desired outlet oil temperature. Steady state was reached after 240 minutes of operation and then maintained for 30 minutes. The stability characteristics of the significant measured parameters at steady state operation are discussed in the following subsections.

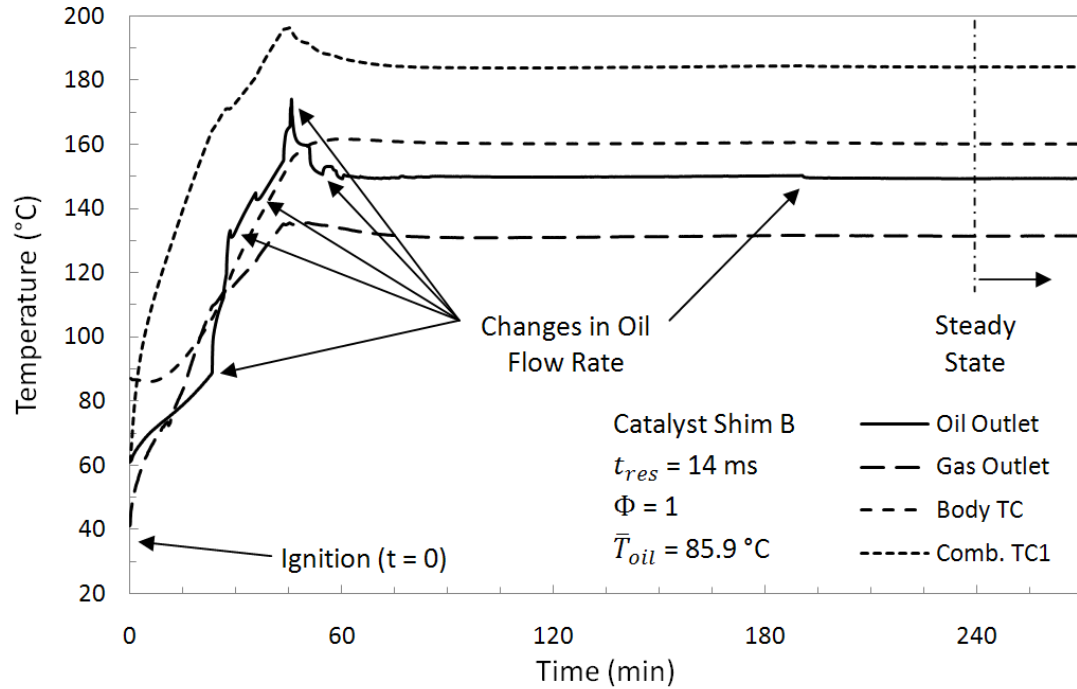


Fig. 7.6: Typical time series temperature data (Exp. 10)

7.2.2. Temperature Stability

The time series profiles of the oil and gas outlet temperatures for 30 minutes of steady state operation are shown in Fig. 7.7. These temperature measurements were consistently stable for all the experiments, with steady state being maintained for at least 15 minutes. For a constant oil flow rate, stable oil outlet temperatures indicate that heat is being transferred to the oil at a constant rate. The standard deviation of the oil outlet temperature was measured to be 0.01 °C at an average temperature of 149.53 °C. Stable gas outlet temperatures are needed in order to estimate the heat losses to the exhaust. The standard deviation of the gas outlet temperature was measured to be 0.02 °C at an average temperature of 131.34 °C.

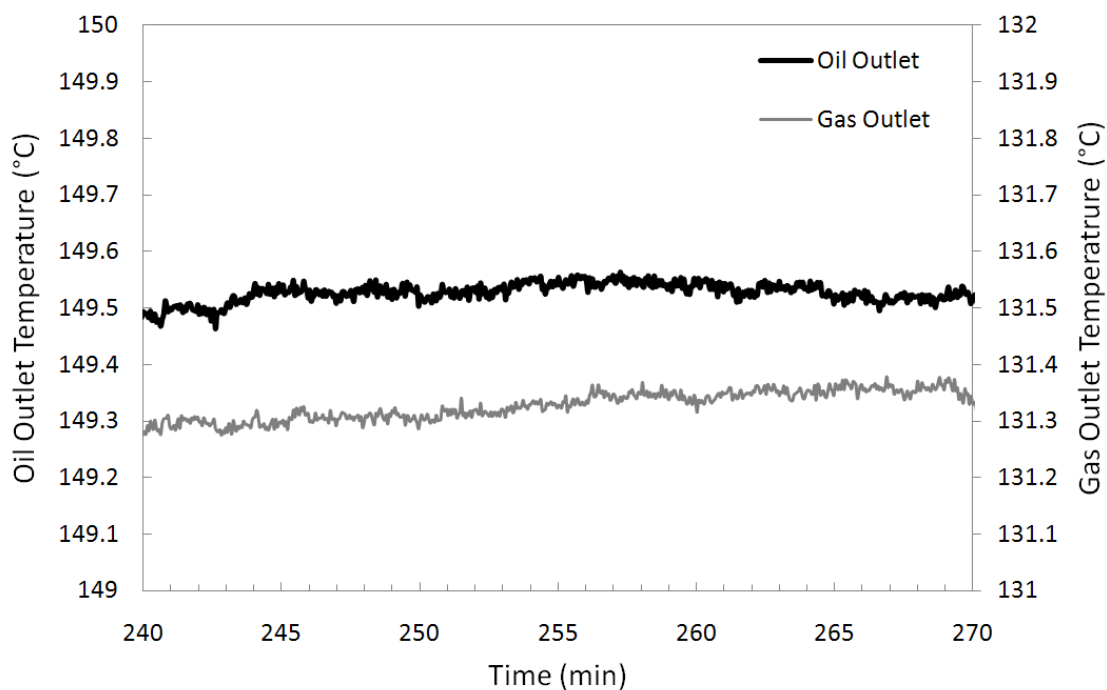


Fig. 7.7: Stability of outlet temperatures at steady state operation (Exp. 10)

7.2.3. Oil Flow Rate Stability

The oil flow rate was controlled upstream by a computer controlled gear pump. As a positive displacement type pump, it was capable of providing stable and precise flow rate control down to 3 ml/min. The actual flow rate was measured by a piston-type positive displacement flowmeter. The accuracy and stability of the oil flow rate was important for accurately determining the heat gained by the oil. A time series profile of the oil flow rate is shown in Fig. 7.8. The standard deviation was 0.1 ml/min, or 0.3 %, at an average flow rate of 30.6 ml/min. This magnitude of variation was typical for all experiments, regardless of the flow rate.

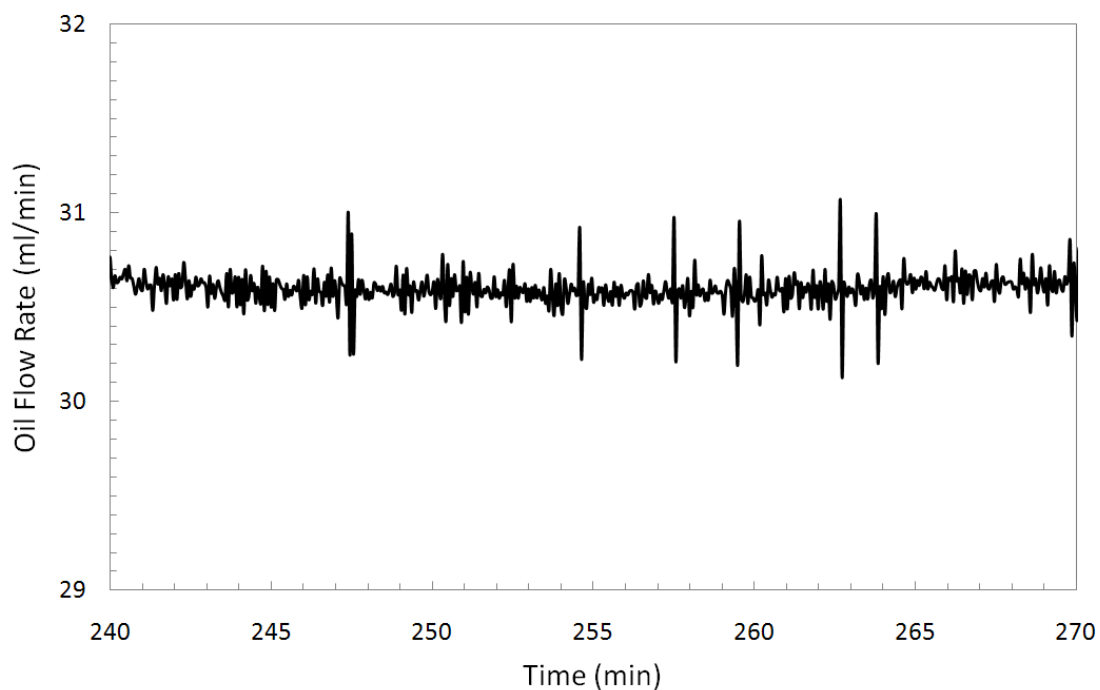


Fig. 7.8: Stability of oil flow rate at steady state operation (Exp. 10)

7.2.4. Gas Flow Rate Stability

The flow rates of H_2 and air were controlled with dedicated AERA Transformer mass flow controllers. Mass flow rate was determined and controlled internally using thermal sensors to trigger a proportional solenoid valve. The time series flow rate profiles for H_2 and air are shown in Fig. 7.9. The standard deviation of the H_2 flow rate was measured to be 0.2 sccm at an average flow rate of 800.3 sccm. The standard deviation of the air flow rate was measured to be 0.8 sccm at an average flow rate of 1904.6 sccm. These flow rates were slightly higher than the setpoints of 799.8 and 1901.2 sccm for H_2 and air, respectively. All calculations were performed based on the measured flow rates, so minor deviations from the setpoint were not a concern.

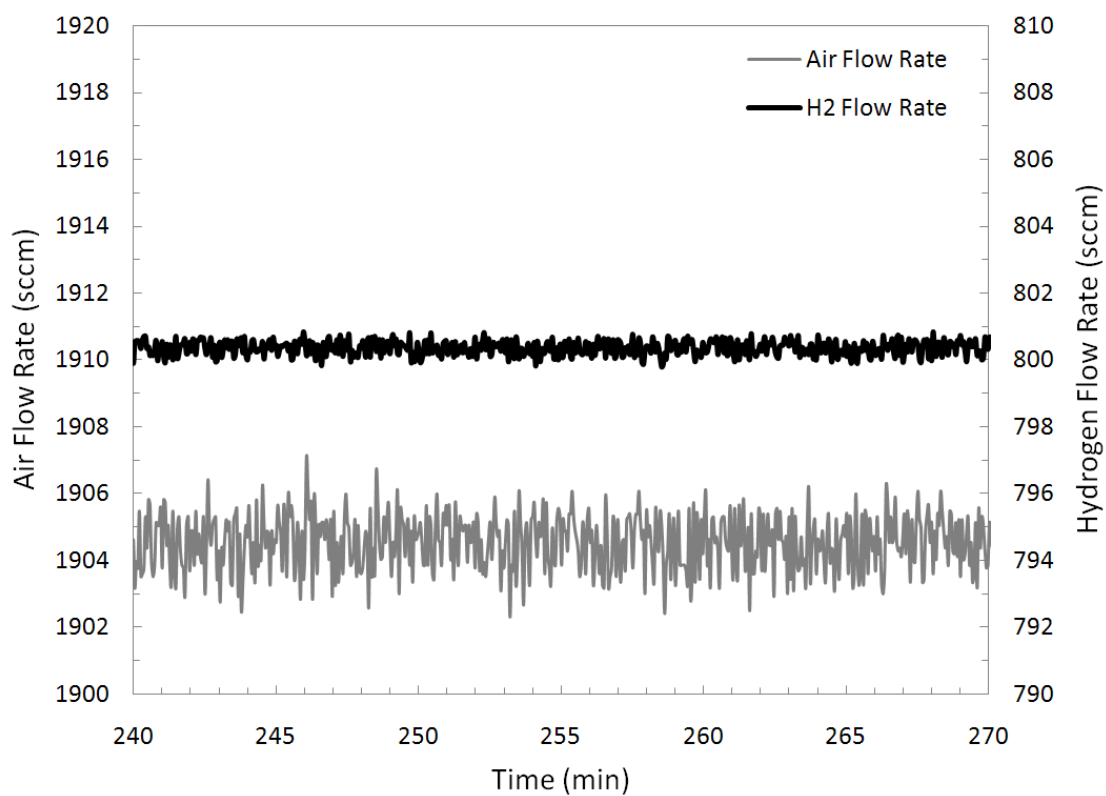


Fig. 7.9: Stability of gas flow rates at steady state operation (Exp. 10)

7.2.5. Gas Chromatograph Repeatability

Samples of the exhaust gas were collected in 0.5 L Tedlar sample bags, obtained from SKC, in order to analyze the hydrogen content in the exhaust. The GC response was fairly stable, as shown in Table 7.2 for the exhaust samples analyzed for fifteen experiments that were analyzed multiple times in the GC.

Table 7.2: Repeatability of gas chromatograph analysis

	% H ₂	Uncertainty (% H ₂)	Average (%)	Standard Deviation (%)	GC sample 1 (%)	GC sample 2 (%)	GC sample 3 (%)
Exp. 25	3.34	0.35	3.34	0.109	3.346	3.227	3.444
Exp. 26	5.91	0.01	5.91	0.002	5.904	5.907	
Exp. 27	5.97	0.59	5.97	0.137	5.875	6.069	
Exp. 28	5.61	1.00	5.61	0.232	5.444	5.771	
Exp. 29	5.32	0.40	5.32	0.093	5.251	5.383	
Exp. 31	3.96	0.01	3.96	0.003	3.960	3.964	
Exp. 32	3.84	0.51	3.84	0.118	3.752	3.919	
Exp. 33	4.38	0.03	4.38	0.006	4.386	4.378	
Exp. 34	6.52	0.45	6.52	0.104	6.597	6.449	
Exp. 35	4.62	0.10	4.62	0.022	4.609	4.641	
Exp. 36	7.10	0.39	7.10	0.090	7.037	7.165	
Exp. 37	6.51	0.13	6.51	0.030	6.485	6.528	
Exp. 38	6.12	0.29	6.12	0.068	6.072	6.168	
Exp. 39	5.60	0.65	5.60	0.152	5.489	5.704	
Exp. 40	5.35	0.34	5.35	0.080	5.289	5.402	
Average Uncertainty (%)		0.349					

The repeatability uncertainty of each sample was calculated as:

$$U_{Precision} = t_{0.05, N-1} \sigma_{\bar{X}} \quad (7.1)$$

where $t_{0.05, N-1}$ is the student t-test factor and $\sigma_{\bar{X}}$ is the standard deviation around the mean, \bar{X} . Not every exhaust sample was analyzed more than once with the GC. For those samples, the average uncertainty was used instead.

7.3. Heat Loss Estimation

A schematic of the energy flows into and out of the μ CHX is shown in Fig. 7.10. Energy is supplied to the μ CHX as H₂, releasing heat during combustion. If the device performed at 100 percent efficiency, all the energy from the supplied H₂ would be gained as heat by the oil. Any deviations from perfect performance can be attributed to energy losses. Two sources of energy losses have been quantified: the heat lost to the exhaust gas and the energy lost to

uncombusted hydrogen in the exhaust. There are additional heat losses that remain unaccounted for in this analysis, most notably heat loss through the insulation. These unmeasured heat losses are therefore determined as the remaining quantity in the energy balance.

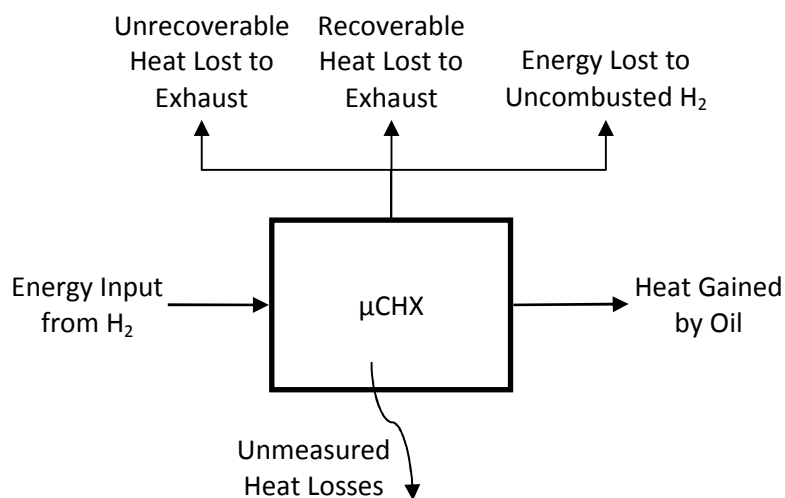


Fig. 7.10: Black box heat flow schematic of μCHX

The heat lost to the exhaust gas can be broken down into the recoverable heat loss and the unrecoverable heat loss. The definition of the lower heating value for hydrogen, used to determine the H_2 energy input, specifies that the exhaust gases are brought down to $25\text{ }^\circ\text{C}$ and that the water is in the vapor phase [48]. However, a minimum exhaust gas temperature of $100\text{ }^\circ\text{C}$ was required in order to prevent water vapor from condensing in the μCHX . Therefore, the sensible heat of bringing the exhaust gas from $100\text{ }^\circ\text{C}$ to $25\text{ }^\circ\text{C}$ is unrecoverable. In contrast, the sensible heat of bringing the exhaust gases from the exhaust temperature to $100\text{ }^\circ\text{C}$ is recoverable. Subdividing the heat lost to exhaust into recoverable and unrecoverable losses helps illuminate the potential efficiency improvement that could be obtained by recovering additional heat from the exhaust gas. The enthalpy difference of the inlet temperature of the gases being below $25\text{ }^\circ\text{C}$ was negligible and therefore neglected.

7.4. Equations Used in Analysis

The equations used in the analysis of the experimental data are described in this section.

7.4.1. Operating Parameters

The equivalence ratio is the fuel/oxidizer ratio normalized by the stoichiometric fuel/oxidizer ratio. Using the ideal gas law for hydrogen and air, the equivalence ratio was calculated as:

$$\Phi = 2.38 \frac{\dot{V}_{H_2}}{\dot{V}_{air}} \quad (7.2)$$

where \dot{V}_{H_2} is the volumetric flow rate of H_2 and \dot{V}_{air} is the volumetric flow rate of air. The mass flow rate of H_2 (\dot{m}_{H_2}) and air (\dot{m}_{air}) was calculated as:

$$\dot{m} = \rho|_{STP} \dot{V} \quad (7.3)$$

where \dot{V} is the flow rate output of the MFC, which regulate based on standard conditions of 0 °C and 101.325 kPa. The mass flow rate of the oil was calculated as:

$$\dot{m}_{oil} = \rho|_{T_{oil}} \dot{V}_{oil} \quad (7.4)$$

where \dot{V}_{oil} is volumetric flow rate of oil and $\rho|_{T_{oil}}$ is the density of the oil. The density of the oil was determined using the temperature dependent properties provided by the oil supplier at the oil temperature measured immediately following the oil flow meter. The channel velocity, valid for the combustion channel (V_c) or recuperator channel (V_r), was calculated as:

$$V_c = \left(\frac{\dot{m}_{H_2}}{\rho_{H_2,inlet}} + \frac{\dot{m}_{air}}{\rho_{air,inlet}} \right) (W * H)^{-1} \quad (7.5)$$

where \dot{m} is the mass flow rate of the fluid, ρ_{inlet} is the fluid density based on the inlet temperature and pressure, W is the channel width and H is the channel height. The residence time in the combustion channel was calculated as:

$$t_{res} = \frac{l}{V_c} \quad (7.6)$$

where l is the length of the catalyst. The oil channel velocity was calculated as:

$$V_{oil} = \frac{\dot{m}_{oil}}{\rho_{inlet}(W * H)} \quad (7.7)$$

where \dot{m}_{oil} is the mass flow rate of the oil, ρ_{inlet} is the oil density based on the inlet temperature, W is the channel width and H is the channel height. The residence time in the oil channel was calculated as:

$$t_{res,oil} = \frac{L}{V_{oil}} \quad (7.8)$$

where L is the length of the oil channel.

7.4.2. Efficiency Parameter

The amount of heat gained by the oil in the μ CHX was calculated as:

$$\dot{Q}_{oil} = \dot{m}_{oil} \left(T_{oil,e} c_p|_{T_{oil,e}} - T_{oil,i} c_p|_{T_{oil,i}} \right) \quad (7.9)$$

where $c_p|_{T_{oil,e}}$ and $c_p|_{T_{oil,i}}$ are the temperature dependent specific heats of the oil provided by the oil supplier at the exit and inlet, respectively. The heat available from hydrogen combustion was calculated as:

$$\dot{Q}_{H_2} = \dot{m}_{H_2} q_{H_2,LHV} \quad (7.10)$$

where $q_{H_2,LHV}$ is the lower heating value for H_2 . The heat available from hydrogen combustion was calculated based on the lower heating value for H_2 , which assumes that the reaction occurs at 25 °C and the water product is in the vapor phase. The lower heating value for H_2 has been calculated using the enthalpies of formation to be 119,950 J/g [48]. The efficiency of the μ CHX was defined as the ratio of heat transferred to the oil compared to the amount of heat available from hydrogen combustion, calculated as:

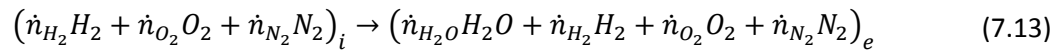
$$\varepsilon = \frac{\dot{Q}_{oil}}{\dot{Q}_{H_2}} \quad (7.11)$$

7.4.3. Heat Loss Calculations

An energy balance was performed on the gas inlet and outlet to determine the amount of heat lost to the exhaust gas. The molar flow rate of the inlet gas species were calculated as:

$$\dot{n}_i = \frac{\dot{m}_i}{\mathcal{M}_i} \quad (7.12)$$

where \mathcal{M}_i is the molar mass of the gas species. For the gas balance, air was assumed to consist solely of O_2 and N_2 , 21 % and 79 % respectively. The associated chemical reaction is:



In order to obtain the molar flow rates of the exhaust products, the volumetric concentration H_2 obtained from the GC was required (C_{H_2}). Based on the species balance of the reaction and using the measured H_2 concentration, the molar flow rate of H_2 exiting the μ CHX was calculated as:

$$\dot{n}_{H_2,e} = \frac{C_{H_2}(-\frac{1}{2}\dot{n}_{H_2,i} + \dot{n}_{O_2,i} + \dot{n}_{N_2,i})}{1 - \frac{3}{2}C_{H_2}} \quad (7.14)$$

where $\dot{n}_{H_2,i}$, $\dot{n}_{O_2,i}$ and $\dot{n}_{N_2,i}$ are the inlet molar flow rates of H_2 , O_2 and N_2 , respectively. The conversion efficiency of H_2 (η_c) was calculated as:

$$\eta_c = 1 - \frac{\dot{n}_{H_2,e}}{\dot{n}_{H_2,i}} \quad (7.15)$$

The molar flow rate of water vapor in the exhaust was then calculated as:

$$\dot{n}_{H_2O,e} = \dot{n}_{H_2,i} - \dot{n}_{H_2,e} \quad (7.16)$$

and the molar flow rate of O_2 in the exhaust was calculated as:

$$\dot{n}_{O_2,e} = \dot{n}_{O_2,i} - \frac{1}{2}\dot{n}_{H_2O,e} \quad (7.17)$$

With the molar flow rates of the exhaust products determined, the potential recoverable heat in the exhaust was calculated as:

$$\dot{Q}_{Ex,rec} = (\dot{n}_{H_2O} \bar{h}_{H_2O} + \dot{n}_{H_2} \bar{h}_{H_2} + \dot{n}_{O_2} \bar{h}_{O_2} + \dot{n}_{N_2} \bar{h}_{N_2})_e \Big|_{T_e} - (\dot{n}_{H_2O} \bar{h}_{H_2O} + \dot{n}_{H_2} \bar{h}_{H_2} + \dot{n}_{O_2} \bar{h}_{O_2} + \dot{n}_{N_2} \bar{h}_{N_2})_e \Big|_{100^\circ\text{C}} \quad (7.18)$$

where \bar{h}_i is the molar enthalpy of a gas species. The molar enthalpy of each species was determined using the temperature dependent enthalpies for ideal gases available in the Engineering Equation Solver (EES) software at the appropriate inlet or outlet temperature. Similarly, the unrecoverable heat in the exhaust gas was calculated as:

$$\dot{Q}_{Ex,unrec} = (\dot{n}_{H_2O} \bar{h}_{H_2O} + \dot{n}_{H_2} \bar{h}_{H_2} + \dot{n}_{O_2} \bar{h}_{O_2} + \dot{n}_{N_2} \bar{h}_{N_2})_e \Big|_{100^\circ\text{C}} - (\dot{n}_{H_2O} \bar{h}_{H_2O} + \dot{n}_{H_2} \bar{h}_{H_2} + \dot{n}_{O_2} \bar{h}_{O_2} + \dot{n}_{N_2} \bar{h}_{N_2})_e \Big|_{25^\circ\text{C}} \quad (7.19)$$

The heat loss from uncombusted hydrogen was calculated as:

$$\dot{Q}_{H_2,loss} = \dot{n}_{H_2,e} \mathcal{M}_{H_2} q_{H_2,LHV} \quad (7.20)$$

The unmeasured heat losses were calculated as:

$$\dot{Q}_{unmeasured} = \dot{Q}_{H_2} - \dot{Q}_{oil} - \dot{Q}_{H_2,loss} - \dot{Q}_{Ex,rec} - \dot{Q}_{Ex,unrec} \quad (7.21)$$

7.5. Uncertainties

The uncertainties of the measured parameters used in the determination of the efficiency calculation and gas balance are listed in Table 7.3. The uncertainties of the other measured values were calculated in the same manner, but are not listed here for brevity. Again, this data is from the base case experiment (Exp. 10) and is representative of the uncertainties in the data collected in each experiment. The precision uncertainty of the measured parameters was calculated as:

$$U_{Precision} = t_{0.05,N-1} \sigma_{\bar{X}} \quad (7.22)$$

where $t_{0.05,N-1}$ is the student t-test factor and $\sigma_{\bar{X}}$ is the standard deviation around the mean, \bar{X} . The student t-test factor was determined based on a 95 % confidence interval and the number of degrees of freedom where N is the number of data points collected. The total uncertainty of the measured value, $U_{\bar{X}}$, was calculated as:

$$U_{\bar{x}} = \sqrt{U_{Precision}^2 + U_{Bias}^2} \quad (7.23)$$

where U_{Bias} is the bias error. The calibration uncertainty was used as the bias uncertainty.

Table 7.3: Uncertainties of measured parameters (Exp. 10)

Parameter	Precision Uncertainty	Bias Uncertainty	Total Uncertainty
Oil Inlet Temperature (°C)	0.04	0.36	0.36
Oil Outlet Temperature (°C)	0.02	0.36	0.36
Gas Inlet Temperature (°C)	0.05	0.36	0.37
Gas Outlet Temperature (°C)	0.04	0.53	0.53
Gas Inlet Pressure (bara)	0.012	0.009	0.016
Oil Flow Rate (ml/min)	0.18	0.06	0.19
H2 Flow Rate (sccm)	0.44	8.00	8.02
Air Flow Rate (sccm)	1.64	19.05	19.12

The uncertainty of some parameters could not be quantified, so the uncertainty had to be estimated. These parameters and their associated uncertainty estimation are listed in Table 7.4. The oil manufacturer provides a datasheet with the temperature dependant oil properties; however, no uncertainties were provided. Instead, a 2 % uncertainty was applied to the supplied data for the oil density and specific heat. These estimations affected the uncertainties of the oil mass flow rate, the heat gained by the oil and the efficiency index. The catalyst length was controlled using masks, so there is an unknown length uncertainty from this process. This also could have potentially resulted in a less uniform deposition near the edges. An uncertainty of 2 mm was applied to the catalyst length as a conservative estimate. This estimation only impacted the determination of the residence time for combustion.

Table 7.4: Estimation of unknown uncertainties

Parameter	Uncertainty Estimation
Oil Density	2 %
Oil Specific Heat	2 %
Catalyst Length	2 mm

Uncertainties of the operating conditions and results of this sample experiment are listed in Table 7.5. The Kline-McClintock method was used for determining the uncertainty of the calculated parameters. The high uncertainty of the oil residence time is primarily due to the inability to obtain an accurate measurement of the oil channel height. Most of the uncertainty associated with the efficiency calculation is due to the uncertainty of the oil properties. If the properties were known with an uncertainty of 1 percent, the uncertainty of the efficiency would be reduced to 1.9 percent.

Table 7.5: Uncertainty of calculated parameters (Exp. 10)

Parameter	Value	Uncertainty	% Uncertainty
Equivalence Ratio	1.00	0.01	1.4 %
Combustion Residence Time (ms)	21	0.8	3.7 %
Oil Residence Time (s)	4.03	0.9	22.4 %
Heat Gained by Oil (W)	138.4	4.4	3.2 %
Heat Input from H ₂ (W)	143.8	1.4	1.0 %
Efficiency (%)	96.2	3.2	N/A

Unfortunately, the Tedlar sample bags slowly leaked H₂, reducing the accuracy of the obtained GC measurements. In an attempt to correct for the leakage rate, four samples were measured on separate occasions in order to determine typical leakage rates. The differences in H₂ content over two days are listed for the four samples in Table 7.6. The average leakage rate was found to be -0.09 % per day, with a precision uncertainty of 0.12 %, calculated according to Eq. (7.22).

Table 7.6: Uncertainty of H₂ content due to leakage

Exp. #	Initial H ₂ Content (%)	Final H ₂ Content (%)	Days Between Analysis	H ₂ Content Change per Day (%)
Exp. 26	5.91	5.60	2	-0.15
Exp. 31	3.96	3.82	2	-0.07
Exp. 33	4.38	4.24	2	-0.07
Exp. 29	5.32	5.19	2	-0.06
Average (%)				-0.09
Uncertainty (%)				0.12

Hydrogen content of each sample was corrected based the average leakage rate and the number of days between sampling and analysis with the GC in an effort to obtain a more realistic measurement of the H₂ content in the exhaust. The longest time between sampling and GC measurement was nine days; correcting for the leakage rate resulted in a 0.79 % increase in H₂ content. Uncertainty of the GC sample was determined as:

$$U_{GC} = \sqrt{U_{Cal}^2 + U_{Repeatability}^2 + (n_{days}U_{Leak})^2} \quad (7.24)$$

where U_{Leak} is the leakage uncertainty and n_{days} is the number of days between sampling and GC analysis.

8. RESULTS AND DISCUSSION

The data collected during the course of the experiments are presented and discussed in this section. Equivalence ratio, residence time and oil flow rate were varied and their effects on μ CHX performance studied. The length and location of catalyst were the two geometric parameters varied. A total of 40 experiments were performed and the data were compiled into seven sets for discussion. Comparisons with the CFD model developed by Ghazvini and Narayanan [1] are made when appropriate.

8.1. Experimental Matrix

A summary of the experiments conducted are listed in Table 8.1 with the primary geometric and fluidic parameters of each experiment. Catalyst shim B was used in experiments examining the effects of varying the parameters of residence time, equivalence ratio and average oil temperature. Catalyst shim C was used in experiments where the residence time and catalyst location were varied. A comparison of similar residence times between catalyst shim B and C indicated the effect of variation in catalyst length on the efficiency of the μ CHX. Details of the different catalyst shims were presented in Chapter 5 (Table 5.3). Initial testing with shim A, with a palladium catalyst, was not sufficiently reactive to obtain performance data; the details of this testing is omitted here and provided in Appendix E. Time-averaged data at steady state operation for each experiment is available in Appendix G.

Table 8.1: Testing matrix of μ CHX experiments

Varied Parameter	Cat. Shim	Experiment #'s	Φ	Res. Time (ms)	Average Oil Temp. (°C)
Initial testing	A	1	0.4	23	N/A
Stability	B, C	2, 3, 23, 26, 27, 34	1	5, 21	85, 92 – 96
Residence time over catalyst	B, C	10-14, 25, 27-35	1	5 – 45	84 – 86
Equivalence ratio	B	8, 10, 15-19, 24	0.3 – 1	19 – 22	84 – 86
Avg. oil temp.	B	3, 10, 20-23	1	20 – 21	64 – 105
Catalyst length	B, C	10, 34	1	20	85
Catalyst location	C, C-rev	27-35, 36-40	1	5 – 14	85, 90

A CFD model was developed concurrently with the research presented in this thesis; however, the model is still idealized, assuming a 2-D flow field with negligible conduction through the device walls. Flow through the headers is also not modeled. Moreover, it has yet to be adapted to the specific geometry of the experimental μ CHX. A schematic of the CFD model geometry is shown in Fig. 8.1. The geometric differences between the experimental μ CHX and the simulated μ CHX include:

- Different channel length ($L_{exp} = 76.2$ mm; $L_{sim} = 30$ mm)
- Different combustion channel heights ($H_{exp} = 0.254$ mm; $H_{sim} = 0.300$ mm)
- Two recuperator and oil channels in the simulation (See section 4.2.1 for details)

Due to these differences and model idealizations, only qualitative comparisons between the CFD model and the experimental results can be made.

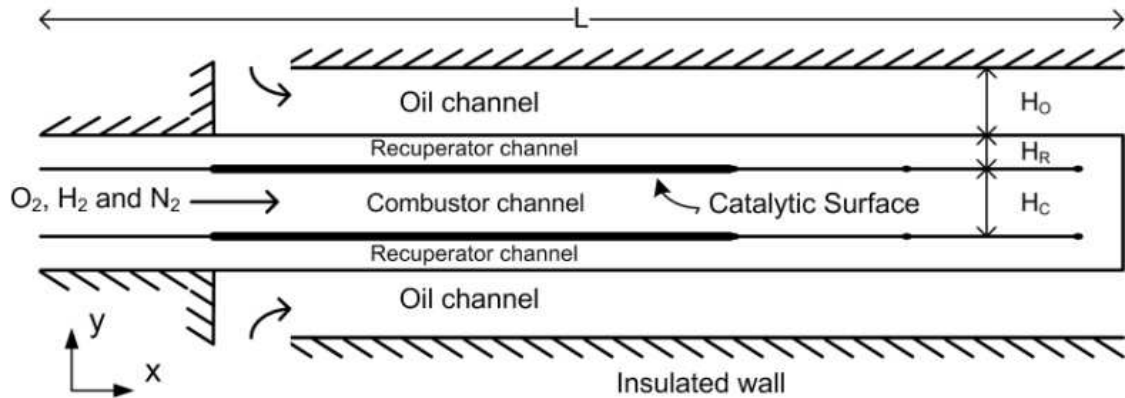


Fig. 8.1: Schematic of CFD model geometry [1]

8.2. Heat Loss Estimation

A simplified one-dimensional resistance model, shown in Fig. 8.2, was developed in order to estimate the conduction heat loss of the μ CHX at different operating temperatures. While this model represents an over-simplification of the expected heat path within the device, such a thermal resistance model allows for a qualitative analysis of the device much like an electrical circuit, where heat flows are analogous to electrical current, temperature difference is analogous to voltage potential and thermal resistance is represented as to electrical resistance [49]. The thermal resistances associated with the μ CHX can be compiled into an equivalent channel resistance and the resistances of heat loss through the insulation can be compiled into an equivalent insulation resistance.

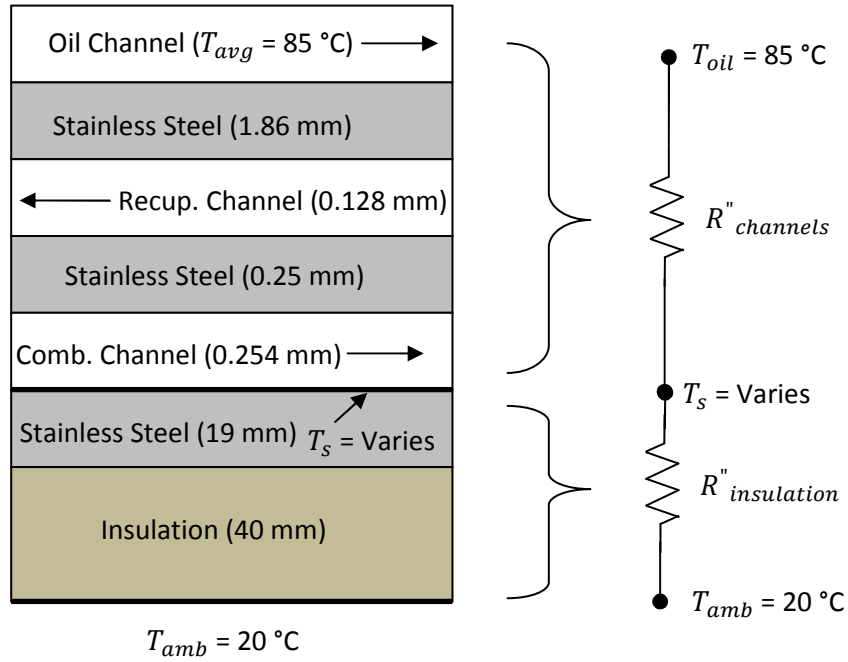


Fig. 8.2: Resistance model of conduction heat losses

The parameters and resistances of each section of the resistance model are shown in Table 8.2. The equivalent resistance of the insulation was found to be almost three orders of magnitude greater than the resistance of the channels. Resistances for the stainless steel sections and the insulation were calculated according to the conduction resistance equation:

$$R''_{cond} = \frac{H}{k} \quad (8.1)$$

where H is the thickness of each section and k is the thermal conductivity of the material. The resistances across the combustion, recuperator and oil channels were calculated according to the convection resistance equation:

$$R''_{conv} = \frac{2H}{Nu_D k} \quad (8.2)$$

where Nu_D is the Nusselt number based on the hydraulic diameter ($D_H \approx 2H$). For the combustion channel and oil channel, the Nusselt number was taken to be 4.86, which is appropriate for an infinite aspect ratio channel of uniform surface temperature with one heated side and one insulated side. The Nusselt number for recuperator channel was taken

to be 7.54, which is appropriate for an infinite aspect ratio channel of uniform surface temperature that is not insulated. The thermal conductivity of air was evaluated at a temperature of 100 °C. The resistances of the channels and insulation are arranged in series, so the equivalent resistance can be found by summing the resistance of each section:

$$R_{eq}'' = \sum R_{section}'' \quad (8.3)$$

The thermal conductivities of the air, oil, stainless steel and insulation were selected assuming temperatures around 100 °C. The thermal conductivities and Nusselt numbers were obtained from Incropera et al. [49], and the results of the resistance analysis using these parameters is shown in Table 8.2. The heat flux to the oil was calculated as:

$$\dot{Q}''_{channels} = \frac{T_s - T_{oil}}{R_{channels}''} \quad (8.4)$$

and the heat flux lost through the insulation was calculated as:

$$\dot{Q}''_{lost} = \frac{T_s - T_{amb}}{R_{insulation}''} \quad (8.5)$$

Table 8.2: Resistance model parameters

Section	Thickness (mm)	k (W/m-K)	R'' (m ² -K/W)	R'' _{equivalent}
Oil channel	0.71	0.131	2.24E-03	6.46E-03
Oil/Recup. (SS) shim	1.82	15.2	1.20E-04	
Recuperator channel (air)	0.128	3.38E-02	1.00E-03	
Recup./Comb. (SS) shim	0.254	15.2	1.67E-05	
Combustion channel (air)	0.254	3.38E-02	3.09E-03	
Base (SS) shim	19	15.2	1.25E-03	1.74
Insulation	40	2.30E-02	1.74E+00	

Ratios of heat flux through the channels and through the insulation were obtained for a variety of surface temperatures and are shown in Fig. 8.3. This chart is based on an average oil temperature of 85 °C. As the internal surface temperature approaches the oil temperature, an increasing quantity of heat is lost through the insulation. This indicates that higher internal temperatures are desired in order to maximize the ratio of heat transferred to the oil. The surface temperatures measured during the experiments ranged between 150 °C and 200 °C, resulting in driving temperature differences between 65 °C and 115 °C. The corresponding heat loss fractions are 0.74 % and 0.58 %, respectively. While the heat loss fraction is estimated to be small for both temperatures, it is important to note that the model predicts 28 % more heat loss for the 65 °C driving temperature difference than for the 115 °C temperature difference.

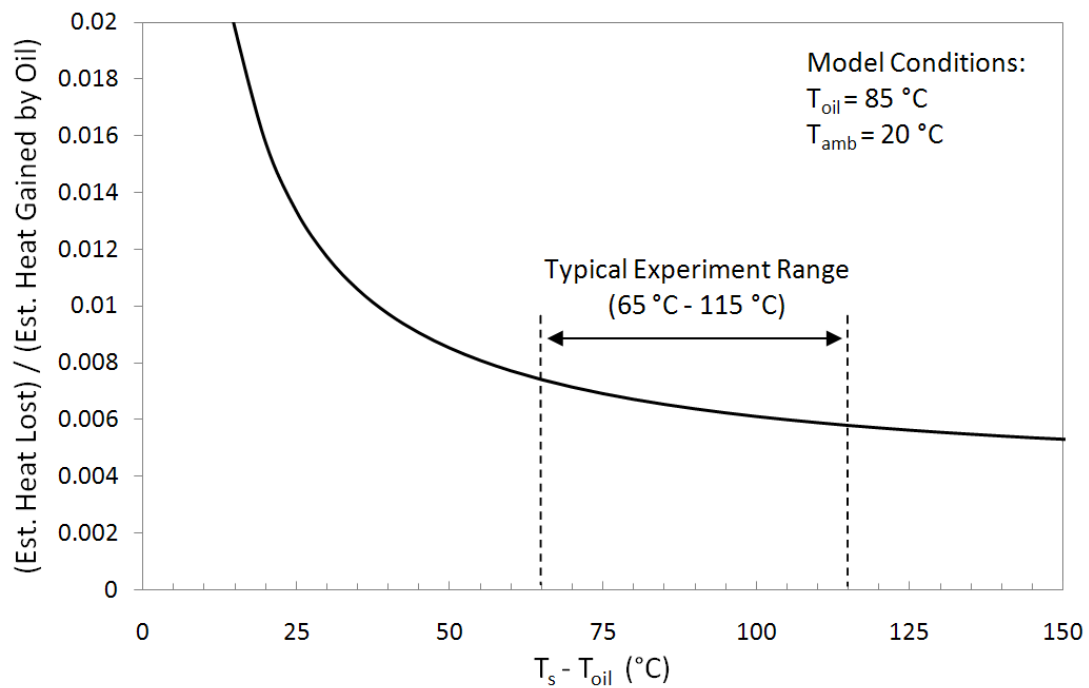


Fig. 8.3: Heat flow ratios for various internal surface temperatures

8.3. Repeatability Experiments

Catalyst shims B and C were tested for stability. The stability of catalyst shims B and C were demonstrated by comparing initial tests to tests run after approximately 80 and 40 hours of operation, respectively.

8.3.1. Stability of Catalyst Shim B

The stability of catalyst shim B was tested by performing an initial experiment and repeating it at a later date with the same fluidic operating conditions. The details of these tests are listed in Table 8.3. These tests were conducted at the maximum hydrogen flow rate and minimum residence time as this was expected to be the most important test condition. Efficiency values obtained were found to be repeatable at similar operating conditions. Experiments 2 and 3 were conducted initially in order to investigate the repeatability of successive experiments. These two tests were conducted with the same oil flow rate and resulted in a similar oil temperature difference and efficiency. The average oil temperature was higher for exp. 3 than for exp. 2 due to a higher inlet oil temperature that was not controlled. Experiment 23 was conducted several weeks later, during which the catalyst had experienced approximately 80 hours of combustion operation. For this experiment, the oil flow rate was adjusted in order to maintain an average oil temperature similar to exp. 3. The efficiency obtained from exp. 23 was found to be nearly identical to the 93.7 percent efficiency obtained in exp. 3. The uncertainty of each obtained efficiency value was ± 3.1 percent.

Table 8.3: Repeatability tests using shim B

	Combustion Residence Time (ms)	Φ	H ₂ Energy Input (W)	Exhaust Temp. (°C)	Average Oil Temp. (°C)	Oil Temp. Difference (°C)	Efficiency (%)
Exp. 2 (4/24)	21	1	143.8	139.0	91.7	145.2	92.8
Exp. 3 (4/26)	21	1	143.8	137.4	94.8	145.9	93.7
Exp. 23 (5/9)	21	1	143.7	143.8	95.7	154.9	93.7

The measured combustion channel temperature profiles for experiments 2, 3 and 23 are shown in Fig. 8.4. A schematic of the μ CHX with catalyst shim B is shown in Fig. 8.5 with the axial thermocouple locations along the combustion channel. Two additional thermocouples are located laterally along the combustion channel in locations 2 and 5 (at 25.4 mm and 63.5 mm, respectively) in order to provide an indication of lateral temperature uniformity.

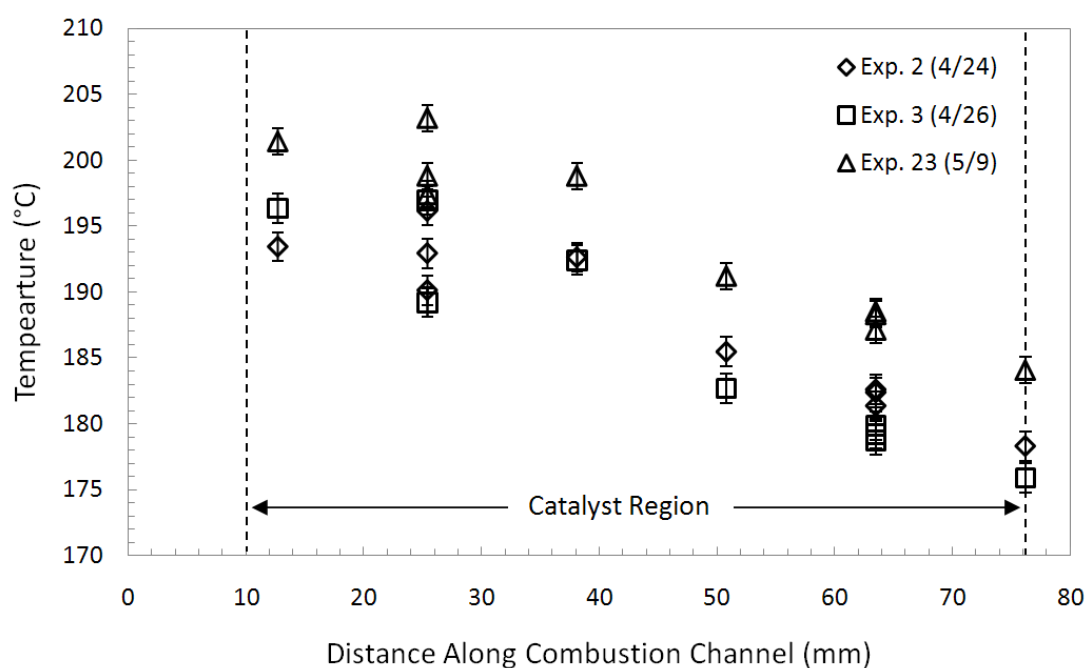


Fig. 8.4: Catalyst shim B combustion repeatability test temperature profiles

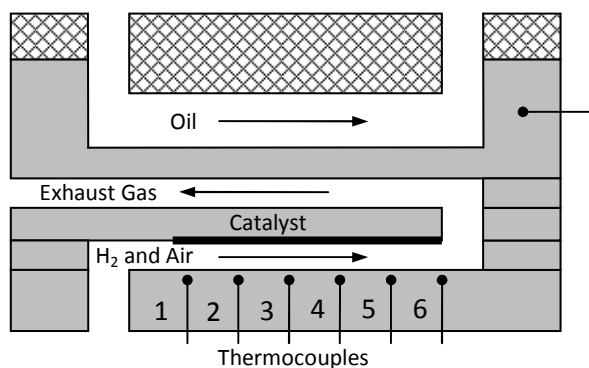


Fig. 8.5: Schematic of μ CHX with catalyst shim B

The temperature profiles of experiments 2 and 3 were similar in shape and magnitude; however, the temperature profile of exp. 23 was similar in shape, but offset higher by about 6 °C. This may be the result of the greater oil temperature difference for exp. 23. Oil entered the combustor near ambient temperature, which was not controlled and varied between 18 °C and 23 °C for the majority of experiments. The inlet oil temperature for exp. 23 was about 4 °C lower than for exp. 3, necessitating a higher oil temperature difference in order to obtain the desired average oil temperature around 95 °C. The higher oil temperature difference of exp. 23 was obtained by reducing the oil flow rate for exp. 23 compared to exp. 3. It was anticipated that lower inlet oil temperature would cause lower exhaust temperature in exp. 23, but this was not observed. However, the higher combustion channel temperatures in exp. 23 plausibly explain the increased oil outlet temperature compared to exp. 3. Experiments examining the impact of varying the oil temperature difference should be performed in order to explain the observed variation in combustion channel temperatures.

The similar shape of the combustion channel temperature profiles provide further indication that the catalyst is not deactivating or degrading. If the catalyst near the inlet was being deactivated over time, then the highest temperatures would likely have been observed farther along the channel for the later experiments. This does not appear to have occurred. In addition, the similar efficiency results between each experiment indicates that the performance of the μ CHX is repeatable and does not show signs of catalyst deactivation,

even after extended periods of testing. As it stands, the cause of variation between the temperature profiles is unknown.

The lateral temperature measurements indicate that there was some temperature non-uniformity (± 4 °C) at beginning of the combustion channel, 25.4 mm from the inlet. As shown in Fig. 8.6, the highest temperature was consistently observed down the centerline of the combustion channel. This may be due either to higher flow through the center, combustion non-uniformities, lateral heat transfer, or some combination of the three. Near the end of the combustion channel, 63.5 mm from inlet, the lateral thermocouples are near parity (± 0.7 °C), indicating that thermal non-uniformities are not significant at this location. This trend of higher centerline temperatures was consistently observed in all experiments.

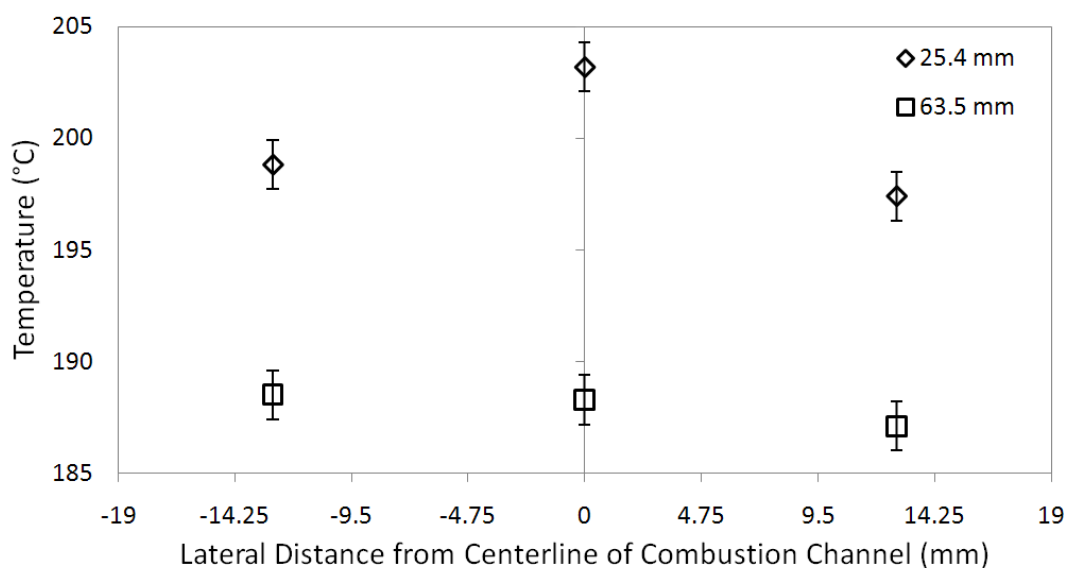


Fig. 8.6: Lateral temperatures of exp. 23 with catalyst shim B

When the μ CHX was disassembled after testing with shim B was completed, the PEEK insert forming the oil channel showed signs of damage at one location. The damage was located directly above the beginning of the catalyst inside the μ CHX. The PEEK part was repaired before the experiments with shim C were conducted. Also, hot spots were observed on the back side of the catalyst shim, indicating either flow or combustion non-uniformities. The repairs to the PEEK part and the hot spots on shim B are discussed further in Appendix H.

8.3.2. Stability of Catalyst Shim C

The stability of catalyst shim C was investigated in the same manner as for catalyst shim B. Two experiments were conducted at the same fluidic operating conditions, but on different days. The details of these experiments are listed in Table 8.4. These tests were conducted at the minimum residence time and at an average oil temperature of 85 °C. Experiments 26 and 27 were conducted to investigate the repeatability of successive experiments. Even though identical gas flow rates were supplied for these tests, a lower inlet pressure was measured for exp. 26 compared to exps. 27 and 34, causing lower gas densities at the inlet and a correspondingly shorter residence time. The cause of this inlet pressure variation remains unknown. After roughly 40 hours of combustion operation, experiment 34 was conducted at the same fluidic conditions to investigate the long term stability of the catalyst. Successive experiments demonstrated decreasing efficiencies. The efficiency drop of 1.8 percent between experiments 26 and 27 may be the result of some initial deactivation of the catalyst. Therefore, the data from exp. 26 is excluded from the variation of residence time experiments examined in the next section. The efficiency difference of 0.8 percent between experiments 27 and 34 may be from a further decline in catalyst activity, or it could just be due to repeatability uncertainty. The uncertainty of each obtained efficiency value was ± 2.6 percent.

Table 8.4: Operating conditions for repeatability test of shim C

	Φ	Inlet Pressure (bara)	Combustion Residence Time (ms)	H ₂ Energy Input (W)	Average Oil Temp. (°C)	Exhaust Temp. (°C)	Efficiency (%)
Exp. 26 (5/17)	1	1.49	4.4	143.7	85.2	128.6	69.6
Exp. 27 (5/18)	1	1.67	4.9	143.7	85.3	128.8	67.8
Exp. 34 (5/21)	1	1.70	5	143.7	85.2	128.3	66.6

Similar temperature profiles were obtained for all three catalyst stability experiments and are shown in Fig. 8.7, and the corresponding μ CHX schematic is shown in Fig. 8.8. The

temperatures along the combustion channel are slightly higher for the experiments that operated at higher efficiencies. Also, the variation between the lateral thermocouples for shim C is smaller than what was observed with shim B, within $\pm 2^\circ\text{C}$ at location 2 and $\pm 0.5^\circ\text{C}$ at location 5.

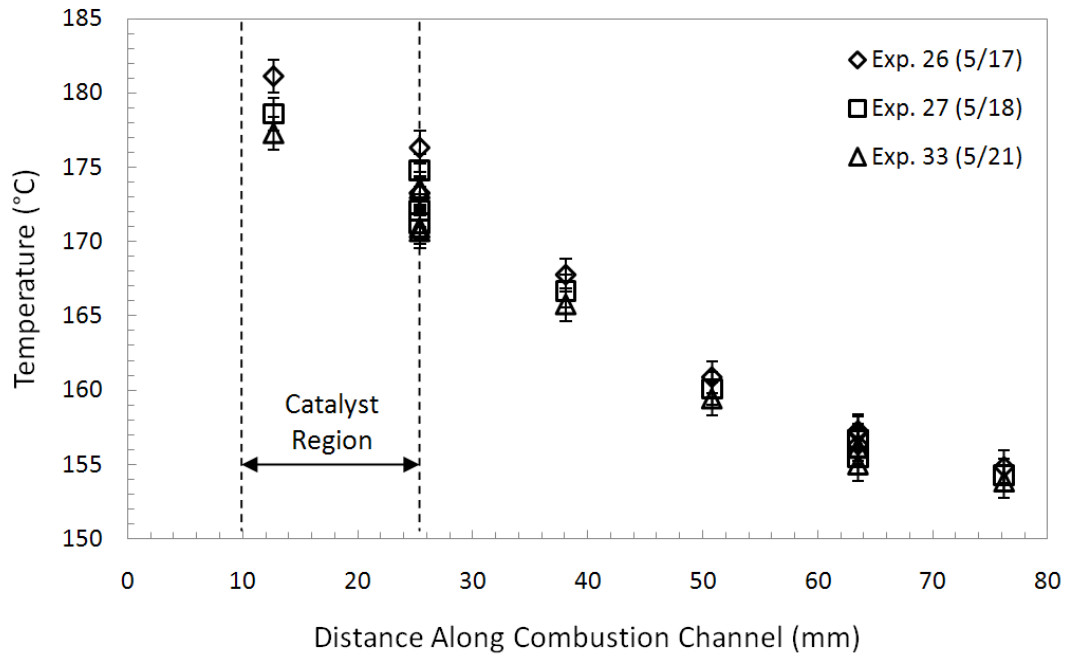


Fig. 8.7: Catalyst shim C combustion temperature repeatability

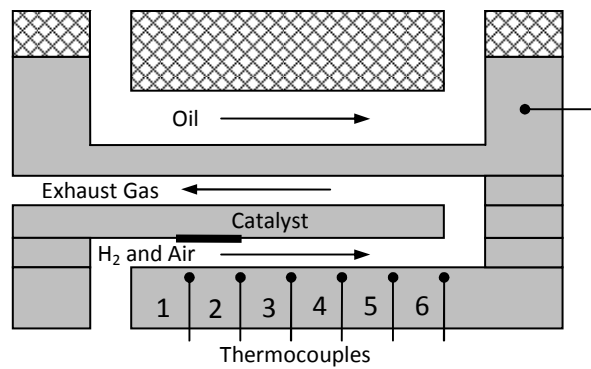


Fig. 8.8: Schematic of μCHX with catalyst shim C

8.4. Variation of Residence Time

Residence time variation tests were conducted on catalyst shims B and C. As discussed in Chapter 7, the residence time was defined as the amount of time the gas mixture was within the catalyst region. Residence time was manipulated by increasing the air and H₂ flow rates metered by the MFCs. The air and H₂ flow rates were adjusted such that a stoichiometric equivalence ratio ($\Phi = 1$) was maintained in each case. As expected, inlet pressure of the gases was higher for the lower residence times due to the increased pressure drop at higher flow rates. An absolute pressure of 1.67 bar was measured at the inlet for the lowest residence time while 1.18 bar was measured for the highest residence time. The impact of the gas density variation due to temperature and pressure at the inlet was taken into account in the calculation of residence time.

Catalyst shims B and C were fabricated with similar area-averaged mass loadings and calcination and reduction procedures, but were of different catalyst lengths. The 77 percent shorter catalyst length of shim C (15.2 mm for shim C compared to 66.0 mm for shim B) allowed for shorter residence times to be obtained with shim C than with shim B. However, varying the catalyst length not only changed the residence time, but also the heat generation rate per unit residence time. As a result, the efficiency results from shim B and C cannot be directly compared as a function of residence time. The effect of varying the catalyst length is discussed in a later section.

8.4.1. Catalyst Shim B Residence Time Experiments

The performance of the μ CHX with catalyst shim B was investigated for various residence times. The typical outlet oil temperature for these experiments was 150 °C, resulting in an average oil temperature of 85 °C. The performance is characterized based on efficiency and hydrogen conversion, the latter helping to indicate a cause of reduced efficiency. The efficiency of the μ CHX was found to decrease linearly as the residence time increased, as shown in Fig. 8.9. The available heat from combustion also decreased with longer residence times because the total gas flow rate had to be reduced in order to obtain higher residence

times, causing a correspondingly lower H_2 flow rate. The hydrogen conversion efficiency was measured to be 93 – 96 percent, with no significant variation with residence time. Higher residence times provide more time for the gases to react on the catalyst, so this result indicates that the combustion reaction was not residence time-limited over the range of residence times tested.

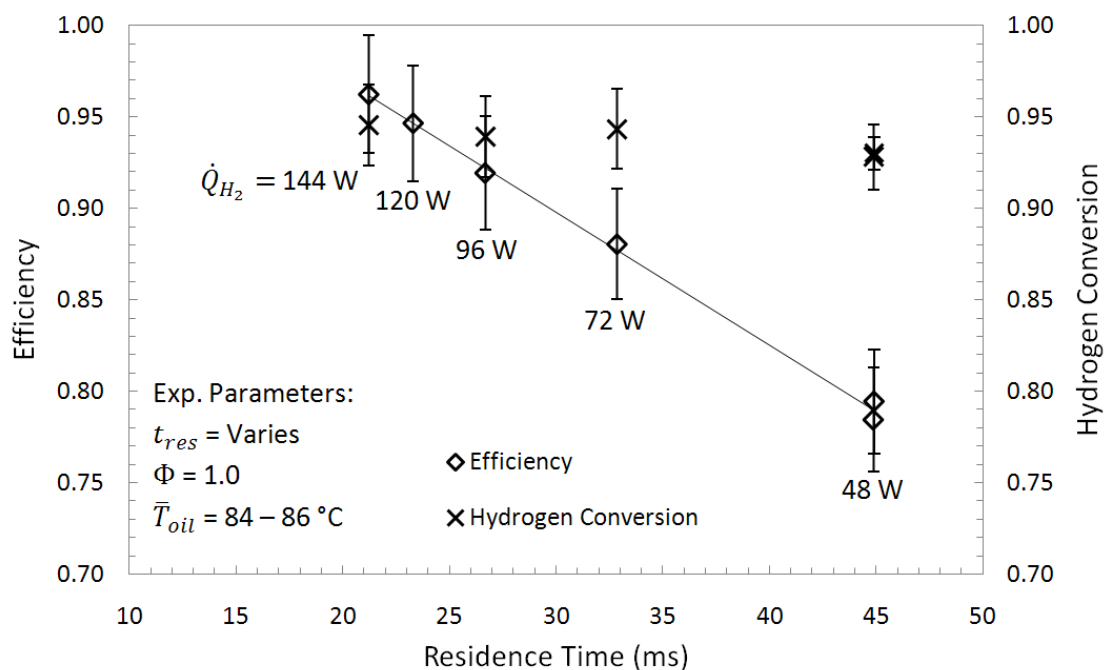


Fig. 8.9: μ CHX performance for residence time variation experiments with catalyst shim B

Hydrogen conversion is not shown for the 120 W data point (23 ms residence time) because it was measured to be 99 percent, which is inconsistent with other GC measurements taken. It is more probable that the bag leaked the H_2 , resulting in an inaccurate reading.

The temperature profiles measured along the combustion channel are shown in Fig. 8.10. A schematic of the μ CHX with catalyst shim B is shown again in Fig. 8.11 for reference. The temperatures shown were obtained from the thermocouples along the centerline of the combustion channel. As discussed in Section 4.3, these temperatures were measured in the stainless steel base about 1 mm below the combustion channel and are therefore only indicative of the temperatures in the combustion channel and not that of the catalyst. The

actual temperatures of gas in the combustion channel were not measured. Also, the additional temperature points off-centerline obtained at 25.4 mm and 63.5 mm are omitted for clarity.

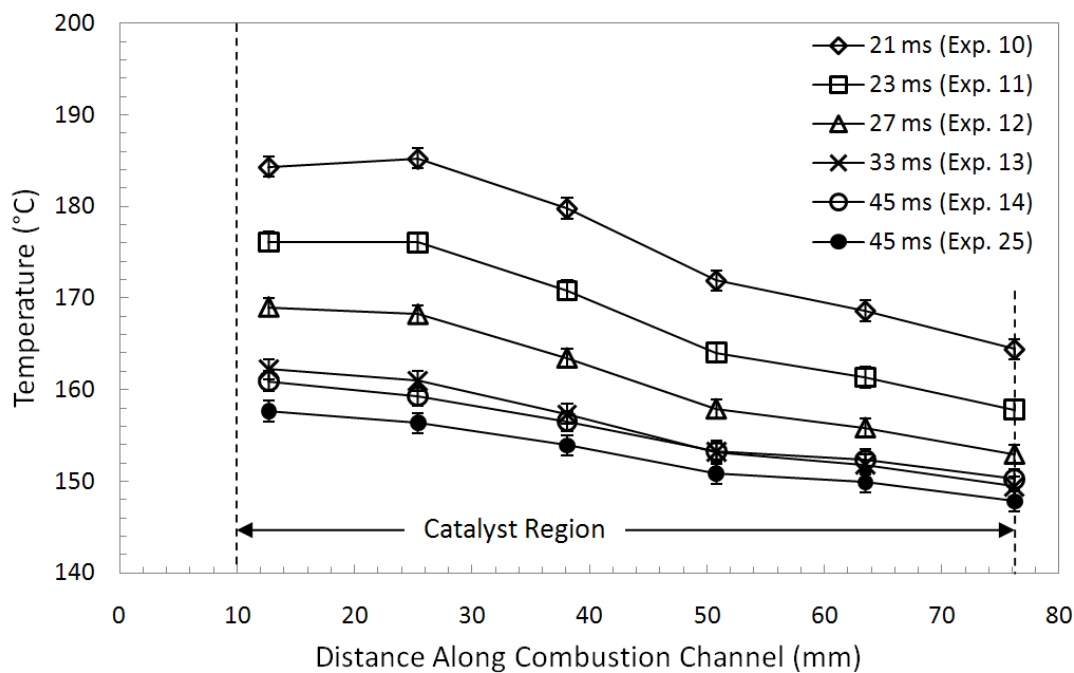


Fig. 8.10: Centerline temperature profiles of residence time variation experiments with catalyst shim B

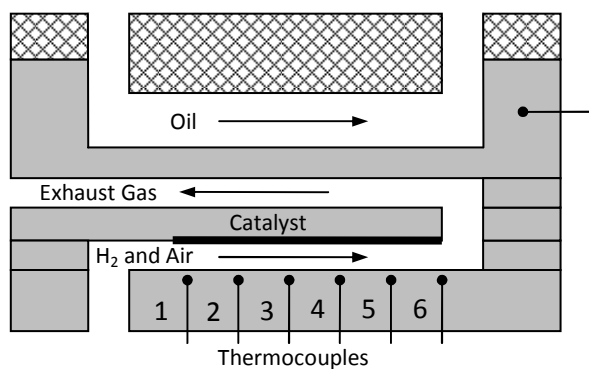


Fig. 8.11: Schematic of μ CHX with catalyst shim B

Higher temperatures were measured at all locations for the experiments that operated at lower residence times. Greater heat release rates occur at the lower residence times due to the higher H_2 flow rate, causing higher temperatures in the combustion channel. The higher efficiencies obtained correspond to the higher measured temperatures along the combustion channel. This observation fits the predictions of the one-dimensional resistance model that was developed in Section 8.2 which indicated that higher temperatures in the combustion channel result in a greater portion of the generated heat being transferred to the oil than being lost through the insulation. In essence, the μ CHX is heat transfer limited at longer residence times due to imperfect insulation.

To further examine the decreasing efficiency trend, the heat loss components are presented in Fig. 8.12. Measured energy losses include uncombusted hydrogen in the exhaust and the sensible heat of the exhaust gas. The sensible heat of the exhaust gas has been separated into recoverable exhaust heat and unrecoverable exhaust heat. The recoverable exhaust heat is the sensible heat that would have been recovered if the exhaust gas exited the μ CHX at 100 °C, the minimum temperature required for water vapor to not condense in the μ CHX. Because the heat input from hydrogen was defined based on the combustion reaction occurring at 25 °C, the unrecoverable exhaust heat is the sensible heat lost from the exhaust gas exiting at 100 °C, not 25 °C. The unmeasured heat loss is the remaining balance of heat, obtained by subtracting the measured heat exiting the μ CHX from the measured heat input to the μ CHX from H_2 . The unmeasured heat losses were observed to mirror the efficiency trend. A more detailed description of the heat paths was presented in Section 7.3. Uncertainty bars are not shown on the exhaust heat losses for clarity because vertical axis is very small in order to illustrate differences between the heat loss components and because the uncertainties were typically in excess of 100 percent of the reported values.

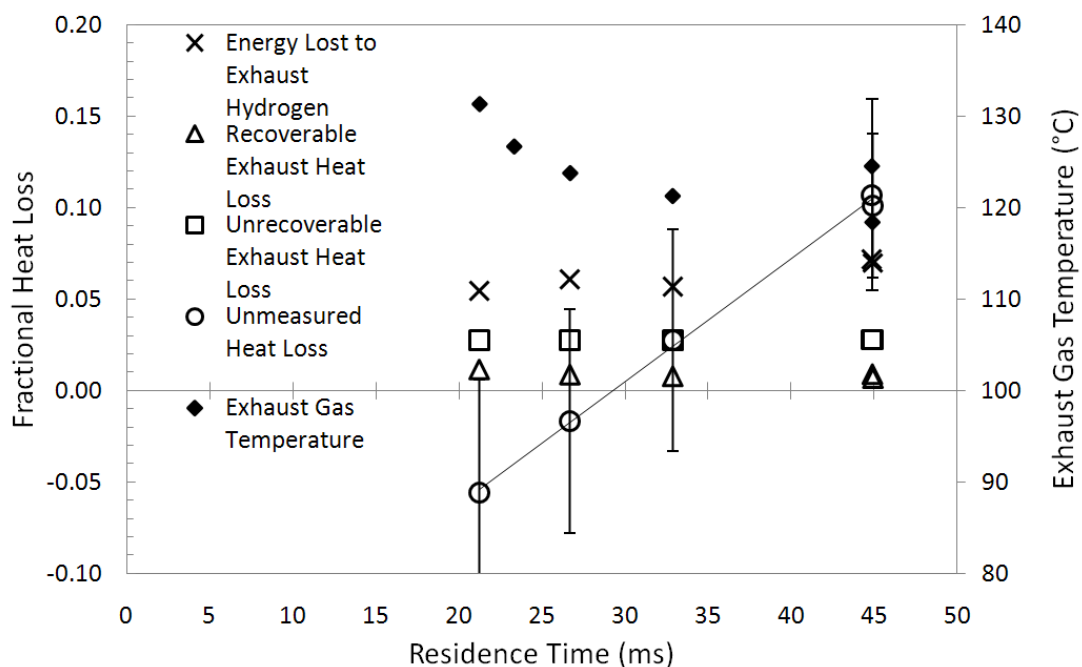


Fig. 8.12: Normalized heat losses for variation of residence time experiments with shim B

Despite the decreasing exhaust temperatures with longer residence times, the potentially recoverable exhaust heat and the unrecoverable exhaust heat were a relatively small and constant fraction of the total heat input. This indicates that minimal performance improvement could be obtained from lower exhaust gas temperatures. Also, the heat lost to uncombusted hydrogen was mostly constant. The unmeasured heat losses were found to be negative for the shortest residence times, seemingly indicating that the system is gaining heat from the environment. However, the vertical axis covers a narrow range in order to illustrate the differences and trends of the heat loss components and the uncertainties are large for the unmeasured heat loss (typically ± 0.06). The margin of error is so large for the unmeasured heat losses because it includes the uncertainties of every measured heat pathway. However, the high uncertainties and negative bias are primarily due to and best explained by systematic bias errors induced by the uncertainty of the oil properties. Despite the large error bars, there is a trend of increased heat loss for longer residence times that can be observed. The increasing trend of the unmeasured heat losses is reasonable based on the previously developed resistance model; heat loss through the insulation is expected to be the primary component of these losses, which was predicted to increase for reduced

combustion channel temperatures. Approximately 16 percent more heat was lost through the insulation for the 20 ms residence time experiment than for the 45 ms residence time experiment, a quantity in alignment with that predicted by the resistance model.

In the report on a combustor oil heat exchanger developed by Sandia National Labs [7], the authors note that the oil manufacturer had overstated the density and specific heat of the oil by 2 percent and 1 – 5 percent, respectively. In their case, the oil density was overstated at lower temperatures. If the properties of the Paratherm MG oil used in for the μ CHX experiments are similarly skewed, then the reported efficiency values would be offset lower and the unmeasured heat losses would be offset upward, as shown in Fig. 8.13. Positive heat losses would have been obtained if the Paratherm MG oil properties are more than 3 percent lower than reported by the manufacturer.

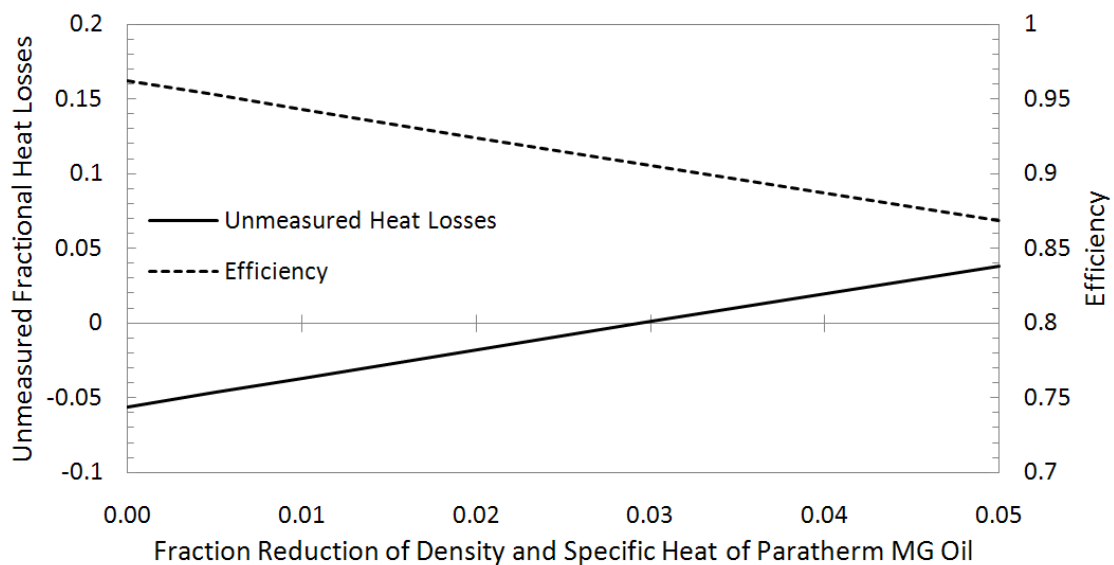


Fig. 8.13: Sensitivity analysis of oil density and specific heat (Data from 21 ms exp. 10)

The pressure drop across the gas channels is presented in Fig. 8.14 as a function of the inlet Reynolds number. The corresponding heat input from H_2 is plotted on the secondary horizontal axis for reference because the inlet Reynolds number is proportionate to the H_2 heat input for the variation of residence time tests. The Reynolds number was calculated based on the inlet conditions, assuming the gas was pure air, allowing for the pressure drop

measured during combustion to be compared to the pressure drop from laminar flow theory [49], calculated as:

$$\Delta P = \frac{f \rho U^2}{2 D_H} L \quad (8.6)$$

where f is the friction factor, ρ is the air density, U is the mean channel velocity, D_H is the hydraulic diameter of the channel and L is the length of the channel. The friction factor for a large aspect ratio channel was calculated as:

$$f = \frac{96}{Re_{D_H}} \quad (8.7)$$

where Re_{D_H} is the hydraulic diameter of the channel. The Reynolds number was calculated as:

$$Re_{D_H} = \frac{\rho U D_H}{\mu} \quad (8.8)$$

where μ is the dynamic viscosity of air. The hydraulic diameter was calculated as:

$$D_H = 2H \quad (8.9)$$

where H is the channel height. The pressure drop from the combustion channel and the recuperator channels were calculated separately and summed together in order to obtain the theoretical pressure drop. Elevated internal gas temperatures would contribute to greater measured pressure drops than is estimated by theoretical model. Also, the pressure drop associated with the headers, entry lengths and turns are expected to be substantial and are not included in the theoretical pressure drop.

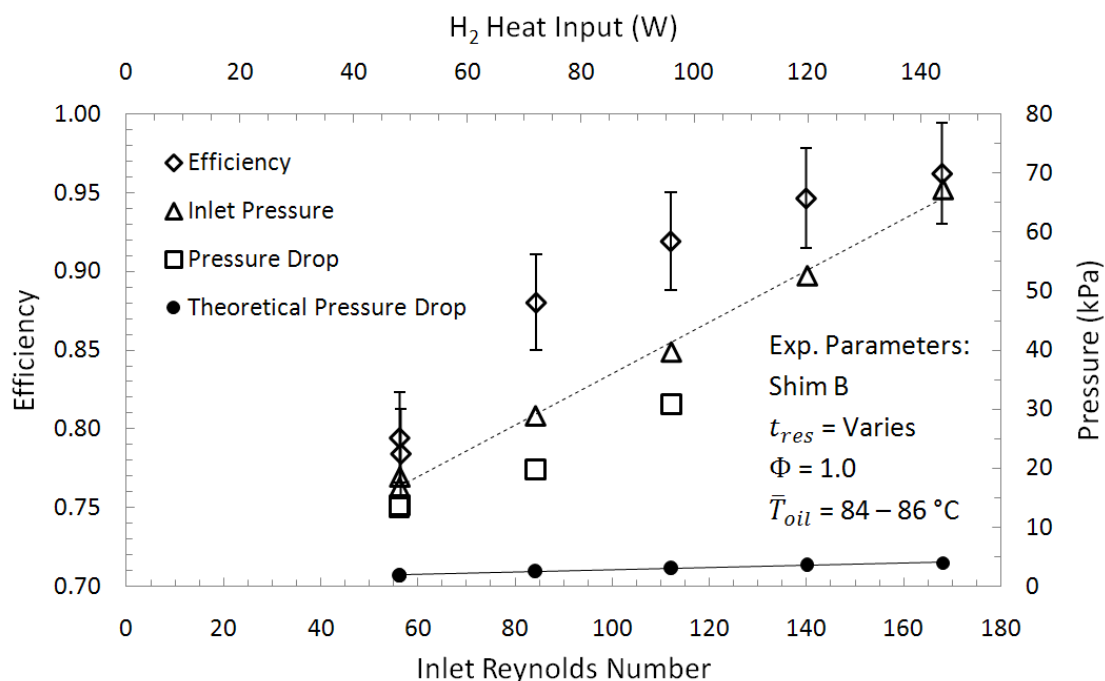


Fig. 8.14: Pressure drop for residence time experiments with catalyst shim B

The differential pressure transducers were limited to a pressure drop of 37 kPa before the signal was clipped. The inlet pressure and pressure drop uncertainties were about ± 1 kPa for each measurement. Because pressure drop data wasn't available at all flow rates, the inlet gas pressure is also shown. The inlet gas pressure is the pressure that was required to force the flow through the μ CHX and through the additional tubing downstream. The inlet pressure will always be higher than the differential pressure across the combustor due to additional pressure drop contribution of the downstream tubing in the experimental facility. Therefore, the inlet pressure can be used as the upper bound for the differential pressure required for each flow rate. The inlet pressure was found to increase linearly with the flow rate to 67 kPa at the maximum power level. This trend fits laminar flow theory, which predicts that pressure drop will linearly increase with flow rate when all other factors are held constant. As expected, the measured pressure drop was significantly higher than theoretical prediction, likely due to the higher viscosities at elevated temperatures and additional geometric features not considered in the theoretical prediction.

8.4.2. Catalyst Shim C Residence Time Experiments

Performance tests were conducted on the μ CHX with catalyst shim C while varying the residence time of the gases over the catalyst. The shorter catalyst length of shim C allowed for shorter residence times to be tested than with shim B. Efficiency and hydrogen conversion are shown as a function of residence time in Fig. 8.15. These experiments were all conducted at an average oil temperature of 85 °C. The sole exception is the experiment at 20 ms, which operated at 83.5 °C due to difficulty achieving a high enough outlet oil temperature. Longer residence times were found to lead to increased efficiencies until about 7 ms. Lower efficiencies were obtained for residence times longer than around 7 ms. The highest efficiencies, around 75 percent were obtained at residence times between 6 and 11 ms. Hydrogen conversion tended to increase with longer residence times, with a maximum hydrogen conversion of 92.4 percent at a residence time of 13.9 ms.

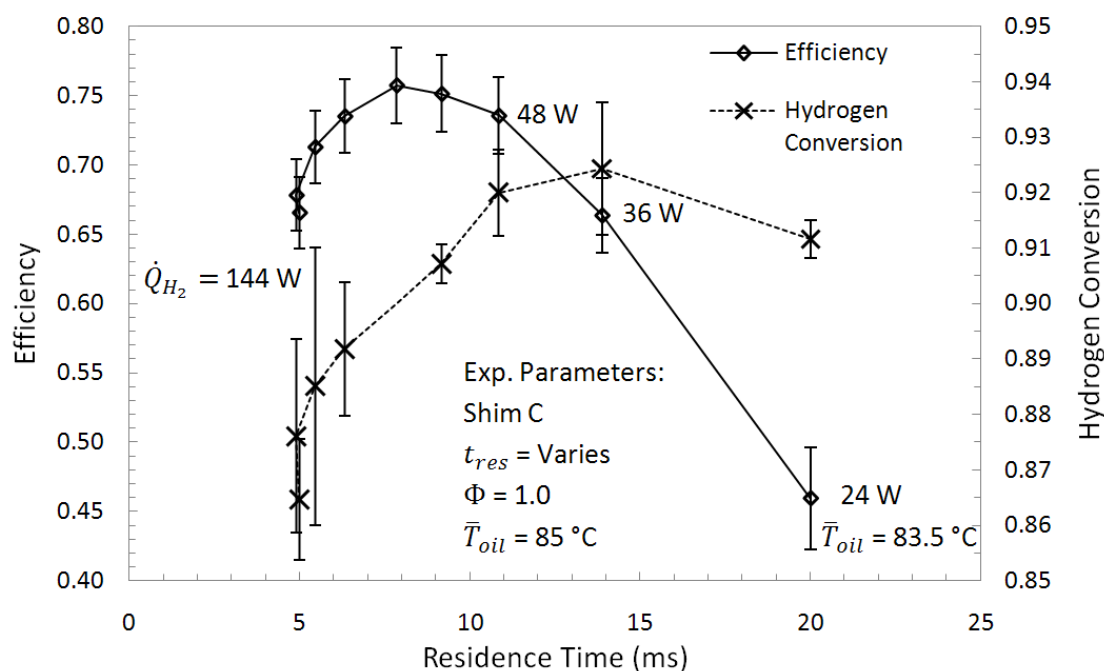


Fig. 8.15: μ CHX performance for residence time variation experiments with catalyst shim C

The increase in efficiency and hydrogen conversion for increased residence times indicate that the reaction is residence time limited until about 11 ms. The decreasing efficiencies at

residence times longer than 7 ms suggest that heat transfer limitations reduce the performance beyond this point. In the same manner as the residence time experiments with shim B, longer residence times were obtained by reducing the flow rate of H_2 and air.

The temperature profiles along the combustion channel for the variation of residence time tests with shim C are shown in Fig. 8.16. A schematic of the μ CHX with catalyst shim C is shown again in Fig. 8.17 for reference. In a similar manner as catalyst shim B, the magnitude of the temperature profiles tended to decrease with longer residence times due to the lower hydrogen input and correspondingly lower heat generation rates. However, different behavior occurs at the highest residence times. The temperature profile with the lowest temperatures was obtained for a residence time of 9.2 ms. At longer residence times, higher temperatures were measured along the combustion channel.

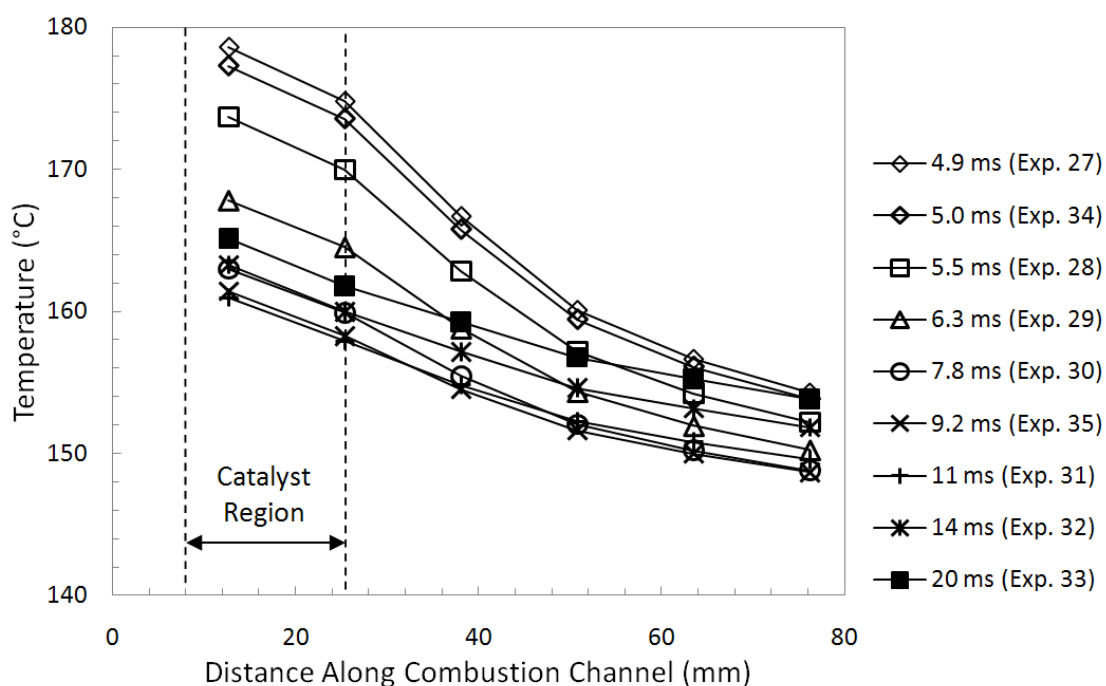


Fig. 8.16: Centerline temperature profiles for residence time variation experiments with catalyst shim C

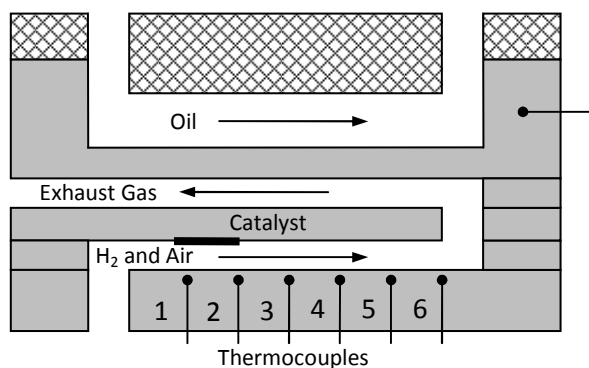


Fig. 8.17: Schematic of μ CHX with catalyst shim C

The temperature profiles for residence times of 7.8 ms, 9.2 ms and 11 ms, were very similar, likely due to their similar efficiencies (75.8 percent, 75.1 percent and 73.6 percent, respectively). These experiments had temperatures at the end of the combustion channel nearly equal to that of the outlet oil temperature. For all the experiments conducted, no combustion channel temperatures were measured below the outlet oil channel temperature. For residence times greater than 11 ms, higher combustion channel temperatures were measured.

The higher combustion channel temperatures at longer residence times were unexpected and were not observed for the variation of residence time experiments with shim B. The higher temperatures are more clearly observed by examining the temperatures at each location as a function of residence time, shown in Fig. 8.18. As previously discussed, these longer residence times resulted in lower efficiencies. Seemingly in contradiction to the variation of residence time experiments with shim B, the highest efficiencies were obtained with shim C at residence times with the lowest combustion channel temperatures. However, it is important to note that experiments with higher temperature profiles operated at lower heat inputs than were tested with shim B. This limits direct comparisons between the two residence time variation experiments. An additional difference is that the experiments with shim C had lower hydrogen conversion because they were more residence time limited than shim B due to the different catalyst lengths, as discussed in a later section (Section 8.7).

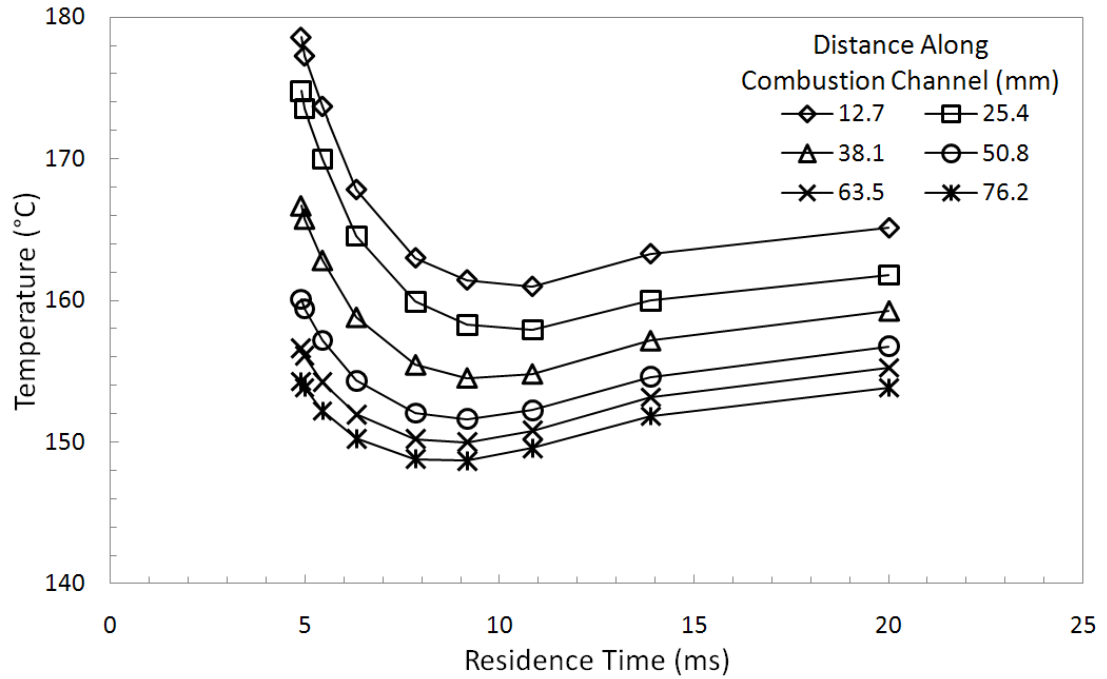


Fig. 8.18: Temperature variation along combustion channel at varying residence times with catalyst shim C

The cause of the increased temperatures cannot be conclusively determined because it was only observed for a limited set of data. A hypothesis is that the increase in temperatures is an artifact of very low heat inputs. These increasing temperature profiles were observed for less than 48 W of H_2 heat input. No experiments were conducted for shim B with heat inputs below this point, potentially explaining why the trend wasn't observed for shim B. In order to maintain the desired average oil temperature, the mass flow rate of the oil was reduced, resulting in increased heat transfer resistance to the oil. The heat transfer resistance to the oil can be represented as:

$$R_{oil} = \frac{1}{\dot{m}_{oil} c_{p,oil}} \quad (8.10)$$

where \dot{m}_{oil} is the oil mass flow rate, $c_{p,oil}$ is the oil specific heat and R_{oil} is the heat transfer resistance to the oil. The low mass flow rate of the oil at heat inputs less than 48 W caused greater heat transfer resistance to the oil, requiring greater combustion channel temperatures to drive heat transfer. The resistance to the oil could not be included in the

one-dimensional resistance model because the resistance to the oil encompasses the entire μCHX while the one-dimensional resistance model only considers a slice of the channel.

While performing experiments at lower residence times, it was difficult to achieve the outlet oil temperature required to obtain the desired average oil temperature of 85 °C. Again, the oil flow rate had to be substantially reduced in order to obtain a high enough outlet oil temperature. For the 20 ms experiment, the desired outlet oil temperature was not achieved so the average oil temperature was 83.5 °C instead. The substantial reduction in oil flow rate resulted in even less heat being captured by the oil, and consequently higher heat loss through the insulation. The trend of increased heat losses for longer residence times are shown in Fig. 8.19. Similar to the residence time experiments with shim B, the proportion of heat lost to the exhaust gas was small and nearly constant. The heat lost to uncombusted hydrogen was the most significant source of measured performance loss. The ratios of unmeasured heat losses were highest for the longest residence times.

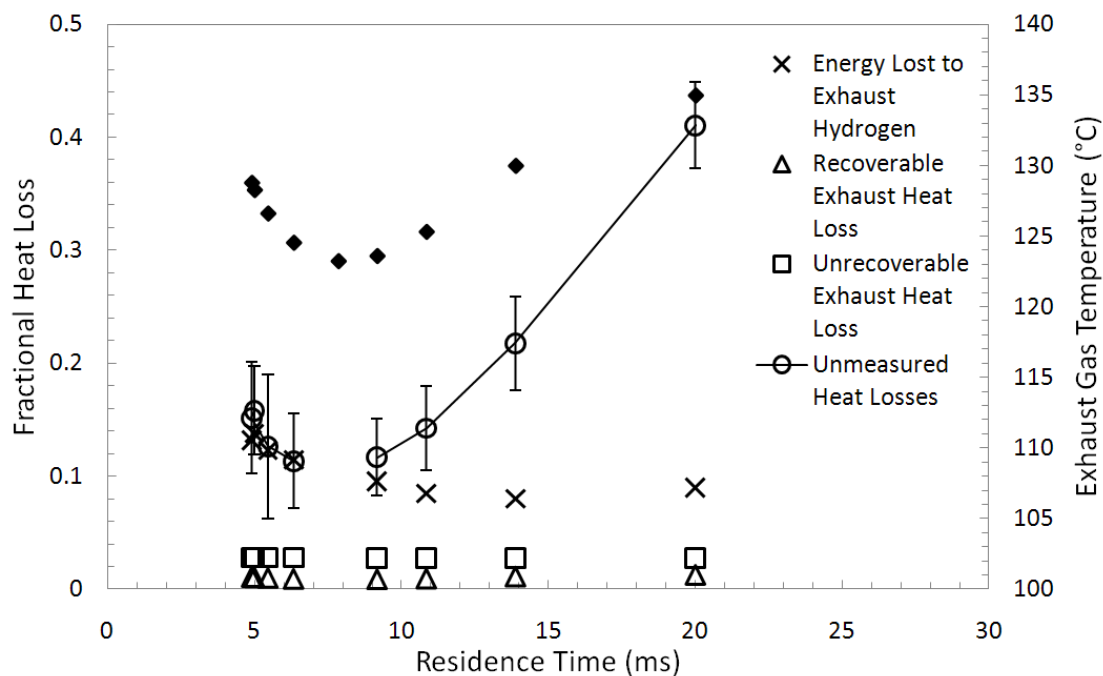


Fig. 8.19: Normalized heat loss for variation of residence time experiments with shim C

The slight increase in unmeasured heat losses for lower residence times were unexpected and seemingly contradict the results from the variation of residence time experiments with shim B and the simple resistance model. At the lower residence times, the primary source of heat loss was expected to be from uncombusted H_2 in the exhaust. A potential explanation is that the GC did not accurately characterize the H_2 concentration in the exhaust gas, instead reporting lower H_2 concentrations than was actually present in the sample bag. As discussed in Section 7.1.4, the hydrogen concentration was obtained in a less than ideal manner. The sample bags slowly leaked H_2 and the GC was not able to be calibrated over the full range of H_2 concentrations tested. While efforts were taken in the data analysis to remove the leakage uncertainty, the systematic error associated with a potentially inaccurate calibration may have biased the low H_2 conversion rates upward. Future investigations should incorporate a GC into the flow and ensure that the GC is calibrated over a much larger range.

The pressure drop as a function of H_2 heat input is shown in Fig. 8.20. As with catalyst shim B, the differential transducer was not able to obtain pressure measurements for the full range of pressures, so the inlet pressure is used to portray the pressure drop across the gas channels. As expected, inlet pressure increased linearly with increasing Reynolds number, with an inlet pressure of 67 kPa for an H_2 heat input of 144 W.

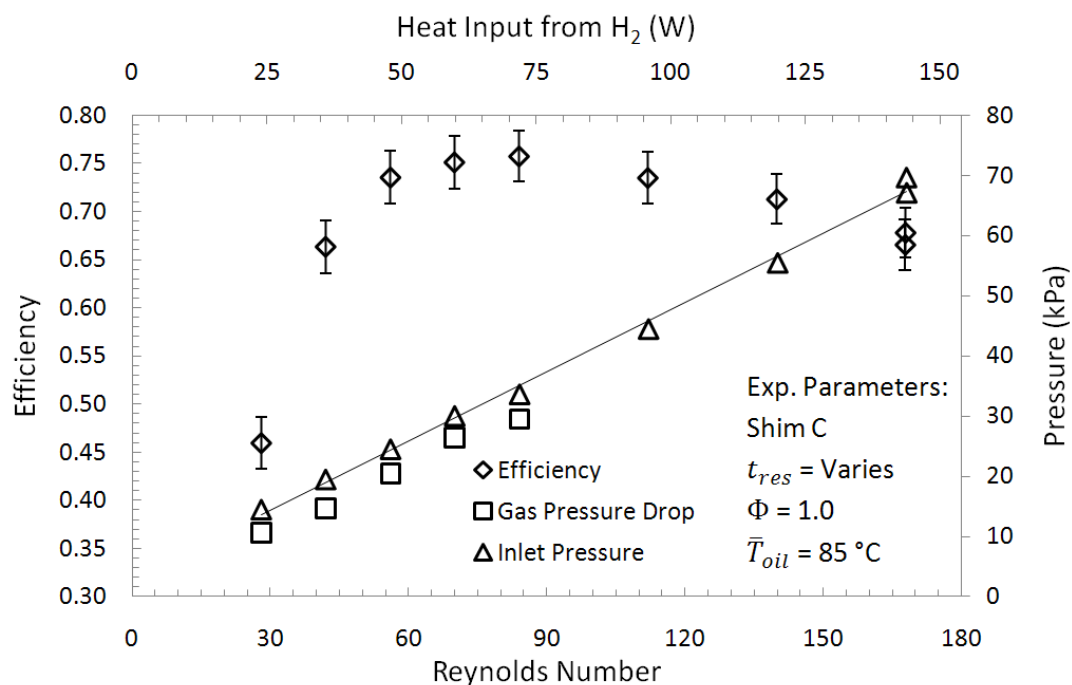


Fig. 8.20: Efficiency and pressure drop with catalyst shim C

8.5. Variation of Equivalence Ratio

The performance of the μCHX with catalyst shim B was tested for equivalence ratios between 0.3 and 1. The performance results are shown in Fig. 8.21. For these tests the combined flow rate of air and H₂ was maintained at 2700 sccm, resulting in residence times between 19 and 22 ms. The slight residence time variation is due to the differences in pressure and temperature at the inlet between experiments. The average temperature of the oil was maintained at $85 \pm 1\text{ }^{\circ}\text{C}$ for the variation of equivalence ratio tests.

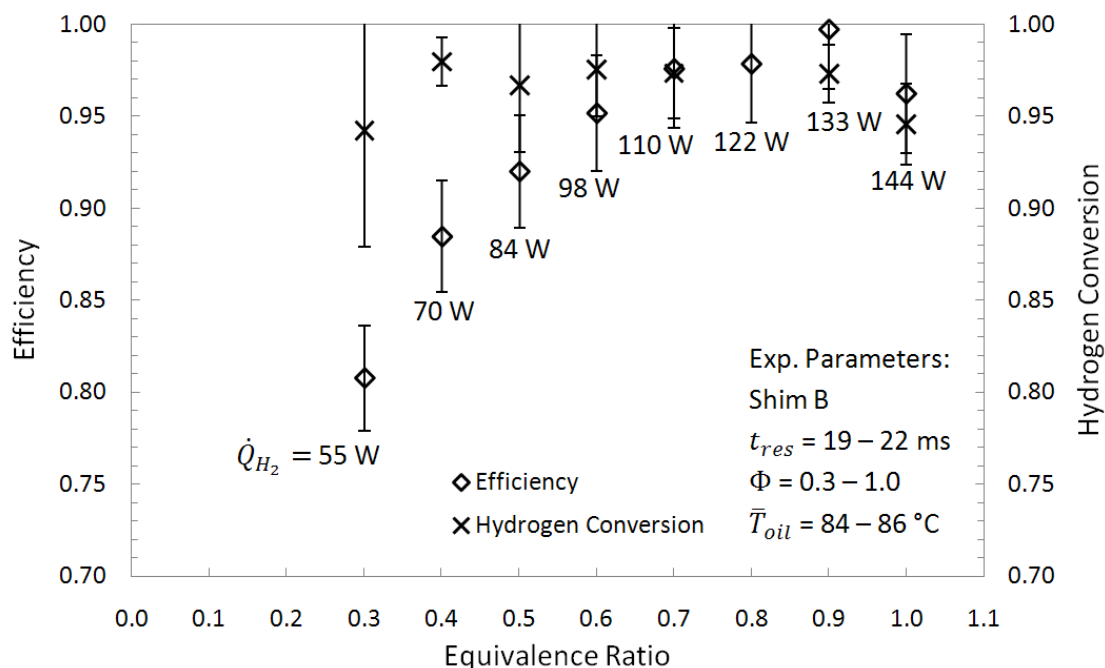


Fig. 8.21: μ CHX performance for equivalence ratio variation experiments with catalyst shim B

Increasing efficiencies were obtained for increasing equivalence ratios and the highest efficiencies were obtained for equivalence ratios between 0.7 and 0.9. Both efficiency and hydrogen conversion were lower at the stoichiometric equivalence ratio, indicating that a slightly lean mixture facilitates maximum conversion of H_2 . While the 99.7 percent efficiency obtained with an equivalence ratio of 0.9 is unreasonably high, the uncertainty range of ± 3.2 percent accounts for a lower, more reasonable performance. Again, if the oil properties were over represented by the manufacturer, as suggested by the unrealized heat loss analysis described in Section 8.4.1, then the actual efficiencies would be offset downward from the presented efficiencies toward the lower bound of the error bars.

Hydrogen conversion from the 0.8 equivalence ratio test was not determined because the GC was not available in the timeframe required for analyzing that particular exhaust gas sample. The hydrogen conversion for all other equivalence ratios was measured to be around 95 percent, supporting the conclusion that the performance of the μ CHX is not residence time limited at residence times around 20 ms. While there appears to be a slight reduction in hydrogen conversion at leaner equivalence ratios, the variation is well within the

uncertainty. The relatively large uncertainties for hydrogen conversion are due to the exhaust gas samples not being analyzed until six or seven days after being collected.

Temperature profiles for the variation of equivalence ratio tests are shown in Fig. 8.22. A schematic of the μ CHX with catalyst shim B is shown in Fig. 8.23 for reference. Again, the outlet oil temperature was maintained near 150 °C for all these tests in order to obtain the desired 85 °C average oil temperature. The magnitude of the temperature profiles tended to decrease with lower equivalence ratios. This was expected due to the lower hydrogen heat input at the lower equivalence ratios. However, different behavior occurs at equivalence ratios near unity, where the temperature profiles are nearly identical despite the different H_2 flow rates and equivalence ratios. Likely, the lower H_2 conversion at the stoichiometric equivalence ratio caused the actual heat release rate to be similar to the 0.9 equivalence ratio experiment, resulting in similar combustion channel temperature profiles.

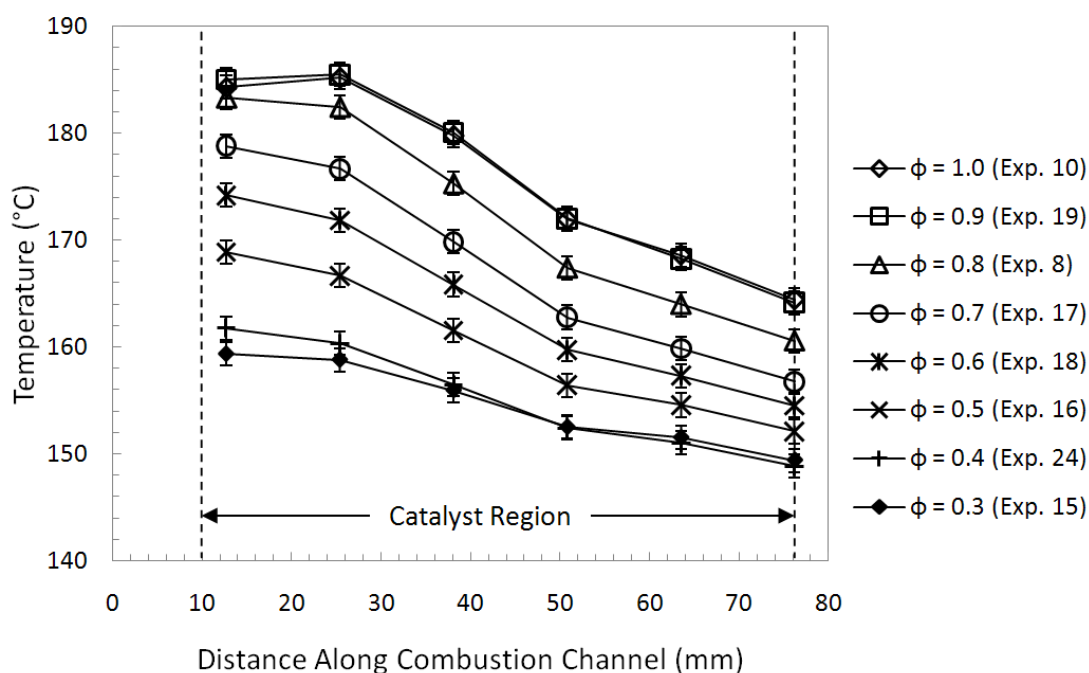


Fig. 8.22: Centerline temperature profiles for equivalence ratio variation experiments

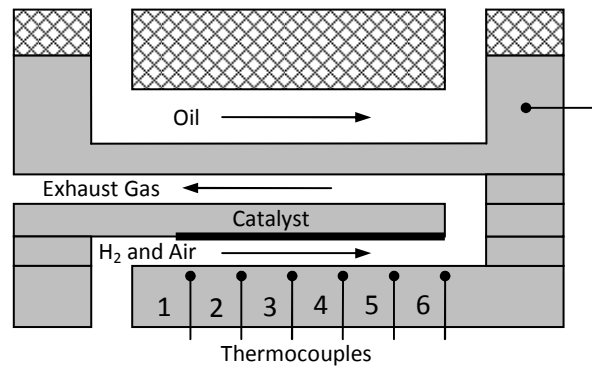


Fig. 8.23: Schematic of μ CHX with catalyst shim B

The trend of declining efficiencies for leaner equivalence ratios can be better understood by considering the heat loss components, shown in Fig. 8.24. The unrecoverable exhaust heat and the potentially recoverable exhaust heat both increase for decreasing equivalence ratios. The lean mixtures contain more air than is required for combustion and therefore carry away greater quantities of heat in the exhaust. Leaner equivalence ratios were found to operate with lower temperatures in the combustion channel, resulting in greater amounts of heat being lost through the insulation, as predicted by the resistance model.

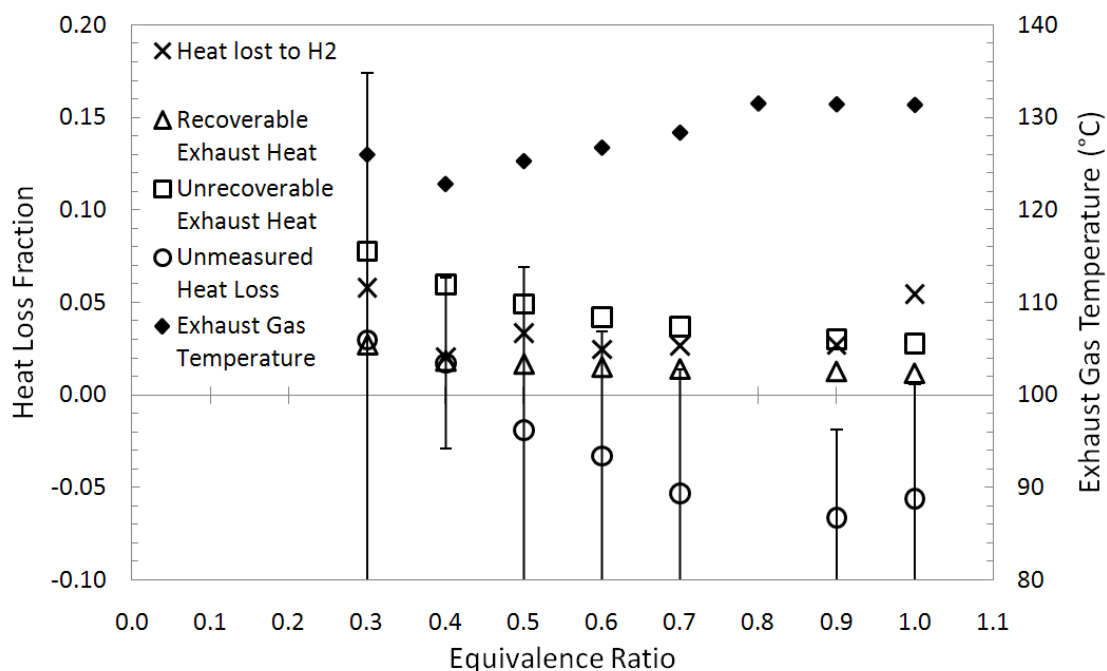


Fig. 8.24: Heat losses for variation of equivalence ratio experiments with shim B

The pressure drop is presented in Fig. 8.25 as a function of equivalence ratio. Total gas flow rate was held constant for these experiments, resulting in nearly constant Reynolds numbers, but the varying equivalence ratio resulted in different H_2 heat inputs. For all these experiments, the pressure drop was greater than could be measured with the differential pressure transducer, so the inlet pressure is used instead as an indicator of the pressure drop across the μ CHX. There were substantial inlet pressure variations between the different equivalence ratios with no discernable connection to any other measured parameter. The measurements were very stable with the calibration being the primary source of uncertainty (± 1 kPa), so this was not a factor. Further investigation is needed in order to determine the cause of such significant pressure variations for the same gas flow rate.

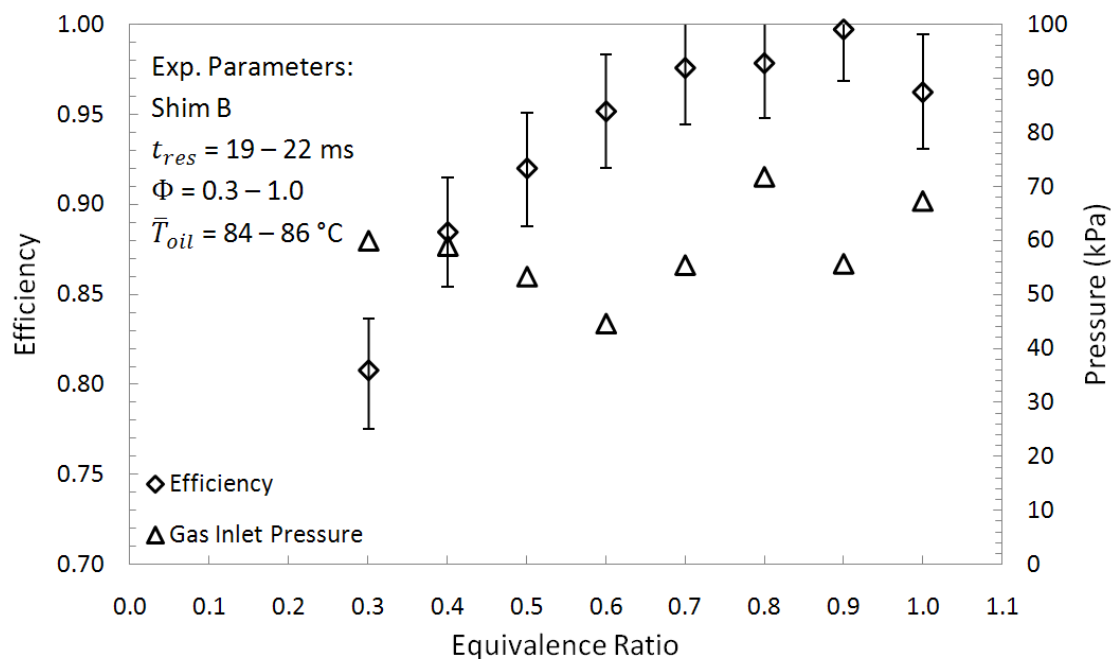


Fig. 8.25: Pressure drop for equivalence ratio tests with catalyst shim B

As discussed in section 8.1, the results from the CFD simulation by Ghazvini and Narayanan [1] are not directly comparable to the experimental results due to the different geometries and simplifications of the CFD model. However, the general trends can be compared and are presented in Fig. 8.27. The highest efficiencies were predicted to occur between equivalence ratios of 0.8 and 0.95, which is similar to what was obtained from the experiments. Stoichiometric equivalence ratios were also accurately predicted to have a slightly lower efficiency due to incomplete combustion. The experimental results indicated higher efficiencies for most equivalence ratios providing further indication that the efficiencies may be overstated, likely due to inaccurate oil properties.

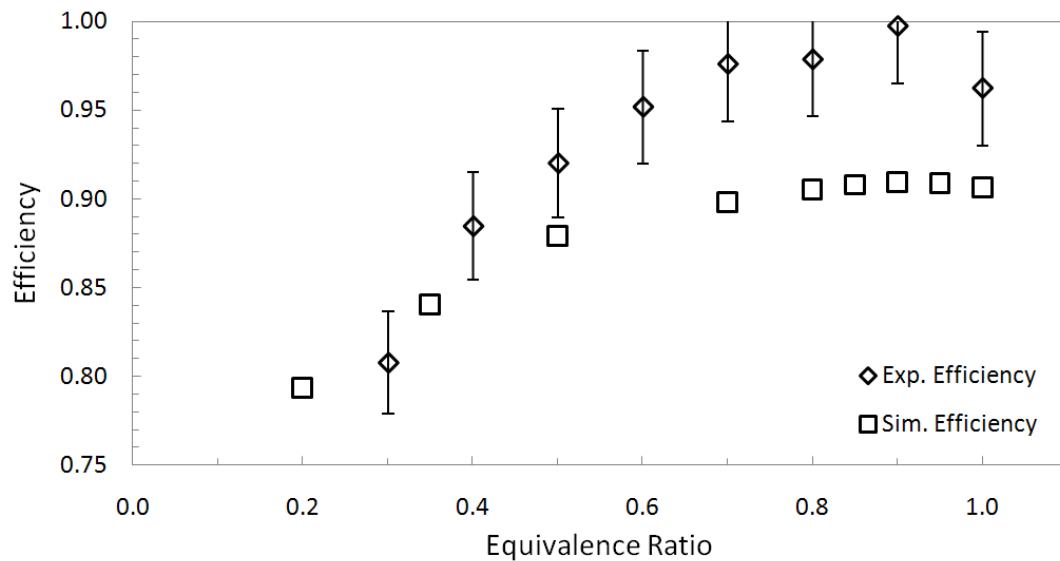


Fig. 8.26: Comparison of experimental equivalence ratio variation results with CFD simulation

8.6. Variation of Average Oil Temperature

The performance of the μ CHX was investigated at various average oil temperatures. Residence time and equivalence ratio were fixed around 21 ms and 1.0, respectively. The efficiency results of these tests are shown in Fig. 8.27. For these experiments, the oil flow rate was adjusted until the desired average oil temperature was obtained. The full temperature range possible with the current experimental setup was investigated. If the inlet oil temperature could be controlled, higher (respectively lower) inlet oil temperatures would allow for higher (lower) average oil temperatures to be investigated. For the fixed oil inlet temperature around 20 °C that was tested, average oil temperatures less than about 63 °C were found to result in exhaust gas temperatures below 100 °C. This was considered undesirable because it would allow the water vapor in the exhaust to condense inside the μ CHX. Average oil temperatures above 105 °C would cause the outlet oil temperature to exceed the 204 °C temperature limit of the PFA tubing.

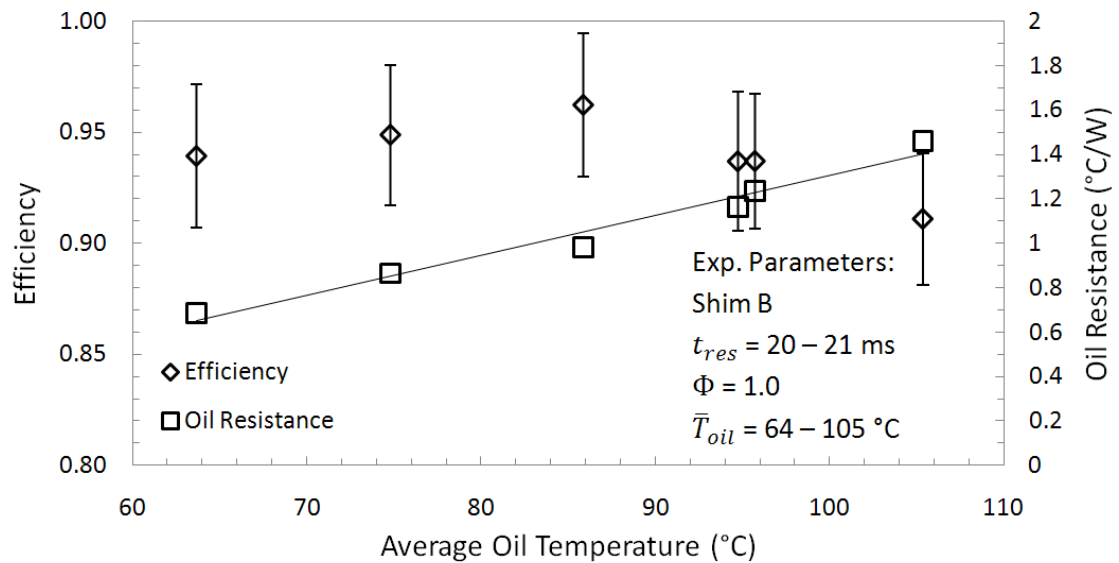


Fig. 8.27: Effects of average oil temperature variation with catalyst shim B

Efficiencies above 90 percent were obtained for all average oil temperatures tested. Variation in the average oil temperature was found to have a minimal effect on the efficiency of heat transfer to the oil. While the trend is mostly within the uncertainty bands, the peak efficiency of 96.2 percent was obtained at an average oil temperature of 85 °C and indicates reduced efficiencies for either higher or lower average oil temperatures. A slight decrease in efficiency for higher oil temperatures is reasonable because one would expect higher heat losses for higher oil temperatures. Also, lower oil mass flow rates were necessary in order to obtain the higher average oil temperatures, resulting in greater heat transfer resistances to the oil (as described in the previous section). This greater resistance also contributes to the lower efficiencies obtained at higher average oil temperatures. Decreased efficiencies for increased oil temperatures do not contradict the one dimensional heat loss model because that model assumed a constant oil temperature. Data for hydrogen conversion were not obtained for the variation of average oil temperature experiments due to limited access to the gas chromatograph.

The temperature profiles along the combustion channel for the variation of average oil temperature experiments are shown in Fig. 8.28. A schematic of the μ CHX with catalyst shim B is shown in Fig. 8.29 for reference. The profile shapes are similar, but offset due to the

different oil temperature conditions. As expected, higher combustion channel temperatures correspond to higher average oil temperatures.

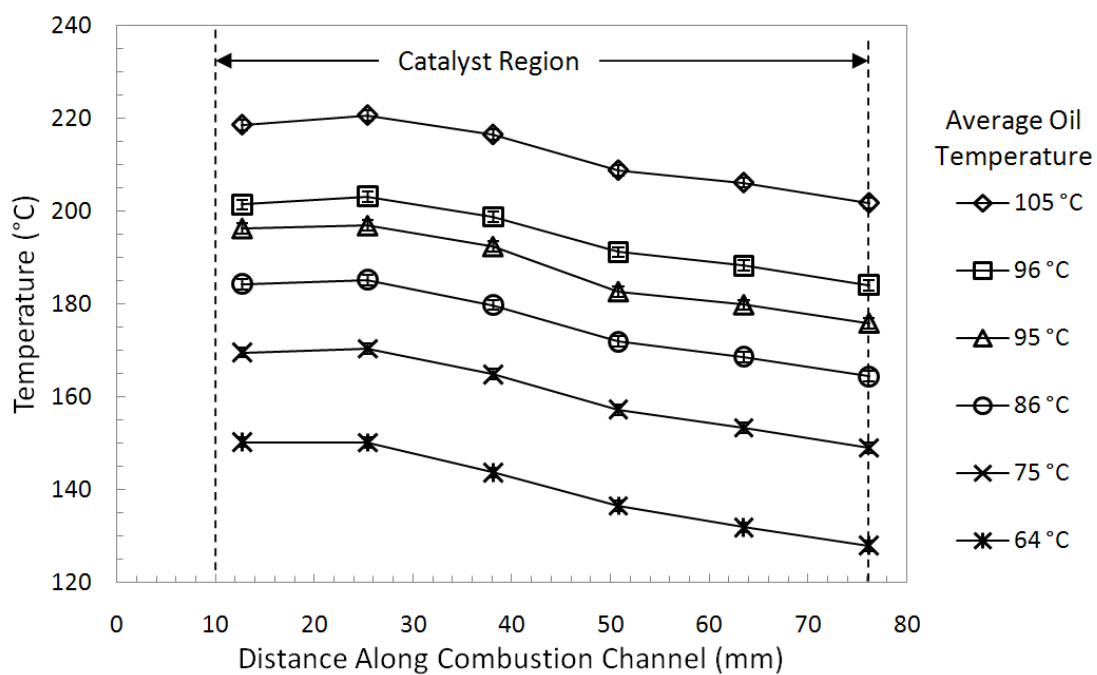


Fig. 8.28: Centerline temperature profiles of average oil temperature variation experiments

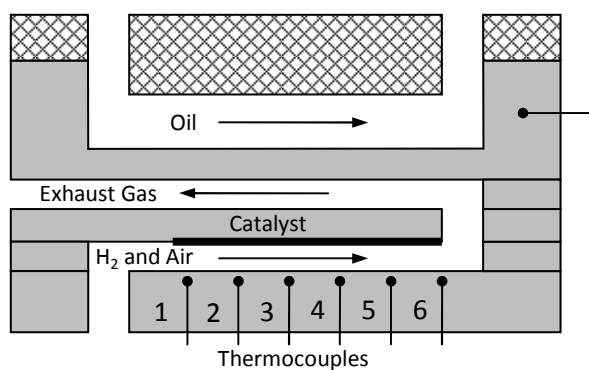


Fig. 8.29: Schematic of μ CHX with catalyst shim B

8.7. Variation of Catalyst Length

In this section, experiments with different catalyst lengths are compared in order to illustrate the variation of catalyst length while holding other parameters constant. Examining performance impact for varied catalyst lengths is important in order to minimize the amount of catalyst required. The performance of the μ CHX was investigated for two different catalyst lengths, 20 percent and 87 percent of the channel length. The variation of residence time experiments previously presented used the different catalyst lengths to investigate a wider range of residence times than could be obtained with a single catalyst length. Results on residence time variation did not include a direct comparison of the two catalyst lengths due to the different hydrogen heat input rate at the same residence time. However, three experiments were conducted that compare the effects of varying catalyst length and are listed in Table 8.5. Experiment 10 and exp. 27 are compared on the basis of similar hydrogen heat input while exp. 10 and exp. 33 are compared on the basis of similar residence time.

Table 8.5: Variation of catalyst length experiments

Exp. #	Cat. Shim	l_{cat} (mm)	$\frac{l_{cat}}{L_{channel}}$ (%)	Φ	H ₂ Heat Input (W)	t_{res}	Avg. Oil Temp. (°C)	Hydrogen Conversion (%)	Efficiency (%)
10	B	66.0	87	1	144	21	85.9	96.2	96.2
27	C	15.2	20	1	144	4.9	85.3	87.6	67.8
33	C	15.2	20	1	24	20	83.5	91.2	45.9

A comparison between the combustion channel temperature profiles of exp. 10, exp. 27 and exp. 33 is shown in Fig. 8.30. Schematics of μ CHXs with the different catalyst lengths are shown for reference in Fig. 8.31.

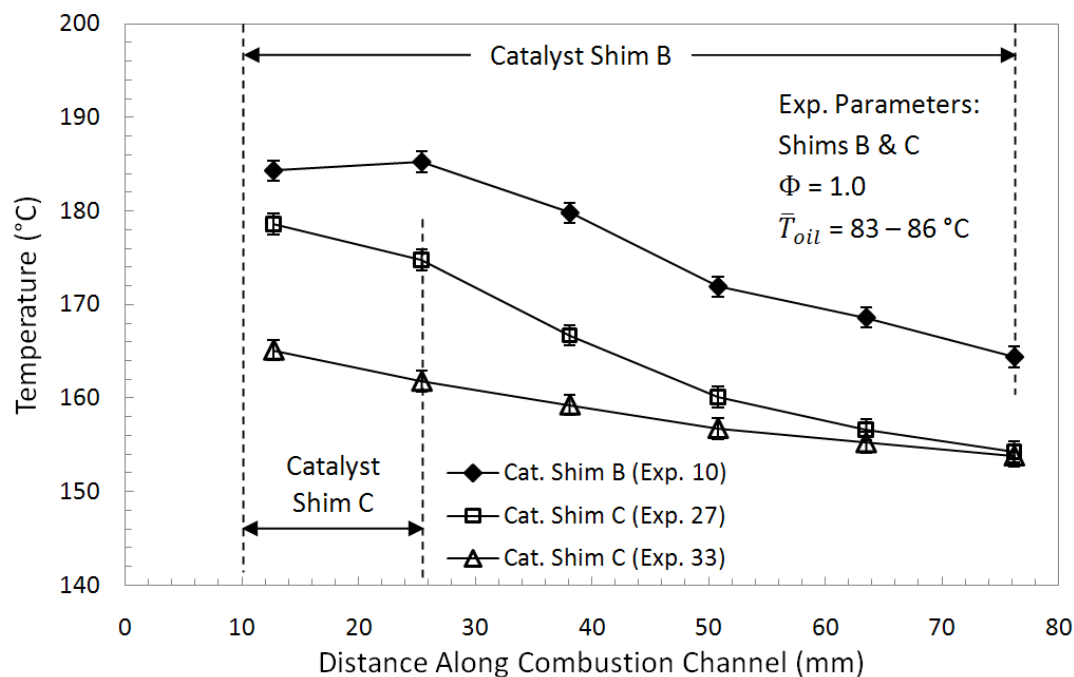


Fig. 8.30: Centerline temperature profile comparison between catalyst shim B and C

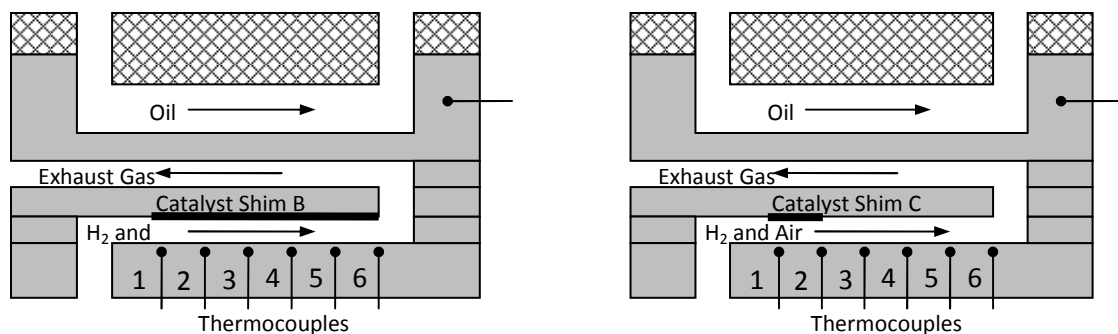


Fig. 8.31: Schematics of μ CHX's with catalyst shims B and C

First, the variation of catalyst length will be considered for constant H_2 heat input. Efficiency and H_2 conversion were both higher for the longer catalyst length of exp. 10, compared to exp. 27. The residence time was also higher for experiment 10, allowing more time for the combustion reaction to occur thereby resulting in higher H_2 conversion. Higher H_2 conversion contributed to increased efficiency, as shown in Table 8.5. Also, the temperature profile of

exp. 10 is 11 °C higher over the whole channel than the temperature profile of exp. 27. According to the heat loss resistance model, these increased temperatures would also contribute to the higher efficiency. Also of interest, exp. 10 (shim B) shows a slight temperature increase from location 1 to location 2, while exp. 27 (shim C) shows a temperature decrease. Catalyst is located over these thermocouples in both experiments, so it was expected that similar temperature profiles would be obtained for thermocouples 1 and 2 due to the similar anticipated heat release there. Based on the results of the variation of residence time experiments, it was concluded that the μ CHX is residence time limited at a residence time of 5 ms. As a result, H_2 would still be combusting at the end of the catalyst for shim C and would be expected to cause higher temperatures there. This could be due to a difference between the catalyst activity of each shim, despite the careful efforts to prepare the catalyst consistently for shims B and C. As it stands, the cause of this temperature decrease is unknown.

Experiments 10 and 33 are compared on the basis of similar residence time. Both experiments operated with high H_2 conversions of 96.2 percent and 91.2 percent, respectively. However, the combustion channel temperatures were much lower for exp. 33 due to the smaller H_2 heat input. The lower combustion channel temperatures contributed to decreased efficiency, causing a greater portion of the heat released from combustion to be lost through the insulation, as shown in Table 8.6. The inlet pressure was very similar between the two experiments that operated at the same hydrogen heat input rate.

Further investigation is needed with additional catalyst lengths in order to better characterize the effects of catalyst length on the performance of the combustor. Furthermore, repeatability experiments should be conducted with catalyst shims of the same length in order to quantify the repeatability of the catalyst deposition method.

Table 8.6: Heat losses and inlet pressures for variation of catalyst length experiments

Exp. #	Cat. Shim	$\frac{l_{cat}}{L_{channel}}$ (%)	H ₂ Heat Input (W)	t_{res}	Energy Lost to H ₂ (%)	Unmeasured Heat Loss (%)	Efficiency (%)	Inlet Pressure (kPa)
10	B	87	144	21	5.5	-5.6	96.2	67.3
27	C	20	144	4.9	13.2	15.1	67.8	67.1
33	C	20	24	20	9.0	41.1	45.9	14.4

8.8. Variation of Catalyst Position

Experiments examining the effects of varied catalyst position were conducted with shim C installed in different locations in the μ CHX. Schematics of the μ CHX with shim C in the standard position and with shim C mounted in a reversed position (shim C-rev) are shown in Fig. 8.32. Mounting shim C in the reversed position placed the catalyst shim directly above the thermocouples allowing the temperature of the catalyst to be measured about 1.25 mm below the catalyst surface. The positions of the catalyst along the combustion channel are listed in Table 8.7. A drawback of shim C-rev was that by having the catalyst directly above the thermocouples, additional heat was expected to be lost due to conduction to the μ CHX body that wasn't a factor for the experiments with shim C in the standard position.

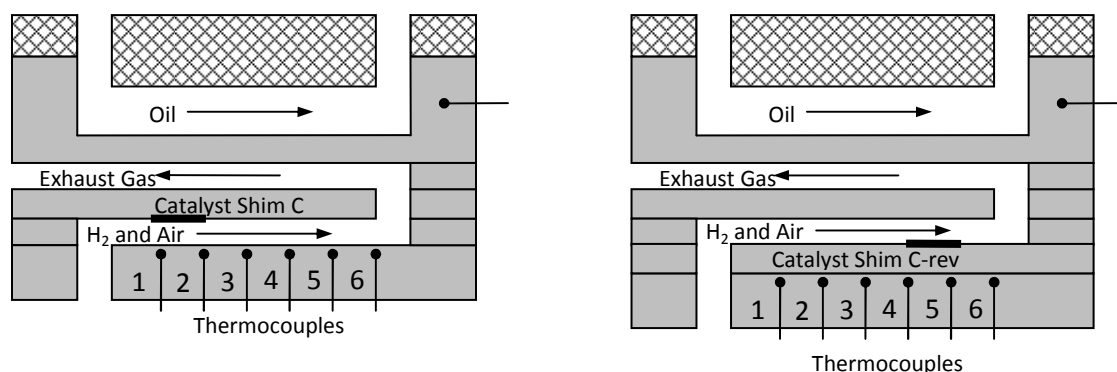
Fig. 8.32: Schematics of μ CHX's with catalyst shims C and C-rev

Table 8.7: Catalyst positions for variation of catalyst location experiments

Catalyst Shim	Entry Length (mm)	Catalyst Length (mm)
Shim C	10.2	15.2
Shim C-rev	50.8	15.2

The impact of catalyst position was investigated by comparing variation of residence time experiments for both catalyst positions, shown in Fig. 8.33. The average oil temperature of the experiments with shim C and C-rev were 85 and 90 °C, respectively. A higher average oil temperature had to be implemented for the experiments with shim C-rev in order to obtain exhaust temperatures above 100 °C. As demonstrated in the variation of average oil temperature experiments (See Section 8.6), changes in average oil temperature have a minor impact on the resulting efficiencies. Experiments with shim C-rev showed similar trends as shim C for efficiency and H₂ conversion, but offset lower. Longer residence times resulted in greater H₂ conversion over the full range of residence times considered. The highest efficiency for shim C-rev was observed to be 65.3 percent at 7.5 ms, compared to 75.8 percent efficiency at 7.8 ms for shim C. Maximum H₂ conversion for shim C-rev was 89.1 percent, compared to 92.4 percent for shim C. Differences in measured H₂ conversion was unexpected, as the catalyst was exactly the same between the experiments. Also, the combustion gases would have been preheated to a higher temperature, which also should have improved hydrogen conversion. The most probable explanation for this behavior is that the catalyst was damaged during disassembly and subsequent reassembly, despite the care that was taken to avoid this.

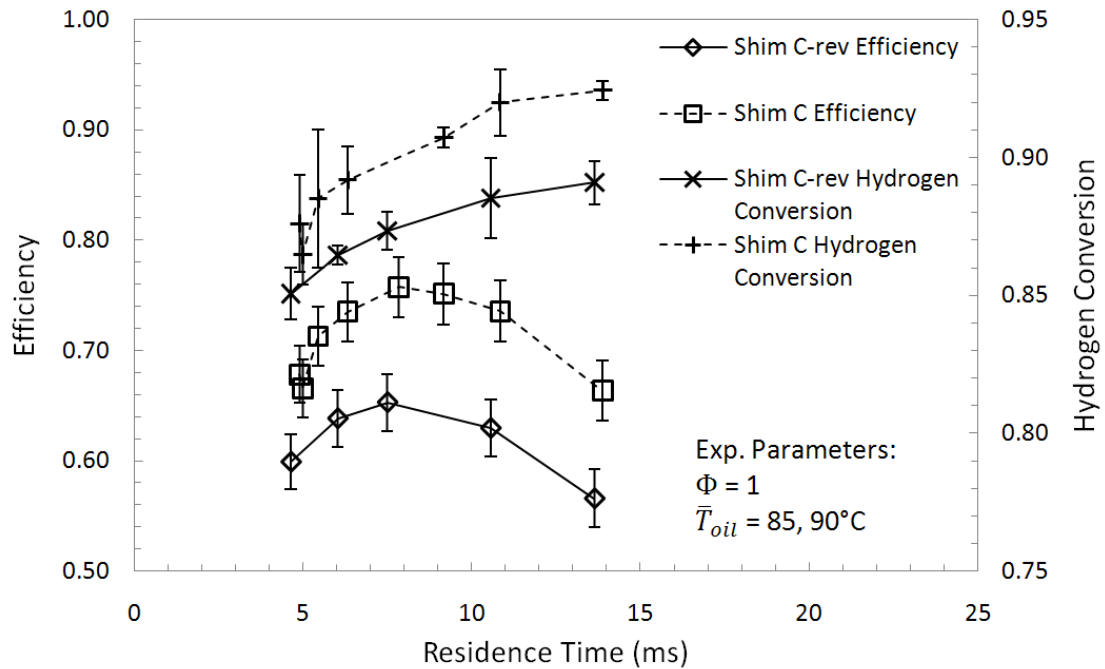


Fig. 8.33: Effect of catalyst position variation

The lower efficiency of shim C-rev may be due to the increased resistance to heat transfer through the combustion channel and reduced resistance to conduction through the body of the μCHX . The initial increase in efficiency for shim C-rev with increasing residence time is due to the corresponding increase in H_2 conversion. The decreasing efficiencies with increasing residence time for shim C-rev after 7 ms are likely due to the same causes as for the variation of residence time experiments conducted with shim C, previously discussed in Section 8.4.2.

Heat losses and exhaust gas temperatures for shim C-rev and shim C are shown in Fig. 8.34. Longer residence times coincide with lower heat input from hydrogen and were found to result in greater proportions of heat loss at residence times longer than 9 ms. As expected, the heat losses for shim C-rev are consistently greater than for shim C, likely due to the catalyst shim being located directly against the stainless steel base. Also, the exhaust gas temperatures were found to be much lower with shim C-rev than for shim C. However, note that the recoverable heat loss fraction to exhaust is minimal for the range of temperatures tested, as discussed in Section 8.4.1.

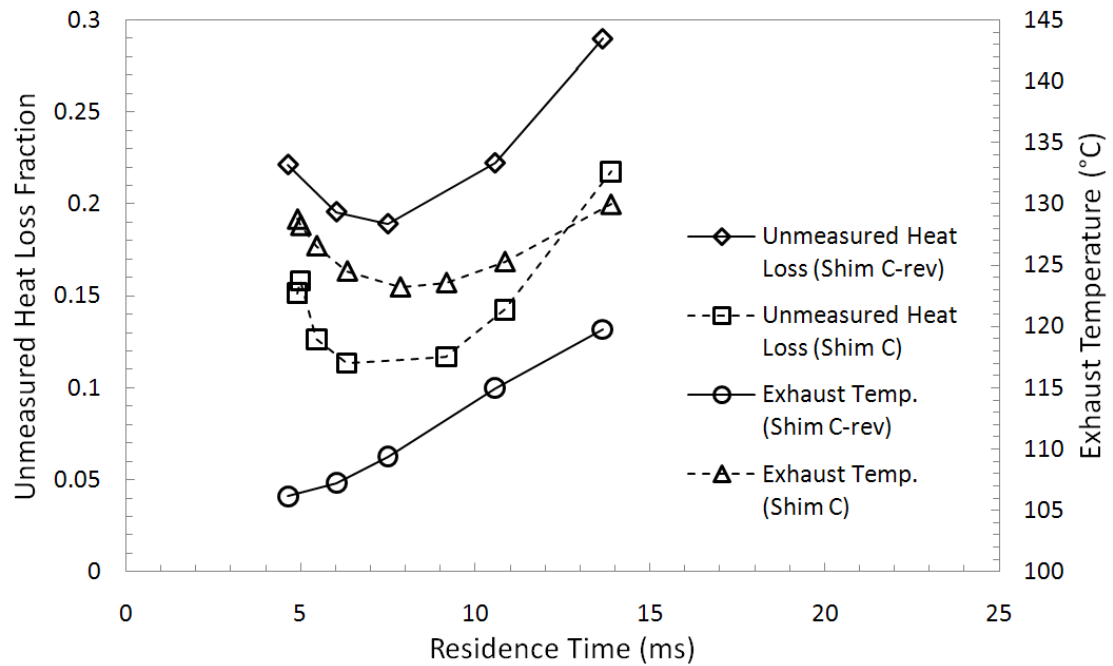


Fig. 8.34: Heat loss for variation catalyst position experiments

The highest temperatures were consistently observed at the catalyst, with both thermocouples in the catalyst region indicating similar temperatures, as shown in Fig. 8.35. It is notable that the highest catalyst temperatures observed are about 500 °C lower than those reported by Norton et al. [12] for H₂ combustion in a microchannel with a similar wall material. Their combustor was fully insulated with no heat exchanger elements, so these lower temperatures indicate the significant reduction in catalyst temperatures observed in the μ CHX design.

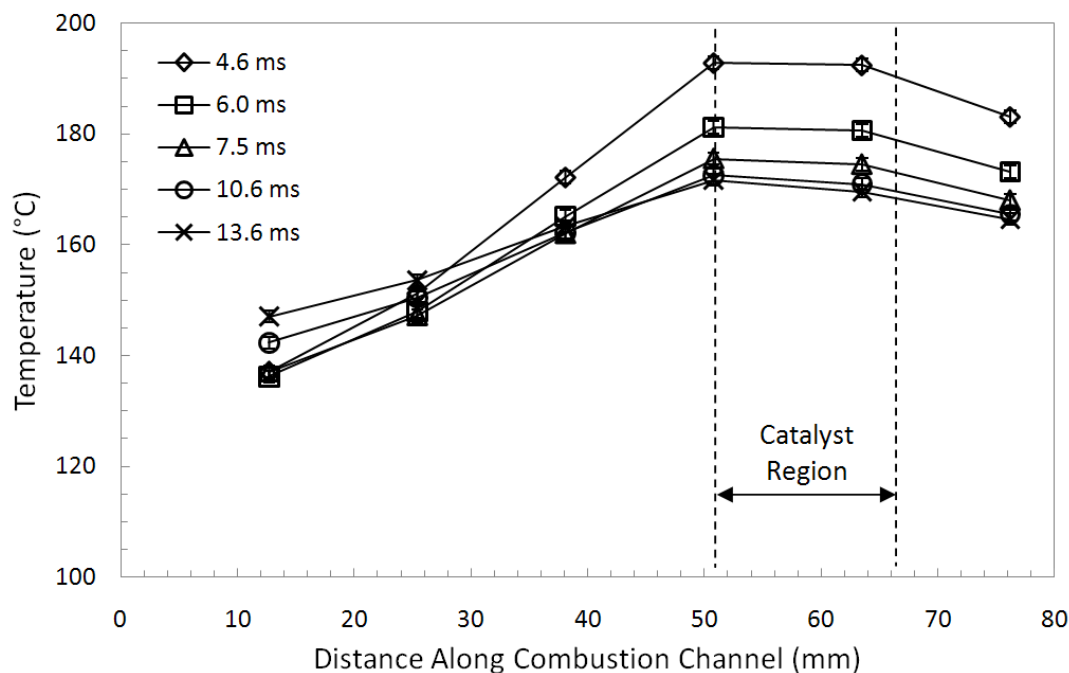


Fig. 8.35: Temperature profiles for residence time variation experiments with shim C-rev

The combustion channel temperatures near the inlet were observed to increase for increasing residence times. These increasing temperatures can more clearly be seen in Fig. 8.36, which plots temperature variation as a function of residence time directly. The temperatures measured by the first two thermocouples increased for residence times longer than 7.5 ms while the temperature at the other locations remained nearly constant. Both the oil and gases enter the μ CHX and are heated as they proceed along their respective channels. Similar trends would be expected for shim C; however, they were not observed due to the lack of thermocouples in the preheat region prior to the catalyst.

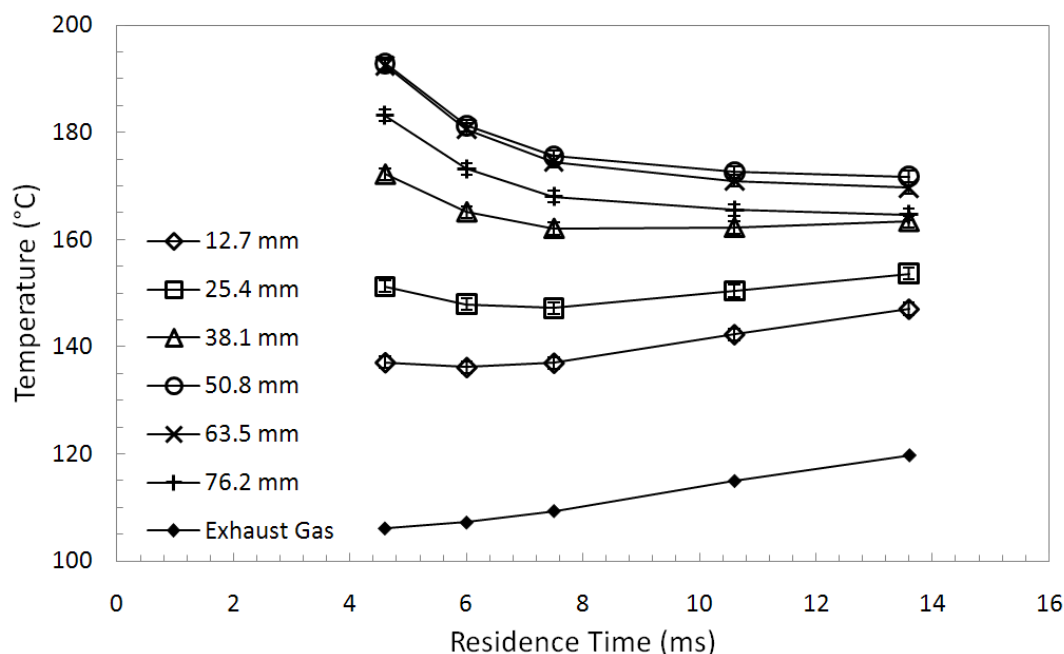


Fig. 8.36: Temperature variation along combustion channel at varying residence times with catalyst shim C-rev

The temperature profiles measured for shim C and shim C-rev at similar residence times are compared in Fig. 8.37. The temperatures in the catalyst region for shim C-rev were higher than the temperatures in the catalyst region for the shim C experiments, likely due to the catalyst being closer to the thermocouples. Having the catalyst located near the end of the combustion channel would be expected to result in higher efficiencies due to the greater temperature differences between the oil and the combustion gases over the whole channel length. Such a configuration should result in thermal profiles more similar to that of a traditional counter-flow heat exchanger. The high temperatures near the inlet for shim C are more similar to a co-flow heat exchanger and therefore would be expected to operate at lower efficiencies. Also, the increased temperatures along the combustion channel for shim C-rev are caused by increased preheating of the inlet gases.

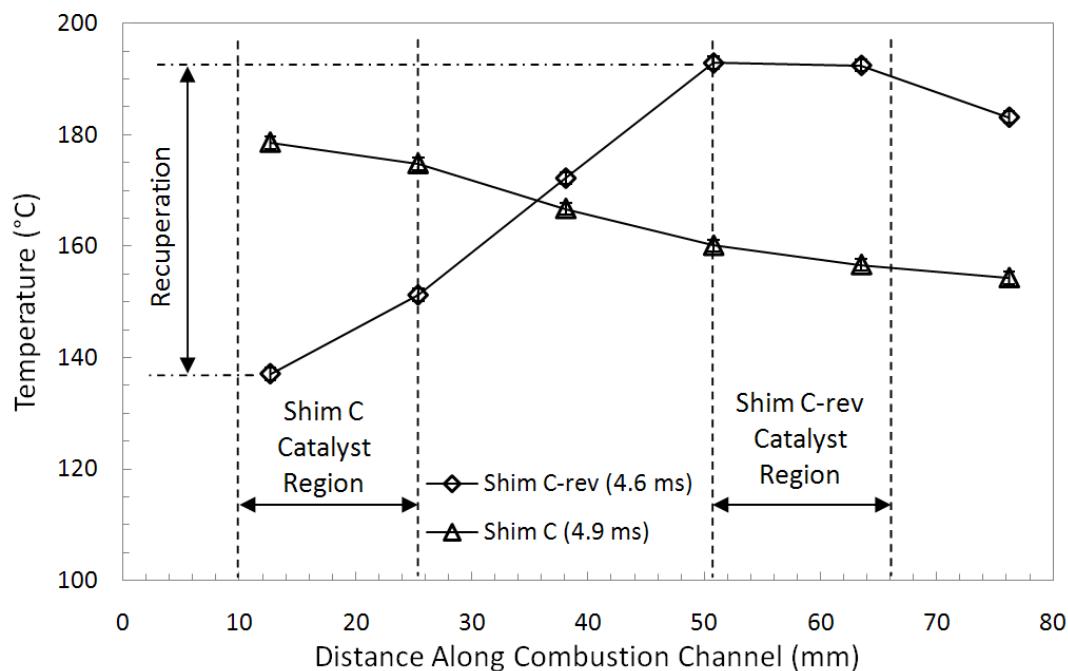


Fig. 8.37: Centerline temperature profiles of variation of catalyst position experiments

The inlet pressure variation for shims C and C-rev are shown in Fig. 8.38. Inlet pressures were consistently higher for the experiments conducted with shim C than for shim C-rev. The lower pressures may be the result of less complete combustion; however, this cannot be conclusively determined with the available data.

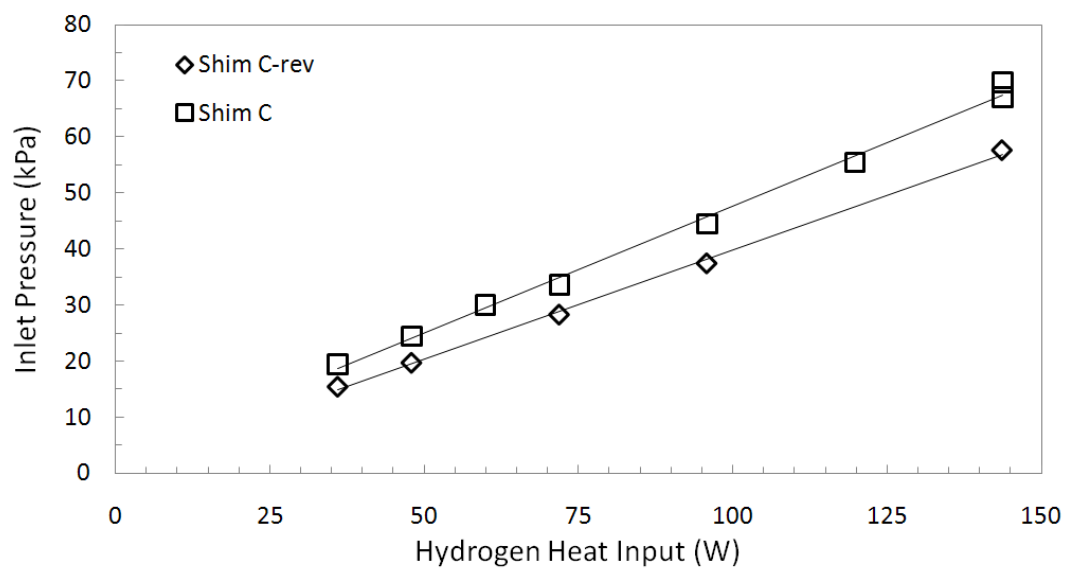


Fig. 8.38: Inlet pressure for variation of catalyst position experiments

9. PRELIMINARY DESIGN OF A LARGE ARRAY COMBUSTOR HEAT EXCHANGER

The unit cell design concept must be scaled up in order to meet the heat generation requirements of a hydrogen storage system. The hydride hydrogen storage materials are still an active field of research, so the exact requirements for the combustor have yet to be fully defined. As a point of comparison, the Sandia combustor [7] was a 30 kW design and was designed for a vehicle scale demonstration hydrogen storage system using sodium alanate [50]. The design of a preliminary large array CHX is presented in this section and is based on scaling the unit cell design with the 90 percent efficiency presented in Chapter 8.

9.1. Design Considerations

There were a few design considerations in scaling up the unit cell design into a large array CHX:

- Unit cell concept must be maintained
- Scaling is performed by numbering up the unit cell
- Uniform flow distribution through all unit cells
- Pressure drop on the gas side should be minimized
- There should be no unsupported spans

Uniform flow of gases and oil is desired through each of the unit cells is a necessity in order for the CHX to perform as designed. Non-uniform oil flow could result in hot spots inside the combustor, potentially burning the oil or causing internal damage. Non-uniform gas flows would potentially cause hot spots in some areas or result in incomplete combustion due to higher residence times than designed for. The full size design was developed under the working assumption that the device would be fabricated by chemically etching shims and diffusion bonding them together. This introduced the design constraint that there could be no unsupported spans in order to distribute the pressure during the diffusion bonding. Schematics of supported and unsupported spans are shown in Fig. 9.1. The unsupported spans will not bond properly, allowing fluids to leak between the channels.

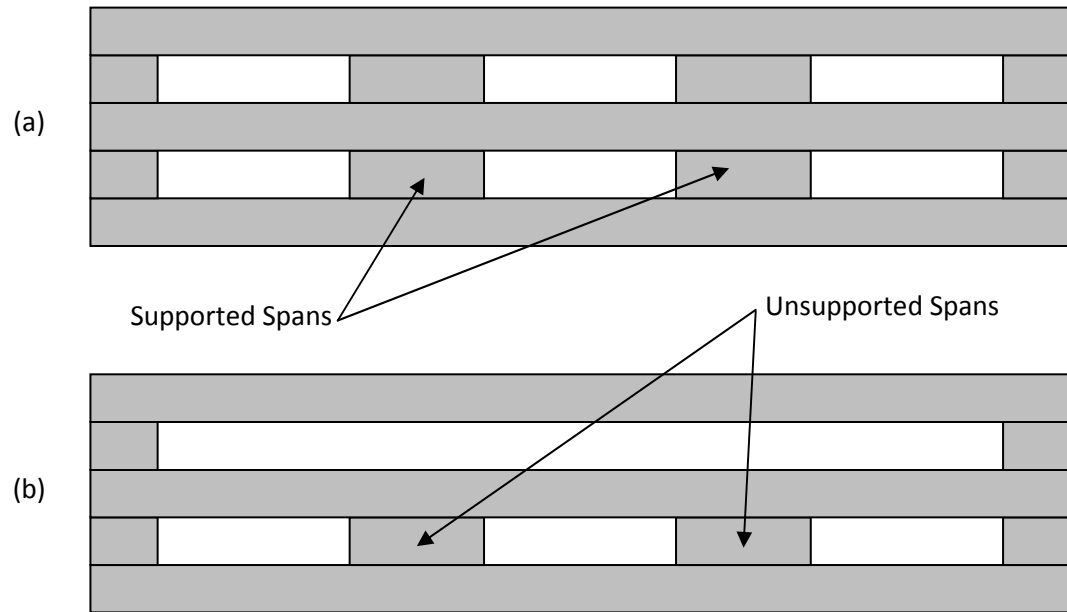


Fig. 9.1: Schematics of (a) supported spans and (b) unsupported spans

9.2. Channel Arrangement

Scaling up the unit cell design for multiple channels resulted in the channel arrangement shown schematically in Fig. 9.2 as the cross-section of a 3 x 2 unit cell layout. A recuperator channel is located between each combustion channel and oil channel in a counter flow configuration. Instead of having two oil channels between each set of recuperator channels, they are merged into a single oil channel.

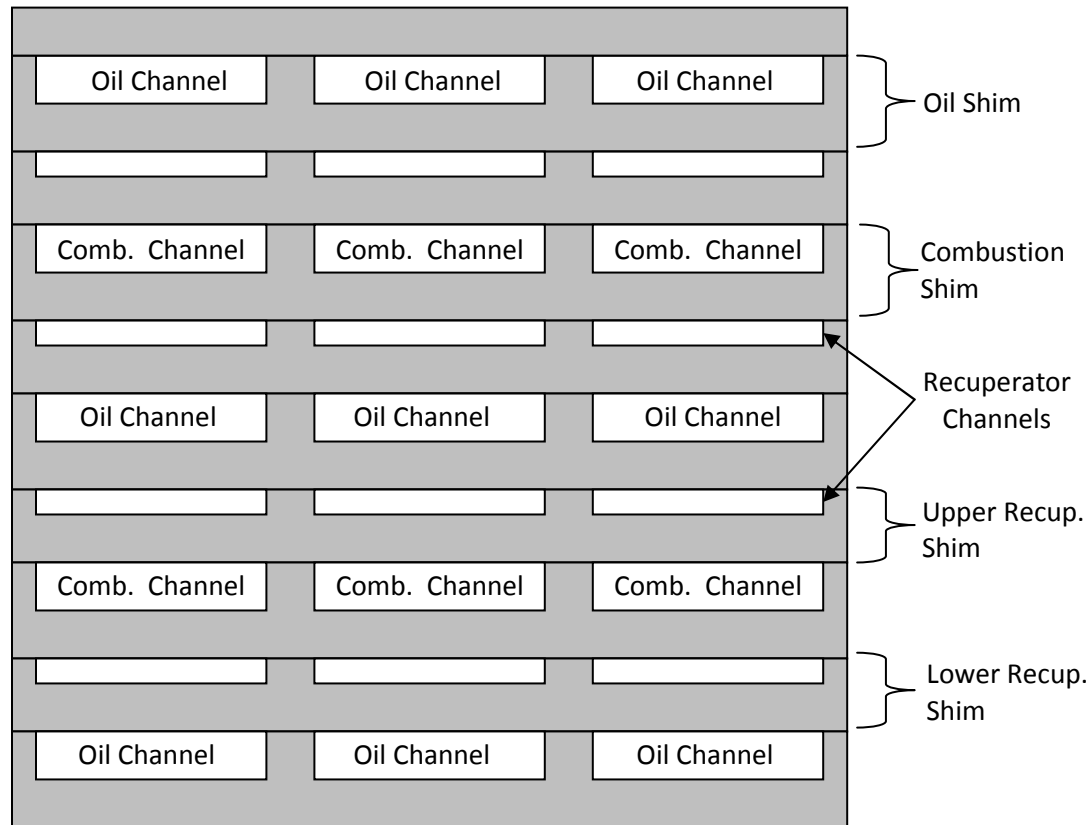


Fig. 9.2: Full size CHX channel arrangement (Cross-section)

When designed as shims, four distinct shim patterns are obtained: oil shims, upper recuperator shims, combustion shims and lower recuperator shims. These shims are identified in Fig. 9.2 and Fig. 9.3. A shim stack with one of each type of shim results in a single unit cell in height with multiple unit cells in width. An assembly with multiple shim stacks then increases the number of unit cells in the vertical direction. The recuperator shims are separated into lower and upper shims in order to incorporate the flow path from the combustion channel to the recuperator. A side profile of a two-shim stack is shown schematically in Fig. 9.3.

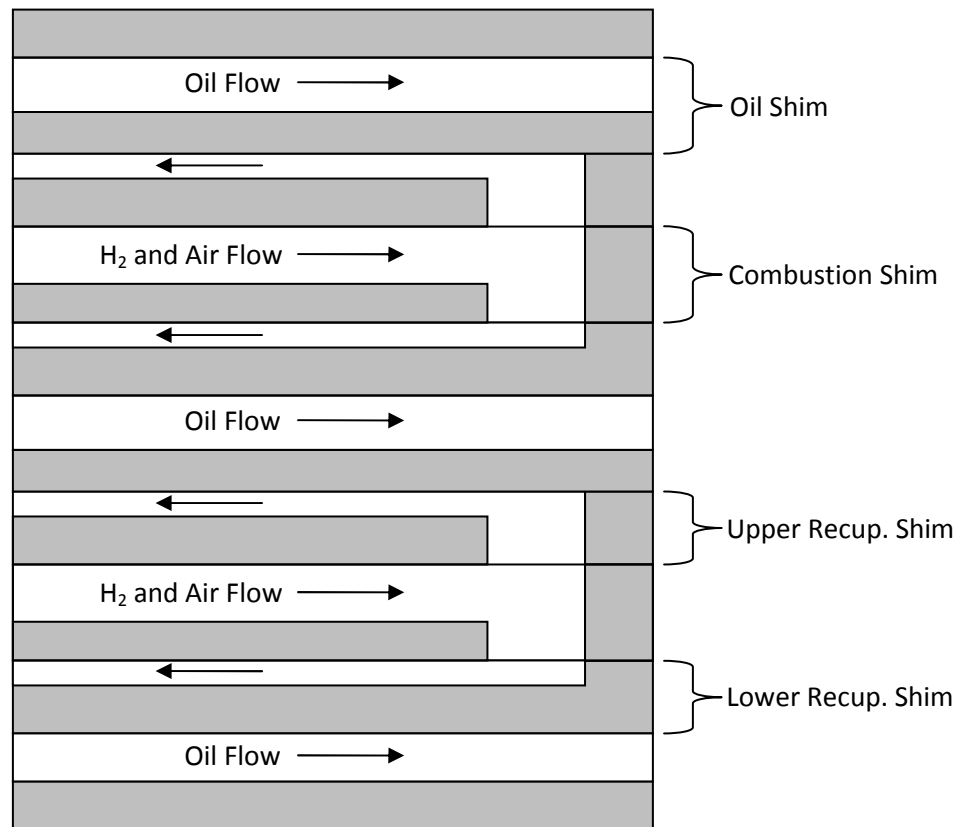


Fig. 9.3: Side profile of shim stackup

9.3. Internal Fluid Distribution and Optimization

The primary challenge that arose in the development of this design was in distribution of the fluid streams to the individual unit cells. A complex fluid header system was required. The headers were designed seeking to provide uniform flow to all channels with consideration for the anticipated pressure drop. As a preliminary approach, the internal headers were designed to maintain a constant flow area. For example, if a single header was feeding 10 channels, then the cross-sectional area of the header was designed to be 10 times greater than the cross-sectional area of the channel. For laminar flow and all other factors constant, the pressure drop increases greatly for smaller hydraulic diameters according to the Hagan-Poiseuille equation:

$$\Delta P \propto \frac{\mu L \dot{V}}{D_H^4} \quad (9.1)$$

where μ is the dynamic viscosity of the fluid, L is the length of the channel, \dot{V} is the volumetric flow rate and D_H is the hydraulic diameter of the channel. Based on this equation, the small channels will have a much higher pressure drop than the headers. This relatively high pressure drop across the channels, compared to the headers, will help equalize the flow rate through each channel. While this constant flow rate approach does not guarantee optimal flow distribution, it was used here with the understanding that a more robust technique (such as CFD) would be used to optimize the design in the future.

An Excel® worksheet was developed in which the parameters of the design could be varied in order to determine the overall size of the combustor for a given heat capacity. The worksheet is provided in Appendix I. The design was developed with a channel width of 10mm, a channel length of 30 mm, and a channel height of 0.3 mm. It was assumed that a positive displacement pump with a high pressure capacity would be used for the oil, making the pressure drop a minimal concern. Based on this assumption, an exception to the header flow area requirement was made for the oil headers, where header area was reduced by a factor of two.

A variety of header designs were considered in order to minimize the size of the device. Initially, a header design was considered in which the fluids were supplied laterally, taking advantage of the rows of similar fluids in each shim. A schematic of the lateral header design is shown in Fig. 9.4. However, this significantly increased the size of the combustor because the constant flow area constraint forced the headers to be very long.

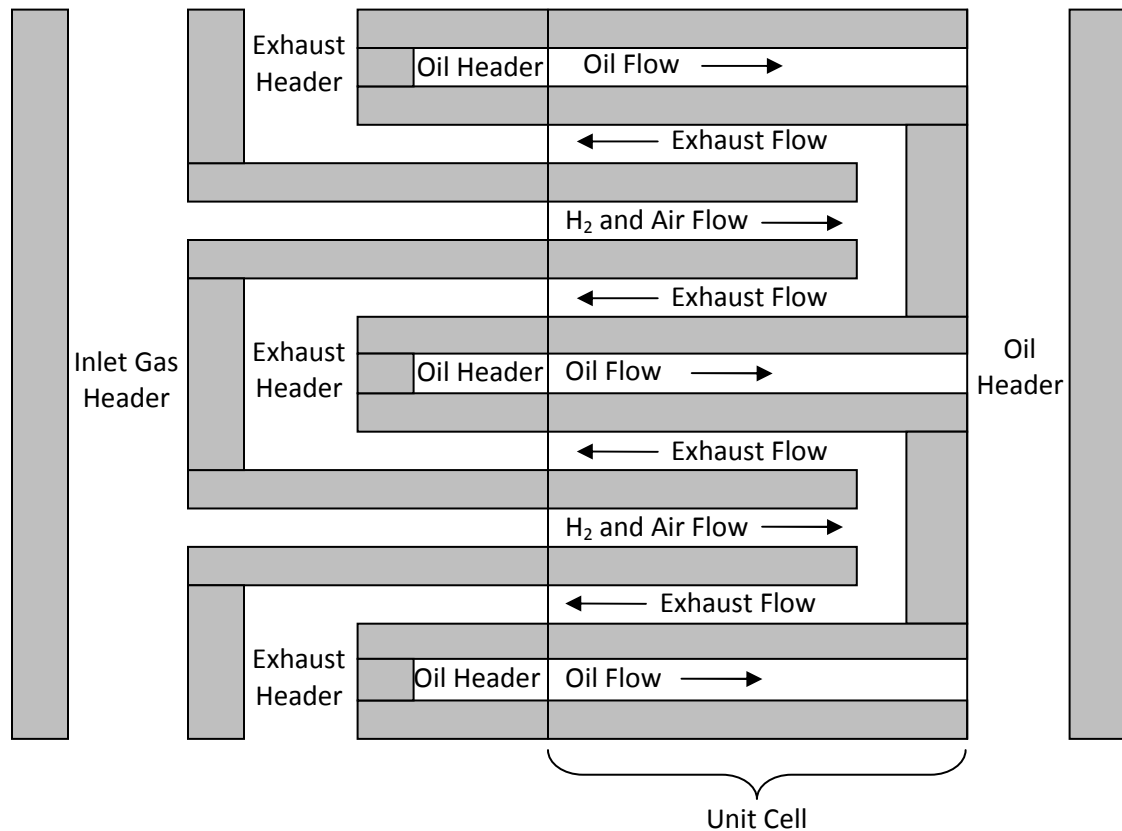


Fig. 9.4: Lateral header schematic (Side view, header flows into page)

Headers were then considered that supplied the fluids vertically through the shims. Multiple header shapes were considered in order to select a design that minimized the size of the combustor. Circular, oval, rectangular and triangular header shapes were considered, with only the triangular header shape showing a reduction in device volume over the lateral header design. A schematic of this header design is shown in Fig. 9.5. The inlet oil flows into the unit cells from the rectangular headers on the outside of the combustor while the hot oil flows up and out through a central, rectangular header.

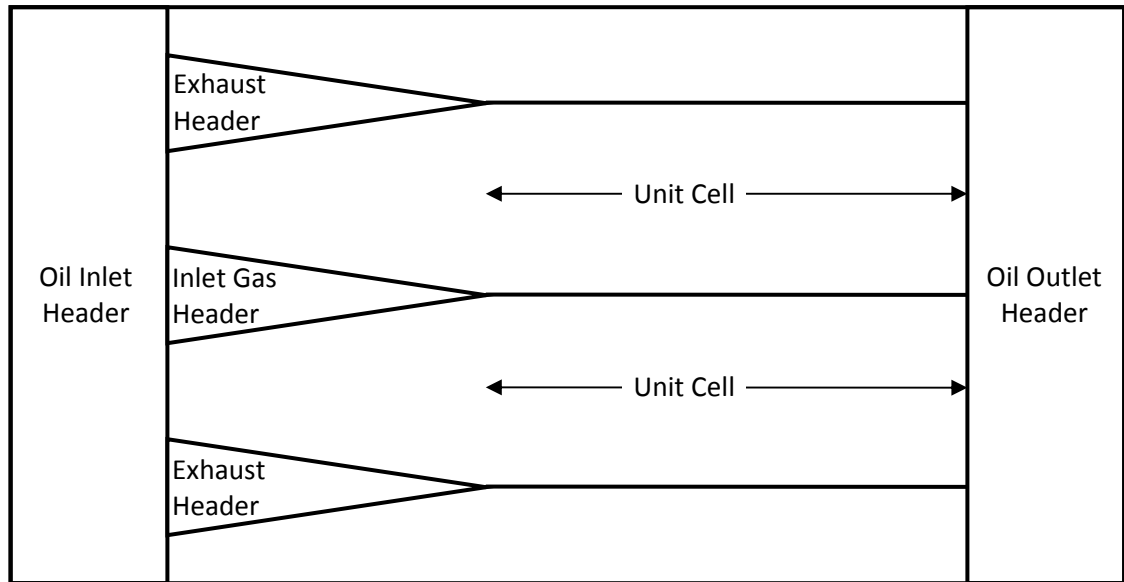


Fig. 9.5: Triangular header schematic (Top view, header flows into page)

Refinement of the triangular header led to the design of hexagonal headers for the combustion gases and pentagonal headers for the exhaust gases. The oil inlets and outlets are rectangular in shape. A schematic of this design is shown in Fig. 9.6.

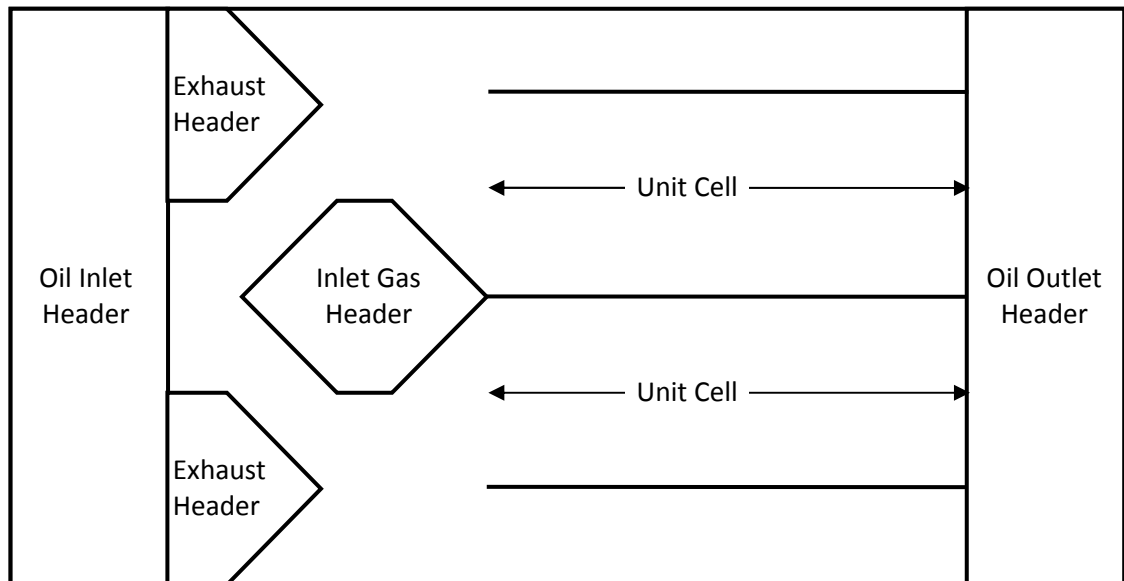


Fig. 9.6: Hexagonal and pentagonal header schematic (Top view, header flows into page)

The hexagonal and pentagonal header design was found to be the most compact. Table 9.1 shows the sizes and volume obtained for a 30 kW CHX with different header designs.

Table 9.1: Header design comparison for a 30 kW CHX

	Lateral Headers	Triangular Headers	Hexagonal and Pentagonal Headers
Length (cm)	21.2	24.3	21.0
Width (cm)	13.2	22.0	22.0
Height (cm)	20.7	7.8	7.8
Volume (L)	5.8	4.2	3.7

9.4. Design Results and Discussion

A 12 kW combustor and a 30 kW CHX have been designed based on the experimental performance results in order to determine the size, weight and cost of full size combustors. The 12 kW combustor design is shown in Fig. 9.7. Again, this is only a preliminary design and is to be optimized in future work based on optimization studies with the experimentally validated CFD code being developed for the unit cell design. Also, the combustor design shown is only of the parts that are to be diffusion bonded together. The final stage of external headers was not designed and is expected to be welded to the top and bottom after the diffusion bonding process. The welded headers are expected to be a relatively small portion of the overall weight and cost of the device.

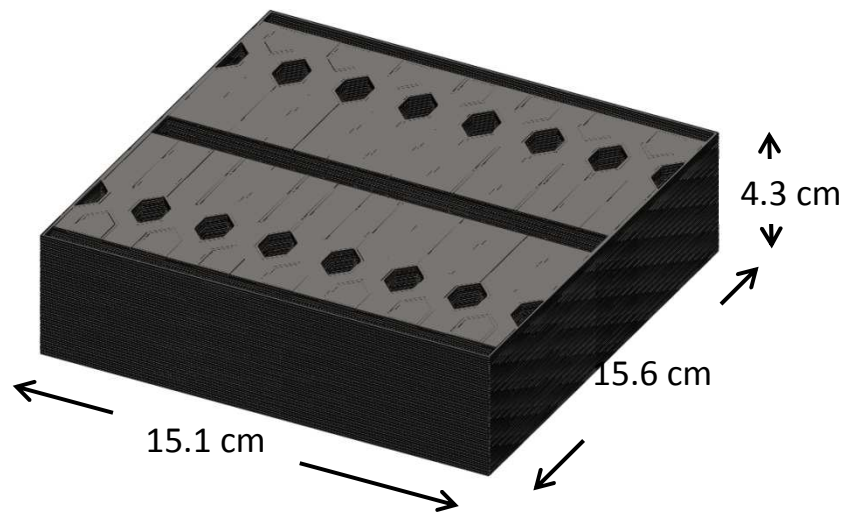


Fig. 9.7: Preliminary 12 kW combustor design

An exploded view of a single stack of shims is shown in Fig. 9.8. A stack refers to a set of shims that is one unit cell in height. The 12 kW combustor design is 2 unit cells in length, 14 units in width and 20 units in height for a total of 560 unit cells.

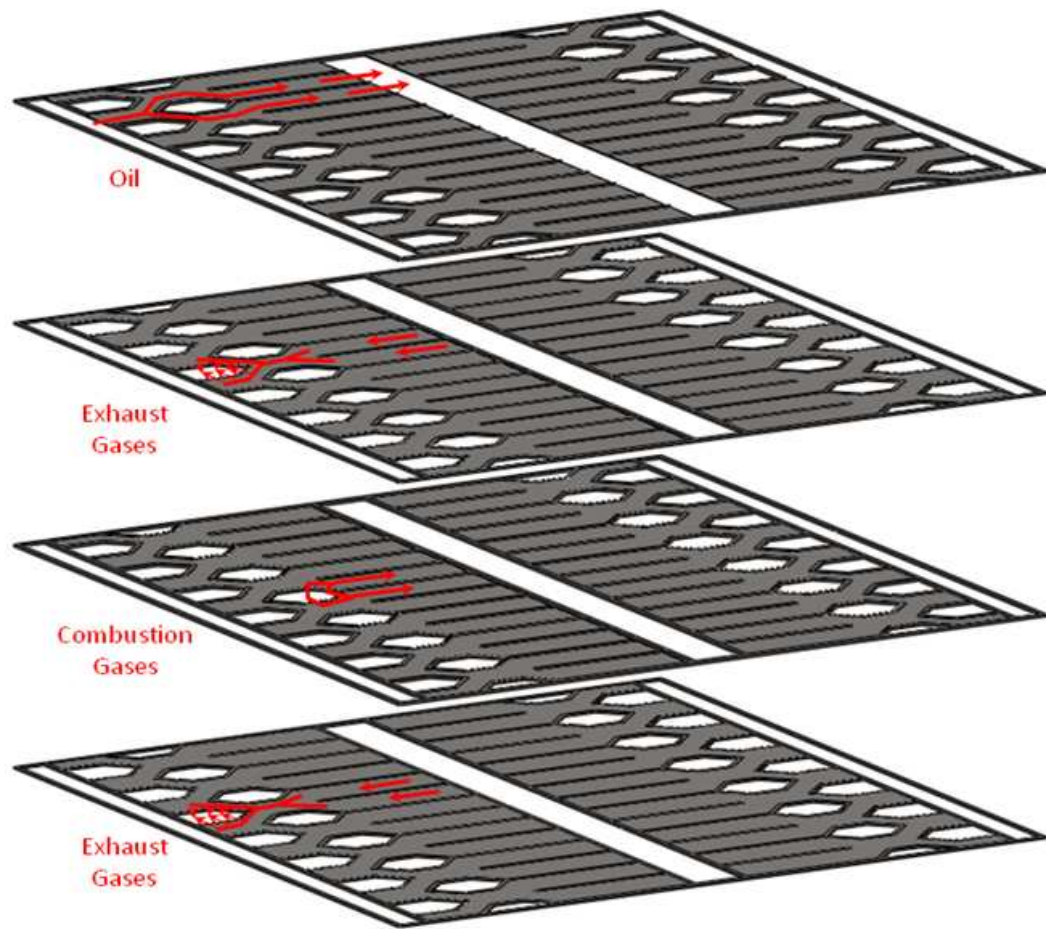


Fig. 9.8: Exploded view of a single stack of shims

The 30 kW combustor was designed in the same manner as the 12 kW combustor, with the difference being that the overall size of the device is larger due to the increased number of unit cells. It was assumed that 316 stainless steel will be the material for both devices and the weight was calculated accordingly. The size envelope, volume and weight of the 12 kW and 30 kW CHX's are shown in Table 9.2, along with the 30 kW Sandia combustor [7] for comparison. Including a conservative 2x volume increase for the final stage of headers and other design changes that may be required for manufacturing, the volume of the 30 kW CHX would be 7.2 liters. As a comparison, the design envelope volume of the Sandia combustor is 36.2 liters. This preliminary full size CHX design demonstrates the potential of the unit cell design to improve upon Sandia's design, which is the current state-of-art.

Table 9.2: Full size combustor comparison

	12 kW CHX	30 kW CHX	30 kW Sandia [7]
Width (cm)	15.1	22.2	32.0
Length (cm)	15.6	21.1	38.1
Height (cm)	4.3	7.9	29.7
Volume (L)	1.0	3.7	36.2
Weight (kg)	3.76	11.74	Unknown

10. FINANCIAL ANALYSIS

This section presents a financial analysis that was conducted on a scaled up design of the μ CHX. The analysis was used to determine the annual cash flows required for the manufacturing operations and the associated breakeven point. A sensitivity analysis was performed to determine the lower limits of the key parameters of profit margin and market share.

10.1. Introduction

The performance of the μ CHX investigated in this thesis represents the first step toward developing a full size CHX, capable of supplying enough heat for a vehicle scale hydrogen storage tank. As a potential commercial product, it is important that the full size CHX can be manufactured cost effectively and be sold profitably. The 12 kW CHX design discussed in the previous chapter was designed to meet the requirements of a vehicle scale hydrogen storage tank. A manufacturing cost model was developed for this design by Leif Steigleder, Dr. Brian Paul of OSU and Steve Leith of Pacific Northwest National Laboratory. This financial analysis was conducted in order to analyze the potential profitability of the project.

10.2. Methodology

Development of this financial analysis involved three distinct steps. First, the detailed cost model provided by Steigleder et al. was used to estimate the costs associated with manufacturing the combustor to obtain an estimated cost per combustor. Second, the intermediate calculations within the cost model were broken out in order to obtain the annual cash flows that would be incurred at different production levels. Lastly, a sales estimate was obtained from literature on estimated hydrogen fuel cell vehicle sales.

10.2.1. 12 kW CHX Cost Model

The cost model developed by Steigleder et al. is proprietary and unpublished; therefore, specific details cannot be discussed here. Instead, the general features of the model and the

general results are presented. The cost model was used to estimate the manufacturing cost of the 12 kW CHX design described in the previous chapter. This cost included fixed expenses, which aren't traditionally included in the accounting definition of cost of goods sold. As a brief overview, the manufacturing process consisted of etching 316 stainless steel panels, depositing the catalyst, then stacking and laser welding the shims together. The analysis was performed for a standard 24" x 24" work piece size. Seven primary cost components were included in the model: tooling, facility, labor, maintenance, raw materials, consumables and utilities. Costs that are directly associated with production are raw materials and consumables. The costs that vary with production levels and provide economies of scale as production increases are maintenance, labor, facility and tool depreciation. The cost per 12 kW CHX is shown for a range of production levels in Fig. 10.1. For increased annual production levels, the cost per device decreased, primarily due the cost of labor and tooling being spread over a greater number of units. The cost to produce a 12 kW CHX was estimated to be \$340 at a volume of 500,000 devices per year.

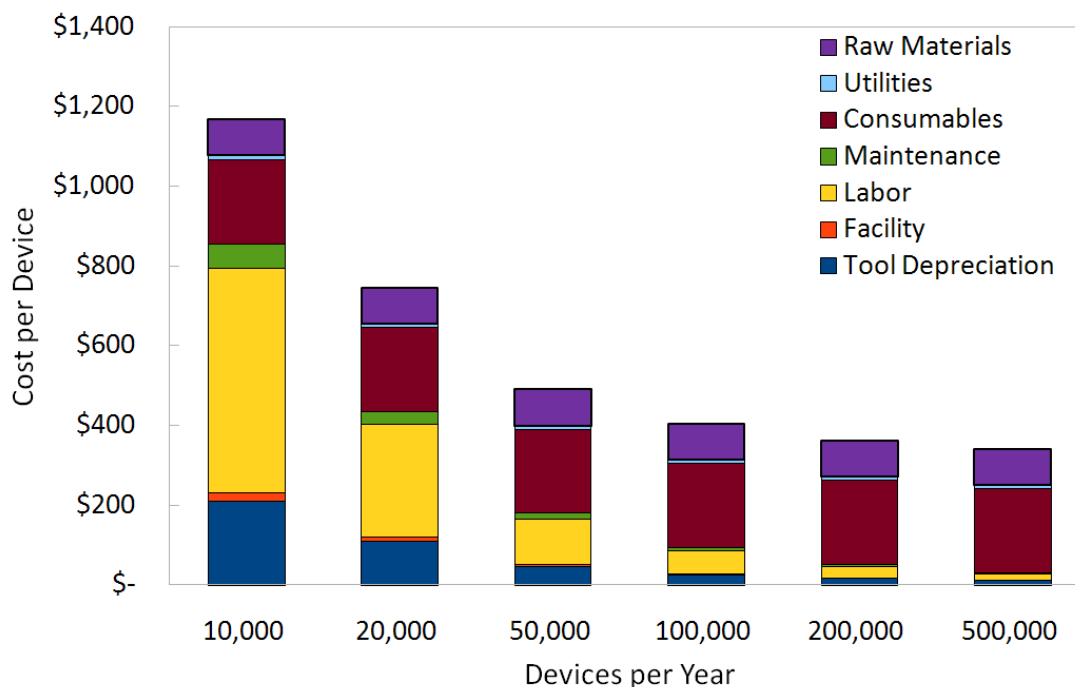


Fig. 10.1: Manufacturing costs at varying production levels (Data from Steigleder et al.)

10.2.1. Cash Flow Analysis

In order to obtain an estimation of the net cash flows generated from this project, the manufacturing costs needed to be converted from a per device basis to an annual basis. Unit costs per device obtained from the model included both the variable costs and an allocation of fixed costs. Each cost component was then categorized according to if it was fixed, variable or mixed in order to extract to the amount of fixed overhead. These cost components and their classification are listed in Table 10.1.

Table 10.1: Cost categories and classification

Cost Category	Classification
Raw Materials	Variable
Consumables	Variable
Utilities	Mixed
Facility	Fixed
Tool Depreciation	Mixed
Maintenance	Mixed
Labor	Mixed

The raw materials and consumable categories are purely variable costs, \$90.24 and \$210.95 per device, respectively. Utilities are mixed, but include both purely fixed and purely variable costs. The fixed costs are those associated with overhead, while the variable cost of \$8.84 is incurred for the production of each unit. These were the only costs that varied on a per unit basis. This resulted in a total of \$310.03 of variable costs per device, regardless of the annual production volume.

According to the cost model, the cost of the facility was determined based on the floor area required for tooling. For greater production volumes more tools are required, increasing the cost of the facility. However for the cash flow analysis, this cost was instead modeled as a fixed cost under the assumption that an entire manufacturing facility would be leased for a fixed annual rate. The facility cost at 500,000 devices per year was used as the fixed facility cost.

The costs associated with tool depreciation, maintenance and labor are dependent on the number of tools required. Each tool required both maintenance and labor, so these expenses scaled with the tooling costs. The majority of the tools required for the manufacturing process had plenty of excess capacity, so only one of each of these tools was required for annual production volumes up to 570,000 devices per year. This volume level was well above the volume levels considered in this analysis. Three of the tools, most notably the laser welding tool, have a more limited production capacity per tool. For these tools, additional tool purchases are required to meet the production volume requirements. This scaling effect was taken into consideration for the tooling, maintenance and labor costs. All tooling costs were assumed to occur in the year prior to their use in production, because the tools would have to be purchased and installed in advance of being incorporated into production. The costs of maintenance and labor were assumed to be incurred in the year in which they were required for production.

10.2.2. Sales Estimate

The annual sales of 12 kW CHX's was estimated based on the projected sales of hydrogen powered fuel cell vehicles. Hydrogen fuel cell vehicle deployment rates were adapted from the work by Melaina [51], who investigated the potential future demand for hydrogen refueling stations. Three deployment scenarios were considered: successful, moderate and delayed. The estimated annual sales numbers are shown in Fig. 10.2. Of these three scenarios, the delayed deployment case was used for this financial analysis as a conservative estimate.

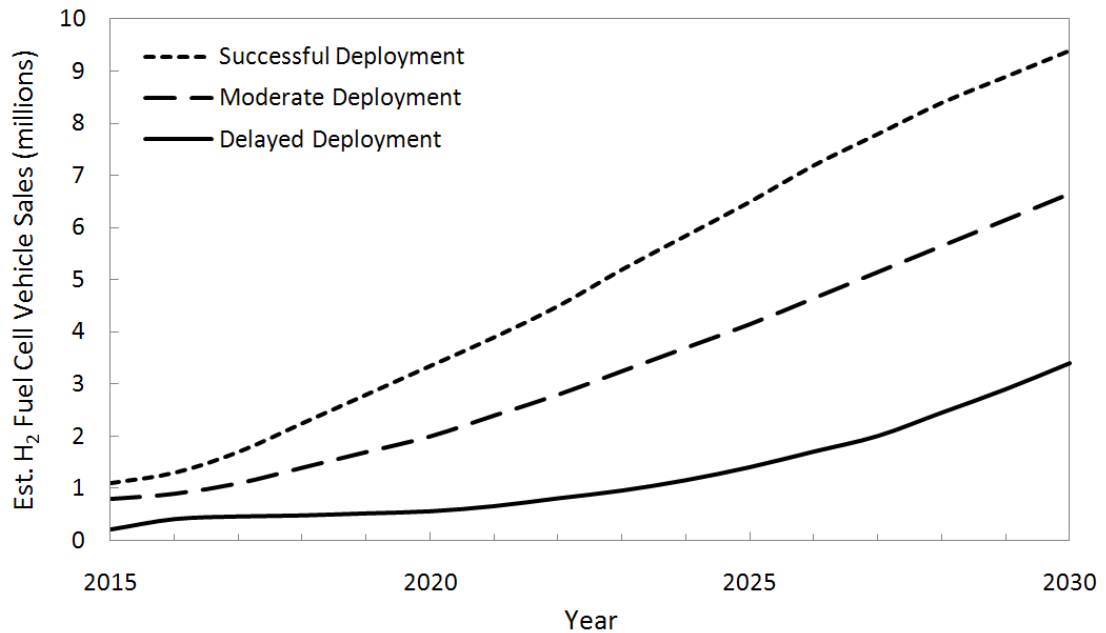


Fig. 10.2: Estimated annual H₂ fuel cell vehicle sales (Adapted from [51])

A company manufacturing the 12 kW CHX's would only supply combustors for a portion of the total vehicle sales. Multiple car manufacturers would be selling these vehicles and they would likely be utilizing competing technologies. Both of these factors would impact the percentage of the market that this manufacturer could capture. As a result, sales were estimated to be a fixed percentage of the hydrogen fuel cell vehicle sales of each year. The effect of varying market share was considered in the sensitivity analysis.

10.3. Results and Discussion

Based on these assumptions, an estimated annual cash flow analysis was performed. It was assumed that the combustors would be sold at a constant price. This price was obtained based on the cost at 500,000 devices per year (\$340) and a fixed profit margin. The impact of profit margin was also considered in a sensitivity analysis. The estimated net revenue at a profit margin of 50 percent and a market share of 10 percent is shown in Fig. 10.3. While the sales estimates used were projected from 2015 to 2030, the cash flow analysis was conducted assuming that the sales market share of sales in 2015 was experienced in year 1.

This was done to generalize the analysis. A spreadsheet with sample calculations of the financial analysis is provided in Appendix J.

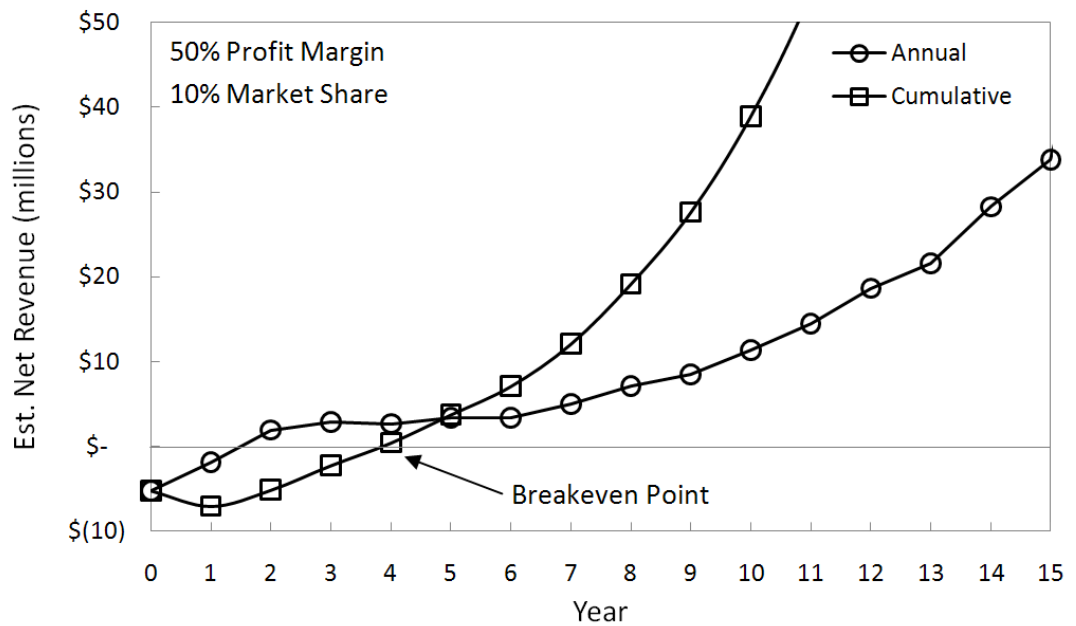


Fig. 10.3: Projected annual and cumulative net revenue

The annual cash flow is expected to be negative for the first couple years as the sales volume is low. This is due to the fixed overhead costs outweighing the revenue from the limited sales volume. As production ramps up to meet the increasing demand, the cumulative sales income eventually surpasses the cumulative expenditures. This is noted as the breakeven point, indicating the time period required in order to recoup the investment. For the 50 percent profit margin and 10 percent market share, the breakeven point is at 4 years. A sensitivity analysis on the breakeven point was conducted in order to analyze the impact of different amounts of market share and different profit margins. Profit margin and market share were each varied individually in order to obtain the breakeven point associated with each combination. The results of the sensitivity analysis are shown in Table 10.2. The number in each cell represents the number of years until the operation breaks even. Shorter payback periods in this analysis are clearly desirable as they indicate more profitable operation. The cell coloring was based on the assumption that payback periods of less than 5 years are acceptable.

Table 10.2: Sensitivity analysis on breakeven point

		Profit Margin (%)								
		20	30	40	50	60	70	80	90	100
Market Share (%)	2	Breakeven Point in Years					15	13	12	11
	4			15	12	10	9	7	6	5
	6		15	12	9	7	5	4	3	3
	8		13	9	6	4	3	3	2	2
	10		11	7	4	3	3	2	2	2
	12		10	5	3	3	2	2	2	2
	14	15	8	4	3	2	2	2	2	2
	16	14	7	4	3	2	2	2	2	2
	18	13	6	3	3	2	2	2	2	2
	20	12	5	3	2	2	2	2	2	1

Based on the results of this sensitivity analysis, it is clear that greater profit margins and increased market share are desirable. The red cells indicate the conditions where the project is a no-go and will not be profitable. The yellow-orange cells indicate riskier prospects, but that the project may be profitable after an extended period of time. Green cells indicate solid profitability and that the investments should be made to begin production. As the time to year 0 decreases, it is expected that the decision makers will be able to obtain more accurate estimations of market share and profit margin that can be achieved. If they find that they will not be able to achieve a market share greater than 4 percent, it is unlikely that the project will be successful. Similarly, if they do not expect to be able to maintain a profit margin greater than 30 percent, then the project will probably not succeed. A good course of action would be to target a market share of 12 percent and a profit margin of 70 percent, which would result in a payback period of 2 years. Such a short payback period would allow for reduced profit margins and market shares while still maintaining a payback period of less than 5 years.

This analysis will require refinement as the hydrogen powered vehicles are further developed and more accurate sales forecasts become available. Also, the analysis shown is not inflation adjusted, so all numbers shown are in constant dollars. While a payback period analysis is generally considered to be inferior to a net present value (NPV) analysis [52], it was used here for multiple reasons. An NPV analysis consists of discounting all future cash flows back to year 0 in order to determine the total value of the project at a single point in time. The discount rate is the first difficulty in correctly calculating the NPV. Accurately determining a discount rate requires an understanding of the rate of return expected by the debt and equity holders of the company, both of which are likely to change in the future. Also, obtaining an accurate NPV requires an estimation of the terminal value of the project. As a developing technology with unknown future prospects, this undertaking would be highly inaccurate. With the sales estimations used here, almost all combinations of market share and profit margin would result in positive NPVs. The breakeven analysis conducted here is actually complementary to an NPV analysis because shorter payback periods would correspond to higher NPV's. In summary, the payback period is focused on here because it can be more accurately estimated at this early stage of development.

10.4. Conclusions

The financial analysis performed here indicates that there is potential for the CHX to be a profitable product. However, there are many unknowns that need to be resolved before this can be known with certainty. Most importantly, the metal hydride hydrogen storage system is still in the development stage. Failure of this hydrogen storage system to become commercially viable would render the CHX developed here unnecessary. However, demonstrating the financial viability of this component is a positive contribution towards the successful development of the system.

11. CONCLUSIONS AND RECOMMENDATIONS

A novel design of an integrated hydrogen combustor recuperator and oil heat exchanger (μ CHX) was designed and tested. Catalyst stability was investigated and the effects of residence time, equivalence ratio and average oil temperature, catalyst length and catalyst position were established.

11.1. Conclusions

Catalyst stability testing indicated that the wet deposited platinum catalyst was stable and produced repeatable results even after several weeks of operation.

The response of the μ CHX to variations in residence time, while maintaining a set equivalence ratio and fixed average oil temperature, was found to result in maximum hydrogen conversion for residence times greater than 20 ms. Efficiencies between 96 and 78 percent were obtained for residence times longer than 20 ms. The efficiency of the μ CHX decreased for longer residence times due to the lower heat input resulting in smaller temperature differences for heat transfer to the oil. Efficiencies were established to be highly dependent on hydrogen conversion, with greater hydrogen conversion supporting higher efficiencies. Shorter residence times were tested with a shorter length of catalyst and demonstrated increasing hydrogen conversion with increased residence time in the range of 5 to 14 ms.

Variation of equivalence ratio, for a fixed residence time and average oil temperature, established that mixtures slightly lean of stoichiometric result in the highest efficiencies. Efficiencies in excess of 90 percent were obtained for equivalence ratios between 0.5 and 1.0. Stoichiometric equivalence ratios resulted in lower hydrogen conversion than lean mixtures, demonstrating that operating with excess air facilitates complete combustion of H_2 . Decreasing efficiencies were obtained for reducing the equivalence ratio below 0.7. Preliminary comparison with the CFD model by Ghazvini and Narayanan [1] showed reasonable preliminary agreement with the observed efficiency trends for equivalence ratio variation.

Average oil temperature variation was found to not have a substantial impact on the efficiency of the μ CHX while holding a fixed equivalence ratio and set residence time. Efficiencies above 90 percent were obtained for average oil temperatures between 63 °C and 105 °C. Increasing the average oil temperature above 85 °C was shown to cause a slight reduction in efficiency. The minimum operating average oil temperatures was found to be 63 °C. Lower average oil temperatures caused the exhaust gas temperature to fall below 100 °C.

Experiments with varied catalyst lengths were compared at a set average oil temperature and fixed equivalence ratio in order to determine an optimal catalyst length. The catalyst length that was 20 percent of the channel length was found to result in lower efficiencies than the 87 percent catalyst length for similar residence times over the catalyst and for similar H_2 heat inputs. A longer catalyst provides higher hydrogen conversion, resulting in the higher efficiencies for the longer catalyst length.

The effects of catalyst position were investigated by performing variation of residence time experiments with the same catalyst shim in two different orientations in the μ CHX. For these tests, equivalence ratio and average oil temperature were held constant. In order to keep the exhaust temperature above 100 °C, the catalyst position near the end of the combustion channel required higher average oil temperatures than for the catalyst position near the inlet of the combustion channel.

A preliminary design of a 30 kW combustor was developed by scaling up the unit cell design based on the demonstrated experimental performance of the μ CHX. The preliminary design indicates the potential for up to an 80 percent size reduction compared to the current state of the art hydrogen combustor oil heat exchanger [7].

The preliminary financial analysis of the 12 kW CHX demonstrated the commercial viability of the CHX if a market share greater than 4 percent or a profit margin greater than 30 percent can be obtained. A target market share of 12 percent and a target profit margin of 70 percent are recommended.

11.2. Recommendations for Future Investigation

The current experimental facility could be improved in order to better investigate the operating characteristics of the unit cell. A gas chromatograph, such as the Agilent 490 GC, should be incorporated into the exhaust line in order to reduce the uncertainties associated with determining the hydrogen conversion. An analysis of the temperature dependent oil properties should be conducted in order to determine their true properties and obtain more accurate calculations of efficiency and heat losses. The diaphragm in the differential pressure transducer on the gas line should be replaced with a diaphragm capable of measuring the large pressure drops observed during operation. Temperature control should be incorporated into the flow loop for the inlet oil and gases in order to maintain constant inlet conditions for all experiments. In particular, the temperature controller for the oil should have sufficient capacity to heat the oil past 100 °C in order to examine the performance of the device for higher inlet oil temperatures and higher average oil temperatures. Furthermore, refinement of the μ CHX design or catalyst is needed in order to mitigate the non-uniformities at the inlet of the combustor channel.

Further experiments varying geometric parameters should be conducted with the current μ CHX test article. Additional experiments varying catalyst length and catalyst position are needed in order to obtain a more complete understanding of their respective impact on the performance of the μ CHX. A study varying the channel height should be conducted in order to determine the effects of channel height on the pressure drop and efficiency. Also, alternative catalysts and deposition techniques should be tested in order to improve H₂ conversion and decrease the total amount of catalyst required for optimum performance.

A smaller, diffusion bonded device of similar internal dimensions could be fabricated in order to investigate the transient response of the μ CHX for the changing flow rate demands of a hydrogen powered vehicle.

A full size CHX, such as the one proposed in chapter 9, should be fabricated in order to demonstrate the performance of the scaled-up unit cell design at the heat output levels required for a vehicle scale hydrogen storage system.

Use of aluminum instead of the stainless steel should be explored in order to further reduce the weight of the full size CHX designs. Aluminum has a density of 2.7 g/cm^3 compared to 8 g/cm^3 for stainless steel. Implementing this change would significantly reduce the weight of the full size CHX. However, aluminum has a lower melting point than stainless steel (500°C compared to 1400°C), so further investigation is required in order to determine if this material change is feasible. This could potentially be investigated by replacing the stainless steel base of the μCHX test article with an IR transparent material and collecting infrared thermal images of the catalyst surface during combustion.

The next step in a more detailed financial analysis would be to conduct a net present value analysis of manufacturing the full size CHX. When the automotive industry begins to prepare hydrogen fuel cell powered cars for mass production, a more detailed financial analysis will be needed in order to provide a more accurate estimation of the profitability of the full size CHX.

REFERENCES

- [1] Ghazvini M., Narayanan V., 2011, "Performance characterization of a microscale integrated combustor recuperator oil heat exchanger", Proceedings of the ASME/JSME 2011 8th Thermal Engineering Joint Conference (AJTEC2011), Honolulu, Hawaii.
- [2] Barreto L., Makihira A., and Riahi K., 2003, "The hydrogen economy in the 21st century: a sustainable development scenario," *International Journal of Hydrogen Energy*, **28**(3), pp. 267-284.
- [3] Fernandez-Pello, C., A., 2002. "Micropower generation using combustion: issues and approaches". *Proceedings of the Combustion Institute*, **29**, pp. 883-899.
- [4] Satyapal S., Petrovic J., Read C., Thomas G., and Ordaz G., 2007, "The U.S. Department of Energy's National Hydrogen Storage Project: Progress towards meeting hydrogen-powered vehicle requirements," *Catalysis Today*, **120**(3-4), pp. 246-256.
- [5] Satyapal S., 2009, DOE Hydrogen Program Annual Merit Review Proceedings, http://www.hydrogen.energy.gov/annual_review09_plenary.html
- [6] Stetson N. T., 2011, DOE Hydrogen Program Annual Merit Review Proceedings, http://www.hydrogen.energy.gov/annual_review11_plenary.html
- [7] Johnson T., and Kanouff M., 2010, Performance Characterization of a Hydrogen Catalytic Heater, Sandia National Laboratories.
- [8] Appel C., Mantzaras J., Schaeren R., Bombach R., Inauen A., Kaeppli B., Hemmerling B., and Stampanoni A., 2002, "An experimental and numerical investigation of homogeneous ignition in catalytically stabilized combustion of hydrogen/air mixtures over platinum," *Combustion and Flame*, **128**(4), pp. 340-368.
- [9] Norton D. G., Wetzel E. D., and Vlachos D. G., 2004, "Fabrication of Single-Channel Catalytic Microburners: Effect of Confinement on the Oxidation of Hydrogen/Air Mixtures," *Industrial & Engineering Chemistry Research*, **43**(16), pp. 4833-4840.
- [10] Choi W., Kwon S., and Dong Shin H., 2008, "Combustion characteristics of hydrogen-air premixed gas in a sub-millimeter scale catalytic combustor," *International Journal of Hydrogen Energy*, **33**(9), pp. 2400-2408.
- [11] Ryi S., Park J., Choi S., Cho S., and Kim S., 2005, "Novel micro fuel processor for PEMFCs with heat generation by catalytic combustion," *Chemical Engineering Journal*, **113**(1), pp. 47-53.
- [12] Norton D. G., Wetzel E. D., and Vlachos D. G., 2006, "Thermal Management in Catalytic Microreactors," *Industrial & Engineering Chemistry Research*, **45**(1), pp. 76-84.
- [13] Janicke M. T., Kestenbaum H., Hagendorf U., Schüth F., Fichtner M., and Schubert K., 2000, "The Controlled Oxidation of Hydrogen from an Explosive Mixture of Gases Using a Microstructured Reactor/Heat Exchanger and Pt/Al₂O₃ Catalyst," *Journal of Catalysis*, **191**(2), pp. 282-293.

- [14] Vican J., Gajdeczko B., Dryer F., Milius D., Aksay I., and Yetter R., 2002, "Development of a microreactor as a thermal source for microelectromechanical systems power generation," *Proceedings of the Combustion Institute*, **29**(1), pp. 909-916.
- [15] Deutschmann O., Schmidt R., Behrendt F., and Warnat J., 1996, "Numerical modeling of catalytic ignition," *Symposium (International) on Combustion*, **26**(1), pp. 1747-1754.
- [16] Deutschmann O., Maier L. I., Riedel U., Stroemman A. H., and Dibble R. W., 2000, "Hydrogen assisted catalytic combustion of methane on platinum," *Catalysis Today*, **59**(1-2), pp. 141-150.
- [17] Mantzaras J., Bombach R., and Schaeren R., 2009, "Hetero-/homogeneous combustion of hydrogen/air mixtures over platinum at pressures up to 10 bar," *Proceedings of the Combustion Institute*, **32**(2), pp. 1937-1945.
- [18] Ahn J., Eastwood C., Sitzki L., and Ronney P. D., 2005, "Gas-phase and catalytic combustion in heat-recirculating burners," *Proceedings of the Combustion Institute*, **30**(2), pp. 2463-2472.
- [19] Maruta K., Takeda K., Ahn J., Borer K., Sitzki L., Ronney P. D., and Deutschmann O., 2002, "Extinction limits of catalytic combustion in microchannels," *Proceedings of the Combustion Institute*, **29**(1), pp. 957-963.
- [20] Lewis B., and Von Elbe G., 1987, *Combustion, flames and explosions of gases*, Academic Press, Inc., Orlando, FL.
- [21] Miesse C. M., Masel R. I., Jensen C. D., Shannon M. A., and Short M., 2004, "Submillimeter-scale combustion," *AIChE J.*, **50**(12), pp. 3206-3214.
- [22] Meille V., 2006, "Review on methods to deposit catalysts on structured surfaces," *Applied Catalysis A: General*, **315**, pp. 1-17.
- [23] Peterson R. B., and Vanderhoff J. A., 2000, "A Catalytic Combustor for Microscale Applications," *Combustion Science and Technology Communications*, **1**, pp. 10-13.
- [24] Behrendt F., Deutschmann O., Schmidt R., and Warnatz J., 1996, "Ignition and Extinction of Hydrogen - Air and Methane - Air Mixtures over Platinum and Palladium," *Heterogeneous Hydrocarbon Oxidation*, American Chemical Society, pp. 49-57.
- [25] Federici J. A., Norton D. G., Brüggemann T., Voit K. W., Wetzel E. D., and Vlachos D. G., 2006, "Catalytic microcombustors with integrated thermoelectric elements for portable power production," *Journal of Power Sources*, **161**(2), pp. 1469-1478.
- [26] Vesper G., 2001, "Experimental and theoretical investigation of H₂ oxidation in a high-temperature catalytic microreactor," *Chemical Engineering Science*, **56**(4), pp. 1265-1273.
- [27] Kiwi-Minsker L., and Renken A., 2005, "Microstructured reactors for catalytic reactions," *Catalysis Today*, **110**(1-2), pp. 2-14.
- [28] Jensen K. F., 2001, "Microreaction engineering – is small better?," *Chemical Engineering Science*, **56**(2), pp. 293-303.

- [29] Norton D. G., and Vlachos D. G., 2005, "Hydrogen assisted self-ignition of propane/air mixtures in catalytic microburners," *Proceedings of the Combustion Institute*, **30**(2), pp. 2473-2480.
- [30] Schwiedernoch R., Tischer S., Deutschmann O., and Warnatz J., 2002, "Experimental and numerical investigation of the ignition of methane combustion in a platinum-coated honeycomb monolith," *Proceedings of the Combustion Institute*, **29**(1), pp. 1005-1011.
- [31] Weinberg F. J., 1971, "Combustion Temperatures: The Future?," *Nature*, **233**(5317), pp. 239-241.
- [32] Lloyd S. A., and Weinberg F. J., 1974, "A burner for mixtures of very low heat content," *Nature*, **251**(5470), pp. 47-49.
- [33] Jones A. R., Lloyd S. A., and Weinberg F. J., 1978, "Combustion in Heat Exchangers," *Proceedings of the Royal Society of London. Series A, Mathematical and Physical Sciences*, **360**(1700), pp. 97-115.
- [34] Hatfield J. M., and Peterson R. B., 2001, "A Catalytically Sustained Microcombustor Burning Propane," *Proceedings of the 2001 International Mechanical Engineering Congress and Exposition (IMECE)*, New York, NY.
- [35] Kim N. I., Kato S., Kataoka T., Yokomori T., Maruyama S., Fujimori T., and Maruta K., 2005, "Flame stabilization and emission of small Swiss-roll combustors as heaters," *Combustion and Flame*, **141**(3), pp. 229-240.
- [36] Sitzki L., Borer K., Wussow S., Maruta E. S. K., and Ronney P. D., 2001, "Combustion in microscale heat-recirculating burners," *The Third Asia-Pacific Conference on Combustion*, Seoul, Korea.
- [37] Vijayan V., and Gupta A. K., 2010, "Combustion and heat transfer at meso-scale with thermal recuperation," *Applied Energy*, **87**(8), pp. 2628-2639.
- [38] Kim N. I., Aizumi S., Yokomori T., Kato S., Fujimori T., and Maruta K., 2007, "Development and scale effects of small Swiss-roll combustors," *Proceedings of the Combustion Institute*, **31**(2), pp. 3243-3250.
- [39] Karim A. M., Federici J. A., and Vlachos D. G., 2008, "Portable power production from methanol in an integrated thermoelectric/microreactor system," *Journal of Power Sources*, **179**(1), pp. 113-120.
- [40] Drost M. K., Call C., Cuta J., and Wegeng R., 1997, "Microchannel Combustor Evaporator Thermal Processes," *Microscale Thermophysical Engineering*, **1**(4), p. 321.
- [41] Nuckols M. L., Van Zandt K., and Finlayson W. S., 2000, "Diver heating using hydrogen catalytic reactions," *OCEANS 2000 MTS/IEEE Conference and Exhibition*, pp. 1371-1374 vol.2.
- [42] White F. M., 2006, *Fluid Mechanics*, McGraw-Hill.
- [43] Paratherm Corporation, 2009, Safety Information, <http://www.paratherm.com/safety/>

- [44] Bowles J. B., 2003, "An assessment of RPN prioritization in a failure modes effects and criticality analysis," Reliability and Maintainability Symposium, pp. 380-386.
- [45] Jayaraman V., Lin Y. S., Pakala M., and Lin R. Y., 1995, "Fabrication of ultrathin metallic membranes on ceramic supports by sputter deposition," Journal of Membrane Science, **99**(1), pp. 89-100.
- [46] Stefanov P., Stoychev D., Valov I., Kakanakova-Georgieva A., and Marinova T., 2000, "Electrochemical deposition of thin zirconia films on stainless steel 316 L," Materials Chemistry and Physics, **65**(2), pp. 222-225.
- [47] Schweizer A. E., and Kerr G. T., 1978, "Thermal decomposition of hexachloroplatinic acid," Inorganic Chemistry, **17**(8), pp. 2326-2327.
- [48] Moran M. J., and Shapiro H. N., 2003, Fundamentals of Engineering Thermodynamics, Wiley.
- [49] Incropera F. P., DeWitt D. P., Bergman T. L., and Lavine A. S., 2006, Introduction to Heat Transfer, Wiley.
- [50] Johnson T., and Kanouff M., 2010, Parameter Study of a Vehicle-Scale Hydrogen Storage System, Sandia National Laboratories.
- [51] Melaina M. W., 2003, "Initiating hydrogen infrastructures: preliminary analysis of a sufficient number of initial hydrogen stations in the US," International Journal of Hydrogen Energy, **28**(7), pp. 743-755.
- [52] Brealey R., Myers S., and Allen F., 2010, Principles of Corporate Finance, McGraw-Hill/Irwin.
- [53] Eilers B. J., 2010, "Microchannel Steam-Methane Reforming Under Constant and Variable Surface Temperature Distributions", M.S. Thesis, Oregon State University.
- [54] Burch R., and Urbano F. J., 1995, "Investigation of the active state of supported palladium catalysts in the combustion of methane," Applied Catalysis A: General, **124**(1), pp. 121-138.

APPENDICES

Appendix A. Part Drawings of Combustor Components

All dimensions are in inches.

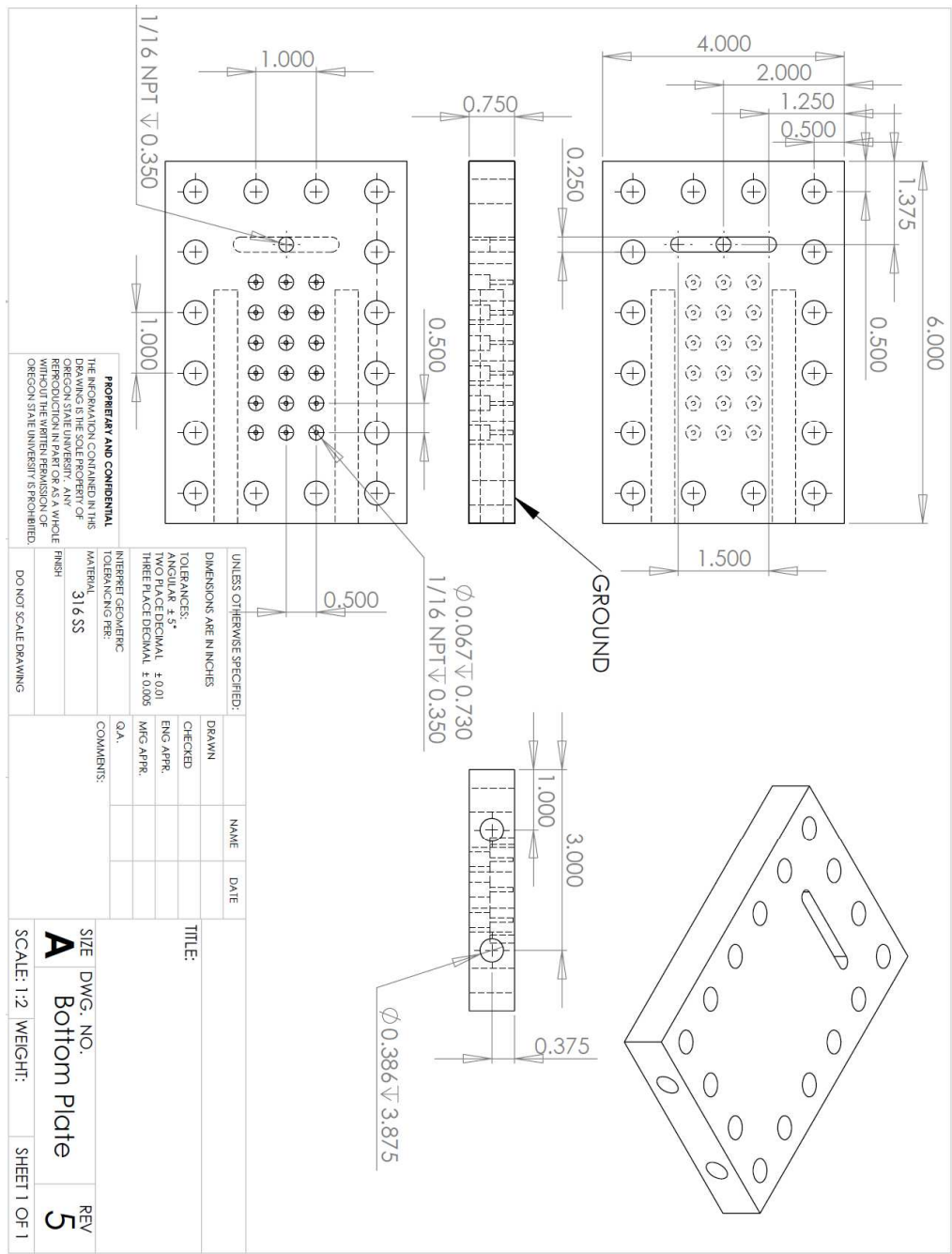


Fig.A.1: CAD drawing of bottom plate

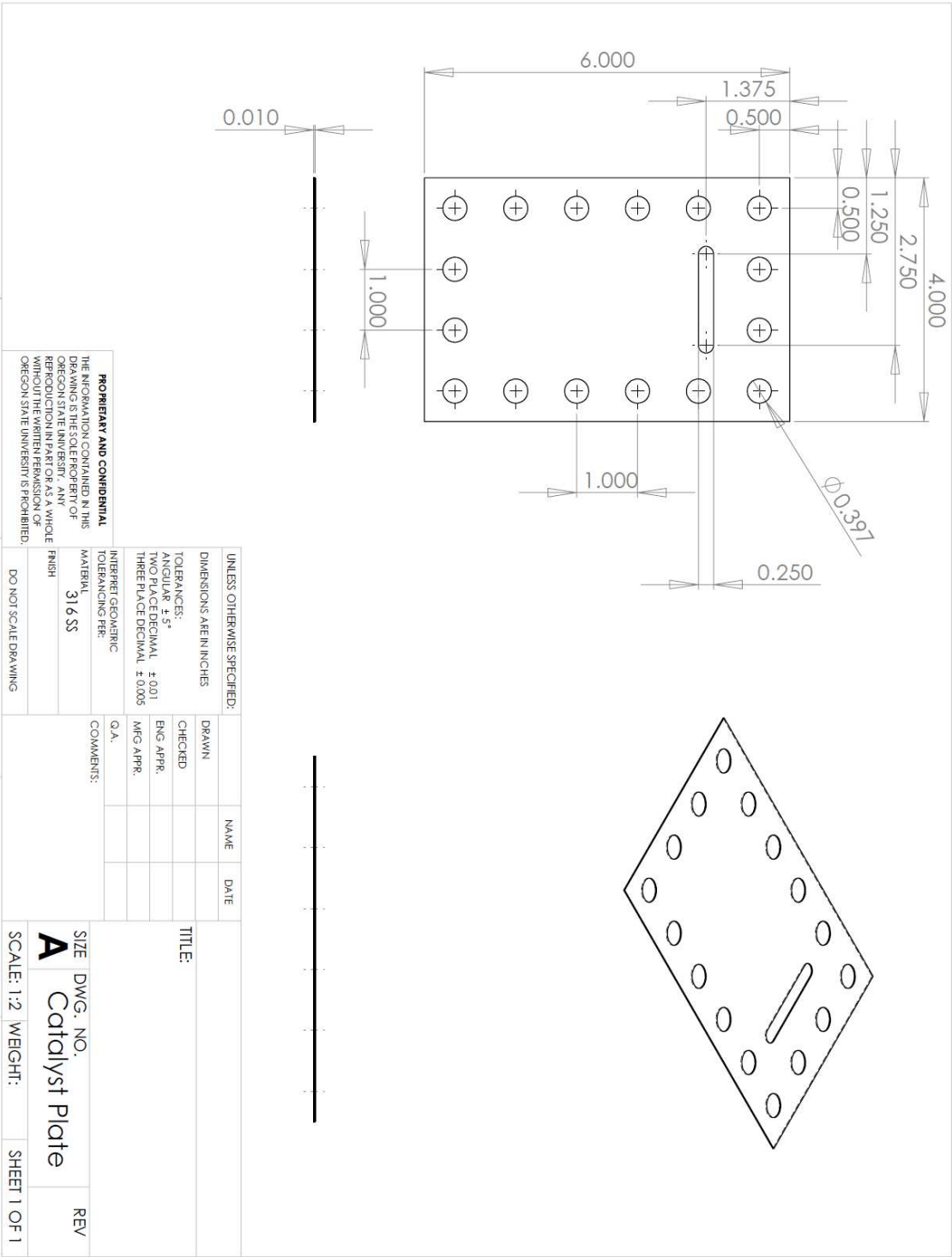


Fig.A.2: CAD drawing of catalyst plate

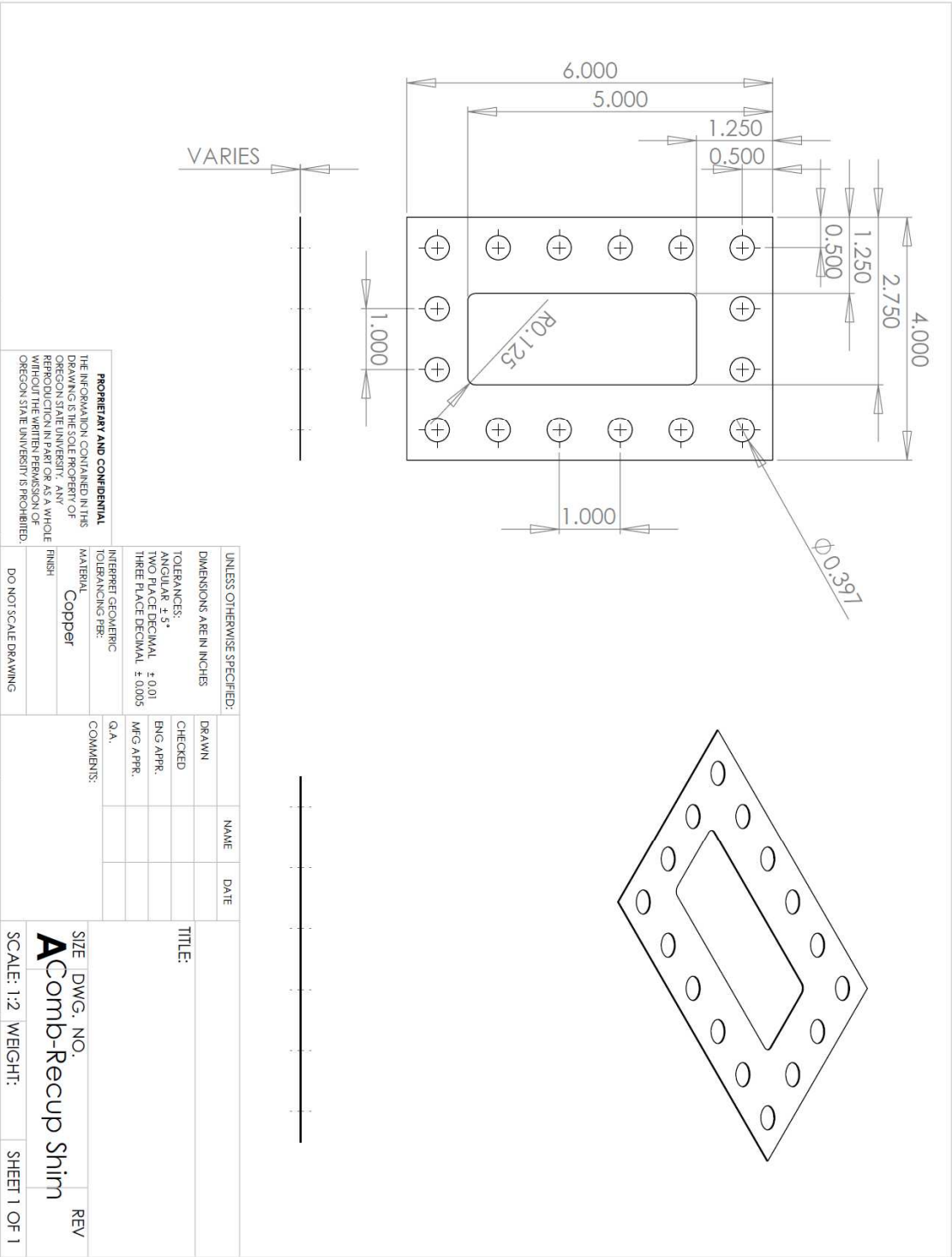


Fig.A.3: CAD drawing of combustor/recuperator shim

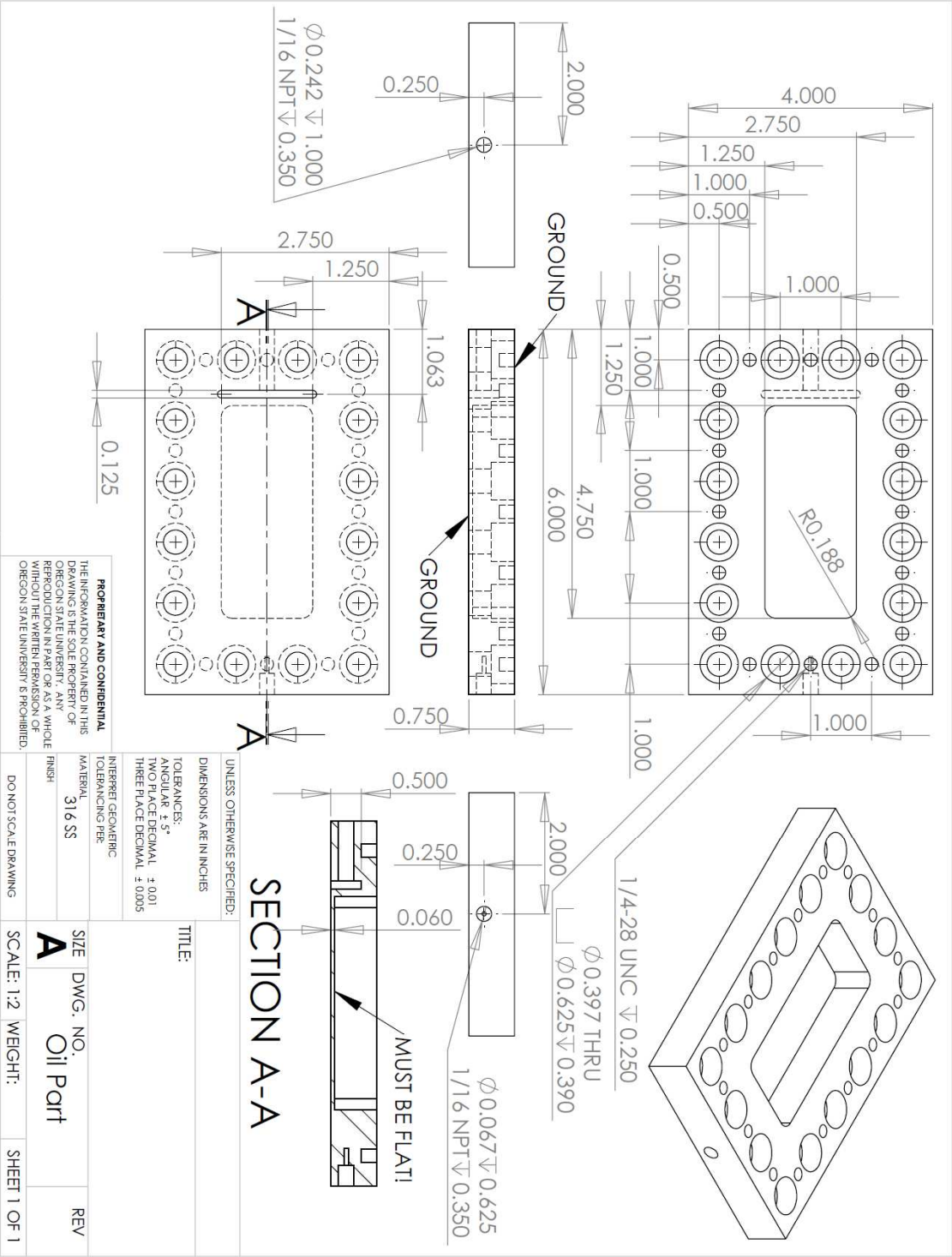


Fig.A.4: CAD drawing of oil part

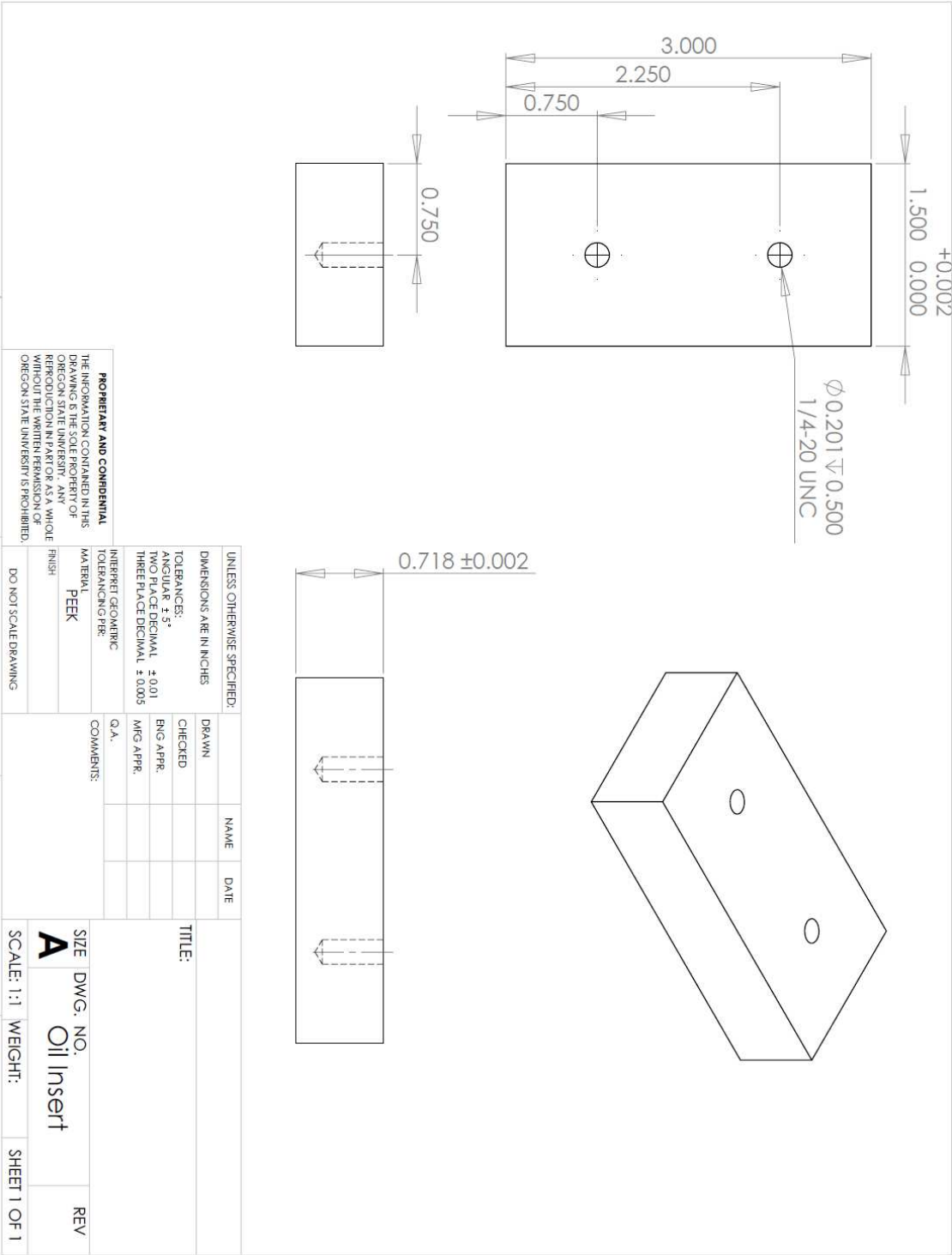


Fig.A.5: CAD drawing of oil insert

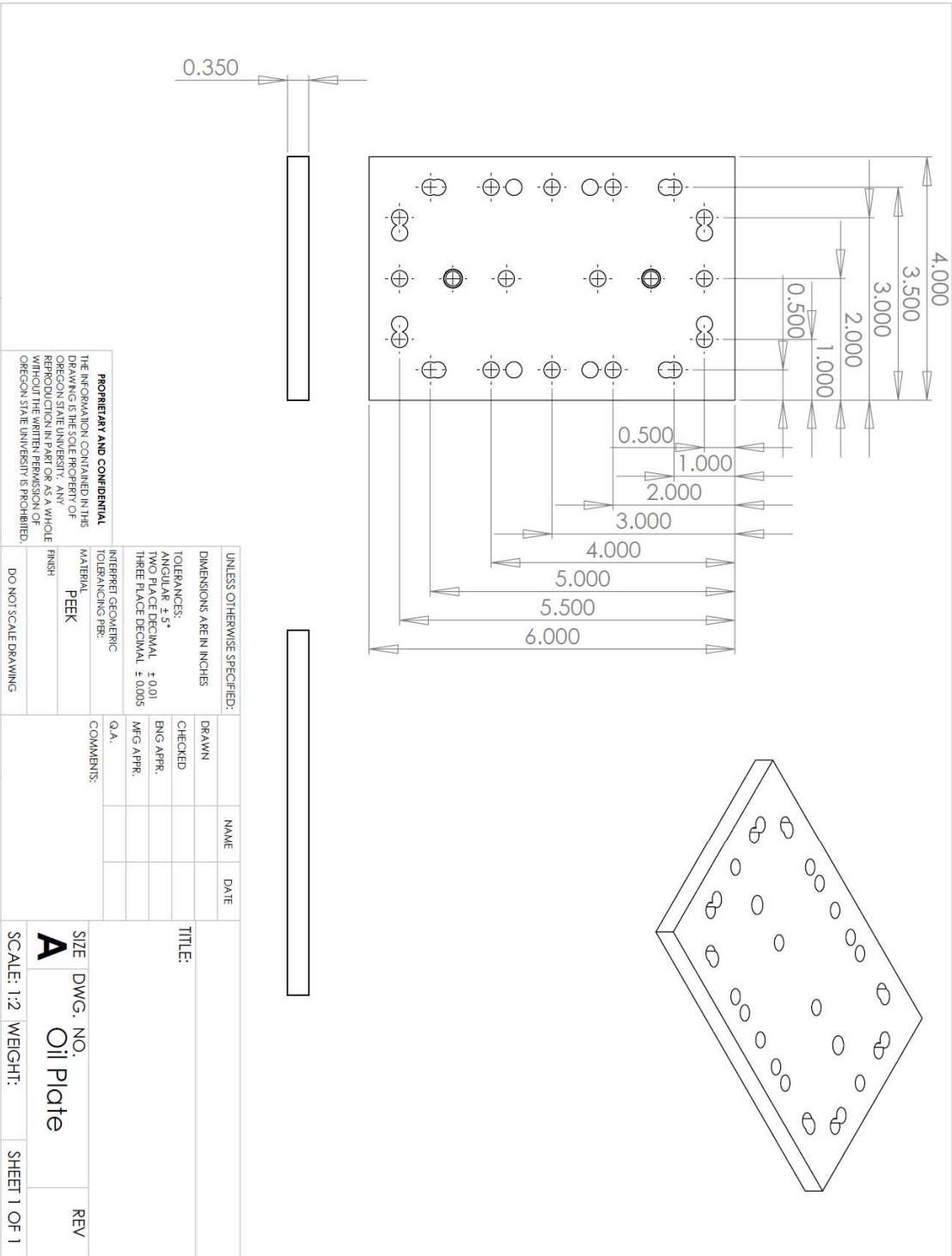


Fig.A.6: CAD drawing of oil plate

Appendix B. LabVIEW VI

The LabVIEW VI consisted of a program that controlled the experiment and saved the resulting data from the system shown in Fig. 4.13. The following are pseudo-code representations of the various sections of the LabVIEW VI.

Thermocouples:

1. Read temperatures from NI-9213
2. Apply calibration parameters
3. Display temperatures
4. Save temperatures

Pressure Transducers:

1. Read pressure transducer voltages from NI-9205
2. Apply calibration parameters to obtain pressures
3. Display pressures
4. Save pressures

Mass Flow Controllers:

1. Manual input of equivalence ratio and total flow rate into the "Front Panel"
2. Convert equivalence ratio and total flow rate into air and H₂ flow rates
3. Display setpoint flow rates of air and H₂
4. Convert flow rates to voltages
5. Output voltages to NI-9263
6. Read actual flow rate voltages from NI-9205
7. Convert voltages to flow rates
8. Display actual flow rates of air and H₂
9. Save actual flow rates of air and H₂

Oil Flow Rate:

1. Manual input of pump speed (0 – 100%)

2. Convert pump speed to voltage
3. Output voltage to NI-9263
4. Read number of flowmeter pulses from USB-6009 during the last program cycle
5. Divide number of pulses by the elapsed time during the last program cycle
6. Convert pulses per second to oil flow rate
7. Display oil flow rate
8. Save oil flow rate

Appendix C. Facility Changes for Full Size CHX Experiments

Instruments that would need to be modified include the differential pressure transducers on the combustor and oil channel sides and the mass flow controllers. The differential pressure transducers are of the capacitance type and work on the principle of change in capacitance due to deflection of an inner diaphragm due to pressure. By changing the stiffness of the diaphragm, the range of pressure measured by the same instrument can be changed. Modification to the mass flow controllers consists of installing a different laminar flow element core and being recalibrated by the manufacturer. The oil flow meter is the only instrument that may need to be replaced for the large flow rate experiments.

Equipment that would need to be replaced only includes the oil pump head. The proportional solenoid valve was unnecessary to control the oil flow rate and can be removed. The pump was selected such that the original motor and controller can still be used and only the pump head needs to be changed to accommodate higher flow rates.

Appendix D. Alternative Catalyst Deposition Methods

D.1. Anodized Aluminum

Norton et al. [12] successfully used anodized aluminum shims as supports for a wet deposited platinum catalyst. An attempt was made to fabricate similar catalysts and supports. A 75 μm aluminum shim was anodized for 48 hours at 40 V in a 0.3 M solution of oxalic acid. The anodizing bath was set in an ice bath in an attempt to maintain a bath temperature around 1 – 2 $^{\circ}\text{C}$. The anodized aluminum was found to be a highly porous support, as shown in Fig. D.1. However, the shim was too fragile and could not be adapted for use in the μCHX .

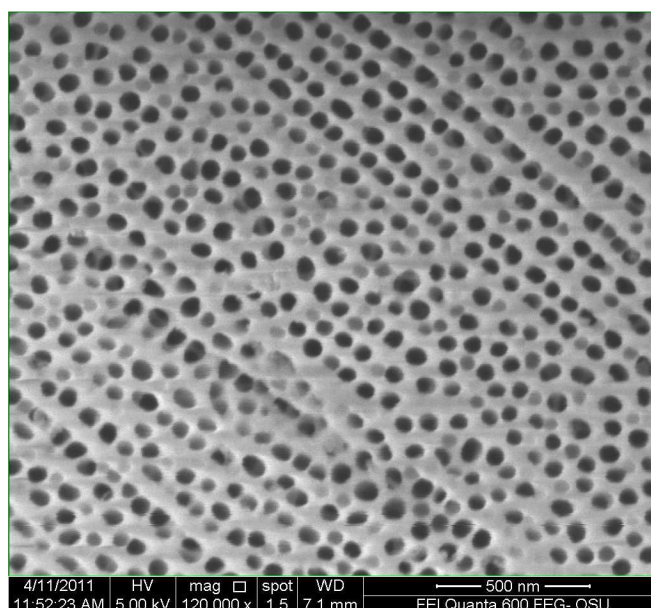


Fig. D.1: Anodized aluminum prior to catalyst deposition

D.2. Palladium/Carbon Paint

For the hydrogen combustor oil heat exchanger developed by Sandia National Labs [7], carbon supported palladium was mixed into a high temperature furnace paint and was painted onto the combustor to act as a catalyst. However, sufficient details were not provided in the report to exactly reproduce their catalyst. In an effort to produce a similar

catalyst, Corr Paint was purchased to be mixed with Pd/C (10 wt%) from Sigma Aldrich. CP4000 is a silicone based high temperature paint that was expected to be gas permeable. No catalysts were actually prepared or tested using this method.

Appendix E. Initial Testing with Catalyst Shim A

Initial testing of the μ CHX was conducted using catalyst shim A which had sputtered palladium as the catalyst. The μ CHX was initially preheated to around 100 °C with the cartridge heaters. The heaters were then turned off and a 0.4 equivalence ratio H_2 /air mixture was introduced to the μ CHX. Catalyst shim A displayed some reactivity, but could not achieve steady state operation. The time series temperature profile is shown in Fig. E.1. No oil was flowing through the μ CHX for this experiment. A distinct, albeit mild, temperature rise in the combustion channel thermocouples was observed when H_2 was introduced. However as time progressed, these temperatures reached a peak and began to decline. The inability to reach a steady state operating condition is indicative that the catalyst was deactivating as the reaction occurred.

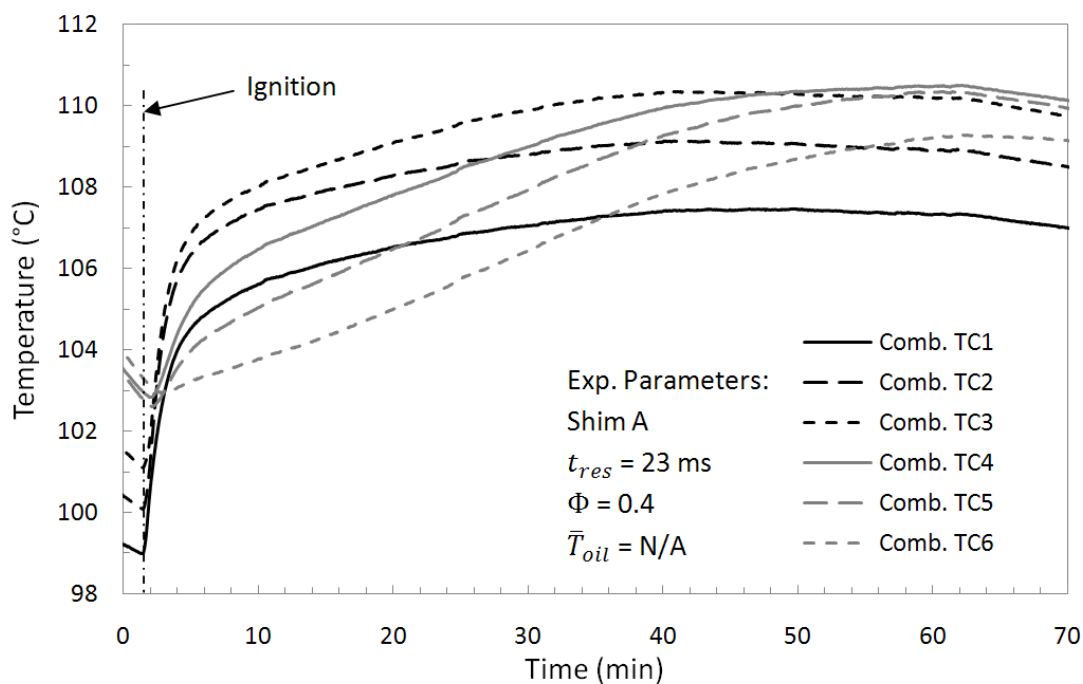


Fig. E.1: Time series temperature profile of catalyst shim A

In an attempt to increase the activity of the catalyst, a reduction procedure for palladium nanoparticles was followed [53]. The μ CHX was brought up to 500 °C with an N_2 flow of 1000 sccm and held at these conditions for 1 hour. Then H_2 at 20 % by volume in N_2 at 500 sccm

was flowed through the μ CHX for 2 hours. The temperature was then increased and held at 600 °C for 1 hour under the H_2/N_2 flow. Upstream valves were then closed, maintaining the H_2/N_2 atmosphere, and the μ CHX was allowed to cool to room temperature.

Subsequent testing indicated that the catalyst was completely deactivated because combustion was not observed at preheat temperatures below 200 °C. Treating the catalyst in air at around 530 °C for 2 hours, based on the pretreatment studies by Burch et al. [54], was found to restore similar reactivity to what was observed prior to the reduction process. No further experiments were performed with catalyst shim A because sufficient reactivity could not be obtained.

Appendix F. Calibration Parameters

Table F.1: Thermocouple Calibration Parameters

Thermocouple	Type	Slope	Intercept (°C)	Curve Fit Uncertainty (°C)	Total Calibration Uncertainty (°C)
TC0	T	0.9973	-0.6084	0.038	0.360
TC1	T	0.9970	-0.5860	0.023	0.357
TC2	T	0.9970	-0.5692	0.039	0.358
TC3	T	0.9972	-0.5286	0.041	0.362
TC4	K	0.9904	-0.0252	0.392	0.529
TC5	K	0.9909	-0.1484	0.382	0.523

Table F.2: Thermocouple Offset Parameters

Thermocouple	Type	Offset (°C)	Offset Uncertainty (°C)
TC6	K	-0.642	0.301
TC7	K	-0.663	0.301
TC8	K	-0.592	0.302
TC9	K	-0.365	0.302
TC10	K	-0.497	0.302
TC11	K	-0.497	0.301
TC12	K	-0.469	0.302
TC13	K	-0.521	0.302
TC14	K	-0.560	0.302
TC15	K	-0.766	0.303

Table F.3: Absolute Pressure Transducer Calibration Parameters

Pressure Transducer	Slope (kPa/V)	Intercept (kPa)	Curve Fit Uncertainty (kPa)	Total Calibration Uncertainty (kPa)
PX32_0	19169.9	-8.71	0.145	0.942
PX32_1	19220.7	1.10	0.218	1.740
PX32_2	19162.8	-5.35	0.173	1.354

Appendix G. Experimental Data

Time averaged and processed data are provided for each experiment.

Table G.1: Data from stability experiments with shims B and C

	Exp. 2	Exp. 3	Exp. 23	Exp. 26	Exp. 27	Exp. 34
Date	4/24/11	4/26/11	5/9/11	5/17/11	5/18/11	5/21/11
Catalyst Shim	B	B	B	C	C	C
\dot{m}_{oil} (g/s)	0.34	0.34	0.32	0.30	0.29	0.28
$T_{exhaust}$ (°C)	139.0	137.3	143.8	128.6	128.8	128.3
$T_{oil,in}$ (°C)	19.1	21.8	18.3	22.1	21.9	22.0
$T_{oil,out}$ (°C)	164.3	167.7	173.2	148.4	148.7	148.3
P_{gas} (bara)	1.633	1.685	1.620	1.491	1.671	1.696
ΔP_{gas} (kPa)	Clipped	Clipped	Clipped	Clipped	Clipped	Clipped
ΔP_{oil} (Pa)	355.4	365.4	367.4	335.6	331.6	334.4
\dot{V}_{gas} (sccm)	2704.0	2703.8	2703.5	2703.4	2703.5	2702.9
Φ	1.0	1.0	1.0	1.0	1.0	1.0
V_{gas} (m/s)	3.14	3.09	3.16	3.49	3.11	3.05
V_{oil} (mm/s)	15.8	15.9	14.8	17.5	17.0	16.7
t_{res} (ms)	21.0	21.4	20.9	4.4	4.9	5.0
\dot{Q}_{H_2} (W)	143.8	143.8	143.7	143.7	143.7	143.7
\dot{Q}_{oil} (W)	133.5	134.7	134.7	100.0	97.5	95.6
Efficiency (%)	92.8	93.7	93.7	69.6	67.8	66.6
$\dot{Q}_{H_2,lost}$ (W)	*	*	*	18.9	18.9	19.8
$\dot{Q}_{exh,rec}$ (W)	*	*	*	1.5	1.5	1.5
$\dot{Q}_{exh,unrec}$ (W)	*	*	*	4.0	4.0	4.0
\dot{Q}_{unmeas} (W)	*	*	*	19.2	21.8	22.7

* GC sample not analyzed, so heat losses could not be accurately characterized

Table G.2: Data from variation of residence time experiments with shim B

	Exp. 10	Exp. 11	Exp. 12	Exp. 13	Exp. 14	Exp. 25
Date	5/3/11	5/3/11	5/3/11	5/3/11	5/5/11	5/10/11
Catalyst Shim	B	B	B	B	B	B
\dot{m}_{oil} (g/s)	0.41	0.34	0.26	0.19	0.11	0.11
$T_{exhaust}$ (°C)	131.3	126.7	123.8	121.2	124.5	118.4
$T_{oil,in}$ (°C)	22.2	22.5	22.5	21.0	18.8	21.5
$T_{oil,out}$ (°C)	149.5	148.5	148.3	148.5	150.4	147.5
P_{gas} (bara)	1.673	37.558	30.857	19.777	13.328	1.185
ΔP_{gas} (kPa)	Clipped	Clipped	30.86	19.78	13.33	13.72
ΔP_{oil} (Pa)	368.0	2255.4	1804.6	1355.0	904.6	273.4
\dot{V}_{gas} (sccm)	2704.9	2255.4	1804.6	1355.0	904.6	905.2
Φ	1.0	2.8	2.5	2.0	1.5	1.0
V_{gas} (m/s)	3.11	5.52	4.82	3.91	2.87	1.47
V_{oil} (mm/s)	18.9	23.3	26.7	32.9	44.9	5.3
t_{res} (ms)	21.2	23.3	26.7	32.9	44.9	44.9
\dot{Q}_{H_2} (W)	143.8	119.9	95.9	72.0	48.1	48.1
\dot{Q}_{oil} (W)	138.4	113.5	88.2	63.4	37.7	38.2
Efficiency (%)	96.2	94.7	91.9	88.0	78.4	79.4
$\dot{Q}_{H_2,lost}$ (W)	7.8	*	5.9	4.1	3.5	3.4
$\dot{Q}_{exh,rec}$ (W)	1.7	*	0.8	0.6	0.4	0.3
$\dot{Q}_{exh,unrec}$ (W)	4.0	*	2.7	2.0	1.3	1.3
\dot{Q}_{unmeas} (W)	-8.0	*	-1.6	2.0	5.1	4.9

* GC sample leaked, so heat losses could not be accurately characterized

Table G.3: Data from variation of residence time experiments with shim C

	Exp. 27	Exp. 28	Exp. 29	Exp. 30	Exp. 31	Exp. 32	Exp. 33	Exp. 34	Exp. 35
Date	5/18/11	5/18/11	5/19/11	5/19/11	5/19/11	5/20/11	5/21/11	5/21/11	5/21/11
Catalyst Shim	C	C	C	C	C	C	C	C	C
\dot{m}_{oil} (g/s)	0.29	0.25	0.21	0.16	0.11	0.07	0.03	0.28	0.13
$T_{exhaust}$ (°C)	128.8	126.6	124.5	123.2	125.3	130.0	135.0	128.3	123.6
$T_{oil,in}$ (°C)	21.9	22.1	22.3	22.4	22.7	23.0	21.3	22.0	21.4
$T_{oil,out}$ (°C)	148.7	148.6	148.5	148.2	147.8	147.9	145.6	148.3	149.1
P_{gas} (bara)	1.671	1.554	1.445	1.336	1.245	1.194	1.144	1.696	1.300
ΔP_{gas} (kPa)	Clipped	Clipped	Clipped	29.52	20.50	14.67	10.60	Clipped	26.40
ΔP_{oil} (Pa)	331.6	319.1	302.2	286.3	266.5	253.4	240.7	334.4	281.7
\dot{V}_{gas} (sccm)	2703.5	2253.5	1803.1	1353.2	903.5	676.9	452.1	2702.9	1126.9
Φ	1.0	1.0	1.0	1.0	1.0	1.0	1.0	1.0	1.0
V_{gas} (m/s)	3.11	2.80	2.41	1.94	1.41	1.10	0.76	3.05	1.66
V_{oil} (mm/s)	17.0	14.9	12.3	9.6	6.2	4.2	2.0	16.7	7.8
t_{res} (ms)	4.9	5.5	6.3	7.8	10.8	13.9	20.0	5.0	9.2
\dot{Q}_{H_2} (W)	143.7	119.8	95.9	72.0	48.0	36.0	24.1	143.7	59.9
\dot{Q}_{oil} (W)	97.5	85.4	70.5	54.5	35.3	23.9	11.0	95.6	45.0
Efficiency (%)	67.8	71.3	73.5	75.8	73.6	66.4	45.9	66.6	75.1
$\dot{Q}_{H_2,lost}$ (W)	18.9	14.7	11.0	0.0	4.1	2.9	2.2	19.8	5.7
$\dot{Q}_{exh,rec}$ (W)	1.5	1.2	0.9	0.6	0.5	0.4	0.3	1.5	0.5
$\dot{Q}_{exh,unrec}$ (W)	4.0	3.3	2.7	2.0	1.3	1.0	0.7	4.0	1.7
\dot{Q}_{unmeas} (W)	21.8	15.1	10.9	14.9	6.8	7.8	9.9	22.7	7.0

Table G.4: Data from variation of equivalence ratio experiments with shim B

	Exp. 8	Exp. 10	Exp. 15	Exp. 16	Exp. 17	Exp. 18	Exp. 19	Exp. 24
Date	4/30/11	5/3/11	5/5/11	5/5/11	5/5/11	5/6/11	5/6/11	5/10/11
Catalyst Shim	B	B	B	B	B	B	B	B
\dot{m}_{oil} (g/s)	0.34	0.41	0.13	0.22	0.31	0.27	0.38	0.18
$T_{exhaust}$ (°C)	131.5	131.3	126.0	125.3	128.3	126.7	131.4	122.8
$T_{oil,in}$ (°C)	19.3	22.2	19.3	19.6	19.5	19.2	19.1	22.1
$T_{oil,out}$ (°C)	150.9	149.5	150.3	150.2	150.2	150.2	150.3	147.9
P_{gas} (bara)	1.718	1.673	1.599	1.533	1.554	1.445	1.556	1.590
ΔP_{gas} (kPa)	Clipped	Clipped	Clipped	Clipped	Clipped	Clipped	Clipped	Clipped
ΔP_{oil} (Pa)	358.2	368.0	281.8	316.5	352.7	321.4	368.4	295.7
\dot{V}_{gas} (sccm)	2705.1	2704.9	2704.5	2704.4	2703.7	2703.5	2703.7	2704.5
Φ	0.8	1.0	0.3	0.5	0.7	0.6	0.9	0.4
V_{gas} (m/s)	2.99	3.11	3.22	3.37	3.32	3.54	3.29	3.27
V_{oil} (mm/s)	15.8	18.9	5.8	10.3	14.3	12.4	17.6	8.6
t_{res} (ms)	22.1	21.2	20.5	19.6	19.9	18.6	20.1	20.2
\dot{Q}_{H_2} (W)	122.3	143.8	54.5	84.5	110.5	97.9	133.3	70.1
\dot{Q}_{oil} (W)	119.7	138.4	44.1	77.7	107.8	93.2	133.0	62.0
Efficiency (%)	97.8	96.2	80.8	92.0	97.6	95.2	99.7	88.5
$\dot{Q}_{H_2,lost}$ (W)	*	7.8	3.2	2.8	2.9	2.4	3.6	1.4
$\dot{Q}_{exh,rec}$ (W)	*	1.7	1.5	1.4	1.5	1.5	1.7	1.3
$\dot{Q}_{exh,unrec}$ (W)	*	4.0	4.2	4.1	4.1	4.1	4.0	4.2
\dot{Q}_{unmeas} (W)	*	-8.0	1.6	-1.6	-5.9	-3.2	-8.9	1.2

* GC sample not analyzed, so heat losses could not be accurately characterized

Table G.5: Data from variation of average oil temperature experiments with shim B

	Exp. 3	Exp. 10	Exp. 20	Exp. 21	Exp. 22	Exp. 23
Date	4/26/11	5/3/11	5/7/11	5/7/11	5/9/11	5/9/11
Catalyst Shim	B	B	B	B	B	B
\dot{m}_{oil} (g/s)	0.34	0.41	0.59	0.47	0.27	0.32
$T_{exhaust}$ (°C)	137.3	131.3	104.8	119.2	156.8	143.8
$T_{oil,in}$ (°C)	21.8	22.2	19.6	19.2	16.9	18.3
$T_{oil,out}$ (°C)	167.7	149.5	107.7	130.5	193.8	173.2
P_{gas} (bara)	1.685	1.673	1.571	1.618	1.650	1.620
ΔP_{gas} (kPa)	Clipped	Clipped	Clipped	Clipped	Clipped	Clipped
ΔP_{oil} (Pa)	365.4	368.0	489.8	407.3	363.2	367.4
\dot{V}_{gas} (sccm)	2703.8	2704.9	2703.6	2703.7	2703.4	2703.5
Φ	1.0	1.0	1.0	1.0	1.0	1.0
V_{gas} (m/s)	3.09	3.11	3.27	3.17	3.09	3.16
V_{oil} (mm/s)	15.9	18.9	27.5	21.6	12.4	14.8
t_{res} (ms)	21.4	21.2	20.2	20.8	21.3	20.9
\dot{Q}_{H_2} (W)	143.8	143.8	143.7	143.7	143.7	143.7
\dot{Q}_{oil} (W)	134.7	138.4	135.0	136.4	130.9	134.7
Efficiency (%)	93.7	96.2	93.9	94.9	91.1	93.7
$\dot{Q}_{H_2,lost}$ (W)	*	7.8	*	*	*	*
$\dot{Q}_{exh,rec}$ (W)	*	1.7	*	*	*	*
$\dot{Q}_{exh,unrec}$ (W)	*	4.0	*	*	*	*
\dot{Q}_{unmeas} (W)	*	-8.0	*	*	*	*

* GC sample not analyzed, so heat losses could not be accurately characterized

Table G.6: Data from variation of average oil temperature experiments with shim B

	Exp. 10	Exp. 27	Exp. 33
Date	5/3/11	5/18/11	5/21/11
Catalyst Shim	B	C	C
\dot{m}_{oil} (g/s)	0.41	0.29	0.03
$T_{exhaust}$ (°C)	131.3	128.8	135.0
$T_{oil,in}$ (°C)	22.2	21.9	21.3
$T_{oil,out}$ (°C)	149.5	148.7	145.6
P_{gas} (bara)	1.673	1.671	1.144
ΔP_{gas} (kPa)	Clipped	Clipped	10.60
ΔP_{oil} (Pa)	368.0	331.6	240.7
\dot{V}_{gas} (sccm)	2704.9	2703.5	452.1
Φ	1.0	1.0	1.0
V_{gas} (m/s)	3.11	3.11	0.76
V_{oil} (mm/s)	18.9	17.0	2.0
t_{res} (ms)	21.2	4.9	20.0
\dot{Q}_{H_2} (W)	143.8	143.7	24.1
\dot{Q}_{oil} (W)	138.4	97.5	11.0
Efficiency (%)	96.2	67.8	45.9
$\dot{Q}_{H_2,lost}$ (W)	7.8	18.9	2.2
$\dot{Q}_{exh,rec}$ (W)	1.7	1.5	0.3
$\dot{Q}_{exh,unrec}$ (W)	4.0	4.0	0.7
\dot{Q}_{unmeas} (W)	-8.0	21.8	9.9

Table G.7: Data from variation of residence time experiments with shim C-rev

	Exp. 36	Exp. 37	Exp. 38	Exp. 39	Exp. 40
Date	5/24/11	5/24/11	5/24/11	5/24/11	5/24/11
Catalyst Shim	C-rev	C-rev	C-rev	C-rev	C-rev
\dot{m}_{oil} (g/s)	0.24	0.17	0.13	0.08	0.06
$T_{exhaust}$ (°C)	106.1	107.2	109.4	115.0	119.8
$T_{oil,in}$ (°C)	22.3	22.3	22.5	21.8	21.2
$T_{oil,out}$ (°C)	157.4	157.6	157.8	157.8	155.0
P_{gas} (bara)	1.576	1.375	1.283	1.198	1.155
ΔP_{gas} (kPa)	Clipped	33.4	24.3	16.0	11.7
ΔP_{oil} (Pa)	315.1	289.4	275.3	260.0	250.0
\dot{V}_{gas} (sccm)	2701.8	1801.3	1351.5	901.5	676.5
Φ	1.0	1.0	1.0	1.0	1.0
V_{gas} (m/s)	3.28	2.53	2.03	1.44	1.12
V_{oil} (mm/s)	14.0	9.9	7.6	4.9	3.3
t_{res} (ms)	4.6	6.0	7.5	10.6	13.6
\dot{Q}_{H_2} (W)	143.7	95.8	71.9	48.0	36.0
\dot{Q}_{oil} (W)	86.1	61.2	46.9	30.2	20.4
Efficiency (%)	59.9	63.8	65.3	63.0	56.6
$\dot{Q}_{H_2,lost}$ (W)	21.5	13.0	9.1	5.5	3.9
$\dot{Q}_{exh,rec}$ (W)	0.3	0.3	0.3	0.3	0.3
$\dot{Q}_{exh,unrec}$ (W)	4.0	2.7	2.0	1.3	1.0
\dot{Q}_{unmeas} (W)	31.8	18.7	13.6	10.7	10.4

Appendix H. Thermal Non-Uniformities in μ CHX

When catalyst shim B was removed from the μ CHX after about 80 hours of combustion operation, discoloration could be seen on the back side of the shim near the beginning of the catalyst region, shown in Fig. H.1. The discoloration is probably due to localized combustion hot spots due to non-uniformities of flow or catalyst activity. Future refinement of the μ CHX or catalyst is needed to mitigate the non-uniformities at the inlet of the combustor channel.

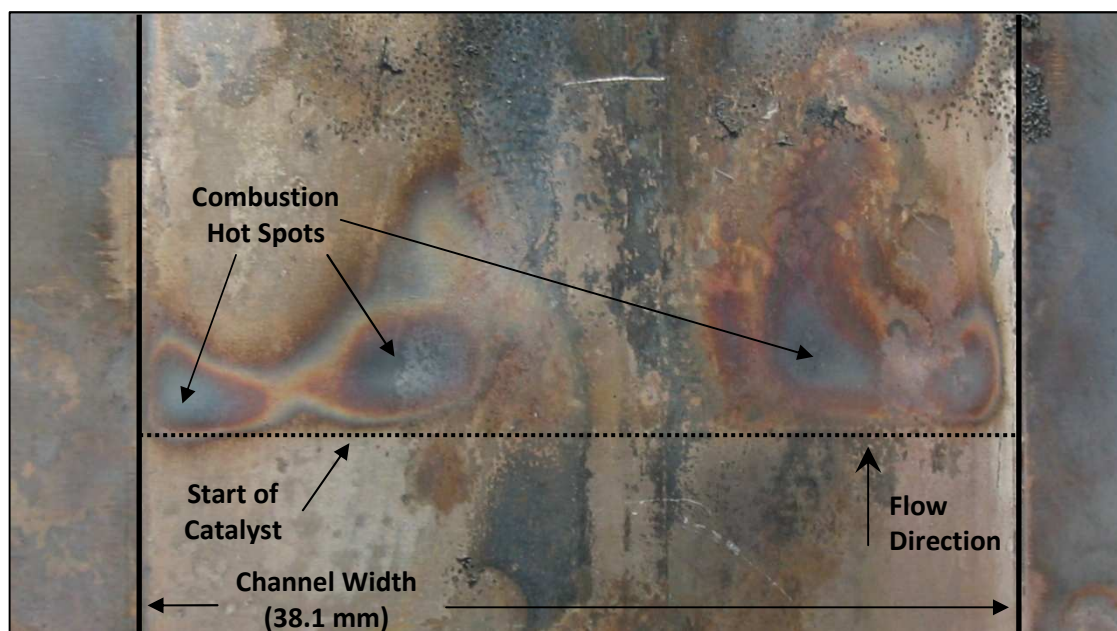


Fig. H.1: Image of back side of catalyst shim B after ~ 80 hours of combustion

All the tests with shim B were conducted without disassembling the μ CHX. When the μ CHX was disassembled, the PEEK insert forming the oil channel was found to have been damaged during the course of the experiments. An image of the damage is shown in Fig. H.2. The PEEK appeared to have melted and reformed. The damage was highly surprising because PEEK has a melting temperature of 340 °C and the highest temperature measured in the combustion channel was around 210 °C. Also, the oil would have been damaged above 300 °C, yet no signs of damaged oil had been observed. The damaged spot on the PEEK was near the inlet and therefore above the hottest section of catalyst. The damage protruded slightly from the surface and had come into contact with the other side of the oil channel. No abnormal performance change was observed between or during any of the experiments, so there is no

way to know which results, if any, had been obtained prior to the damage occurring. The stability experiments demonstrated the repeatability of the results, as demonstrated in this section, so the rest of the results from the experiments conducted with shim B will still be presented and discussed.

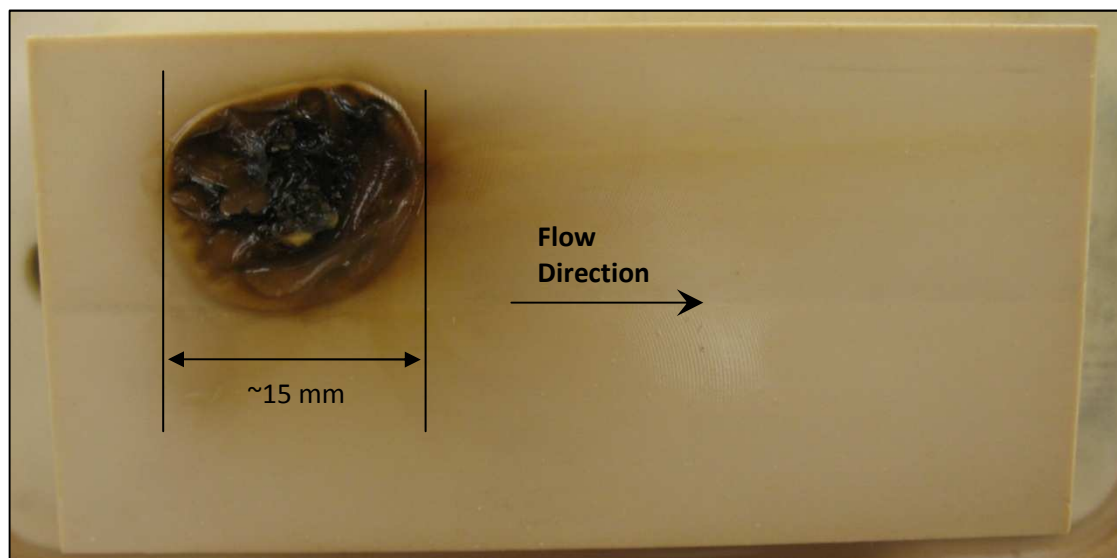


Fig. H.2: Damaged PEEK insert (observed after experiments with shim B had been completed)

Before the μ CHX for the experiments with catalyst shim C, the PEEK insert was repaired. The damaged portion was milled out and filled with J-B Weld. The repaired PEEK insert is shown in Fig. H.3.



Fig. H.3: Repaired PEEK insert

Appendix I. Full Size CHX Calculator

The Excel® worksheet developed to determine the overall size of the combustor for a given heat capacity. An image of the spreadsheet is shown with the formula results in Fig. I.1 and is shown with the formulas in Fig. I.2.

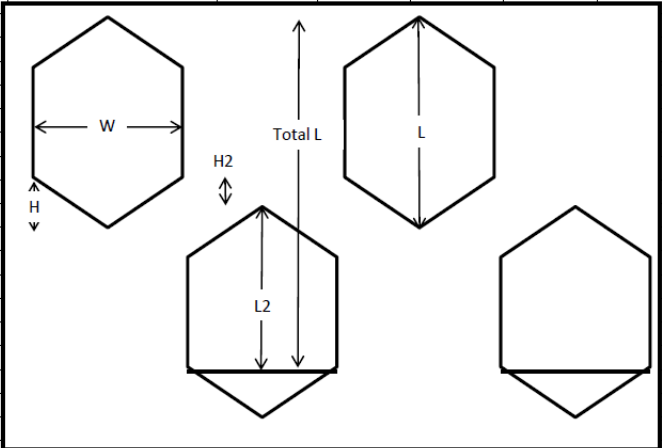
	A	B	C	D	E	F	G	H	I	J
1	Constants					Comb. Channel	Recup. Channel	Inlet Oil Channel	Outlet Oil Header	
2	Length (mm)	30			Height (mm)	0.3	0.15	0.3		
3	Width (mm)	10			Area each (mm^2)	3	1.5	3		
4	Thickness (mm)	0.3			Area Total (mm^2)	3	3	3		
5	Bonding Gap (mm)	1			Total Flow Area (mm^2)	1680	1680	1680	1680	
6	# of Unit Cells	560			Flow area per Hex (mm^2)	120	120	N/A	N/A	
7	Turn length (mm)	0.5			Width (mm)	10		11.00		
8	Heat Gen. per cell (W)	23.7			Length (mm)	17.0		5.45		
9					Height (mm)	5.0				
10	Unit Cell Dimensions				Constriction	50%				
11	Unit Cell Length (mm)	75.31			Length2 (mm)	14.5				
12	Unit Cell Width (mm)	11			Height2 (mm)	3.90				
13	Unit Cell Height (mm)	2.1			Total Length (mm)	30.40				
14	Mass (g)	6.5								
15										
16	Full Scale Size									
17	# long	2								
18	# wide	14	20							
19	# high	20								
20	# of Unit Cells	560								
21	Total Length (mm)	150.6	5.9 (in)							
22	Total Width (mm)	154.0	6.1 (in)							
23	Total Height (mm)	42.0	1.7 (in)							
24	Total Volume (cm^3)	974.2								
25	Total Heat Output (kW)	13.3								
26	Total Mass Estimate (kg)	3.6								
27										
28	Mass for 2 x 14 x 20 CHX									
29										
30										
31	Mass of Top Cap (g)	44.63								
32	Mass of stack (g)	3647.2								
33	Mass of Bottom Cap (g)	63.42								
34	Total Mass (kg)	3.76	1.2673969	32%						

Fig. I.1: Excel® calculator for determining full size CHX dimensions (Bold cells are calculated)

A		B		C		D		E		F		G	
		Constants				Comb. Channel		Recup. Channel		Inlet Oil Channel		Outlet Oil Header	
1	Length (mm)	30	Height (mm)	0.3	$=D2*5853$	0.15	$=E2*5853$	0.3	$=F2*5853$				
2	Width (mm)	10	Area each (mm ²)	$=D2*5853$	$=D2*5853$	$=E2*5853$	$=F2*5853$						
3	Thickness (mm)	0.3	Area Total (mm ²)	$=1*D3$	$=D4*58520$	$=E4*58520$	$=F4*58520$						
4	Bonding Gap (mm)	1	Total Flow Area (mm ²)	$=D4*58520$	$=D4*58520$	$=E4*58520$	$=F4*58520$						
5	# of Unit Cells	560	Flow area per Hex (mm ²)	$=58519*D4^2$	$=58519*D4^2$	$=E4*58520$	$=F4*58520$						
6	Turn length (mm)	0.5	Width (mm)	10	$=58519*D4^2$	$=58519*D4^2$	$=E4*58520$						
7	Heat Gen. per cell (W)	$=71.2/3$	Length (mm)	$=2*D9+(D6-D9*D7)/D7$	$=2*D9+(D6-D9*D7)/D7$	$=E4*58520$	$=F4*58520$						
8			Height (mm)	$=0.5*D7$	$=0.5*D7$	$=E4*58520$	$=F4*58520$						
9			Constriction	$=1-(2*B3+2*B5-(D7+2*B5))/(2*B3)$	$=1-(2*B3+2*B5-(D7+2*B5))/(2*B3)$	$=E4*58520$	$=F4*58520$						
10	Unit Cell Length (mm)	$=B5+B2+B5+(F4*B19)/(B5+B3)+D13+B5+B8+B5$	Length2 (mm)	$=D9+(D6-D5*D9*D7)/D7$	$=D9+(D6-D5*D9*D7)/D7$	$=E4*58520$	$=F4*58520$						
11	Unit Cell Width (mm)	$=B5+B3$	Height2 (mm)	$=2*(D9+2*5855)/SQRT(2)-(B3*(1-D10)+5855)$	$=2*(D9+2*5855)/SQRT(2)-(B3*(1-D10)+5855)$	$=E4*58520$	$=F4*58520$						
12	Unit Cell Height (mm)	$=F2*B4+E2*B4+D2*B4+E2*B4$	Total Length (mm)	$=D12+D11+D8-D9$	$=D12+D11+D8-D9$	$=E4*58520$	$=F4*58520$						
13	Mass (g)	$=182.36/(2*14)$											
14													
15													
16													
17	# long	2											
18	# wide	14											
19	# high	$=ROUND(B6/PRODUCT(B17:B18),0)$											
20	# of Unit Cells	$=PRODUCT(B17:B19)$											
21	Total Length (mm)	$=B17*B11$											
22	Total Width (mm)	$=B18*B12$											
23	Total Height (mm)	$=B19*B13$											
24	Total Volume (cm ³)	$=PRODUCT(B21:B23)/1000$											
25	Total Heat Output (kW)	$=B20*B8/1000$											
26	Total Mass Estimate (kg)	$=B20*B14/1000$											
27													
28													
29													
30													
31	Mass of Top Cap (g)	44.63											
32	Mass of stack (g)	$=182.36*B19$											
33	Mass of Bottom Cap (g)	63.42											
34	Total Mass (kg)	$=SUM(B29:B33)/1000$											

Fig. I.2: Excel® calculator for determining full size CHX dimensions (Formulas shown)

Appendix J. Calculations for Financial Analysis

Sensitivity Parameters		Year	0	1	2	3	4	5
Market Share	10%	Sales (units)	0	20000	40000	45000	47000	51000
Profit Margin	50%	Sales Price per unit	\$ 510.63	\$ 510.63	\$ 510.63	\$ 510.63	\$ 510.63	\$ 510.63
		Sales Revenue	\$ -	\$ 10,212,573	\$ 20,425,146	\$ 22,978,290	\$ 23,999,547	\$ 26,042,062
EXPENSES								
		Initial Tools	\$ 1,167,234	\$ -	\$ -	\$ -	\$ -	\$ -
		Tooling 547xli-30	\$ -	\$ -	\$ -	\$ -	\$ -	\$ -
		Tooling "Stacker"	\$ 296,400	\$ 592,800	\$ 652,080	\$ 652,080	\$ 711,360	\$ 770,640
		Tooling "Welder"	\$ 572,000	\$ 1,144,000	\$ 1,144,000	\$ 1,144,000	\$ 1,716,000	\$ 1,716,000
		Facility	\$ 3,168,800	\$ 3,168,800	\$ 3,168,800	\$ 3,168,800	\$ 3,168,800	\$ 3,168,800
		Labor & Maintenance	\$ -	\$ 734,148	\$ 734,148	\$ 734,148	\$ 734,148	\$ 734,148
		L&M 547xli-30	\$ -	\$ -	\$ -	\$ -	\$ -	\$ -
		L&M "Stacker"	\$ -	\$ 133,000	\$ 266,000	\$ 292,600	\$ 292,600	\$ 319,200
		L&M "Welder"	\$ -	\$ 56,750	\$ 113,500	\$ 113,500	\$ 113,500	\$ 170,250
		Raw Materials	\$ -	\$ 4,219,000	\$ 8,438,000	\$ 9,492,750	\$ 9,914,650	\$ 10,758,450
		Consumables	\$ -	\$ 1,804,800	\$ 3,609,600	\$ 4,060,800	\$ 4,241,280	\$ 4,602,240
		Utilities	\$ 25,112	\$ 201,982	\$ 378,853	\$ 423,070	\$ 440,757	\$ 476,132
		TOTAL EXPENSES	\$ 5,229,546	\$ 12,055,280	\$ 18,504,980	\$ 20,081,748	\$ 21,333,095	\$ 22,715,859
		Annual	\$ (5,229,546)	\$ (1,842,707)	\$ 1,920,166	\$ 2,896,542	\$ 2,666,452	\$ 3,326,202
		Cumulative	\$ (5,229,546)	\$ (7,072,252)	\$ (5,152,086)	\$ (2,255,545)	\$ 410,907	\$ 3,737,110

Fig. J.1: Calculations for financial analysis, years 0 – 5

Year	6	7	8	9	10
Sales (units)	55000	65000	80000	95000	115000
Sales Price per unit	\$ 510.63	\$ 510.63	\$ 510.63	\$ 510.63	\$ 510.63
Sales Revenue	\$ 28,084,576	\$ 33,190,863	\$ 40,850,293	\$ 48,509,723	\$ 58,722,296
EXPENSES					
Initial Tools	\$ -	\$ -	\$ -	\$ -	\$ -
Tooling 547xli-30	\$ -	\$ -	\$ -	\$ -	\$ -
Tooling "Stacker"	\$ 948,480	\$ 1,185,600	\$ 1,422,720	\$ 1,719,120	\$ 2,074,800
Tooling "Welder"	\$ 2,288,000	\$ 2,288,000	\$ 2,860,000	\$ 4,004,000	\$ 4,576,000
Facility	\$ 3,168,800	\$ 3,168,800	\$ 3,168,800	\$ 3,168,800	\$ 3,168,800
Labor & Maintenance	\$ 734,148	\$ 734,148	\$ 734,148	\$ 734,148	\$ 734,148
L&M 547xli-30	\$ -	\$ -	\$ -	\$ -	\$ -
L&M "Stacker"	\$ 345,800	\$ 425,600	\$ 532,000	\$ 638,400	\$ 771,400
L&M "Welder"	\$ 170,250	\$ 227,000	\$ 227,000	\$ 283,750	\$ 397,250
Raw Materials	\$ 11,602,250	\$ 13,711,750	\$ 16,876,000	\$ 20,040,250	\$ 24,259,250
Consumables	\$ 4,963,200	\$ 5,865,600	\$ 7,219,200	\$ 8,572,800	\$ 10,377,600
Utilities	\$ 511,506	\$ 599,941	\$ 732,594	\$ 865,247	\$ 1,042,117
TOTAL EXPENSES	\$ 24,732,433	\$ 28,206,438	\$ 33,772,461	\$ 40,026,514	\$ 47,401,365
Annual	\$ 3,352,143	\$ 4,984,424	\$ 7,077,832	\$ 8,483,209	\$ 11,320,931
Cumulative	\$ 7,089,253	\$ 12,073,677	\$ 19,151,509	\$ 27,634,717	\$ 38,955,649

Fig. J.2: Calculations for financial analysis, years 6 – 10

Year	11	12	13	14	15
Sales (units)	140000	170000	200000	245000	290000
Sales Price per unit	\$ 510.63	\$ 510.63	\$ 510.63	\$ 510.63	\$ 510.63
Sales Revenue	\$ 71,488,012	\$ 86,806,872	\$ 102,125,732	\$ 125,104,022	\$ 148,082,311
EXPENSES					
Initial Tools	\$ -	\$ -	\$ -	\$ -	\$ -
Tooling 547xli-30	\$ -	\$ -	\$ 318,656	\$ 318,656	\$ 318,656
Tooling "Stacker"	\$ 2,549,040	\$ 2,964,000	\$ 3,675,360	\$ 4,327,440	\$ 5,098,080
Tooling "Welder"	\$ 5,720,000	\$ 6,864,000	\$ 8,580,000	\$ 9,724,000	\$ 12,012,000
Facility	\$ 3,168,800	\$ 3,168,800	\$ 3,168,800	\$ 3,168,800	\$ 3,168,800
Labor & Maintenance	\$ 734,148	\$ 734,148	\$ 734,148	\$ 734,148	\$ 734,148
L&M 547xli-30	\$ -	\$ -	\$ -	\$ 78,020	\$ 78,020
L&M "Stacker"	\$ 931,000	\$ 1,143,800	\$ 1,330,000	\$ 1,649,200	\$ 1,941,800
L&M "Welder"	\$ 454,000	\$ 567,500	\$ 681,000	\$ 851,250	\$ 964,750
Raw Materials	\$ 29,533,000	\$ 35,861,500	\$ 42,190,000	\$ 51,682,750	\$ 61,175,500
Consumables	\$ 12,633,600	\$ 15,340,800	\$ 18,048,000	\$ 22,108,800	\$ 26,169,600
Utilities	\$ 1,263,205	\$ 1,528,511	\$ 1,793,816	\$ 2,191,775	\$ 2,589,733
TOTAL EXPENSES	\$ 56,986,793	\$ 68,173,058	\$ 80,519,780	\$ 96,834,838	\$ 114,251,087
Annual	\$ 14,501,220	\$ 18,633,814	\$ 21,605,952	\$ 28,269,183	\$ 33,831,225
Cumulative	\$ 53,456,868	\$ 72,090,682	\$ 93,696,635	\$ 121,965,818	\$ 155,797,043

Fig. J.3: Calculations for financial analysis, years 11 – 15